PhD-FSTM-2020-24

The Faculty of Science, Technology and Medicine

DISSERTATION

Defence held on 29/06/2020 in Esch-sur-Alzette

to obtain the degree of

DOCTEUR DE L'UNIVERSITÉ DU LUXEMBOURG

EN PHYSIQUE

by

Alberto LOMUSCIO
Born on 01 August 1991 in Andria (Italy)

OPTICAL DEFECT SPECTROSCOPY IN $CuInS_2$ THIN FILMS AND SOLAR CELLS

Dissertation defence committee

Dr. Susanne Siebentritt, dissertation supervisor
Professor, Université du Luxembourg

Dr. Simona Binetti
Professor, University of Milano-Bicocca

Dr. Thomas Schmidt, Chairman
Professor, Université du Luxembourg

Dr. Roland Scheer
Professor, Martin-Luther-University of Halle-Wittenberg

Dr. Alex Redinger, Vice Chairman
Professor, Université du Luxembourg

Contents

Abstract

Pure-sulphide $Cu(In,Ga)S_2$ solar cells have reached certified power conversion efficiency as high as 15.5 %. While this record performance has been achieved by growing the semiconducting absorber at very high temperature with a copper deficient composition, all other previous records were based on chalcopyrite films deposited under Cu excess. Still, this world record is far from the theoretical power conversion achievable in single junction solar cell for this semiconductor (about 30 %), which has a tunable band gap between 1.5 and 2.4 eV.

This thesis aims to gain insight into the optoelectronic properties of this semiconductor, particularly $CuInS_2$, looking at their variation as a function of the deposition temperature and of the absorber composition. The investigations are carried out mainly by photoluminescence (PL) spectroscopy, which allows to measure the quasi Fermi level splitting (QFLS), that is an upper limit of the maximum open circuit voltage (V_{OC}) an absorber is capable of. PL spectroscopy is used to get insights onto the electronic defects as well, both the shallow ones, which contribute to the doping, and the deep ones, which enhance non-radiative recombination.

By increasing the Cu content in the as-grown compositions, the morphology and microstructure of the thin films improve, as they show larger grains and less structural defects than films deposited with Cu deficiency. The composition affects the QFLS as well, which is significantly higher for sample deposited under Cu excess, in contrast to the observations in selenide chalcopyrite. The increment of the process temperature leads to an improvement of the QFLS too, although absorbers grown in Cu deficiency are less influenced, likely because of a lower sodium content in the high-temperature glass used as substrate. The QFLS increase correlates with the lowering of a deep defect related band, which manifests itself with a peak maximum at around 0.8 eV in room temperature PL spectra.

In literature, the low efficiencies exhibited by $Cu(In,Ga)S_2$–based solar cells are often attributed to interface problems at the p-n junction, i.e. at the absorber-buffer layer interface. In this work, the comparison of the QFLS and V_{OC} of pure sulphides CIGS with those measured on selenides clearly points out that the lower efficiencies exhibited by the former are caused also by the intrinsic lower optoelectronic quality of $Cu(In,Ga)S_2$ films.

To shed light on the electronic structure, high quality $CuInS_2$ films are deeply investigated by means of low temperature PL. Four shallow defects are detected: one shallow donor at about 30 meV from the conduction band and three shallow acceptors at about 105, 145 and 170 meV from the valence band. The first of these acceptors dominates the band edge luminescence of sample grown with composition close to the stoichiometry, whereas the second deeper acceptor is characteristic of absorbers deposited in Cu rich regime. The deepest of these acceptors seems to be present over a wide range of compositions, although its luminescence is observable only for slight Cu-poor samples with sodium incorporation during the deposition. The quality of the examined films allows the observations of phonon coupling of these shallow defects for the first time in this semiconductor. All these observations on shallow defects and their phonon coupling behaviour allowed to revise the defect model for this semiconductor.

The findings of this thesis reveal the strong similarity of the shallow defects structure with selenium based compounds. On the other hand, the presence of deep defects in $CuInS_2$ strongly limits the optoelectronic quality of the bulk material, causing the gap in power conversion efficiencies compared to low-band gap $Cu(In,Ga)Se_2$ solar cells, which show efficiencies above 23%.

Chapter 1
Introduction

At the time of writing this thesis, the entire world has been facing a pandemic crisis caused by the SARS-CoV-2 virus. The combination of health and economic crises leads to consider this pandemic "*the most challenging crisis the world faces since the Second World War*" as warned by Antonio Guterres, secretary general of the United Nations [1]. The number of people involved in this crisis has risen up to billions within few months, taking into account those under confinement. The hope to solve the health crisis resides in a vaccine, which hopefully should be ready to be used in 12-18 months, i.e. in 2021. But there is another crisis that the humankind has to face, which is the climate change.

Actually, the climate change is already on the rise and the risk is that the pandemic crisis overshadows the climate one, postponing new policy initiatives. One of these is the "Green deal" initiative launched by Ursula von der Leyen, president of the European Commission [2]: one of the priorities is the carbon neutrality by 2050, which is a step needed to limit the global warming to 1.5 Celsius degree, as laid down in the Paris agreement [3]. This can be achieved by a drastic reduction of the greenhouse gas emissions, above all CO_2; this goal, in turn, can be reached by boosting the power generation by means of renewable energies, such as photovoltaics.

Photovoltaics market has been growing very fast in the last 10 years, with an annual growth rate of PV installation of about 37 % and with a total cumulative installations of about 490 GWp at the end of 2018 [4]. With such high growth rate, most of the scenarios have been readjusted as they repeatedly "underestimated the potential of the solar energy" [5].

The annual PV production is dominated by the silicon technology, with a market share that exceeds 90 % considering both mono and multi crystalline silicon. Among thin film technologies, cadmium telluride (CdTe) and copper indium gallium di-selenide ($Cu(In,Ga)Se_2$ or CIGSe) have the highest market share [4], with cell efficiencies of 22.1 % and 23.35 %, respectively [6]. PV systems based on thin films have a lower life cycle carbon emissions per kilowatt hour compared to silicon [7] (the main source of emissions for PV is given by the production and installation of the system). Additionally, thin film based solar cells can be made flexible and lightweight [8] making them an attractive technology for a variety of applications, such as building integrated photovoltaics (BIPV).

The efficiency of the PV systems is an essential aspect to enhance further the use of photovoltaic as established alternative for power generation. The efficiencies of photovoltaic devices can be significantly improved by using multijunction (or tandem) solar cells. This solution is based on stacking onto each other two or more solar cells, each of them optimized to absorb a certain portion of the solar spectrum: in this way, the Shockley-Queisser limit for single junction can be overcome [9]. Si and CIGSe technologies, reaching efficiencies above 23 % (on lab scale), are the preferred candidates for bottom cells to absorb the near infrared region (NIR) of the solar spectrum, as they have a band gap (E_G) around 1.1 eV (the band gap of CIGSe absorbers can be tuned between 1.0 and 1.7 eV, by varying the gallium content in the alloy, but the highest efficiencies are achieved with band gap about 1.1 eV [10]). Most of the research on tandem solar cells is focused on perovskite cells on top of Si or CIGSe as bottom cell [11-14] with efficiencies as high as 29.1 % and 24.2 %, respectively [15]. Still, the development of perovskite based solar systems is hindered by stability issues characterizing this technology [16].

Copper indium gallium disulphide ($Cu(In,Ga)S_2$ or CIGS) is a system closely related to CIGSe and potentially a good candidate for top cell. The band gap of this semiconducting material can be tuned between 1.5 eV (pure $CuInS_2$) and 2.5 eV (pure $CuGaS_2$) [17], thus matching well the solar spectrum for energy conversion both for single- and multijunction devices [18]. Furthermore, several industrial producers of chalcopyrite solar cells use a sulphur rich surface with a composition close to $CuInS_2$ [19, 20], including the current champion device with a power conversion efficiency of 23.35 % [10].

Besides alloying with gallium (which leads to a band gap widening), the chalcopyrite CIGS material can tolerate deviations from the stoichiometric point when the final [Cu]/ ([Ga] + [In]), or CGI, is < 1; in this case the absorbers are named “Cu-poor”. On the other hand, when there is an excess of copper during the deposition, leading to as-grown compositions with CGI > 1, the final films consist of a stoichiometric chalcopyrite phase and of a secondary phase Cu_xS [21]: CIGS films grown in these condition are named “Cu-rich”.

One of the first solar cells based on $CuInS_2$ (composition not given) has been fabricated in late 1980’s [22] and was showing an efficiency of 7.3 %. In the following years, efforts have been undertaken to boost the performance of solar devices based on this material, either pure CIS or alloying with gallium to form CIGS [23-25], all of them based on Cu-rich thin films; those based on films deposited under Cu-deficiency have shown always lower power conversion efficiencies. The last certified record efficiency of pure sulphide based solar cell is 15.5 %, achieved in 2016 at Solar Frontier laboratories [26]. This last achievement represented a breakthrough for this material and was made possible by a significant increment of the process temperature during the growth of the absorber (above those used traditionally, i.e. > 590 °C) and by using Cu-poor CIGS absorbers [27].

Still, $Cu(In,Ga)S_2$-based solar cells suffer from a low efficiency if compared to their counterpart $Cu(In,Ga)Se_2$-based solar cells. This is mainly caused by a low open circuit voltage (V_{OC}) in CIGS solar cells with respect to the band gap in the sulphide solar cells. Considering the champion sulphide device, a V_{OC} loss, defined as E_G/q - V_{OC}, of about 650 mV is found, whereas for selenide-based solar cells the V_{OC} loss is only about 350 mV [10].

In this context, with the last record efficiency achieved by using a Cu-poor CIGS absorber grown at very high temperature but still with a high Voc loss, this thesis aims to bring new insights into the optoelectronic quality of $CuInS_2$, which is part of the record efficiency alloy. Particularly, this thesis will focus on the effects driven by the change of the deposition temperature and by the variation of the as-grown composition. The characterization of the absorbers has been conducted mainly by photoluminescence (PL) spectroscopy: it is a non-destructive and contactless technique, it does not require a specific sample preparation prior to the measurements and can be used to investigate bare absorbers, i.e. without additional layers needed for a finished photovoltaic device. Given the importance of this technique for the achievement of the results discussed throughout this thesis, the basic principles of the PL spectroscopy are explained in detail in chapter 2, together with the experimental setup used to carry out the experiments. The same chapter starts with a discussion on the crystal structure of $CuInS_2$ and its phase diagram, along with a section on point defects that might be present in the compound. A general overview on the working principles of a photovoltaic device based on p-n junction is given as well in chapter 2, which ends up with a review on point defect models developed for $CuInS_2$ over the years.

Chapter 3 introduces the physical vapour deposition system which has been used to deposit the thin films analysed and discussed in this work. This machine has been built up at the beginning of this thesis; putting it into service has been the first task of this thesis work. Therefore along with its description, the deposition processes optimized to grow the CIS films are explained, describing the differences between one- and two-stage deposition and between Cu-poor and Cu-rich growth conditions. This chapter discusses the effects of composition and deposition temperature on (micro) structural properties observed experimentally by scanning electron microscopy (SEM), X-Ray diffraction (XRD) and transmission electron microscopy (TEM).

Chapter 4 contains the PL analysis performed at room temperature to extract the quasi Fermi level splitting (QFLS), which is an upper limit of the open circuit voltage. Firstly, the stability of the QFLS is studied when absorbers are exposed to air, to find out whether they need a passivation layer to avoid degradation. Then, the effects of the absorber composition and processing temperature on the QFLS and deep defects are investigated, looking also at the change of the V_{OC} of the corresponding finished devices. This chapter ends with a comparison of QFLS and V_{OC} between selenides and sulphides absorbers, to shed light on the intrinsic limitations of the latter, which accordingly lead to lower efficiencies in the final devices.

Chapter 5 presents a deep investigation on the electronic structure of $CuInS_2$ films. Particularly shallow defects, which contribute to the doping of a semiconductor, are analysed and their presence is correlated to the growth conditions (such as composition). The phonon coupling behaviour of these shallow defects, observed for the first time for this material, is described as well: it has a significant influence on the interpretation of the results and leads to a revision of the previous models for shallow defects. Moreover, some preliminary results about two deep defect related PL bands are introduced. Finally, a revised recombination model is proposed and compared to previous findings obtained experimentally or by theoretically calculations.

Chapter 6 gives a summary of the results discussed throughout this thesis together with an outlook.

Chapter 2
Fundamentals and review

In the following chapter, an introduction on the crystal structure of Cu(In,Ga)S_2 is given, discussing the chalcopyrite structure, which characterizes this material (section 2.1) , and its phase diagram (section 2.2). An overview of possible intrinsic point defects that may be present in such structure is given in section 2.3. Section 2.4 will discuss the basics about the p-n junction and photovoltaic solar cell, showing briefly the main parameters and potential losses of a device. Photoluminescence (PL) spectroscopy is the main techniques used in the framework of this thesis, therefore the entire section 2.5 is dedicated to the discussion of its basic principles with the typical transitions that can be observed in standard measurements, both at room and low temperature. This section includes a description of the experimental setup used to carry out the measurements as well as the evaluation procedure to extract quasi Fermi level splitting values from absolute calibrated PL.

Finally, this chapter ends up with section 2.6, which gives a review about the defects models developed over the years for the $CuInS_2$ system, both those derived experimentally and those theoretically calculated. These defects models will be compared in chapter 5 to the new recombination model proposed in this thesis.

2.1 Chalcopyrite structure

Copper indium disulphide ($CuInS_2$) has a chalcopyrite (CP) crystal structure. The term chalcopyrite comes from the mineral copper iron disulphide ($CuFeS_2$) which can be found naturally. The chalcopyrite structure has tetragonal symmetry and can be considered as a superstructure of the zinc blende (ZB). Both structures, ZB and CP, are depicted in figure 2.1.

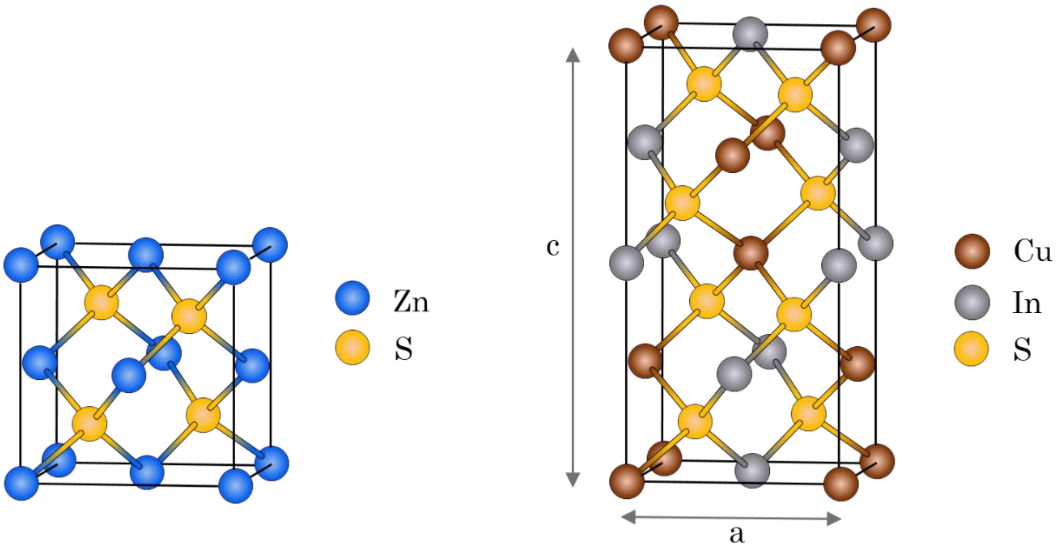

Figure 2.1: (left) unit cell of the zinc blende structure in the case of zinc sulphide (ZnS) crystal; (right) unit cell of the chalcopyrite structure in the case of copper indium disulphide ($CuInS_2$) crystal.

The zinc blende structure has a face-centered cubic structure with lattice sites occupied by the element of the group II (Zn in the figure) and of the group VI (S in the figure), respectively. Crystals made up of III-V group elements may crystallize in ZB structure as well: by way of example, in the photovoltaic field, gallium arsenide (GaAs) has a ZB structure. The chalcopyrite structure can be obtained from the zinc blende one by replacing the atoms of the group II (bivalent, as zinc in the figure) in the ZB alternately with the atom of the group I (monovalent, as Cu in the figure) and group III (trivalent, as In in the figure). The introduction of an additional element in the cation sub-lattice reduces the symmetry for the CP structure. The higher complexity of the CP structure compared to the ZB one requires the introduction of two parameters, which are the tetragonal distortion (η) and the anion displacement (u), respectively, defined as follows:

$$\eta = c/2a \qquad \text{eq. 2.1}$$

$$u = \frac{1}{4} + \frac{R_{AC}^2 - R_{BC}^2}{a^2} \qquad \text{eq. 2.2}$$

with a lattice constant along x and y directions and c lattice constant along the z direction, while R_{AC} and R_{BC} are the bond lengths between the anion C and the cation A and B, respectively, assuming the notation $A^I B^{III} C_2^{VI}$ for the CP compound.

For the ZB structure, η and u are 1 and ¼, respectively, whereas for CP structure these two parameters deviate from these values because of the different bond lengths R_{AC} and R_{BC}. The tetragonal distortion for $CuInS_2$ is $\eta = 1.008$, as determined from equation 2.1 by using the values measured in [28] for the lattice constants a and c (i.e. 5.5214 Å and 11.1301 Å, respectively, which are very close to the lattice constants measured in [29]). A value above 1 for η means the CP unit cell is slightly dilated along the c-axis. The tetragonal distortion leads to additional peaks observed in X-ray diffractograms, as will be shown and discussed in chapter 3. The parameter u describes the displacement of the anion from its ideal tetrahedral site. Specifically for $CuInS_2$, the Cu-S bond is estimated to be shorter than In-S one [29], thus the S atoms slightly move towards the Cu atoms.

By partially replacing atoms in the compound $A^I B^{III} C_2^{VI}$ with isovalent substitutions, such as alloying with Ga, it is possible to get still a CP crystal structure keeping the number of electrons per site unchanged. The two systems $CuInS_2$ and $CuGaS_2$ have shown complete solid solubility over the whole composition [28] to form the quaternary compound $CuIn_{1-x}Ga_xS_2$, with x called also GGI to refer to the ratio of the trivalent metals contents, i.e. [Ga]/([Ga]+ [In]).

Both $CuInS_2$ and $CuGaS_2$ have absorption coefficients in the range of 10^4-10^5 cm^{-1} [30] and the band gap of the quaternary compound $CuIn_{1-x}Ga_xS_2$ can be tuned between 1.52 eV ($x = 0$) and 2.43 eV ($x = 1$) [31] (those values refer to room temperature band gaps). The compositional dependence of the band gap of this solid solution, CIGS, can be expressed by the following equation:

$$E_G = E_G^{CIS}(1 - x) + E_G^{CGS}x - bx(1 - x) \qquad \text{eq. 2.3}$$

with E_G band gap of the alloy $CuIn_{1-x}Ga_xS_2$, E_G^{CIS} band gap of $CuInS_2$, E_G^{CGS} band gap of $CuGaS_2$ and b bowing coefficient. By using the band gaps mentioned above and a bowing coefficient of 0.2 eV [32], the dependence of the alloy band gap on the GGI has been calculated and depicted in figure 2.2.

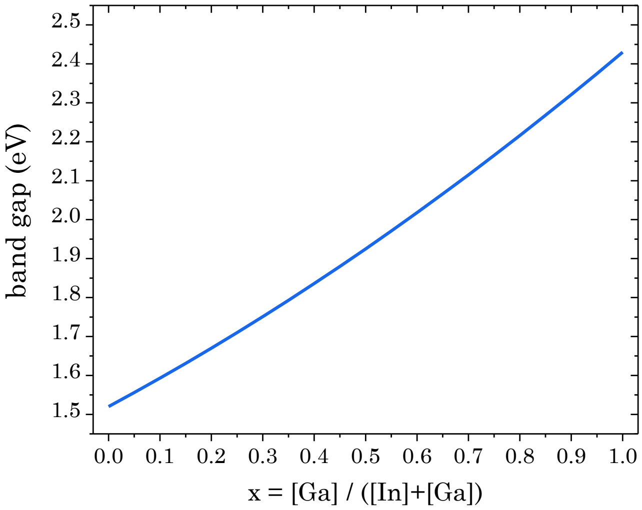

Figure 2.2: dependence of the $CuIn_{1-x}Ga_xS_2$ room temperature band gap on the [Ga]/([Ga]+ [In]) ratio. The evolution of the band gap is calculated with equation 2.3 and using the bowing coefficient of 0.2 eV determined experimentally in [32].

Except two CIGS samples, whose QFLS are discussed in section 4.5, all results presented in this thesis refer to pure $CuInS_2$ absorbers. For this reason, in the next section, only the $CuInS_2$ phase diagram is discussed.

2.2 Phase diagram

The chalcopyrite phase (γ) described in the previous section is not the only phase which can occur during the growth (in the specific case in presence of Cu, In and S). In fact, the presence of multiple phases and their composition are controlled mainly by the temperature at which the growth takes place and by the relative availability of the constituents. The crystal growth aspects of this ternary compound and the phase relations in the system Cu_2S-In_2S_3 were deeply investigated by Binsma et. al in [21] and the resulting phase diagram is depicted in figure 2.3.

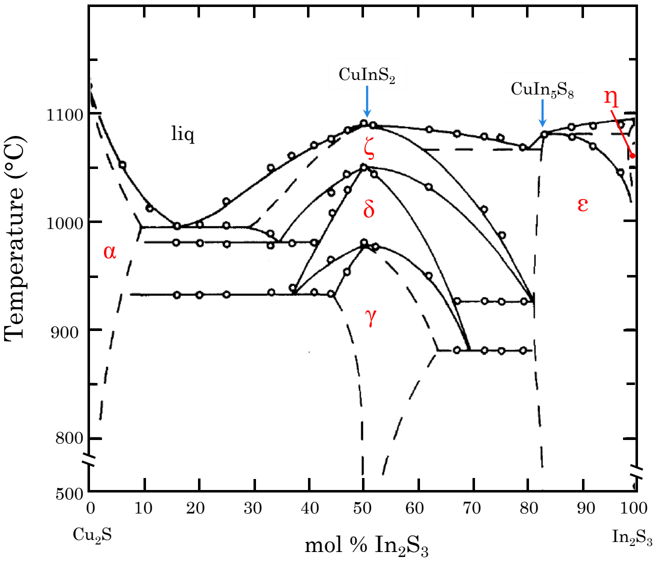

Figure 2.3: Pseudo-binary phase diagram Cu_2S-In_2S_3 as a function of the mol % of In_2S_3 and temperature. Note the break along the temperature-axis. Only the single phase regions are indicated by their respective symbols, e.g. γ for the chalcopyrite phase. Diagram adapted from [21]. The two arrows indicate the melting point of the stoichiometric phases $CuInS_2$ and $CuIn_5S_8$, respectively. The phase diagram aspects close to the melting point of $CuInS_2$ shown in this picture have been confirmed also by [33]

The chalcopyrite γ phase has the stoichiometric point at 50 mol % of In_2S_3. The γ phase is stable up to 980 °C, where $CuInS_2$ has a phase transition to zinc blende (or sphalerite) δ structure: the originally ordered cation sublattice becomes disordered, and Cu and In are randomly distributed on the cation sites. This last phase, in turn, changes structure at about 1045 °C, where it transforms into the wurtzite modification. The melting point of the $CuInS_2$ compound is measured to be 1090 °C. The $CuIn_5S_8$ phase, ε, shows only thiospinel structure up to its melting point, which is 1085 °C. Its homogeneity region extends from about 83 mol % of In_2S_3 to the phase boundary with ε-η two-phase region, where η is the high temperature modification of In_2S_3. This two-phase region, or the homogeneity region of In_2S_2, is not discussed in [21] for temperatures lower than 1000 °C. At first sight, the ε phase seems to exist at 100 % mol of In_2S_3, which can't actually be. The α phase is the Cu_xS phase.

Typically, the process temperatures during the growth of CIS films by coevaporation are below 800 °C. In this thesis temperatures as high as 650 °C have been employed. For those temperatures values (i.e. bottom part of the phase diagram depicted in the figure) the chalcopyrite phase extends up to about 54 % of In_2S_3. Therefore the γ phase can tolerate deviations from the stoichiometric composition (i.e. can be grown off-stoichiometric) into the In_2S_3 side. The CIS films deposited in these conditions will be called in this thesis "Cu-poor", as they have a lack of copper content compared to the stoichiometric value. For higher percentage of the indium-based binary compound, there is co-segregation of chalcopyrite γ and thiospinel ε phases. The tolerance of off-stoichiometric growth is absent in the opposite side, where for $In_2S_3 \leq 50\%$ there is co-segregation of γ and α phases. Therefore the presence of Cu-excess during the growth does not translate into a chalcopyrite phase off-stoichiometric but in a higher amount of Cu_xS phase segregation (together with stoichiometric γ phase). In this thesis samples grown under Cu-excess will be named "Cu-rich" to refer to the deposition conditions although the CIS layers have a composition very close to the stoichiometric value. The Cu/In ratios given in this thesis (unless stated otherwise) will refer to the as-grown samples, thus those values take into account secondary phase if present. Most of the characterizations presented in this thesis (such as photoluminescence) are performed on etched samples, i.e. samples treated in potassium cyanide-(KCN-) containing solutions. This treatment selectively removes Cu_xS phases [34]. This Cu-chalcogenide phase has been found to have a degenerate p-type character [35]. Given this metallic nature, the Cu_xS phase needs to be removed to get working devices, otherwise solar cells would exhibit severe shunting behaviour.

2.3 Point defects

The understanding of the effects of the intrinsic point defects on the optoelectronic properties of CIS thin films is one of the aims of this thesis work, which is focused on electronic aspect of the defects, rather than structural or chemical one. Point defects are responsible for the doping behaviour of a semiconductor as well as for detrimental recombination centers. The growth conditions, besides determining the phases that segregate at a certain relative composition, as shown in the previous section, can drastically change the nature and the amount of specific point defects, thus, e.g. the doping. By way of example, in [23] it has been shown that polycrystalline CIS absorbers grown under slight Cu-poor condition exhibit a doping of about 10^{13} -10^{14} cm^{-3}, whereas those deposited under Cu-rich conditions, after KCN etching, show a doping of about 10^{17} cm^{-3}. A review on defect levels found over the years in $CuInS_2$ is given in section 2.6, while chapter 5 will discuss in detail their dependence on the absorber composition observed in this thesis and will end up with a revised defect model. The correlation between growth conditions and defect levels found experimentally can help to shed light on the chemical nature of the intrinsic defect which give rise to the corresponding defect levels. This can also be supported by theoretical calculations, if available, on the electronic structure and charge transition level within the band gap. Nevertheless, even without taking into account extrinsic point defects which may originate, e.g., from the diffusion of elements from the substrate into the absorber during the growth (above all sodium from soda lime glass), these attributions still remain not straightforward. In fact, in a ternary compound like $CuInS_2$, there are many possible intrinsic point defects which may be present, as listed in the following:

- Vacancies, which originate from atoms missing from their ideal position within the crystal structure, such as V_{Cu}, V_{In} and V_S.
- Interstitials, which originate from atoms placed in positions between crystal lattice sites, like Cu_i, In_i and S_i.
- Antisites, formed when atoms occupy the crystal sites of other atoms of the compound, such as Cu_{In} or In_{Cu}.
- Complexes, which originate from defect pairs, like V_{Cu} - V_S, Cu_i - $2V_{Cu}$ or In_{Cu} - $2V_{Cu}$.

Some of the defects listed above are schematically represented in the chalcopyrite unit cell depicted in figure 2.4. All these defects make the understanding of the electronic structure of this compound very challenging, but at the same time it is necessary to predict, explain and/or control its optoelectronic properties by varying, e.g. the deposition conditions or by employing post deposition treatments.

While the background discussed so far is specific for ternary chalcopyrite compounds, particularly $CuInS_2$, the next section will deal with a more general view about p-n junctions and basic principle of photovoltaic devices that can be applied to other semiconductors as well.

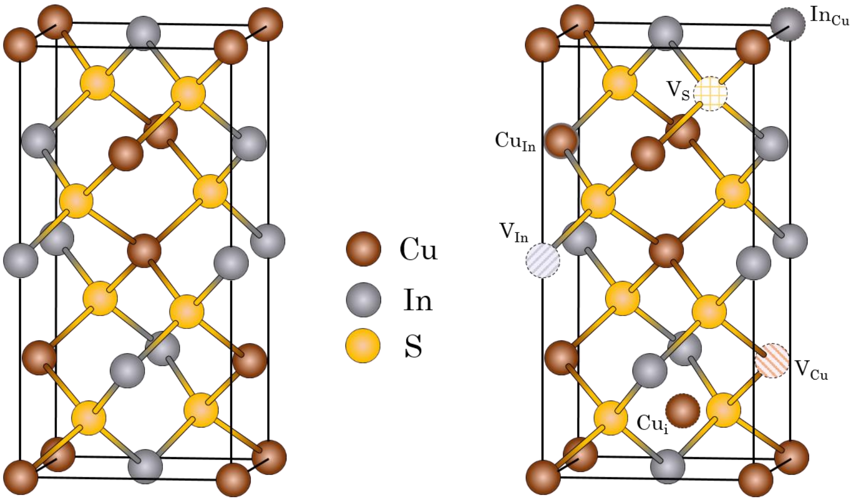

Crystal structure
without point defects

Crystal structure
with point defects

Figure 2.4: schematic representation of a $CuInS_2$ unit cell (left) without point defects and (right) with some of the point defects listed in the main text.

2.4 p-n junction and photovoltaic cells

This section will discuss the basic physical principles of the p-n junction which is the essential part of the photovoltaic cells. Some textbooks have been chosen as references for this section [31, 36, 37], although the physics behind the solar cells can be found in any textbook dealing with this topic. The main parameters characterizing a photovoltaic device will be introduced, together with an overview of the layer stack of the solar cells investigated in this work.

2.4.1 p-n junction in the dark and under illumination

A photovoltaic device absorbs (sun) light and generates electrical power. This process takes place if (i) charge carriers are generated and (ii) they reach the terminals/external contacts before recombining. A semiconductor is the material that best fits these requirements: e.g. the light absorbed by a metal would excite free carriers, which would lose their energy in few picoseconds by thermalization. On the other hand, a semiconductor can absorber light with photon energy higher than its band gap, i.e. $h\omega \geq E_G$. Electron-hole pairs are thus generated by excitation of electrons from the valence band (V.B.) into the conduction band (C.B.). Then, the carriers thermalize to the edge of the corresponding bands within few picoseconds, but the recombination is hampered due to the gap between the two bands, i.e. by the absence of a continuum of states which is present in a metal.

Most of the photovoltaic technologies, including the one discussed in this thesis, i.e. solar cells based on polycrystalline chalcopyrite thin films, use p-n junctions. The contact between two materials of opposite doping (n- and p-type) creates at the junction a space charge region (SCR) which contributes to the photo generated charge carriers separation. The formation of a p-n junction at room temperature can be explained by a Gedankenexperiment, as described in the following. The left side of figure 2.4.1 displays a simplified scheme of the band diagram of a p-type and n-type doped semiconductor, respectively. The position of the Fermi level within the band gap depends on the doping and the effective density of states of the band (V.B. for p-type semiconductor and C.B. for n-type one). The right side of figure 2.4.1 depicts instead the p-n junction (in equilibrium) formed when semiconductors with opposite doping are put into contact with each other. Particularly, a homojunction is formed if the same material is used (with opposite doping, as show in figure 2.4.1); the other case (with two different semiconductors) is called heterojunction.

Due to the different kind of doping, the p-n junction formation gives rise to the gradient in concentration of free charge carriers which leads to the diffusion of electrons from the n-type semiconductor to the p-type one. The same process, but in the opposite direction, takes place for holes. This diffusion currents build up at the same time a positive (negative) charge in the n-type (p-type) semiconductor, highlighted in figure 2.4.1 with a + (−): this, in turn, leads to the creation of an electrical potential difference which opposes the diffusion currents. Under equilibrium, the built-in electrical potential V_{bi} compensates completely the driving force given by the concentration (or chemical) gradients, thus no charge current flows, which translated into a flat electro-chemical Fermi level. Figure 2.4.1 displays two regions on both sides of the p-n junction (but far from the interface) called quasi-neutral regions (QNR): they are regions that are barely affected by the formation of the junction, i.e. regions not depleted of the free carriers.

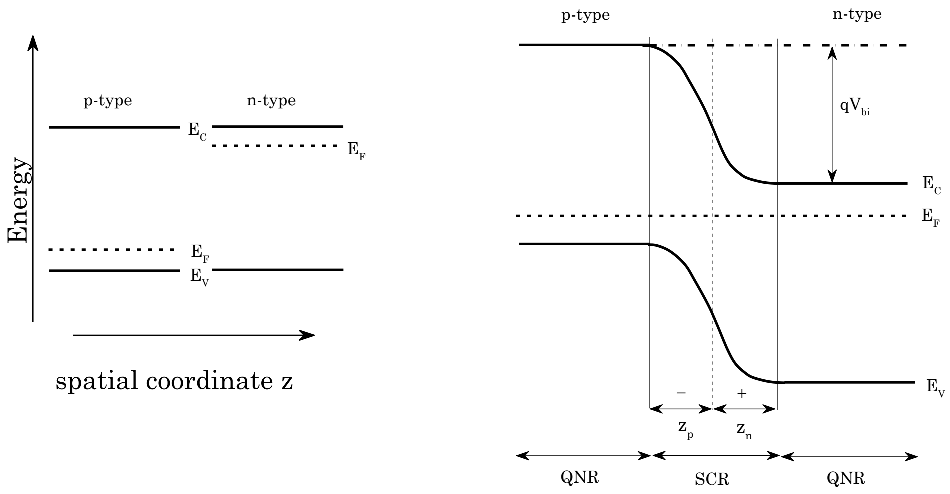

Figure 2.4.1: simplified energy band diagram of two semiconductors, p- and n-type doped respectively, (left) before and (right) after junction formation (in equilibrium). The scheme on the right highlights the formation of a built-in potential V_{bi} and of the quasi neutral regions (QNR) and space charge region (SCR): this last one extends over z_p in the p-type doped semiconductor and z_n in the n-type doped one.

The depletion of the majority charge carriers in each side of the p-n junction (with an extension that depends on the doping) leads to the formation of the depletion or space charge region (SCR). Its total width w is given by the sum of the respective depletion regions in the two semiconductors, i.e. z_p and z_n, and can be varied by applying a voltage V or under illumination. It can be shown that:

$$w = z_p + z_n = \sqrt{\frac{2\epsilon_0\epsilon_r}{q}\left(\frac{1}{N_A}+\frac{1}{N_D}\right)(V_{bi}-V)} \qquad \text{eq. 2.4.1}$$

with ϵ_0 being the vacuum permittivity, ϵ_r the dielectric constant, q elementary charge and N_A and N_D doping concentrations in the p-type and n-type doped semiconductors, respectively. By applying a positive voltage (i.e. a negative voltage to the n-type side and a positive voltage to the p-type side), the potential barrier at the junction is reduced, which leads to a charge carrier current driven by diffusion: electrons move from the n-type semiconductor to the p-type one, whereas holes flow in the opposite direction. An electrical current is thus established through the junction. Due to this injection of non-equilibrium minority carriers, the minority quasi Fermi level (QFL) shifts. This non-equilibrium condition ends up with the formation of the quasi Fermi level splitting (QFLS, which will be discussed more in detail in section 2.5.1). The difference of the electron quasi Fermi level in the n-type semiconductor and the hole quasi Fermi level in the p-type semiconductor is equal to the applied voltage (neglecting ohmic losses). Additionally, as seen from equation 2.4.1, a positive voltage reduces the width of the space charge region. At a given applied voltage, the current density J that flows through the junction is given by the Shockley equation:

$$\mathrm{J} = J_0\left(\exp\left(\frac{qV}{AkT}\right) - 1\right) \qquad \text{eq. 2.4.2}$$

with k Boltzmann constant, T temperature and J_0 saturation current density, which is the current density that flows under reverse bias. A is the diode quality or ideality factor, and its value usually ranges typically within 1 and 2. It gives an indication on how closely the diode works as an ideal one (i.e. A=1).

Under illumination, if the photons impinging the p-n junction have enough energy (i.e. $h\omega \geq E_G$), electron-hole pairs are created. Similarly to the case of an applied voltage, electrons and hole cannot be described by one common electrochemical potential (as under thermal equilibrium); instead, they can be described by the electrons quasi Fermi level $E_{F,n}$ and the holes quasi Fermi level $E_{F,p}$. If a load is connected to the device (which includes the p-n junction), a voltage is built up at the two terminals. Without an external load and with contact connected, the device is short-circuited, i.e. there is not voltage difference between the two contacts but a net current density flows, called short circuit current J_{SC}. The relationship between current density and voltage for a p-n junction under illumination reads:

$$\mathrm{J} = J_0 \left(\exp\left(\frac{qV}{AkT}\right) - 1\right) - J_{ph} \qquad \text{eq. 2.4.3}$$

with J_{ph} photocurrent density. The "–" preceding the J_{ph} highlights that the generated photocurrent flows in the opposite direction compared to the dark diode forward current. For zero applied voltage, the total current density equals the photocurrent density which, with no applied voltage, is J_{SC}. On the other hand, the voltage at which the total current density equals zero is called open circuit voltage V_{OC}. This voltage can be derived from equation 2.4.3 (considering also that $qV_{OC} \gg AkT$) and reads:

$$V_{OC} = \frac{AkT}{q} \ln\left(\frac{J_{ph}}{J_0}\right) \qquad \text{eq. 2.4.4}$$

It is worth mentioning that under illumination the voltage that is built up at the contacts is given by the difference of the electron quasi Fermi level at the n-type doped semiconductor contact and the hole quasi Fermi level at the p-type doped semiconductor contact: in other words, the difference of the quasi Fermi level of the majority carriers. However, the QFLS within the absorber can be also higher than that at the contacts: this occurs, e.g., if interface recombination is present (which is discussed in section 2.4.4). This is the reason why the QFLS measured directly on the absorber itself under illumination (i.e. under open circuit conditions) represents the upper limit of the open circuit voltage that the final device can potentially achieve.

2.4.2 J-V characteristics

Both J_{SC} and V_{OC} are important parameters characterizing a photovoltaic device and can be extracted by measuring the density current-voltage (J-V) characteristics. Figure 2.4.2 gives an example of a J-V characteristics; its measurement allows the determination of the power density ($P = \mathrm{J} \times V$) that a photovoltaic device can generate. P is depicted with a red line in figure 2.4.2, which highlights the maximum (absolute) power density P_m. This power is given by the product $P_m = \mathrm{J}_{mp} \times V_{mp}$. A key parameter to quantify the performance of a photovoltaic device is the power conversion efficiency η, defined as:

$$\eta = \frac{P_m}{P_{in}} = \frac{\mathrm{J}_{mp} \times V_{mp}}{P_{in}} = \frac{V_{OC} \times J_{SC} \times \mathrm{FF}}{P_{in}} \qquad \text{eq. 2.4.5}$$

with FF being the fill factor and P_{in} incident power density. The fill factor is given as the ratio between the maximum power and the product of open circuit voltage and short circuit current, i.e. $\mathrm{FF} = P_m/(V_{OC} \times J_{SC})$: it is a measure of the “squareness” of the J-V curve, as depicted in figure 2.4.2 with green rectangles. The efficiency depends on the incident power density; therefore a standard value is used during the measurements of the J-V curves under illumination, to allow comparison between different cells and above all to simulate the sun light. In fact, solar simulators are usually set to emit a spectrum that “approximates” the AM1.5 solar one, which reflects the solar spectrum incident onto the Earth and corresponding to a solar zenith angle of 48.2°. This incident power is about 1000 W/m^2. AM 1.5 solar simulator has been used in this thesis to carry out J-V measurements.

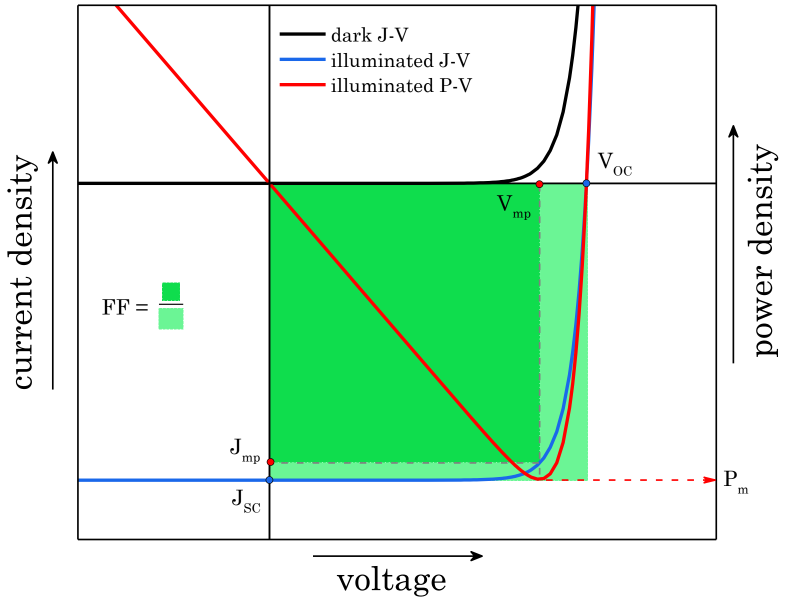

Figure 2.4.2: current density-voltage (J-V) characteristic under dark (black) and under illumination (blue) and power density-voltage curve (red). The maximum power density that can be extracted is indicated as P_m. The main parameters characterizing a solar device are shown as well, together with a visual explanation of the fill factor FF.

2.4.3 $CuInS_2$ solar cell structure

In section 2.4.1 the basic principles about the p-n junction in the dark and under illuminations have been illustrated while in section 2.4.2 the main parameters characterizing a photovoltaic device have bene discussed, such as V_{OC} and J_{SC} . The p-n junction represents the asymmetry which separates the photo generated carriers. However, more layers or components than just a p-n junction (and electrical contacts) are needed to build up a working solar cell. A typical solar cell stack used for $CuInS_2$ absorbers (including those analysed in this work) is shown in figure 2.4.3, together with a cross section acquired by scanning electron microscope of a solar cell fabricated in this work.

The first component of the stack is the substrate, which is commonly a glass, with a thickness of 1 to 3 mm. Alternatively, a flexible substrate could be used (like polyimide foil), which has been employed for the closely related system $Cu(In,Ga)Se_2$ [38]: by using this substrate (compared to a glass) flexible solar cells can be fabricated, with power conversion efficiencies exceeding 20 % [8]. In this thesis two kind of glass have been used: the standard soda lime glass (SLG) and a high temperature glass (HTG): this last one allows process temperatures higher than 600 °C. A comparison of the thermal and chemical properties between the two glasses can be found in appendix 3.1.

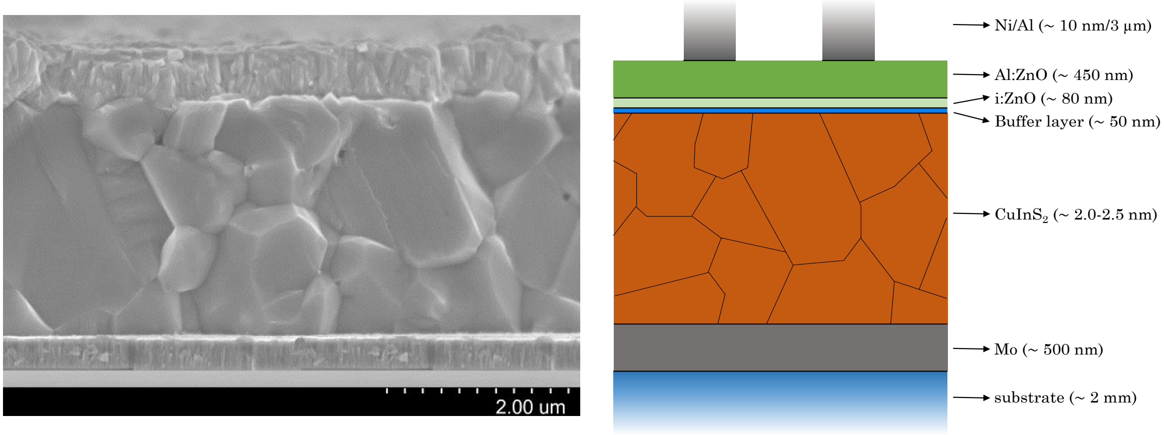

Figure 2.4.3: (left) cross section of a $CuInS_2$ solar cell stack analysed in this work acquired my means of SEM. (right) schematic representation of a $CuInS_2$ solar cell indicating all layers composing the stack and the corresponding thicknesses. In this work, glass has been used as substrate while the buffer layers are made of cadmium sulphide (CdS) or zinc-oxy-sulphide (Zn(O,S)).

The choice of the glass (and in general of the substrate) is essential as it influences the properties of the absorbers. By way of example, a substrate with a coefficient of thermal expansion as close as possible to the absorber one is preferred, because this would induce a lower strain during the cooling process that follows the growth process [39].

A molybdenum (Mo) back contact layer is then deposited on the glass by sputtering at room temperature. The thickness is about 500 nm. Its choice is based on the relatively low cost of the material, its high melting point (about 2700 °C) and its low diffusivity in the chalcopyrite film. Additionally, during the absorber growth, it partially reacts with the chalcogen vapour to form a thin layer of MoS_2 (typically in the order of 50 nm). For selenium-based compounds, the formation of a thin layer of $MoSe_2$ was shown to lead to an ohmic contact between the Mo layer and the back surface of the chalcopyrite absorber [40, 41]. Although a similar detailed investigation for the $Mo/MoS_2/CuInS_2$ structure is still missing, MoS_2 plays likely a similar role in sulphides based solar cells: e.g., in [42] the $Mo/CuInS_2$ electrical contact is shown to be ohmic.

On the top of the Mo layer the $CuInS_2$ film is deposited. Several growth methods have been reported to deposit thin films CIS. In the past, techniques have been used such as single source evaporation (using a single-phase ternary powder) [43], coevaporation from individual sources [23], reactive magnetron sputtering [44], chemical vapour transport [45], spray pyrolysis [46] and electrodeposition [47]. Nevertheless, the highest efficiencies have been achieved with devices based on $CuInS_2$ (or $Cu(In,Ga)S_2$) absorbers deposited by either coevaporation of the single elements or by reactive annealing (in elemental sulphur S or hydrogen sulphide H_2S gas) of precursor layer of metallic phases [24, 27, 48, 49]. The coevaporation process has been used in this thesis and will be explained in detail in chapter 3. The final thickness of the absorber is about 2.0-2.5 μm.

Afterwards, a thin buffer layer is deposited with a thickness of around 30-50 nm. Cadmium sulphide (CdS) is the most common buffer material used in chalcopyrite solar cells; it is typically deposited by chemical bath deposition, n-type doped and has a band gap of about 2.4 eV. Despite the high band gap and the low thickness, it still absorbs partially the high energy portion of the solar spectrum, which in turn leads to a lower performance of the photovoltaic device. This issue, together with the toxicity of cadmium, has driven (and still drives) a lot of efforts to replace it with a less toxic material with higher band gap. Zinc-oxy-sulphide (Zn(O,S)) is one of the alternative buffer layers which allows to get conversion efficiencies close to (or even higher than) those achieved by employing CdS, both for selenides [10] and sulphides based solar cells [49]. In this thesis both CdS and Zn(O,S) have been employed as buffer layers (details about the recipes can be found in [50]); in addition to the issues previously discussed, CdS forms an unfavourable band alignment with $CuInS_2$ [51, 52], as will be discussed in the next section.

Following the buffer, the transparent front contact (or window layer) is deposited. It is actually made of two different layers: an intrinsic zinc oxide layer (i-ZnO) and a heavily n-type doped ($\sim 10^{20}$ cm^{-3}) aluminium doped zinc oxide (Al:ZnO or AZO). Both are deposited typically by sputtering. The high band gap (about 3.35 eV) ensures a high transparency for a wide spectral range. The intrinsic layer has a thickness of about 50-100 nm and despite its high resistivity, it was shown to improve reproducibility and stability of the final devices [53]. The high doping of the Al:ZnO layer enhances the electrical conductivity; on the other hand, it leads to free carriers absorption (although this is not particularly detrimental for wide band gap absorbers, like $CuInS_2$) . Alternative transparent conductive oxides have been studied in the past to solve this issues, such as biased-zinc oxide (b-ZnO) [54].

The carrier collection is improved by depositing a metal grid on the top of the window layer. In the current work it is made of 10 nm of nickel and about 3 μm of aluminium contacts, both deposited by electron beam evaporation.

The current champion device based on $Cu(In,Ga)S_2$ absorber shows a certified efficiency of 15.5 % and the solar cell stack includes a high temperature glass (not specified) as substrate, a Mo back contact, CIGS absorber, zinc-magnesium oxide as buffer layer (deposited by atomic layer deposition) covered by a window layer made of i:ZnO and indium doped tin-oxide (ITO).

The front electrode is made of Ni/Al covered by magnesium fluoride (MgF): this last layer is often used as antireflection (AR) coating, thus to improve the device efficiency.

2.4.4 Recombination processes in a solar cell

This section will introduce some of the main recombination processes or energy losses that may occur in a photovoltaic device. For more details, the interested reader is referred to textbooks, such as [31].

For simplicity, figure 2.4.4 displays a schematic heterostructure solar cell with back contact, absorber and window layer in equilibrium. Once absorbed, photons create electron-hole pairs. These carriers thermalize to the edges of the bands (1), transferring partially their energy to the lattice by emitting phonons. This energy loss can be reduced by employing, e.g., multijunction solar cells. The path (2) is an unavoidable process and stands for the radiative recombination which occurs between CB and VB. Processes (3) and (7) represent interface recombination, taking place at the back surface and at absorber/window interface, respectively. Recombination through channel (3) can be reduced by employing, e.g., an absorber with graded band gap. Particularly, a higher conduction band near the back surface drives the minority carriers (in p-type absorbers) towards the space charge region, thus reducing the photocurrent loss. Photo-generated carriers can also recombine before being collected because of a low diffusion length L_n (path (4)), which depends on the lifetime and on the diffusivity. Process (4) strongly depends on process (5). (5) and (6) include recombination through deep defects in the QNR and in the SCR, respectively: it is called Shockley-Read-Hall recombination (SRH) and is detrimental for photovoltaic device performances as it enhances non radiative recombination. It can be reduced by lowering the concentration of the defect(s) responsible of SRH recombination. Shallow defects are thermally emptied at room temperature, contributing to the doping, and are not harmful in terms of minority carrier density lowering.

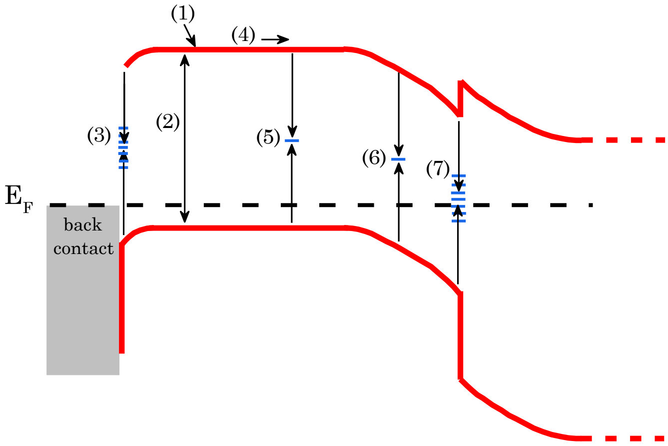

Figure 2.4.4: scheme of a heterostructure back-contact/absorber/window layer together with the main recombination processes or energy losses that may occur under illumination. The horizontal short blue lines represent defect states.

Recombination at the absorber/window (or absorber/buffer) interface strongly depends also on the band alignment of the two layers. The two main configurations which can occur are depicted in figure 2.4.5. At one hand there is the cliff configuration, where the interface band gap is lower than the absorber band gap; the interface band gap is defined as the difference between the minimum of the C.B. and the maximum of the V.B. at the interface. In the cliff case, the conduction band offset is negative, i.e. the C.B. minimum of the window (or buffer) layer lies at energies lower than the C.B. minimum of the absorber. In the spike configuration the conduction band offset is positive, leading to an interface band gap that equals the absorber band gap. The spike configuration is preferred as it reduces interface recombination [31] as long as the barrier (which is a consequence of the CBO > 0) is not too high (≤ 0.3-0.4 eV) and does not hinder carrier collection. On the contrary, a cliff configuration significantly enhances interface recombination, lowering the performance of solar cells.

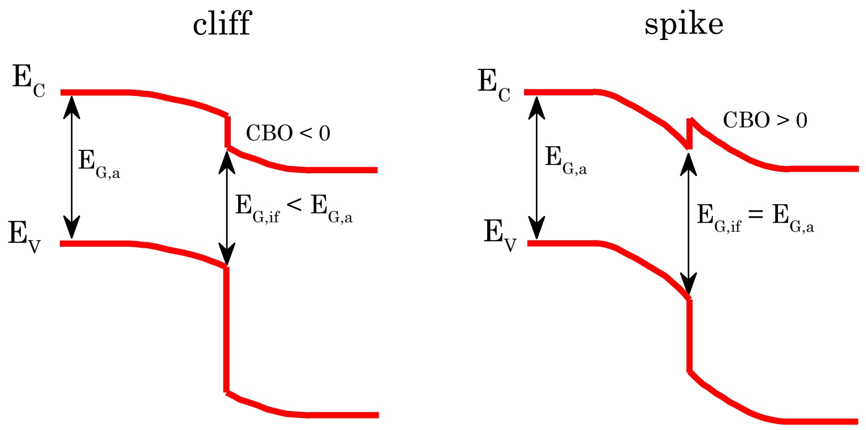

Figure 2.4.5: energy band diagram at the absorber/window interface: (left) cliff configuration, with an interface band gap lower than absorber band gap (i.e. $E_{G,if} < E_{G,a}$); (right) spike configuration, with an interface band gap that is equal to the absorber band gap (i.e. $E_{G,if} = E_{G,a}$). The conduction band offset (CBO) is calculated as difference between C.B. minimum of the window layer and C.B. minimum of the absorber layer, respectively.

The analysis of the open circuit voltage as a function of the temperature can reveal if the interface recombination is the main recombination channel in a photovoltaic device. In fact, the saturation current density J_0 is thermally activated with an energy of $E_{a,rec}$, which represents the activation energy of the main recombination path. The temperature dependence of the saturation current density is given by:

$$J_0 = J_{00} \exp\left(-\frac{E_{a,rec}}{AkT}\right) \qquad \text{eq. 2.4.6}$$

with J_{00} reference current density. Equation 2.4.6 allows to rewrite equation 2.4.4 as follows:

$$V_{OC} = \frac{E_{a,rec}}{q} + \frac{AkT}{q} \ln\left(\frac{J_{ph}}{J_{00}}\right) \qquad \text{eq. 2.4.7}$$

Therefore, by measuring the open circuit voltage as a function of the temperature, the extrapolated energy at 0 K gives the activation energy of the dominant recombination path, assuming J_{00} and A only weakly temperature dependent within the fitting region. If the activation energy has the same value of the band gap of the absorber, then the main recombination channels take place within the bulk of the absorber. On the other hand, if the interface recombination dominates, a value lower than the absorber band gap is extrapolated. This can take place, e.g., if there is a high density of interface defects or if the CBO at the interface is negative, i.e. cliff configuration. The last case is particularly relevant for Cu(In,Ga)S_2 based solar cells which employ CdS as buffer layer: reports in the past have shown that an unfavourable band alignment is formed (CBO < 0) both for CIGS with low Ga concentration [51] and for pure CIS [52]. This leads to an activation energy extrapolated at 0 K which is lower than the absorber band gap, i.e. $E_{a,rec} < 1.5\ eV$ [55]. Temperature dependent analysis of the open circuit voltage have been conducted in the framework of this thesis and will be discussed in chapter 4.

In this section the key aspects of the p-n junction and of a photovoltaic device have been discussed. As seen in section 2.4.3, a real device includes several layers stacked onto each other. To minimize losses between quasi Fermi level splitting within the absorber and voltage measured at the contacts, each of these layers needs to be optimized (such as doping of the buffer layer or band offset between buffer and window layer). In addition, equation 2.4.3 defining the relationship J-V under illumination is typically extended to closely describe a real device, including, e.g., shunt and series resistances. However, this thesis focuses mostly on the electronic structure of the semiconducting absorber, therefore a more in-depth description of these aspects concerning the final devices would lie outside the scope of this thesis: an interested reader is referred to references such as [31].

2.5 Photoluminescence

Photoluminescence (PL) spectroscopy is the main characterization technique used in the framework of this thesis; therefore, it will be explained in detail in the following. It is a non-contact and non-destructive method which allows to get insights about the electronic structure or quality of the material under investigation (e.g. point defects-related transitions or quasi Fermi level splitting). In this section the main features of this technique will be discussed: first of all, the basic principles behind this phenomenon together with the transitions which can be observed in a typical PL measurements, along with their characteristic experimental features which help to discern the different kinds of the transitions. Then a brief section on phonon coupling will describe the fundamental principles about the electron-phonon coupling which will be essential in understanding some of the results shown in chapter 5. Afterwards, a detailed description of the experimental setup used to carry out PL analysis is given, together with the procedures to get spectrally and intensity corrected spectra from raw data. This section ends up with the discussion on the quasi Fermi level splitting and its experimental evaluation, which is one of the milestones of this thesis, deeply related to the experimental findings reported in chapter 4

Especially for the first sections, the basic concepts about photoluminescence principles, observable transitions and phonon coupling can be found in any textbook which deals with these topics. Particularly some textbooks have been chosen as references to write the following sections [56-59] , together with some reports which will be cited in the following.

2.5.1 Basic principles and observable transitions

Photoluminescence belongs to the “big family” of luminescence phenomena where a material upon being excited by an external excitation emits radiation through photon emission. Particularly, in photoluminescence the excitation takes place through absorption of photons with an energy higher than the band gap of the semiconductor under investigation, $E_{ph} > E_G$. By way of example, if the semiconductor is excited by an incident electron beam with high enough energy, the emission of radiation would then be called cathodoluminescence.

Before being excited, the semiconductor is in thermal equilibrium. In this state, following the principle of detailed balance (and neglecting stimulated emission), the generation rate of electron-hole pairs in the conduction and valence band is equal to their rate of radiative recombination $R_{VC,0}$, thus:

$$P_{VC}(E)\rho(E) = R_{VC,0}(E) \qquad \text{eq. 2.5.1}$$

with E photon energy, P_{VC} absorption rate (energy dependent) per photon and ρ photon density of states. This relation is known as van Roosbroek–Shockley relation and it is defined for equilibrium. Considering the absorption rate, it is inversely proportional to the mean lifetime of the photons in the semiconductor, $\tau(E)$, which in turn can be expressed as ratio between the mean free path and the velocity inside the semiconductor: the mean free path is basically $1/\alpha$(E) with α(E) absorption coefficient, while the velocity is given by c/n_r with c speed of light in vacuum and n_r refractive index of the semiconductor. Therefore combining this expressions for P_{VC} and replacing the photon density of states ρ with the Planck distribution at temperature T, equation 2.5.1 becomes

$$P_{VC}(E) = \frac{\alpha(E)c}{n_r} \qquad \rho(E) = \frac{n_r^3 E^2}{\hbar^3 \pi^2 c^3} \frac{1}{\left[e^{E/k_B T} - 1\right]} \quad \rightarrow \quad R_{VC,0}(E) = \frac{n_r^2 \alpha(E) E^2}{\hbar^3 \pi^2 c^2} \frac{1}{\left[e^{E/k_B T} - 1\right]} \qquad \text{eq. 2.5.2}$$

The equation above describes the spontaneous recombination rate for a semiconductor under thermal equilibrium. In a photoluminescence experiment (or in a solar cell), this equilibrium is altered by excitation with an external energy source.

Thus, in photoluminescence, the first step is the absorption of photons to create electron-hole pairs. Assuming the surface of the sample at $x = 0$ with an energy dependent reflectivity of the surface $R(E)$, the photon flux density $\Phi(x)$ at a certain position x inside the semiconductor follows the Lambert-Beer law:

$$\Phi\,(x) = \Phi_0(1 - R(E))e^{-\alpha(E)x} \qquad \text{eq. 2.5.3}$$

with Φ_0 the incident photon flux and $\alpha(E)$ absorption coefficient characteristic of the sample excited. For chalcopyrite films, the absorption coefficient is about 10^5 cm^{-1}, therefore within a thickness of about 100 nm the initial excitation flux density inside the semiconductor drops to $1/e \sim 0.37$. Chalcopyrite thin films used in photovoltaic devices have usually a thickness in the range of 1.5-3.0 µm, hence it is reasonable to assume there is not transmitted flux outside the film. In some circumstances, especially to reduce the consumption of rare earth elements, thin films for PV can be lowered down to few hundred of nanometres, employing reflectors at the back surface to enhance the absorption probability. As this last case (very thin films) is not employed in the framework of this thesis, it will not be further discussed.

Assuming each photon which penetrates into the material generates an electron-hole pair and any loss in photon flux density is due to these generations, then the generation rate of carriers is proportional to the change of the flux density through the film, thus to the derivative of the equation 2.5.3:

$$G\,(x) = -\frac{\partial \Phi\,(x)}{\partial x} = \Phi_0 \alpha(E)(1 - R(E))e^{-\alpha(E)x} \qquad \text{eq. 2.5.4}$$

Upon absorption, the generated carriers thermalize within their respective bands, colliding with the crystal lattice and creating phonons, in a timescale of 10^{-12} s after generation. After thermalization, the carriers reach a quasi-thermal equilibrium distribution, which does not depend on the spectral distribution of the absorbed photons (which influences their distribution just after the absorption, before they relax to the edge of the bands). This is a relevant aspect, which allows measurements of quasi Fermi level splitting also using a monochromatic light as excitation source (as will be explained in the following), simulating the photon flux of the sunlight which instead has a spectrum composed by a broad distribution of photon energies. As the radiative recombination has a larger characteristic time than the thermalization, these quasi-thermal distributions are achieved under continuous illumination, reaching a steady state. Thus, the concentration of electrons n and holes p in the conduction and valence band, respectively, can be described by the effective density of states of the corresponding band and the Fermi-Dirac statistics. Particularly, if the Fermi-Dirac statistics can be approximated to the Boltzmann one (i.e. non-degenerate semiconductors), then:

$$p = N_V \exp(-\frac{E_{F,p}-E_V}{k_B T}) \qquad \text{and } n = N_C \exp(-\frac{E_C - F,n}{k_B T}) \qquad \text{eq. 2.5.5}$$

for holes and electrons densities, respectively. N_V and N_c represent the effective density of states of the valence and conduction bands, respectively and $E_{F,p/n}$ the Fermi level for holes/electrons. Both distributions expressed in equations 2.5.5 use the Boltzmann statistics, which typically can be applied if the absolute energy separation between the Fermi level of holes/electrons and the valence/conduction band edges is higher than $3k_BT$. The spontaneous emission rate is proportional to the carrier density of the initial and final stage: for a band-to-band transition, thus, to the electrons/holes in the conduction/valence band. Under illumination, the net spontaneous radiative recombination rate R_{net}^{rad} is given by:

$$R_{net}^{rad} = R_{ill}^{rad} - R_0^{rad} = Bnp - Bn_0p_0 = B\left(N_C N_V \exp\left(-\frac{E_G}{k_BT}\right)\exp\left(\frac{\Delta\mu}{k_BT}\right) - n_i^2\right) = Bn_i^2\left(\exp\left(\frac{\Delta\mu}{k_BT}\right) - 1\right) \qquad \text{eq. 2.5.6}$$

with B radiative recombination coefficient, R_{ill}^{rad} and R_0^{rad} the radiative recombination rate under illumination and at thermal equilibrium, p_0 and n_0 the carrier concentration at thermal equilibrium and $\Delta\mu$ quasi Fermi level splitting. From the equation above it is evident that for a given semiconductor, the radiative recombination rate or emission rate is exponentially proportional to the quasi Fermi level splitting. The QFLS is, in fact, a mark of the quality of an absorber as it represents an upper limit of the open circuit voltage.

The expression for $R_{VC,0}(E)$ (equation 2.5.2), taking its Boltzmann approximation (which is valid when considering $E >> k_BT$), is related to R_0^{rad} by:

$$R_0^{rad} = Bn_i^2 = \int_0^\infty R_{VC,0}(E)dE \qquad \text{eq. 2.5.7}$$

Combining eq. 2.5.2 and 2.5.5 – 2.5.7, the recombination rate in non-equilibrium $R_{VC}(E)$ can be expressed as:

$$R_{ill}^{rad} = \exp\left(\frac{\Delta\mu}{k_BT}\right)R_0^{rad} \qquad \rightarrow \qquad R_{VC}(E) = \frac{n_r^2\alpha(E)E^2}{\hbar^3\pi^2c^2}e^{-\frac{(E-\Delta\mu)}{k_BT}} \qquad \text{eq. 2.5.8}$$

The expression just derived is the Boltzmann approximation of the Planck's generalized law for a so-called "grey body" with an absorption coefficient $\alpha(E)$, refractive index n_r and under non-equilibrium condition, thus with a quasi-Fermi level splitting of $\Delta\mu$. Nevertheless, this rate refers to the radiative recombination processes band-to-band, within the sample, while in a PL experiments only the photons emitted outside the absorbers can be measured. A general analytical expression of Planck's generalized law with the Bose-Einstein statistics has been derived by Würfel in [60] and it is given in equation 2.5.9. It expresses the photon flux density per energy interval measured in a steady state PL measurement and it is based on an introduction of a chemical potential for photons.

$$Y_{PL}(E) = \frac{1}{4\pi^2\hbar^3c^2}\frac{a(E)E^2}{\exp\left(\frac{E-\Delta\mu}{k_BT}\right)-1} \qquad \text{eq. 2.5.9}$$

a(E) is the absorptivity of the absorber, which comes from the integration across the whole thickness d of the sample and it can be related to the absorption coefficient $\alpha(E)$ through the simplified expression:

$$a(E) = (1 - R(E))[1 - \exp(-\alpha(E)d)] \qquad \text{eq. 2.5.10}$$

Due to this integration, the expression 2.5.9 is valid if the quasi Fermi levels are flat across the whole absorber. The pre-factors of equation 2.5.8 and 2.5.9 differ by a term of $1/4n_r^2$, which takes into account the emitted photons that are able to escape the absorber and that contribute to the photon current. Beyond a certain critical angle, the photons emitted within the absorber are internally reflected. Equation 2.5.9 results back into the Planck's law for thermal radiation for black body assuming absorptivity equals to 1 and same chemical potential for electron and holes, i.e. thermal equilibrium, thus $\Delta\mu = 0$. Additionally, it is valid for homogenous material properties. The equation 2.5.9 is the starting point for QFLS measurements and evaluation, and it will be discussed in section 2.5.4.

Having described the band-to-band transitions by means of the generalized Planck's law, transitions observable at lower temperatures will be discussed in the following. In fact, by lowering the temperature, the radiative recombination is increased as, e.g. the mobility of charge carriers is reduced, and thus their recombination through non-radiative recombination paths is inhibited.

Free-to-bound transitions

The radiative recombination between a free carrier and a charge bound to an impurity is called free-to-bound transition (F-B): thus, it can include the recombination of an electron photo excited in the conduction band with a hole bound to an acceptor or the opposite case (hole in valence band with electron bound to a donor). The probability to observe these transitions increases at low temperatures as the re-emission of trapped charge carriers from impurities into the bands is lowered. On the other hand, deep defects within band gap can trap carriers also at room temperature, where the PL spectra will be then characterized both by band-to-band and free-to-bound transitions. This last case applies to $CuInS_2$, as will be shown throughout this thesis. The emitted photons from F-B transitions have an energy $h\nu$:

$$h\nu = E_G - E_{D/A} + \frac{k_B T}{2} \qquad \text{eq. 2.5.11}$$

with $E_{D/A}$ binding energy of the defect state, while the last term takes into account the electron/hole density distribution in the conduction/valence band involved in the F-B transition. Therefore when the temperature is raised, the F-B transition shows a shift according to the temperature dependence of the band gap, together with the small influence of the last term in equation 2.5.11. At the same time, the peak of an F-B transition does not show any shift when the excitation intensity is changed.

Donor-acceptor transitions

Semiconductors may have both acceptors (A) and donors (D): a transition which involves a recombination between a charge carrier in a neutral donor and neutral acceptor is called donor-acceptor (DA) pair transition. After recombination, both defects are ionized, positive (D) and negative (A) charge defect, respectively. Contrary to the F-B case, for DA pair transitions the emitted photons have an energy $h\nu$:

$$h\nu = E_G - E_D - E_A + \frac{e^2}{4\pi\varepsilon_0\varepsilon_r r} \qquad \text{eq. 2.5.12}$$

with E_D and E_A being the donor and acceptor binding energy, respectively, while the last term is the Coulomb contribution that takes into account the interaction of the ionized donor and ionized acceptor following the DA recombination. Particularly, e is the elementary charge, ε_0 the vacuum permittivity, ε_r the relative permittivity of the semiconductor material and r the distance between the ionized donor and ionized acceptor. Due to the Coulomb interaction, the PL emission of a DA pair transition shows a blue shift if the excitation intensity is increased: in fact, in this circumstance, more donors and acceptors would be excited, decreasing the average distance between defects involved in a DA pair transition. The dependence of the PL peak of a DA transition E_{DA} on the excitation intensity φ is given by the empirical equation:

$$E_{DA}(\varphi) = E_{DA}(\varphi_{ex,max}) + \beta log_{10}\left(\frac{\varphi_{ex}}{\varphi_{ex,max}}\right) \qquad \text{eq. 2.5.13}$$

A blue shift of the PL peak is also observed if the temperature is increased: in fact, more carriers would be re-emitted from the defect states to the bands, and the DA pair transitions more probable will be those with shorter distance between donor and acceptor (thus with higher Coulomb interaction). If the temperature is high enough to thermally ionize the shallower defect, the DA pair transition becomes an F-B transition.

Free and bound excitons

At low temperatures, transitions related to free excitons may be observed. They are the result of the recombination of an electron-hole pair bound together by Coulomb interaction, which lowers the energy compared to the band gap value. These transitions are observable if the binding energy of the free exciton is higher than thermal energy, thus $E_{FX} > k_BT$. Beside the temperature, an additional requirement which enhances the probability to create excitons, thus to measure their annihilations radiatively, is the quality of the semiconductor: in fact, the presence of defects generates electrical fields locally and may overcome the attractive potential of the excitons, making them unstable and preventing their related luminescence. Therefore, the observation of excitonic luminescence is considered a mark of the crystal quality of a semiconductor.

A free exciton can be treated with a modified Bohr model of the hydrogen atom, with the proton replaced by the hole and considering the effective masses of hole m_h^* and electron m_e^*. In addition, the attractive electrostatic force between the two carriers is partially shielded in the semiconductor by the dielectric constant ε_r. Therefore, the binding energy of a free exciton E_{FX} is given by:

$$E_{FX(n)} = \frac{m_r e^4}{2\hbar^2(4\pi\varepsilon_0\varepsilon_r)^2}\frac{1}{n^2} = \frac{R_y m_r}{\varepsilon_r^2 m_0}\frac{1}{n^2} \qquad \text{eq. 2.5.14}$$

with the Rydberg constant $R_y = 13.6$ eV, n quantum number, m_0 free electron mass and m_r the reduced electron-hole mass given by:

$$\frac{1}{m_r} = \frac{1}{m_h^*} + \frac{1}{m_e^*} \qquad \text{eq. 2.5.15}$$

Assuming typical values $\varepsilon_r \approx 10$ and $m_r/m_0 \approx 0.1$, it is possible to have an estimation of common values for binding energy at the ground state, which is in the order of tens of meV. The PL peaks related to free excitons are given by the difference between bandgap and binding energy and thus follow the temperature dependence of the bandgap. For high quality crystals, emissions from excited states of free excitons may be measured. In this case, from the spectral separation of the emission lines corresponding to the ground state and first excited state of the free exciton, its binding energy can be accurately determined. At the same time, if the binding energy is known, the band gap can be estimated as well, eventually also its temperature dependence as long as the free exciton emission line is observed.

Particularly for $CuInS_2$, Yakushev et al. in [61] could observe the ground state and the first two excited states of the free excitons by photoluminescence performed on high quality single crystals, determining a free exciton binding energy of 18.5 meV. This value is in good agreement with that previously found by Binsma et al. [62] , i.e. 20 meV, by analysing the quenching of the free exciton photoluminescence intensity.

A free exciton can also be trapped by an impurity present in the crystal lattice, becoming in this way a bound exciton. A free exciton can be bound both to donors and acceptors in their neutral or charged state (positive and negative, respectively). Thus, the binding energy of such exciton is slightly higher compared to the free exciton one, therefore the emission lines related to bound exciton are red shifted. The binding energies of the bound excitons depends on the ratio of the effective masses $\sigma = m_e^*/m_h^*$ [63]. Additionally, they also depend on the chemical nature of the impurity (donor or acceptor), i.e. on the binding energy of the defect to which the exciton is bound: in fact, Haynes found out empirically the spectral positions of exciton bound to neutral donors were related to the specific dopant added to silicon [64]. The relationship between the binding energy of a bound exciton E_{BE} and the binding energy of the defect $E_{D/A}$ is given by the Hayne's rule as follows:

$$E_{BE} = c_n E_{D/A} + E_{FX} \qquad \text{eq. 2.5.16}$$

for excitons bound to neutral defects, whereas for those bound to charged defects:

$$E_{BE} = c_q E_{D/A} \qquad \text{eq. 2.5.17}$$

The constants c_n and c_q depend on the ratio of the effective masses, and have been calculated both for neutral defects [65] and for singly charged defects [66]. Therefore at low temperature, the difference between band gap (at that temperature) and the photon energy related to a bound exciton allows to determine directly the binding energy of the defect. If the effective masses of the semiconductor under investigation are known, by applying equations 2.5.16 and 2.5.17, the activation energies of the defects involved in such emissions can be determined. Specifically for $CuInS_2$, the effective masses have been estimated experimentally in [67], with $m_e^* = 0.16 m_0$ and

$m_h^* = 1.3m_0$. With these effective mass values and based on the results of [65] and [66], Binsma et al. [62] have estimated the proportionality factors for both neutral and charged defects cases: c_n 0.27 and 0.06 for excitons bound to neutral donor and neutral acceptor, respectively and c_q 1.04 and 1.5 for excitons bound to ionized donor and acceptor, respectively.

The spectral positions of the free and bound excitons do not change if the excitation intensity is increased (as long as it is not high enough to heat the sample). On the other hand, if the temperature is increased, these emission lines follow the change of the band gap as a function of the temperature, as long as the thermal energy $k_B T$ does not overcome the binding energy of the bound or free exciton.

Excitation intensity dependence of PL transitions

In the previous sections describing the transitions observable at low temperatures, the dependence of their spectral positions on the excitation intensity has been discussed. Particularly, free-to-bound transitions as well as excitonic ones (both free and bound) do not show any shift when the excitation intensity is varied. In contrast, donor-acceptor transitions show a blue shift when the excitation intensity is increased. This section, which is mainly based on the work of Spindler et al. [68], will briefly discuss the dependence of intensity of these PL transitions on the excitation intensity.

In the simplified cases, the intensity of the PL transitions follows a power law behavior, i.e. $I_{PL} \sim I_{Ex}^k$ [69]. The exponent k assumes values between 1 and 2 (thus super-linear behavior) for excitonic emissions and below 1 for F-B and DA emissions. However, dependencies more complex than single power law have been reported for excitation intensity photoluminescence [68, 69]. Based on the rate equations of different processes, Spindler *et al.* have shown in [68] that the exponent k can take on only fixed values of multiples of ½ at low temperatures, where only photo-excited carriers are available. The differences are due to the availability of competing recombination channels (even through deep defects) between the defects (or levels) involved. The change of exponent for different excitation occurs when one of the defects involved in the transition or in one of the competing transitions saturates. This leads to a curved dependence in the log-log plot, which can be fitted in general with exponents different from n/2: the latter case occurs predominantly in transitions regions between two limiting cases of a single power law. Spindler *et al.* showed also that the attribution of the PL emissions to specific transitions, like excitonic or free-to-bound ones, based on the k values is not straightforward: in fact, e.g. if a deep defect is present, the intensity of donor-acceptor transitions can follow a super linear power law behaviour. Table 2.1 gives an overview of the power law exponents for the general case where a semiconductor has both shallow defects (one donor and one acceptor) and a deep defect (donor like). The density of the defects, shallow donor, shallow acceptor and deep level, are indicated by N_D, N_A and N_S, respectively. The density of neutral defects (i.e. occupied by the corresponding carriers, e.g. holes for the shallow acceptor) are marked with *0* as superscript, for example N_A^0 for neutral acceptors. The corresponding constant total defect densities are indicated with T as superscript, e.g. N_A^T.

Table 2.1 shows all possible cases which may take place with the above mentioned defects. For instance, (a) refers to the very low excitation case, i.e. when the neutral defect densities are negligible compared to the total defects densities. The opposite extreme case (f) is reached at very high excitations, i.e. when all defects are neutralized by the occupation of the corresponding excess carriers, thus they become saturated. In between (b) – (e) represent the cases when one or two defects become saturated. The upper half part of table 2.1 lists the k_i values of neutral densities defined as $k_i = d\log\left(N_i^0\right)/d\log(I_{Ex})$. For instance, for the case (f), the three defect levels become saturated, therefore the corresponding densities of neutral defects cannot vary when the excitation is further increased, thus the three k values, k_D, k_A and k_S, equal zero. The second half part of table 2.1 lists instead the k_i values of the transitions with intensities I_i, defined similarly as $k_i = d\log(I_i)/d\log(I_{Ex})$. The k value of each transition is given by the sum of the k values of the neutral densities of levels involved in such transition. This is a consequence of the linear relationship between the rate of a transition and the product of the densities of the available levels involved in the transition. Additionally, the transition coefficients are assumed to be prefactors independent of the generation rate. By way of example, as shown in table 2.1, the k value of a donor-acceptor transition is the sum of the k values of the neutral donor and neutral acceptor densities, i.e. $k_{DA} = k_D + k_A$. It is worth noting that table 2.1 can be simplified to the case of a semiconductor with no deep level: in fact this situation can be treated as the deep defect cannot capture carriers, thus as the fully saturated case. In this situation, column (a) and (c) can be neglected and, for instance, a donor-acceptor transition can only assume a sublinear power law behavior. The k values of bound excitons k_{BX}, which are not included in table 2.1, can be easily calculated as $k_{BX} = k_n + k_p + k_{D/A}$, where the last term refers to the k value of the neutral density of neutral donor or acceptor depending on the nature of the exciton, i.e. if it is bound to a donor or acceptor, respectively. In fact, the rate of a bound exciton recombination depends also on the density of the defect to which the exciton is bound. Finally, if the deep level is acceptor like, table 2.1 is still valid as long as the the values of k_n and k_p as well as k_D and k_A are interchanged.

Table 2.1: overview of the power law exponents in the general case of a semiconductor with a shallow donor, a shallow acceptor and a deep donor-like defect. Adapted from [68].

	(a)	(b)	(c)	(d)	(e)	(f)
	$N_D^0 \ll N_D^T$ $N_S^0 \ll N_S^T$ $N_A^0 \ll N_A^T$	$N_D^0 \ll N_D^T$ $N_S^0 \approx N_S^T$ $N_A^0 \ll N_A^T$	$N_D^0 \ll N_D^T$ $N_S^0 \ll N_S^T$ $N_A^0 \approx N_A^T$	$N_D^0 \ll N_D^T$ $N_S^0 \approx N_S^T$ $N_A^0 \approx N_A^T$	$N_D^0 \approx N_D^T$ $N_S^0 \approx N_S^T$ $N_A^0 \ll N_A^T$	$N_D^0 \approx N_D^T$ $N_S^0 \approx N_S^T$ $N_A^0 \approx N_A^T$
k_n	1	1	1	1	1/2	1/2
k_p	1	1	1/2	1/2	1	1/2
k_D	1	1/2	1	1/2	0	0
k_A	1/2	1/2	0	0	1/2	0
k_S	1/2	0	1/2	0	0	0
	Low ϕ	…	…	…	…	High ϕ
k_{FX}	2	2	3/2	3/2	3/2	1
k_{FB_D}	2	3/2	3/2	1	1	1/2
k_{FB_A}	3/2	3/2	1	1	1	1/2
k_{FB_S}	3/2	1	1	1/2	1	1/2
k_{DA}	3/2	1	1	1/2	1/2	0
k_{SA}	1	1/2	1/2	0	1/2	0

The curved dependence in the log-log plot (which is likely to be observed when the excitation power is varied over more than three orders of magnitude, e.g. see figure 5.9 in section 5.1.3) can be fitted with the following equation [68] :

$$I_{PL} \propto \frac{\Phi^{k_1+k_2}}{1+\left(\frac{\Phi}{\Phi_0}\right)^{k_1}} \qquad \text{eq. 2.5.18}$$

with I_{PL} being the integrated PL flux, Φ excitation intensity (or flux) and Φ_0 turning point (or crossover excitation). The fitting function is derived by the multiplication of carrier densities in the initial state and in the final state involved in the transition under investigation; the carrier densities, in turn, are proportional to the occupation of the states involved, with electrons and holes, respectively. The equation 2.5.18 reflects the case when one of the states involved in the transition gets saturated in the range of excitation intensities investigated, and thus its occupation can no longer increase with excitation. For low excitation ($\Phi << \Phi_0$) the power law exponent converges to $k = k_1 + k_2 = k_{low}$. For high excitation ($\Phi >> \Phi_0$), neglecting 1 in the denominator, the power law exponent converges to $k = k_1 + k_2 - k_1 = k_{high}$. Thus, depending on the excitation, different exponents can be observed. The crossover excitation is the excitation intensity where the lines corresponding to the single power law in low and high excitation cross each other. A more general equation than 2.5.18 is given in [68] as well, which includes the situation where also the second level involved in the transition becomes saturated: in this case a second crossover excitation must be included in the equation.

Summarizing, when the excitation power is tuned over less than three orders of magnitude, the log-log plot shows likely a linear trend which can be fitted with single power law with a k exponent different from n/2. However, if the experimental conditions allow a wider range of excitation investigation, a curved dependence is observed in the log-log plot, which can be fitted with a combination of multiple power laws with exponents values multiple of 1/2. Curved dependences have been observed in this work and will be discussed in chapter 5.

2.5.2 Phonon coupling

The recombination transitions described in the previous section may occur also with the emission of phonons, giving rise to the so called "phonon replica", which manifests itself at lower energies compared to the main emission (the one that does not involve phonons) and need to be distinguished from transitions related to different bound excitons or to deeper defects. The phonon replica are a consequence of the electron-phonon coupling and, depending on its strength, the interpretation of a PL spectrum relative to a specific transition may become very challenging, as will be discussed in the following.

The strength of the electron-phonon coupling depends on the nature of the defect involved. The wave function of a shallow defect extends over several lattice constants and it is delocalized; vice versa, for deep defects, the wave functions are strongly localized. The degree of localization has a significant impact on the electronic properties which then show up in photoluminescence experiments. In fact, for a delocalized wave function, the corresponding electron density will extends over several lattice constants, therefore it will be low at the defect site and it will not affect the atomic position of the neighbouring atoms. On the contrary, when the electron density is strongly localized, the change of the charge state of the defect (which takes place in a PL experiments by emission or capture of electrons) will influence substantially the crystal lattice surrounding the deep defect involved in the emission, i.e. its neighbouring atoms will rearrange themselves. A change of the geometry has an effect on the electronic state when the defect gets excited (or when it relaxes back to the ground state). This situation can be well described by using the 1-D configuration coordinate diagram [70], where the configuration coordinate Q could e.g. represent the bond length between the defect and the host atom (this last one embodies the neighbouring atoms). A simplified scheme is depicted in figure 2.5.1. The bond is described by a harmonic oscillator, thus the energy of the defect is proportional to the square of the bond length and the change of the geometry upon excitation/absorption is described by a change of the equilibrium bond length Q corresponding to the energetic minima of the ground and excited state: in other words, the minimum of the vibrational energy of the excited state does not lie at the same Q value of the minimum of the ground state. The energetic separation of the equilibrium configuration of the ground and excited state is called zero-phonon line energy, E_{ZPL}. Due to the different equilibrium minima, the emitted photon energy (E_{em} in the scheme) corresponding to the highest transition probability, i.e. maximum in the PL spectrum $h\nu_{max}$, is lowered compared to the zero-phonon line energy by an amount called Frank-Condon shift, d_{FC}. Thus:

$$h\nu_{max} = E_{ZPL} - d_{FC} \qquad \text{eq. 2.5.19}$$

The Franck-Condon contribution is dissipated by emission of phonons. Assuming an average (or dominant) optical phonon energy $\hbar\omega$, the average number S of phonons involved in the recombination transition is given by:

$$S = \frac{d_{FC}}{\hbar\omega} \qquad \text{eq. 2.5.20}$$

with S called Huang-Rhys factor and it gives an indication of the strength of the electron-phonon coupling for a specific defect.

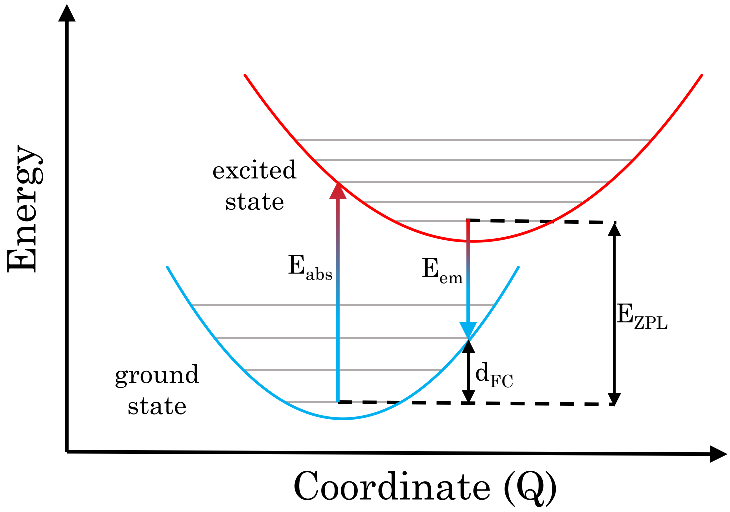

Figure 2.5.1: simplified scheme of the configuration energy diagram adapted from ref. [70].

Taking into consideration the emission into the different vibration levels of the ground state, the PL spectrum will be characterized by the zero-phonon line followed at lower energies by a series of equidistant peaks called *phonon replicas*. The spectral distance is given by the phonon energy $\hbar\omega$, whereas the intensity profile of the replicas follows a Poisson distribution:

$$I_n = e^{-S} \frac{S^n}{n!} \qquad \text{eq. 2.5.21}$$

with n number of phonons emitted in the emission line with intensity I_n. Typically, the deeper the defect involved in the transition, the higher Franck-Condon shift is expected, thus higher Huang-Rhys factor. From equation 2.5.21 it can be easily deducted that when S exceeds 1, the zero-phonon line (n = 0) does not manifest itself anymore as the highest emission line. This can be appreciated in figure 2.5.2. In all represented cases, the zero-phonon line lies at 1.25 eV and the phonon energy has been fixed at 40 meV (i.e. spectral distance between two consecutive replicas). If the FWHM is set at a value lower than phonon energy (15 meV), the series of equidistant peaks are resolved: if the S factor increases above 1, the PL peak shows a red shift, which is stronger for higher S value. For instance, for S = 8, the PL peak is around 0.95 eV, i.e. 200 meV lower than the zero-phonon line. The interpretation of such bands becomes even more tricky when the FWHM is as high as the phonon energy or higher (70 meV in the scheme), which translates in the observation of a single asymmetric broad peak. Experimentally, deep defects which involve strong phonon coupling give rise to asymmetric broad PL bands, as shown in figure 2.5.2 for cases with higher FQHM. A typical example is given by the deep recombination centres in the well-studied GaN [71]. It is worth to point out once more that all exemplary photoluminescence spectra shown in fig. 2.5.2 have the same zero-phonon line. Therefore the interpretation of the measured broad PL bands, if they involve phonon coupling, in terms of recombination models can be challenging, as well as the comparison with defect models obtained by e.g. electrical characterization or derived by theoretical calculations. At the same time broad deep bands can also be due to broad defect distributions.

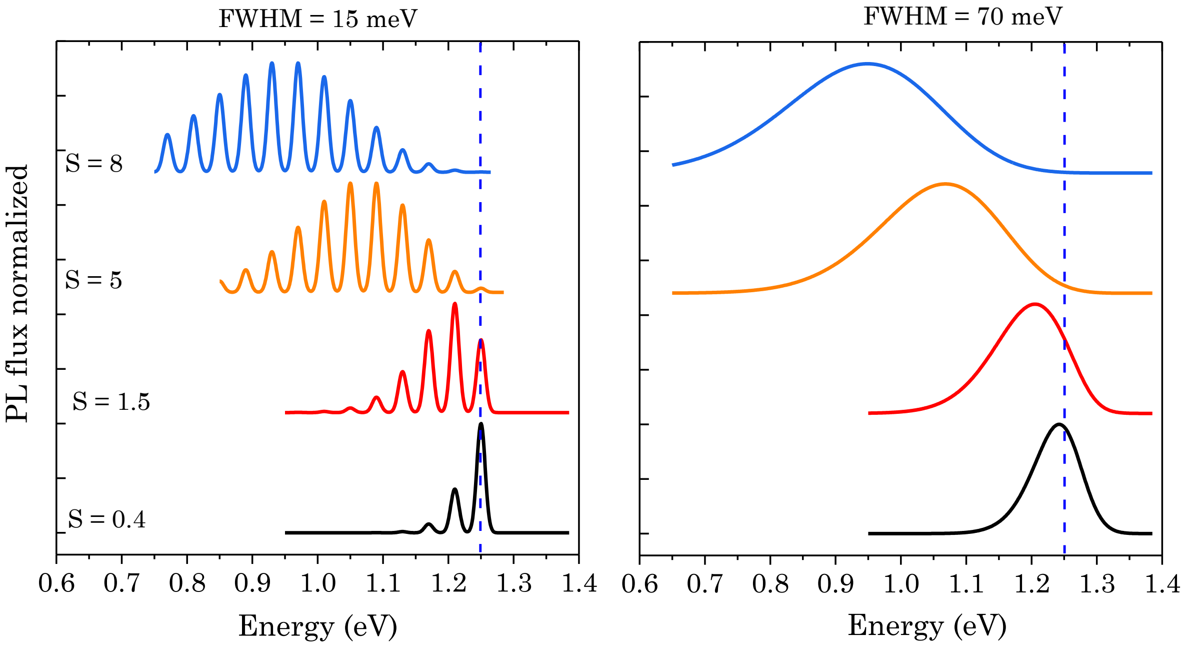

Figure 2.5.2: schematic representation of the PL band related to the recombination transition with the zero-phonon line at 1.25 eV (indicated with a vertical dashed line) in different scenarios: on one hand, different Huang-Rhys factor have been applied to eq. 2.5.21, on the other hand, for the same S factor two different FWHM of the Gaussian profile of the phonon replica have been fixed, 15 and 70 meV, respectively. In all cases, the phonon energy has been fixed to 40 meV.

2.5.3 Experimental setup

In this section a brief explanation of the photoluminescence experimental setup used in the framework of this thesis is given. It consists in a home-built setup which allows measurement both at room and low temperature (down to about 5-10 K). Its simplified scheme is shown in figure 2.5.3. The investigations can be carried out by using a continuous wave (CW) diode laser with an output wavelength of either 404 nm or 663 nm (about 3.07 eV and 1.87 eV, respectively). In front of each laser a bandpass filter is placed, with a center wavelength of 405 nm and 660 nm and with a full width half maximum of 10 nm in both cases: although these filters may reduce the incident laser powers, they allow to get rid of any unwanted wavelengths of the laser beam.

The laser light can be intentionally attenuated by using a set of neutral filters, from OD0 to OD4: the number indicates the optical density or attenuation factor, e.g. OD2 attenuates the incident flux by 100 times, OD0 stands for no filter inserted in optical path. The actual attenuations for these filters have been measured for a more precise analysis, as will be explained in the following.

Then the laser beam passes through the hole in the first parabolic mirror and it is absorbed by the sample, which is mounted either on the room temperature stage or inside an optical cryostat used for low temperature measurements. In both cases, the sample stage can be moved in the three dimensions, one to catch the optical focus of the setup, the other two to analyse different spots on the same sample surface. The laser spot diameter (which can be measured with a camera, as explained shortly) is usually in the range of 2.5-3 mm, but it can be eventually reduced to almost 80-100 μm by using an optical convex lens, thus increasing the excitation intensity. Once the PL radiation is emitted from the sample surface, it is collected through the two UV-enhanced aluminium coated off-axis parabolic (OAP) mirrors. This coating allows a reflection above 80% over a wide spectral range (from about 250 nm to 10 μm) with a constant focal length. By using these two OAP mirrors, the emitted PL radiation can achromatically be firstly collimated (first OAP) and then focused (second OAP) into an optical fiber. The PL emitted signal can be eventually reduced in intensity by employing an optional neutral density filter (placed between the two parabolic mirrors) to avoid detector saturation, if needed. Before being collected into the optical fiber, the emitted radiation passes through long pass filter(s), which blocks the laser beam eventually reflected back by the sample (or by the optical quartz windows of the cryostat) and avoids second order effects in the long wavelength range.

The emitted PL signal is thus collected by a low-OH content silica multimode optical fiber (usually abbreviated as low-OH fiber): it allows only a constant and low attenuation of the signal up to 2200nm essentially due to the low OH content in the silica, avoiding strong absorption peaks in the NIR wavelength range. Then, the collected PL signal reaches one of the two spectrograph shown in the scheme, depending on the spectral range under investigation and it is then directed onto the corresponding grating to be spectrally resolved. Finally, the signal is detected by either a Si-camera (used for a spectral range 300-1100nm) or an InGaAs-array detector (for a range of about 900 nm to 1600 nm) or an extended InGaAs-array detector (used to investigate a spectral range 1400-2200 nm). Concerning the spectrographs, the one “200-1600 nm” can spectrally resolve the PL signal into a grating with a line density of either 100 lines/mm or 300 lines/mm. The final resolutions of the experiments depends on both the grating (i.e. its line density) and optical fiber (i.e. its inner core dimeter) used: in most of the PL measurements of this thesis, a fiber with a core diameter of either 200 µm or 550 µm is used. Therefore the wavelength resolution in the visible can vary from about Δλ = 2 nm (using fiber core diameter of 200 µm and grating density of 300 lines/mm) to about Δλ = 16 nm (using fiber core diameter of 550 µm and grating density of 100 lines/mm). The other spectrograph used for longer wavelengths has a grating density of 90 lines/mm and a resolution of about Δλ = 30 nm.

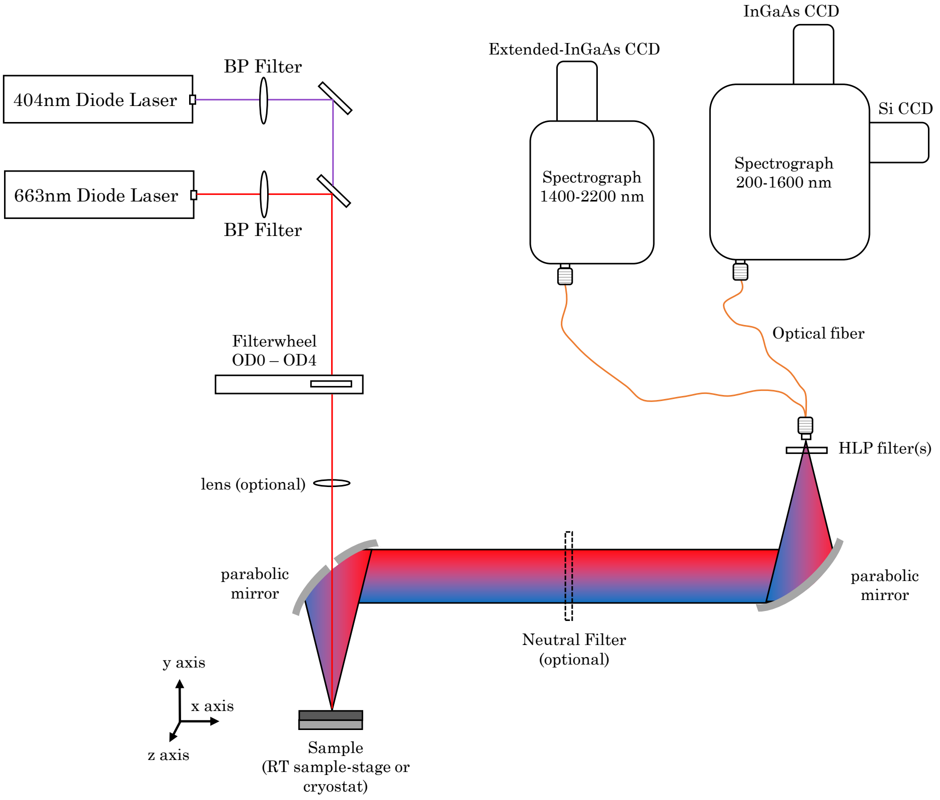

Figure 2.5.3: scheme of the home-built photoluminescence setup used for all PL measurement discussed in this thesis. The mirror placed in front of the band pass (BP) filter of the 663nm laser can be easily flipped down if the 404nm laser is needed to carry out the experiments. In absence of a fiber coupler/splitter, the PL signal cannot be guided in the two spectrograph at the same time, thus a reposition of the fiber is necessary if a different spectrograph needs to be used.

From raw data to corrected spectra: spectral correction

The measured spectra are acquired in *counts* as a function of the wavelength expressed in nm (see figure 2.5.4 as example). In order to take into consideration the different spectral sensitivity of the PL setup (quantum efficiency of the CCD cameras, reflectivity of the mirrors, spectral attenuation of the fiber used), a calibrated halogen lamp is used. Its emitted spectrum (ξ^{corr}) is known and is provided by the company and expressed in µW/(cm² x nm). From the measured lamp spectrum (ξ^{meas}), it is possible to get the *correction function C* defined as

$$C = \frac{\xi^{corr}}{\xi^{meas}} \left[\frac{\mu W}{cm^2 \times nm \times counts}\right] \qquad \text{eq. 2.5.22}$$

Therefore, the spectral correction is performed multiplying the single PL spectrum measured (χ^{meas}) by this function C

$$\chi^{corr} = C \times \chi^{meas} \qquad \text{eq. 2.5.23}$$

with χ^{corr} expressed in μW/(cm^2 x nm) as a function of the wavelength (nm). It is worth mentioning that in order to apply this correction function to the PL spectrum, the spectral calibration has to be performed under identical experimental geometries of the PL measurements, such as fiber, grating or camera. The PL spectrum in λ space is then converted in energies space by using the Jacobian conversion [72] taking into consideration the relationship $E = hc/\lambda$ and the energy conservation $f(\lambda)d\lambda = f(E)dE$, thus applying to y-axis and x-axis the following transformation:

$$y\left[\frac{\mu W}{cm^2 \times nm}\right] \rightarrow y \times \frac{x^2}{hc}\left[\frac{\mu W}{cm^2 \times eV}\right] \qquad \text{eq. 2.5.24}$$

$$\text{x [nm]} \rightarrow \frac{hc}{x}[eV] \qquad \text{eq. 2.5.25}$$

Finally, to get the photon flux density from the power density, the last conversion is applied to the y-axis:

$$y\left[\frac{\mu W}{cm^2 \times eV}\right] \rightarrow y \times \frac{6.241 \times 10^{12}}{x}\left[\frac{\#\, photons}{cm^2 \times s \times eV}\right] \qquad \text{eq. 2.5.26}$$

where firstly the power is converted to energy per seconds (with 6.241 x $10^{12} = 10^{-6}/e$ and e elementary charge to get energy in eV), then it is divided by the photon energy (x) to get the amount of photons.

Thus, the spectral correction can significantly change the shape of the measured spectra. Not in all reports in literature it is explicitly stated that the spectral correction is applied. Additionally, when comparing the spectra shown in this thesis with those that can be found in literature, one needs to consider if the PL spectra are plotted as PL intensity or PL flux: from figure 2.5.4(d), in fact, it is clear this also affects the PL spectrum shape.

The halogen lamp is thus used for the spectral calibration which significantly changes the measured PL spectrum shape. This lamp cannot be used for intensity calibration as its measured signal is not absolute. In other words, the emitted spectrum provided by the company is measured with an unknown geometry (e.g. an integrating sphere may also be used). Therefore, when the lamp is measured in the home-built PL setup, the recorded signal has an intensity that is proportional (but lower) to the intensity provided by the company. This in turn leads to a final PL spectrum which is actually expressed as a photon flux that is proportional to the absolute photon flux. This proportionality factor is derived through intensity correction that is explained in the next section.

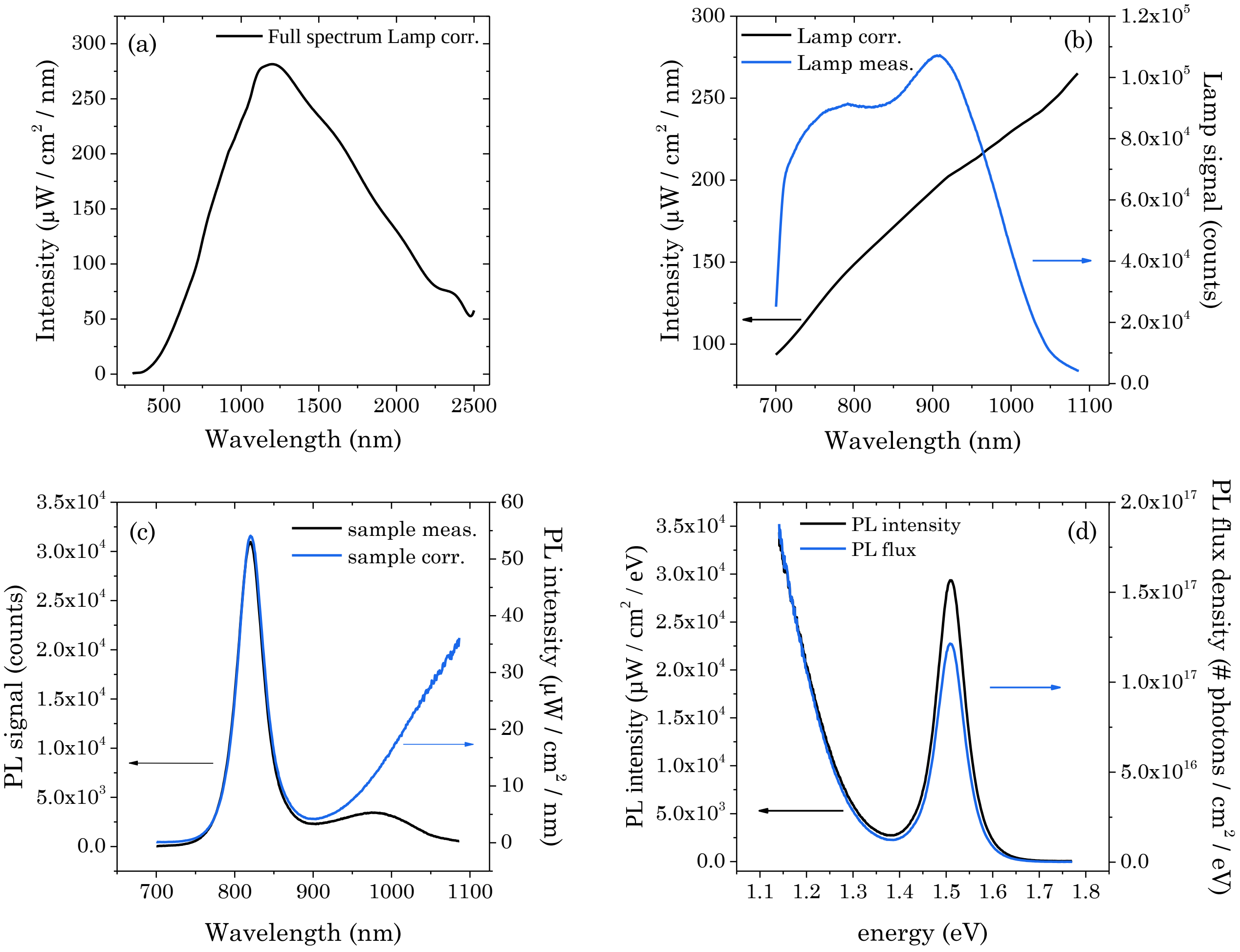

Figure 2.5.4: (a) full spectrum of the calibrated halogen lamp; (b) measured spectrum of the halogen lamp together with the corresponding calibrated spectrum in the same spectral region; (c) measured and spectrally corrected spectrum of a CIS absorber; (d) conversion in energy space of the spectrally corrected spectrum of the CIS absorber together with the conversion from power density to photon flux density.

From raw data to corrected spectra: intensity correction

The correction described in the previous section takes into account the different spectral sensitivity of the experimental setup. At the same time, while the spectral shape gives meaningful information about the optical properties of the sample investigated, the PL intensity or PL flux plotted over the energy has no meaning if the intensity correction (or calibration) is not conducted. In this case the photon flux is expressed in arbitrary units (arb. units or a. u. in this thesis), because it is only proportional to the absolute photon flux, which instead is expressed as # photons /s/ cm^2/eV.

The knowledge of the absolute photon flux is essential above all for the quasi Fermi level splitting measurements and evaluation, which are explained in the next section.

The intensity calibration is performed by measuring a reference with known intensity. While for spectral calibration a reference halogen lamp is used with its known spectrum, for intensity calibration the laser photon flux is taken as reference. The calibration is based on the comparison between the photon flux of the laser beam measured independently of the PL setup configuration (for collection) and the photon flux measured though the optical elements of signal collection (i.e. OAP, fiber, spectrograph and detection camera).

Hence, the photon flux density of the laser beam at a certain power is firstly calculated by measuring its radius and power. The radius is estimated by analysing the laser beam intensity shape which is recorded through a camera with a CMOS (complementary metal-oxide semiconductor) sensor placed at the sample position. Particularly, the intensity profile can be approximated to a Gaussian profile, as shown in figure 2.5.5 which shows the beam shape for the red laser with and without the convex leans in the optical path. In both cases, as shown by the fit of the x-profile, the laser beam has a Gaussian profile in the two directions.

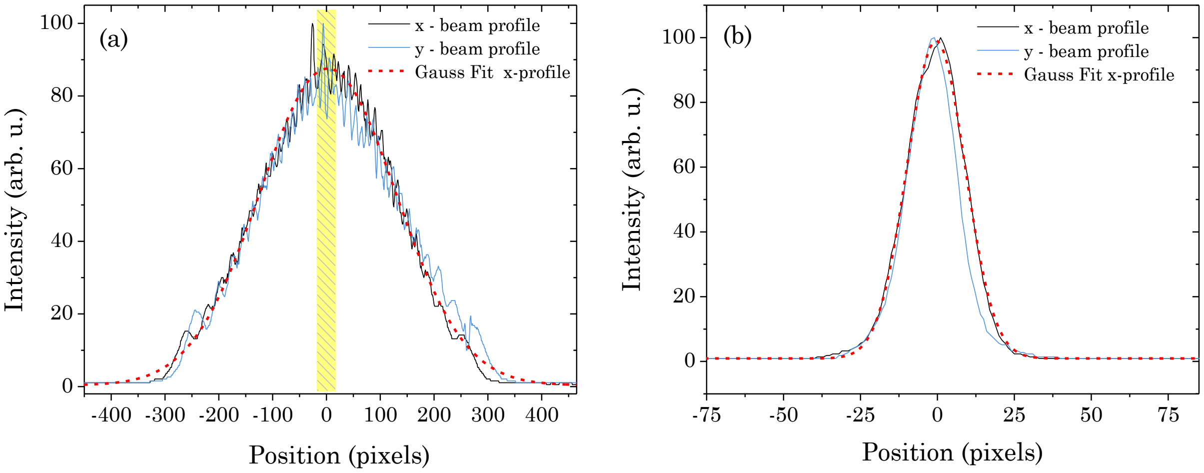

Figure 2.5.5: beam profiles of the red laser in the x and y directions together with Gaussian fit of the x-beam profile; (a) without focusing lens, (b) with focusing lens. The width of the profiles is expressed in pixels (of the CMOS sensor): each pixel corresponds to 5.2 µm. The yellow patterned box indicates the extension of the collection spot diameter when a fiber with inner core diameter of 200 µm is used (i.e. about 38 pixels in the picture).

For a laser beam with a Gaussian profile, the radius is defined as the position where the intensity transmitted drops by a factor of $1/e^2 = 0.135$ of the maximum value. The intensity profile depicted in figure 2.5.5 can be expressed by a standard Gaussian distribution:

$$I(r) = I_0 e^{-\frac{r^2}{2\sigma^2}} \qquad \text{eq. 2.5.27}$$

with I_0 being the peak intensity and σ^2 variance. According to the previous definition, the beam radius w is defined as $r = 2\sigma$. The total power P_0 transmitted by the beam is given by the integration of the intensity along x and y dimensions:

$$P_0 = \iint_{-\infty}^{\infty} I \, dxdy = \int_0^{2\pi} \int_0^{\infty} I(r)\, r \, drd\varphi = 2\pi\sigma^2 I_0 \qquad \text{eq. 2.5.28}$$

The aforementioned definition of laser beam radius allows to have a simple expression of the peak intensity I_0 given by

$$I_0 = \frac{P_0}{2\pi\sigma^2} = \frac{2P_0}{\pi w^2} \qquad \text{eq. 2.5.29}$$

For the red laser, the beam laser radius measured without lens is around 1.38 mm, whereas the one measured using the focusing lens is about 90 μm.

The total power transmitted by the beam P_0 is measured by putting at the sample position a powermeter (which is a photodiode power sensor). The photon flux density of the laser at the peak maximum is thus determined as

$$\Phi_0 = \frac{2P_0\lambda}{\pi w^2 hc} \qquad \text{eq. 2.5.30}$$

where the power is divided by the energy of the laser photon ($h \times c/\lambda$). This photon flux is actually the flux measured in a PL experiment, as the collection is only from the very center, as will be discussed also in section 2.5.4.

Before discussing the actual laser photon flux measured through the collection path of the PL setup, it worth mentioning that when an absorber is placed at the sample position, the photon flux just calculated represents the excitation incident photon flux density. This is a key parameter when comparing different experiments about photoluminescence spectra on the same material. In fact, in several scientific reports only the excitation power laser is given: this information might be meaningless without any information about the laser spot dimension.

In order to measure the photon flux density through the collection path of the PL setup, a reflector is needed at the sample position to reflect back the laser beam and measured in the end with the Si-CCD detector. This reflector might be a mirror, but this choice would not "simulate" the emission of the PL radiation from the sample surface. For this purpose, a spectralon diffusor with a lambertian surface is placed at the sample position and reflects back the laser beam. The reflectivity of this diffusor is higher than 99 % over a wide spectral range (from about 350 nm to 2200 nm). The lambertian reflectance is needed because it simulates the PL emission from the sample surface, which has a Lambertian profile as well [73]. The measured laser line, with a finite broadening due to the collection optics elements of the PL setup (e.g. fiber and spectrograph used), is spectrally corrected (following a similar step as shown in 2.5.4(c) for a PL spectrum), giving the laser profile in unit of μW/(cm^2 x nm). The integration over wavelength gives the total power *collected* by the PL setup and together with the photon energy of the laser used, the photon flux density *collected* can be extracted. The ratio between the photon flux density calculated with the beam radius and power measurements Φ_0 and this photon flux density *collected* gives the intensity (or flux) calibration factor. Applying this factor to the y-axis values of the spectrally corrected spectra, it is possible to get the real photon flux density emitted from the samples: in this case it would be expressed as #photons/s/cm^2/eV, otherwise in arbitrary units if the intensity calibration is not performed.

Excitation intensity dependence

By measuring the radius and total power incident on the sample, it is possible to get the excitation flux density, as described in the previous section. On the other hand, even without these information (if the absolute photon flux density is not needed), it is possible to vary the incident laser power to access to a wide range of excitation intensity. For this purpose, the filter wheel shown in figure 2.5.3 is used. The filter wheel contains 4 different neutral filters, called also optical density filter, OD1 to OD4, which attenuate the incident laser power. The numbers 1 – 4 refers to the attenuation factor provided by the optical filter: i.e. for a filter OD×, the incident beam will be attenuated by a factor of $10^{\times}$. The attenuation value depends on the laser wavelength, as shown in figure 2.5.6.

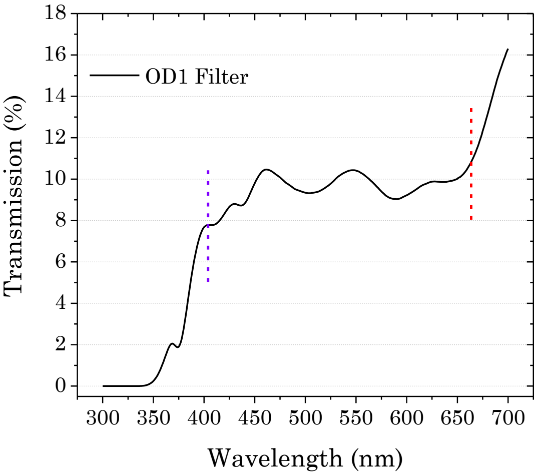

Figure 2.5.6: transmission values of the optical density filter 1 (OD1) as reported in https://www.thorlabs.com. The two dashed lines represent the wavelengths of the two laser used in this work, 404 nm and 663 nm.

It is clear, then, that for precise and reliable measurements it is essential to consider the transmission of the filter used for the specific laser wavelength. In table 2.1 the transmission values based on own measurements are reported. For each filter, they have been determined by measuring the laser power with a power meter, with and without filter placed in the optical path. This procedure has been done for four different powers (1mW, 2mW, 4mW, 8mW). The values reported are average ones. Those referring to the OD1 filter approach very well to the expected values (see figure 2.5.6).

Table 2.2: transmittance values of the neutral density filters used in this thesis, determined experimentally for both 404 nm- and the 663 nm-laser. For each filter, the transmittance value is obtained by changing the laser output power and taking an average value. The standard deviation for all listed values is in the range of 0.6 – 1.0 %.

Filter	Laser 404 nm	Laser 663 nm
OD 0 (no filter)	1	1
OD 1	7.79×10^{-2}	1.06×10^{-1}
OD 2	3.02×10^{-3}	1.18×10^{-2}
OD 3	1.85×10^{-4}	1.44×10^{-3}
OD 4	9.56×10^{-6}	1.50×10^{-4}

2.5.4 Quasi Fermi level splitting measurement - evaluation

In section 2.5.3 the PL setup has been described, together with the procedure to perform both spectral and intensity calibration on the raw data. In this way, the final PL spectra are expressed as absolute PL flux (given in #photons/s/cm^2/eV) plotted over energy (eV) and they can be analysed to extract the quasi Fermi level splitting (QFLS). For this purpose, Planck's generalized law is used, equation 2.5.9, which is valid for actually homogenous excitation. This condition is satisfied because the collection spot diameter (around 200 µm) is much smaller than the excitation spot dimeter (without using the lens, $d = 2\ x\ r$ ~ 2.6 mm). To have a direct visualization, considering the laser beam shape in figure 2.5.5 and taking into consideration that each pixel equals to 5.2 µm, the collection spot diameter extends only for about 38 pixels (yellow patterned box in figure 2.5.5).

As already stated in section 2.5.1, Planck's generalized law describes the emitted photon flux density per energy interval in a steady state condition. Therefore, to gain access to the band-to-band QFLS, it would be enough to fit the spectrum over the energy of the band gap luminescence emitted from the sample. Figure 2.5.7 reports an example of PL spectrum for a CuInS$_2$ sample grown in the framework of this thesis. However, only the PL flux density is not sufficient to extract the QFLS as the absorptivity would be still an unknown parameter. The absorptivity can be independently estimated through spectrophotometry spectroscopy by measuring the transmittance and reflectance of the thin film, which would then require deposition on glass (w/o Molybdenum coating) or exfoliation of the film from the Mo-coated glass. To circumvent these additional steps necessary for the absorptivity determination, some assumptions can be considered.

Firstly, as the Planck's generalized law describes the emitted photon flux density per energy interval, its application (to describe the experimental values) over the whole range of the band gap luminescence is not needed; instead, if a narrower range is chosen which lies at energy sufficiently higher than the band gap (typically > 0.1 eV above E_G), the absorptivity can be approximated to be unity, thus $a(E) \approx 1$. At the same time, for such energy range, it can be assumed as well that $E - \Delta\mu \gg k_BT$, which in turn allows a Boltzmann approximation for the Bose-Einstein term, thus neglecting 1 in the denominator. With these approximations and applying a natural logarithmic on both terms, equation 2.5.9 can be rearranged as follows:

$$Y_{PL}(E) = \frac{1}{4\pi^2\hbar^3c^2}\frac{a(E)E^2}{\exp\left(\frac{E-\Delta\mu}{k_BT}\right)-1} \approx \frac{E^2\exp\left[-\left(\frac{E-\Delta\mu}{k_BT}\right)\right]}{4\pi^2\hbar^3c^2} \rightarrow \ln\left(\frac{Y_{PL}}{CE^2}\right) = -\frac{E-\Delta\mu}{k_BT} \qquad \text{eq. 2.5.31}$$

with C a constant that contains all the other constants, and has a value of about 10^{23} /s/cm^2/eV^3. Therefore, if the PL spectrum shown in figure 2.5.7(a) is converted following equation 2.5.31, a semi-logarithmic plot is obtained (figure 2.5.7(b)). Analysing the high energy wing of the band gap luminesce by a linear fit, both temperature and quasi Fermi level can be extracted.

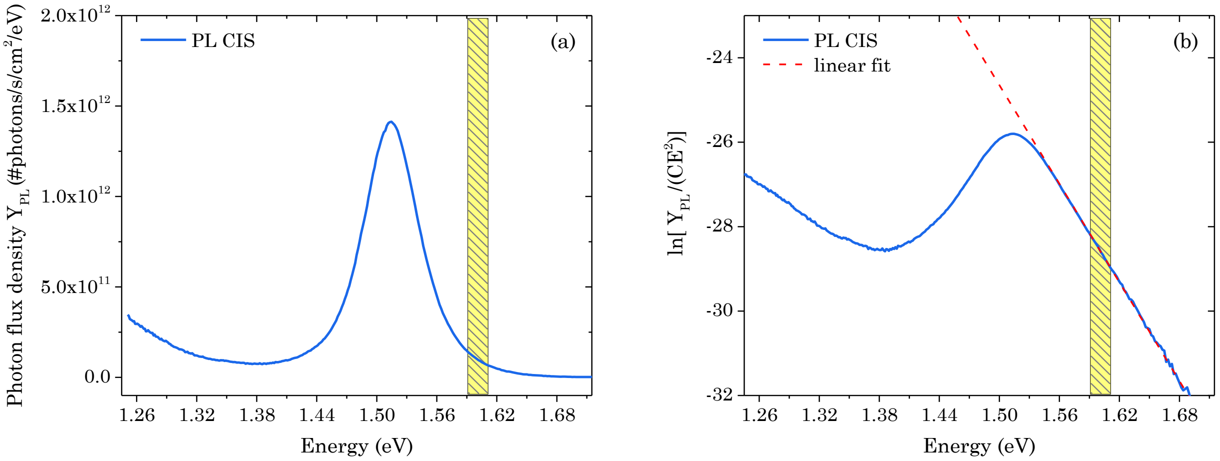

Figure 2.5.7: (a) absolute photon flux density of a CIS sample plotted over energy; (b) semi-logarithmic plot of the PL flux density (divided by C and E^2) plotted over energy together with a linear fit of the high energy wing. In both cases the fitting range is highlighted with a patterned box which lies at about 100 meV above the PL peak.

Quasi Fermi level measurements are carried out at room temperature, thus from the slope of the linear fit a value of about 298 K is expected. Although this is true for high quality films (with high QFLS), it can deviate also significantly from this value, reaching a temperature much higher by tens of K. This is essentially caused by the fitting range chosen to extract the QFLS (highlighted in figure 2.5.7 with a yellow patterned box). In fact, in this energy range, the photon flux density is just 2 % of the whole band-to-band emitted photon flux density and for samples with low QFLS, thus low corresponding fluxes, any unwanted background of the PL setup may decrease the signal to noise ratio. This then translates into a change of the slope of high energy wing, hence it leads to an overestimation of the temperature. Although the main interest is not focused on the temperature determination, its overestimation, assuming the same photon flux density, leads at the same time to an underestimation of the QFLS. This can be easily seen rearranging equation 2.5.31 and taking the derivative of QFLS with respect to T:

$$\ln\left(\frac{Y_{PL}}{CE^2}\right) = -\frac{E-\Delta\mu}{k_B T} \rightarrow \Delta\mu = k_B T \ln\left(\frac{Y_{PL}}{CE^2}\right) + E \rightarrow \frac{\partial\Delta\mu}{\partial T} = k_B \ln\left(\frac{Y_{PL}}{CE^2}\right) \quad \text{eq. 2.5.32}$$

For the sample considered above, the logarithmic term has a value of about -28 in the fitting range. Taking into consideration the Boltzmann constant, 8.6173×10^{-5} eV K^{-1}, the QFLS decreases linearly approximatively 2.5 meV K^{-1} when the temperature increases. As said previously, if the temperature is set as a free parameter during the fitting, it can reach values well above 298 K, which translates into an underestimation of the QFLS by several tens of meV. This issue can be addressed by measuring the real temperature of the sample (under excitation of the laser beam) with an infrared thermometer, which indeed gives a value of 298 ± 1 K. In all QFLS evaluations performed in the framework of this thesis, the temperature has been kept constant at 298 K in the fitting procedure.

Finally, it is worth mentioning once more (as explained in section 2.5.1) that in a steady state measurement, the carriers distributions at the edges of the bands (thus after thermalization) do not depend on the spectral distribution of the absorbed photons but just on the incident flux density. Therefore, while the performance of the photovoltaic solar cells are usually tested under illumination which resembles the A.M.1.5 solar spectrum, quasi Fermi level splitting measurements are carried out by using a monochromatic light as excitation source. In order to compare the open circuit voltages measured in a solar simulator with the quasi Fermi level splitting values, the laser excitation flux needs to be tuned to achieve an equivalent illumination of 1 sun. Assuming all photons of the laser beam are absorbed (due to their high energy compared to the band gap), the incident flux density can be calculated by applying equation 2.5.30. This flux is compared to the flux density absorbed for a certain band gap from the A.M.1.5 solar spectrum, assuming a step-like absorption at the band gap. The ratio between the two is called equivalent flux or illumination. The comparison of QFLS and VOC can be done if this ratio is 1. In some circumstances, to ease the measurements (for low quality absorbers) or just to compare QFLS of different samples, equivalent illuminations higher than 1 sun will be used.

2.6 Defects model review in $CuInS_2$ absorber layers and devices

One of the first contributions that reports a detailed study on point defects in $CuInS_2$ has been published in 1982, a work by Binsma et al [74]. In this section an overview over the last four decades of the main investigations on point defects in $CuInS_2$ is given. A summary of the experimental findings described in the following is shown in figure 2.6.1. As stated in section 2.4, understanding the presence and the effect of these defects is significant to predict, to control or to explain the optoelectronic properties of the corresponding absorbers. A shallow defect, e.g., can increase the doping of the semiconductor, whereas a deep defect is detrimental as it increments the non-radiative recombination, thus, e.g., reduce the quasi Fermi level splitting.

Binsma et al. investigated $CuInS_2$ crystals and polycrystalline by means of photoluminescence spectroscopy [62, 74]: deviations from the stoichiometry were achieved by equilibrating for 60 h at 750 °C the samples with excess of Cu (i.e. with Cu/Cu_2S) and with excess of In (i.e. with $In/CuIn_5S_8$). They found two emissions characteristic of samples annealed with excess of Cu, at 1.39 eV and 1.36 eV, whereas samples annealed with excess of In were showing two other characteristic lines, at 1.44 eV and 1.41 eV, respectively. The defect model proposed in their work included two donors, respectively at 35 meV and 72 meV from the conduction band and two acceptors, at around 100 meV and 150 meV from the valence band. The activation energies of the two acceptors were estimated by the analysis of the quenching of the emission intensity of the respective lines. The deeper acceptor (at around 150 meV) was previously found by Look and Manthuruthil in [67] by electrical measurements, which also revealed the presence of a deep donor at about 350 meV from the conduction band. Given the correlation between the stoichiometry or treatments on the samples and the emission lines observed, the 100 meV acceptor has been tentatively attributed to V_{Cu}, whereas the 150 meV to V_{In} or Cu_{In} [74]. Single crystal $CuInS_2$ were also analysed by Ueng et al. in [75] by electrical and photoluminescence analysis, proposing a defect model with a shallow acceptor at 100 meV and 3 shallow donors at 35 meV, 70 meV and 145 meV, respectively. Töpper at al. in [76] studied Cu-rich polycrystalline films co-evaporated on Mo-coated glass substrates by photoluminescence, investigating the optical properties of the as-grown films and after post deposition treatments (annealing at 200 °C in hydrogen or oxygen atmosphere). They found a correlation between the hydrogen annealing and the enhancement of the 1.44 eV emission line, which previously in [74] occurred only in samples annealed with an excess of In. The intensity of this line could drastically be reduced after annealing in oxygen atmosphere. This behaviour has been explained by assuming the oxygen occupation (during O_2 annealing) or oxygen removal (by hydrogen annealing) from sulphur vacancies, thus reducing or increasing, respectively, the emission line at 1.44 eV. This transition, in fact, by means of excitation and intensity dependence, was related to a DA between a shallow donor, at 35 meV (tentatively ascribed to sulphur vacancies), and a shallow acceptor at about 65 meV. It is important to mention in all spectra they observed a broad band in the energy range of 1.2-1.3 eV and in some cases an additional emission at 1.37 eV.

The PL peaks at 1.445 eV and 1.25 eV have been observed also by Luck et. al [77], who investigated the effect of sodium in Cu-rich CIS thin films grown by rapid thermal annealing and their corresponding devices. Although the power conversion efficiencies and the external quantum efficiencies were barely affected by the amount of sodium incorporated, the 1.445 eV emission line anti-correlated to sodium (lower PL intensity for samples deposited with higher amount of Na). This is consistent with the model suggested by Binsma [74] who proposed copper vacancy as possible origin for the acceptor defect (at about 100 meV) involved in the 1.44 eV transition. In fact, assuming a similarity to what has been calculated for Cu(In,Ga)Se_2 in [78], it is likely sodium occupies copper vacancies to form an electrically inactive sodium on copper antisite defect, i.e. Na_{Cu}, as this defect has the lowest formation energy compared to other doping sites (e.g. Na_{In}) [78]. In this way, the sodium partially “passivates” copper vacancies, therefore the relative photoluminescence emission would show a lower intensity. By means of admittance spectroscopy, Luck et al. found also a defect at about 300 meV above the valence band by analysing solar cells prepared with different glass substrates. This deep defect at 300 meV has been found also by admittance spectroscopy in Cu-rich CIS devices, independently of the buffer layer used (i.e. Zn(O,S) or CdS) together with an additional deeper defect at about 500 meV [79]. By using deep-level transient spectroscopy (DLTS), the authors related both deep defects to acceptors and found an increasing density of the deepest defect (at 500 meV) correlated with a decreasing open circuit voltage [79].

Admittance spectroscopy has been used extensively also by Siemer at al., who analysed devices made from absorber prepared with a wide range of deposition conditions or techniques [80]. Particularly, Cu-rich samples prepared by coevaporation of Cu, In and S or by annealing in elemental sulphur of sputtered metal precursors showed again in both cases two deep acceptors at about 300 meV and 500 meV above the valence band. The 300 meV defect was also found in samples prepared from sequential evaporation of Cu and In followed by annealing in elemental sulphur. Admittance spectra of co-evaporated absorbers prepared under slightly Cu-poor conditions were instead characterized by two defects, at 180 meV and 600 meV respectively, although their nature is not discussed in their work. Finally, devices including CIS absorbers deposited by sputtering of metal stacks followed by a rapid thermal annealing (RTP) were instead showing a capacitance step with an activation energy of 140 meV. As this defect was showing an energy shift to 100 meV upon annealing in air, the authors attributed this feature to interface rather than bulk defect: this is based on the assumption a bulk defect cannot change its energy by annealing at temperature below 200 °C. The same group has investigated devices based on Cu-rich absorbers grown by sequential process using two different annealing procedures [81]. The analysis conducted by means of DLTS revealed again the presence of a deep acceptor at about 350 meV from the valence band and an additional deep donor at about 250 meV from the conduction band.

One of the last investigations on the point defects in $CuInS_2$ is given in [82] where Eberhardt et al. studied both epitaxial and polycrystalline CIS thin films. By means of excitation intensity and temperature dependent photoluminescence measurements, they suggested a defect model which includes two shallow acceptors at about 70 meV and 120 meV above valence band and two shallow donors at about 46 meV and 87 meV from the conduction band. Particularly for the epitaxial thin films, they observed also the 1.20-1.25 eV transition and an additional donor-acceptor transition centered at around 1.03 eV.

Figure 2.6.1 shows a summary of the point defect energy levels estimated in the aforementioned works. It is clear there is not agreement and well developed model for the electronic structure of this material, neither for the shallow defects, nor for deeper ones. For instance, by PL spectroscopy two deep transitions have been observed (at 1 eV and 1.25 eV) but their origin is unknown. On the other hand, two specific capacitance steps with an activation energy of about

300 meV and 500 meV have been found in several cases, attributed to deep acceptors. Although at first sight (of the summary defect picture) it could come naturally to attribute these features found by electrical measurement to the PL transitions mentioned above, one needs to take into consideration also the strong electron-phonon coupling typical of deep defects. In fact, as explained in section 2.5.2, PL transitions which involve deep defects do not show their maxima at the zero-phonon line, therefore their correlations with defects activation energy found by e.g. admittance spectroscopy is not straightforward. Additionally, there is not a clear picture of shallow defect structure: one or two acceptor and from one to three shallow donors have been proposed.

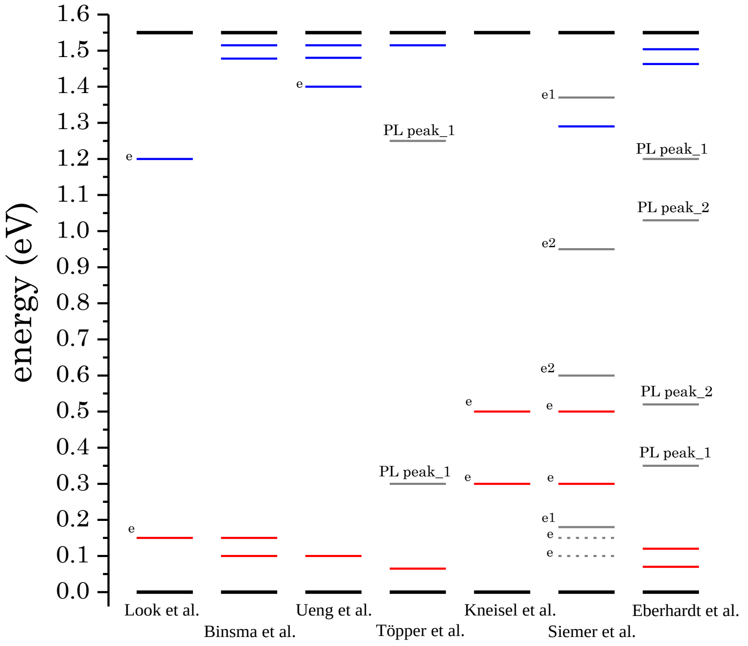

Figure 2.6.1: overview of the activation energies of point defects in $CuInS_2$ determined by means of electrical measurements (marked with "e") and photoluminescence spectroscopy (not marked). The acceptors and donors are drawn with red and blue lines, respectively. In grey defect states with an unknown character, in dashed lines states attributed to interface defects. Additionally, the PL peak positions of the two deep transitions (at around 1 eV and 1.25 eV deep) have been reported, although their origin is not known yet, thus they do not refer to specific defects but to transitions, marked with "PL peak". Both these "PL peak" positions and the defects found by electrical measurements with unknown character have been represented twice (marked with the same number) within the band gap but specular to the mid gap, as they could originate either from deep acceptor(s) or deep donor(s).

Besides the energy positions of the point defects within the band gap, their chemical attribution in the past has been speculative, i.e. it has been based on correlation between the experimental conditions used to fabricate absorbers and the observation of specific transitions in photoluminescence (or specific features in admittance spectroscopy, Hall or DLTS). By way of example, the shallow donor at about 35 meV is believed to be a sulphur vacancy, although there are no direct proofs which support this attribution.

A support for these attributions (or feedbacks for defects not yet correlated with specific point defects) may come from theoretical calculations. Recently, calculations performed using screened-exchange Heyd-Scuseria-Ernzerhof (HSE06) hybrid density functional [83] have shown great improvements in describing accurately the electronic properties of $CuInSe_2$ and $CuGaSe_2$ in terms of band gaps and energy positions of the point defects [84-88] . In fact, most of these works match very well the latest defect recombination models derived experimentally proposed for these two chalcopyrite materials [89, 90].

At the time of writing this thesis, only two reports can be found which attempt to calculate the electronic structure of $CuInS_2$ using HSE06 hybrid density functional, [91] and [92]. Table 2.3 gives a comparison of the computational details used in these two reports, together with those used in Pohl et al. [84], as this last one shows a good match between theoretical calculations and experimental findings [89] for selenium-based chalcopyrites. Additionally, in the comparison, a second report of Pohl et al. [93] is included: in this work, the authors studied the copper vacancy thermodynamics (e.g. formation enthalpies) in $CuInSe_2$, $CuGaSe_2$ and their sulphides counterparts. In both reports, Pohl et al. used the same computational parameters, and they could get calculated bad gap values that perfectly matched the experimental ones (both for selenides and sulphides). It is important to keep in mind these kind of calculations use the conventional density functional (e.g. GGA, generalized gradient approximation) together with a fraction of Hartree-Fock mixing. The standard portion of the Hartree-Fock exchange is usually $\alpha = 0.25$, to facilitate also the comparison between different reports. An additional important parameter to take into consideration is the inverse screening length ω ($Å^{-1}$). In the HSE06 functional, the Coulomb operator is split into short range (SR) and long range (LR) components. The SR component includes both a GGA functional and a Hartree-Fock functional, whereas the LR component uses only the GGA one. The parameter ω governs the relative amount of SR and LR components: if $\omega = 0$ $Å^{-1}$, the LR contribution becomes zero and the Coulomb operator is given only by the SR component [83].

However, it is important to consider that the same band gap (and lattice parameters) for a specific semiconductor can be obtained by using a different combination of α and ω. On the other hand, the tuning of these two parameters leads to variation (also significantly) of defect formation energies and charge transitions levels within the band gap: for instance, Han et al. have done calculations on $CuGaSe_2$ by using $\alpha = 0.26$ with $\omega = 0.08$ and $\alpha = 0.25$ with $\omega = 0.13$, respectively, obtaining differences in energy levels up to 0.20-0.25 eV [94].

Additionally, these calculations are performed considering a defect placed into a supercell with a certain number of atoms, which can vary from 32 up to 432 atoms. The numbers of atoms selected depends on the computation costs a specific work can effort to. Nevertheless, it has been shown it can significantly change both the formation energies and the charge transition level energies of point defects [88].

A further detailed discussion about theoretical calculation based on HSE06 is beyond the scope of this thesis; however it is clear all parameters involved in these computational processes to get e.g. the optoelectronic properties of a semiconductor may influence the final defect model that is derived, together with their formation energies. This explains the reason behind dissimilarities (in some cases relevant) between different reports which investigate the same material.

Table 2.3: comparison of the computational parameters of HSE06 functional calculations for $CuInS_2$ and $CuInSe_2$.

Report	E_G calculated (eV)	Screening parameter ω Å^{-1}	Hartree-Fock mixing	Atoms in supercells
Chen [91] ($CuInS_2$)	1.40	0.13	?	64
Yang [92] ($CuInS_2$)	1.5	?	0.36	32
Pohl [93] ($CuInS_2$)	1.53	0.13	0.25	64
Pohl [84] ($CuInSe_2$)	1.07	0.13	0.25	64

In the Chen et al. report [91], the Hartree-Fock mixing is not given, although the standard and default value is 0.25, whereas the screening parameter is set explicitly to the same value previously used by Pohl et al., i.e. 0.13 Å^{-1}. The dissimilar band gap value (1.40 eV vs 1.53 eV) is not discussed in their work. On the other hand, in the Yang et al. report [92], the screening parameter is not indicated, whereas the Hartree-Fock mixing is adjusted to 0.36 in order to match the experimental band gap value. In figure 2.6.2 a comparison of the calculated charge transition levels of point defects is given.

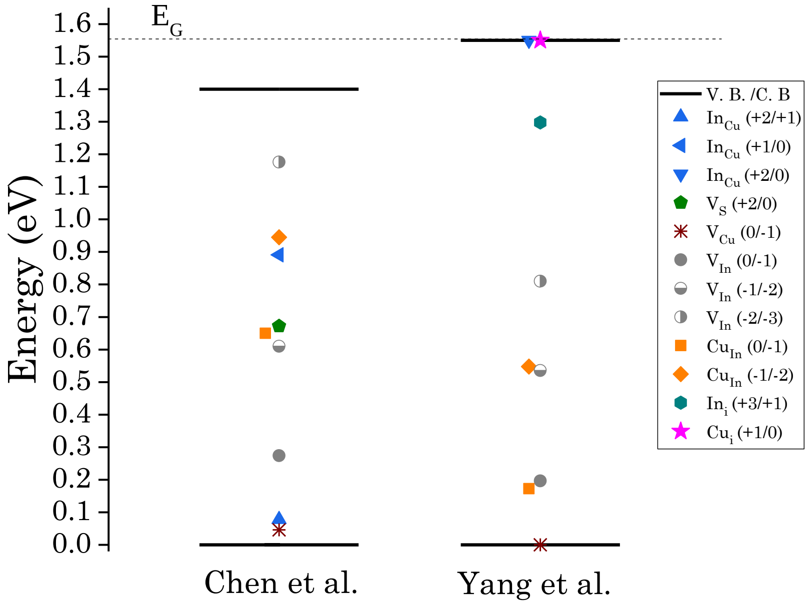

Figure 2.6.2: overview of the charge transition levels of point defects in $CuInS_2$ determined in Chen et al. ([91]) and Yang et al. ([92]). The dashed horizontal line represents the experimental band gap value for this semiconductor (1.55 eV). For each kind of defect, different charge states have been drawn with the same colour and similar shape (for instance, In_{Cu} with blue triangles but different orientations). In some cases (see right side scheme), shallow defects with an activation energy within the error of the calculations (typically about 100 meV) are drawn directly on the valence band (for acceptors) or on the conduction band (for donors). Some charge transition levels have been laterally shifted for a better visibility.

From the comparison of the two investigations on the point defects in $CuInS_2$ a few considerations can be drawn (beside the different calculated band gap):

a) In both reports, V_{Cu} is the shallowest acceptor;

b) Cu_{In} and V_{In} have both their charge transitions levels within the band gap (two and three states, respectively): in Yang et al., they are all shallower compared to Chen et al.;

c) Sulphur vacancies defects (V_S) are intentionally not investigated in Yang et al. because they are believed to have very high formation energy due to the standard growth conditions (under high sulphur overpressure) whereas in Chen et al. the calculated charge transition level lies around mid-gap;

d) The main difference between the two reports is given by the In_{Cu} defect: in Chen et al., two charge transition levels lie within the band gap (one of them deep in the gap), whereas in Yang et al. this defect has only one (double) charge transition level very close to the conduction band (shallow donor drawn on the C. B.);

e) Two more donors are investigated in Yang et al.: In_i and Cu_i, with the last one very shallow

In both reports, the authors do not refer or compare their results to experimental findings.

From this overview on both experimental defect energies (or transition observed in PL) and theoretically calculated ones, it becomes evident that a consistent and well developed defect recombination model for $CuInS_2$ is still missing. In chapter 5 the shallow defects electronic structure will be investigated in detail and in section 5.5 a refined point defects model for $CuInS_2$ will be given together with a comparison of previous findings reported in literature and the theoretical calculations discussed here.

Chapter 3

Absorber growth

In this chapter a detailed description of the absorbers growth is given. The $CuInS_2$ polycrystalline thin films have been deposited by physical vapour deposition (PVD in the following) on molybdenum (Mo) coated glass substrates. The glasses used as substrates have been either the standard soda lime glass (SLG) or a high softening temperature glass (in the following it will be named “HT glass”). More information about the thermal properties and composition of these two glasses are reported in Appendix 3.1. In the rest of the thesis, the specific substrate (SLG or HT glass) used will be always specified. In fact, the absorber properties are influenced also by the diffusion of elements of the glass through the molybdenum layer, e.g. the alkali elements.

First, a description of the PVD system is given. The first task of this thesis has been taking the PVD into service as this system has been mounted at the beginning of this thesis work. Therefore, its calibration and the development and optimization of the growth process have been carried out at first place.

The different process conditions used to deposit the absorbers will be explained as well as their influence on the structural properties, with a focus on the effect of the stoichiometry and process temperature.

The knowledge and experience acquired by using the abovementioned system have been used in the second part of this thesis to define the specifications of a new and more complex physical vapour deposition system. The taking into service of this second PVD has been one of the tasks of the last part of this thesis. Although some CIS absorbers have been deposited by using this system, mostly to optimize the buffer layer deposition in a parallel project, all results presented in this thesis are based on samples grown with the first mentioned PVD system. For these reasons, only this last PVD used to produce samples discussed in this thesis is described in the following.

3.1 Physical vapour deposition system

Several growth methods have been reported in the past to deposit thin films $CuInS_2$ [23, 43-47]. Some of them have been mentioned in the defect model review (section 2.6). The highest efficiencies have been achieved with devices based on $CuInS_2$ (or $Cu(In,Ga)S_2$) absorbers deposited by either coevaporation of the single elements or by reactive annealing (in elemental sulphur S or hydrogen sulphide H_2S gas) of precursor layer of metallic phases [24, 27, 48, 49]. One way to classify them is the distinction between vacuum and non-vacuum methods. The physical vapour deposition belongs to the first category and has been used in the framework of this work to deposit absorbers whose properties are discussed throughout this thesis. The basic principle behind this method, in this work, is the evaporation at low pressures (in the present case in the range of about $10^{-4} – 10^{-6}$ mbar) of elements (copper and indium) by heating them to high vapour pressure in chalcogenide atmosphere (sulphur in the present case). The high vacuum provides a long mean free path much higher than the distance between the vaporization sources and the substrates.

The thermal evaporation of the elements copper, indium and sulphur (with a melting point of about 1085 °C, 157 °C and 115°C, respectively) is achieved by heating crucibles which contain the corresponding element.

A scheme of the PVD system is given in Figure 3.1.

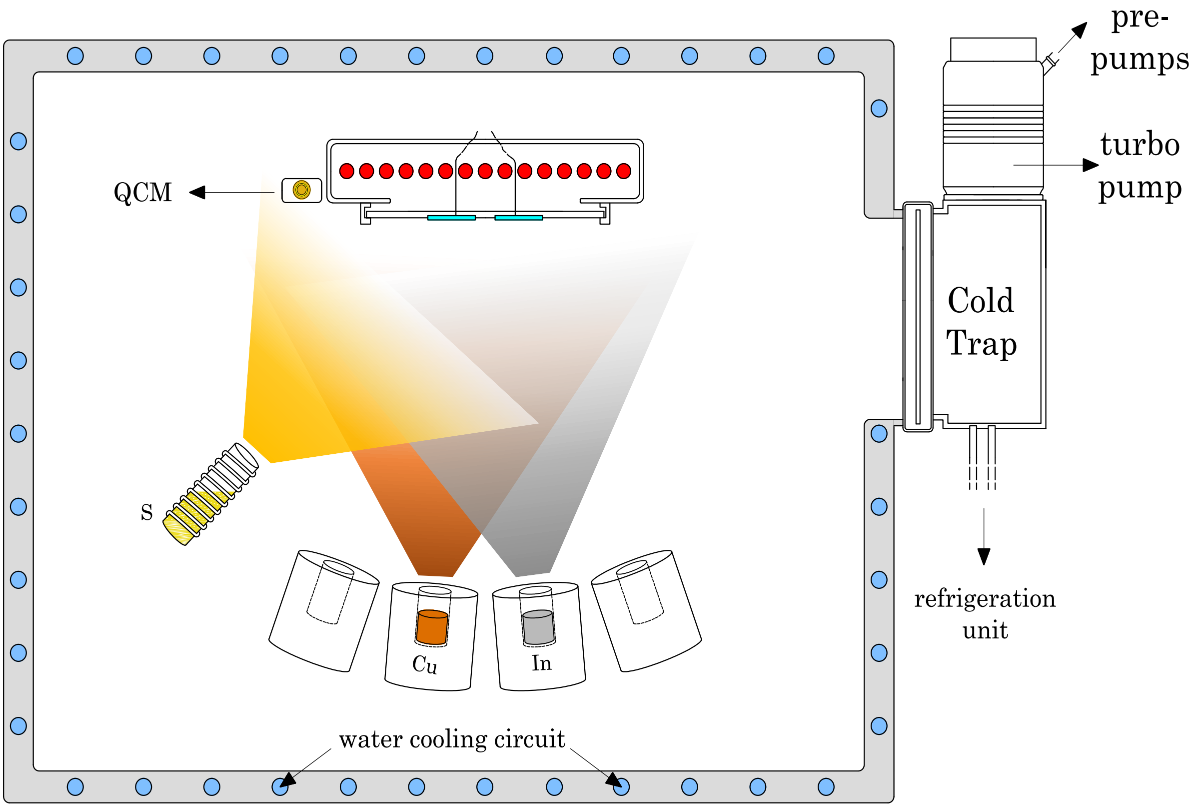

Figure 3.1: simplified scheme of the PVD used to deposit $CuInS_2$ absorber layers.

The core of the PVD system is the growth chamber. The base pressure inside the growth chamber is around 2.5×10^{-6} mbar and is achieved by means of two pre-pumps and one turbomolecular pump. The latter one is not directly attached to the growth chamber but it is preceded by a so called “cold trap” connected to a refrigeration unit. The “cold trap” is kept in a temperature range between -40 °C and -30 °C in order to catch all materials which are not deposited inside the main chamber, thus preventing mostly sulphur condensation in the vacuum line. Figure 3.2 shows a picture of the inner part of the cold trap and the bottom part of the turbomolecular pump. Is it clear that most of the sulphur condensates at the bottom of the trap (that is the coldest part) whereas the turbine blades are clean.

Figure 3.2: (left) inner part of the cold trap, the yellowish material is sulphur condensed mostly at the bottom; (right) turbine blades of the turbomolecular pump. Picture taken during a maintenance of the machine after two years of operation.

The walls of the chamber are surrounded by a water cooling circuit that keeps the temperature in a range of 15°C-20°C; this allows the condensations on the walls of most of the particles that are not evaporated on the substrates or pumped away. Moreover, it allows to reach lower base pressure.

Inside the growth chamber, on the bottom, there are four thermal evaporation sources, which can reach temperatures up to 1500°C. Each of them is equipped with an alumina crucible together with a PBN (pyrolytic boron nitride) liner; an internally mounted thermocouple monitors source temperature without exposure to vapours. For copper and indium evaporation these sources have been used.

An additional thermal evaporation coil source equipped with a Pyrex crucible has been used for sulphur evaporation. The temperature is monitored with a thermocouple directly in contact with the bottom of the crucible.

The substrates are placed on a sample holder, which is mounted in front of the heating elements (i.e. infrared lamps). The substrates temperature is accurately monitored by three thermocouples which touch directly their back surface. This PVD system is not provided with a rotating system for the substrates and this consequently leads to a gradient in the final composition of the absorbers grown, as discussed in section 3.2.

In order to control and optimize the growth of the thin films, it is essential to know the flux rates of the elements that correspond to a certain temperature. The flux rates can be monitored and calibrated by the quartz crystal microbalance (in the following QCM). It is placed few centimetres away from the sample holder in order to “read” flux rates as close as possible to those received from the substrates. The core of the QCM is a piezoelectric material (usually quartz) that can be made to oscillate at a defined frequency. When there is a change of mass (added or removed) on the electrode surface, this will cause a variation in the frequency of oscillation: this variation is correlated to the rate of deposition. As a variation in temperature may slightly change the frequency of oscillation, leading to an incorrect measured deposition rates, the QCM system is equipped with an independent water cooling system, to keep the temperature as most stable as possible.

3.2 Calibration of the elemental flux rates

The calibration of the elemental flux rates (Copper and Indium) has been performed using the QCM and a lab scale (semi-micro balance with a readability of 0.00001 g). For each element, the beam flux can be controlled by adjusting the temperature of the corresponding thermal evaporation source. The relationship between the evaporation rate r of the heated surface and its temperature T (expressed in Kelvin) is:

$$ln(r) = b\left(\frac{1}{T}\right) + a \qquad \text{eq. 3.1}$$

which is a simplified form of the Hertz-Knudsen equation [95], with a and b constants. Experimentally, the evaporation rate is rarely known and, actually, the condensation (or growth) rate at the substrates is the quantity that matters. These two rates are proportional if the mean free path is much higher than the source to substrate distance. This condition is ensured by the base pressure inside the growth chamber (in the range of 10^{-6}-10^{-5} mbar). By measuring the growth rates (with a QCM, as will be explained shortly) at different temperatures, the two constants can be determined. Figure 3.3 reports an example concerning the indium calibration.

Once the a and b constants are determined, the relationship (r,T) between rate and temperature is known. To control the composition of the films deposited, it is essential to keep as constant as possible this relationship. This is achieved, for example, with reproducibility of the crucible filling heights (or mass). This latter procedure has been carried out after each deposition run because the PVD system used in this work is not equipped with a load lock chamber which allows to keep the main growth chamber under vacuum while loading substrates.

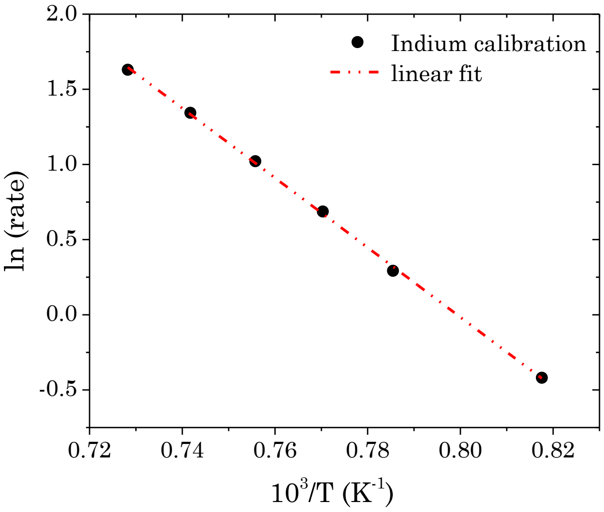

Figure 3.3: experimental values (black dots) of the deposition rates as a function of the corresponding temperatures. The dash-dot line is a linear fit and confirms the trends described in equation 3.1.

Thus, after each deposition run it was necessary to "break" the vacuum to load new substrates (and to fill the crucible or liners with the corresponding elements).

Another key aspect in keeping constant the relationship (r,T) is to a have a stable relation between temperature measurements and real evaporation surface temperature which, in other words, is the relation between the measurement of the thermocouple (TC) and the crucible temperature. This is achieved by keeping the position of the thermal evaporation sources as constant as possible to guarantee the same thermal contact between the TC tip and the base of the crucible. This is the reason why PBN liners have been used (instead of filling directly the crucibles with Cu or In pellets): in this way, during the procedure of the removal, refilling and weighing, the crucibles are not moved.

One main difficulty arises from a calibration performed by QCM: the quartz head is not in the same position (relative to the evaporation sources) as the substrates. This can be corrected by using a "tooling factor" and its calculation is done using mass measurements of the substrates before and after calibration deposition (this procedure works reasonably well for thick enough films). In this way the mass of the film deposited can be measured, thus its thickness can be extracted if density and area covered by the film are known. The areas have been experimentally measured using an optical microscope. The QCM reading can be calibrated to thickness (and this over time and rates) if the film condensed on the quartz is solid. Additional parameters needed for QCM reading are density of the evaporated material as well as the ratio of the acoustic impedance of the material and of the crystal. Then the tooling factor for the element X is determined as follows:

$$tooling\ factor_X = \frac{thickness_{QCM-X}}{thickness_{SUB-X}} = \frac{thickness_{QCM}}{mass_X/\rho_X/area_X} \qquad \text{eq. 3.2}$$

with $thickness_{QCM\text{-}X}$ the one given by the QCM reading and $thickness_{SUB\text{-}X}$ the one extracted from the measurement of the mass of the X element (measured using the semi-micro balance) deposited with a density ρ_X on an $area_X$.

Tooling factors in the range of 0.75-0.90 have been found for the several copper and indium calibrations performed during this work. Within the same calibration run, there is not just a unique tooling factor, as the thickness of the deposited films slightly changes form substrate to substrate. Typically, the substrate closer to the center of the sample holder has been used as reference. Factor below 1 are expected as the substrates are placed in front of the thermal evaporations sources and the radial distance is shorter than the one compared to the QCM, thus higher thickness of the deposited films are expected.

It is worth mentioning that the tooling factor can slightly change between a calibration process and a real absorber growth, leading to final thin films compositions not in line to those expected. This might be due, for example, to the different base pressure (in the range of 10^{-6} mbar during a calibration whereas 10^{-5}-10^{-4} mbar during a common growth process) or different substrate temperatures. The last point is critical if high temperatures for the substrates are used. In fact, it has been shown in the past by means of high temperature mass spectrometry [96, 97] that for selenium based ternary chalcopyrites the decomposition process starts at around 550°C – 600°C with outgassing of Se_2 species followed by the desorption of In_2Se. The temperature range may slightly differ from sample to sample with different stoichiometry, but also for Cu-rich films the first species to be desorbed are Se_2 and In_2Se [96]. This material loss leads, consequently, to a change of the surface stoichiometry and additionally to a reorganization of the film morphology if very high temperatures (> 650°C) are used. A decomposition study has been conducted on $CuInS_2$ as well [98], showing similar results, both in terms of temperature at which the process starts (about 600 °C) and of first species detected, i.e. S_2 and In_2S. This is why the temperature of the thermal evaporation sources need to be readjusted to get the same composition if a high temperature is used for the substrates. In this thesis work it has been found systematically that using the same source temperatures, the absorbers grown at 590 °C or even at 650 °C show higher Cu/In than those deposited at 550 °C.

The composition of all the samples analysed in this work has been determined by SEM-energy dispersive X-ray spectroscopy (EDX) with an acceleration voltage of 20 kV. The Cu/In ratios reported in the following are those obtained by EDX, if not stated otherwise. Due to the absence of a rotating system for the substrates, a gradient in composition of thin films deposited within the same run has been observed. This gradient is unavoidable and has been reduced as much as possible by a careful alignment of the thermal evaporation sources. Typically, a standard deviation of 0.05-0.08 has been found for the Cu/In ratio of absorbers grown within the same deposition run. This variation in composition may lead to a significant change of the structural and electronic properties of the films, particularly for those deposited with Cu/In ratio ≤ 1, as will be shown throughout this thesis. For this reason, in the framework of this thesis, all results will be presented together with the Cu/In ratio measured on the same sample onto which the corresponding measurement have been carried out, in order to avoid misinterpretations due to compositional gradient.

Concerning the sulphur source, few more words are needed. As mentioned before, a separate source with a Pyrex crucible has been used. Usually, for chalcogenide evaporation (Se or S), a more sophisticated source would be preferred, which would include a crucible, where sulphur is melted, sealed with a valve. The regulation of the valve by adjusting its opening would allow to precisely control the sulphur flow rate. The valve opens into an injection tube that includes an independently heated cracking zone: the temperature of this last component can be increased up to 800 °C – 1000°C to get cracked sulphur, thus to split the species of S_8 into smaller and more reactive species like S_2 [99].

Nevertheless, in this PVD system, the sulphur flow rate can be adjusted only by changing the crucible temperature, thus changing its vapour pressure. The temperature used for this source has been in the range of 110°C-130°C. The pressure of the growth chamber has been considered as a parameter to monitor the amount of sulphur evaporated: in fact, during a deposition process, the pressure is mainly due to the chalcogenide evaporation. Although less accurate and precise than the source equipped with a sealed crucible together with a valve, this procedure allows anyway to get reproducible absorber thin films, as confirmed by their characterization (e.g. similar quasi Fermi level splitting values for absorber grown in similar runs, i.e. substrate and evaporation sources temperatures and pressure).

3.3 Deposition of $CuInS_2$ absorber layers

In this section the steps followed during a typical deposition run will be described. They are schematically reported in the flowchart in figure 3.4. As mentioned before, the PVD system used for the absorbers growth is not equipped with a load lock, which would drastically reduce the time between two consecutive processes as it allows to maintain the process chamber under vacuum while loading new substrates. Thus, after each process, it is necessary to cool down (lower than 100°C) all the sources and substrates before venting and opening the chamber, "breaking" in this way the vacuum. As the pumping down step from atmospheric pressure to a base pressure of around 2.5×10^{-6} mbar takes around 3-4 hours, only one deposition process per day is possible.

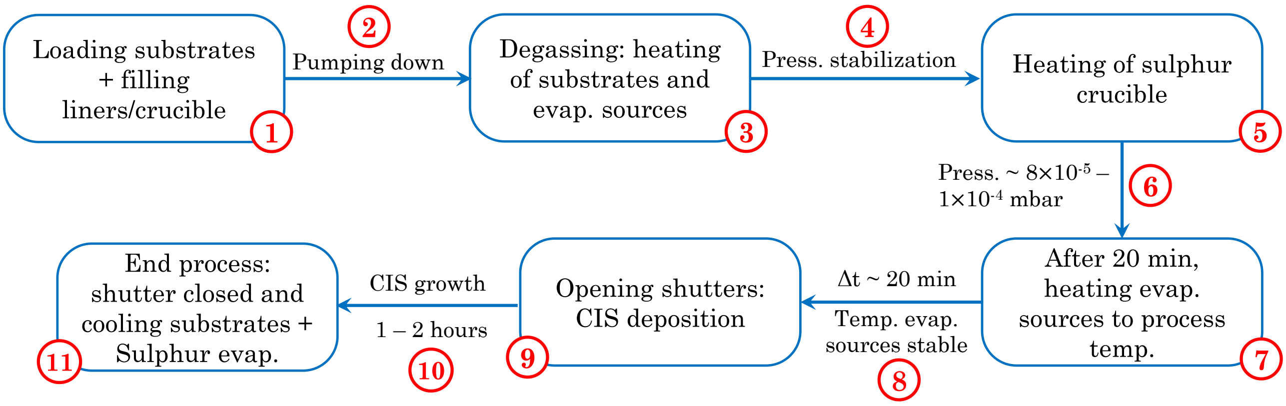

Figure 3.4: flowchart representing all steps involved in a standard CIS deposition. For a detailed description, refer to the main text.

Therefore a growth process starts with the loading of 4 substrates with a size of 2.5 cm x 2.5 cm. Once the substrates are put in place, the three thermocouples are pushed down in order to directly touch the back side of the glasses. Then, the PBN liners and the Pyrex crucible are filled with the corresponding elements, with copper, indium (eventually gallium) and sulphur, respectively (step 1). The liners containing metals are weighed in order to fill them with same mass used for the calibration process (thus to get the same evaporation rates from process to process). Then the chamber is pumped down to reach the base pressure. Usually, due to the several hours required for this last step, the sample loading and the filling step are performed the day before the actual growth in order to let the main chamber be pumped down over night (step 2).

Therefore, the actual absorber growth starts with the heating of both the substrates at the process temperature and the thermal sources at temperatures (e.g. 1000°C for Cu and 600°C for In) much lower than those used during the deposition (step 3). Substrates and sources are kept at these temperatures for about 1 h in order to "degas" the main chamber (mainly to pump away the sulphur condensed on the walls, sources and sample holder during the cooling down step of the process performed before). Once the pressure has reached a stable value (from the base pressure it can also reach for few minutes peaks of 1×10^{-4} mbar, before stabilizing at around 1.5 -3.5 × 10^{-5} mbar, step 4), the heating of the sulphur crucible begins (step 5). The temperature of the sulphur crucible is adjusted to get a stable pressure in the range of 8×10^{-5} – 1×10^{-4} mbar (step 6). After 20 min, the thermal sources are heated up to the process temperature (Cu in the range of 1300-1400°C, In in the range of 850-950°C, step 7). Once the sources have reached a stable temperature and power (this step requires typically 20 min more, step 8), the shutters placed on top of them are opened and the deposition of CIS layers starts (step 9).

Therefore, the timeframe between the stabilization of the pressure in the range of 8×10^{-5} – 1×10^{-4} mbar and the opening of the Cu and In shutters is about 40 min. This step is basically a pre-sulfurization process of the substrates (molybdenum-coated glass): in fact, although the Cu and In shutters are still closed, there is already a sulphur flux evaporated towards the substrates which are heated at the process temperature. This step allows the formation of a thin layer of MoS_2. As explained in section 2.4.3, this thin layer leads to an ohmic contact between the Mo layer and the back surface of the chalcopyrite absorber.

The formation of this layer is proven by Raman characterization (Figure 3.5) of Mo-coated SLG sulfurized for 40 min in the same work conditions of a standard CIS deposition (except the metals evaporation).

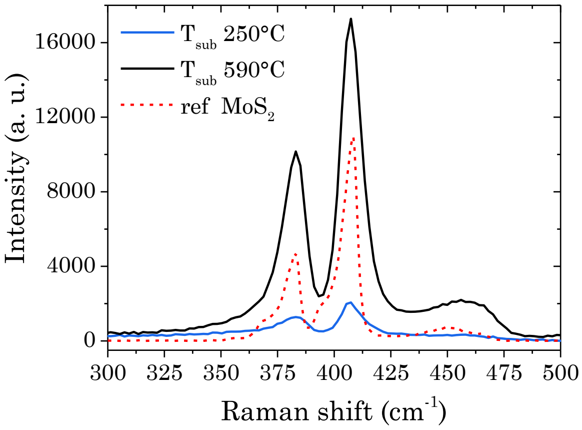

Figure 3.5: Raman spectra of MoS_2 layers obtained with a sulfurization of Mo-coated SLG performed for the same time with T_{sub} at 250°C and 590°C. In red dashed line, the reference spectrum (RRUFF ID: R060124).

As both experimental spectra have been measured with the same setup conditions, it is clear that the substrate temperature significantly influences the formation of the MoS_2, leading likely to a thicker layer if higher temperatures are used.

To avoid influences of the formation of the MoS_2 on the optoelectronic properties of the absorbers and on the performances of final devices, this pre-sulfurization step has been kept constant (i.e. for about 40 min at 590°C), regardless of the specific process used to grow the CIS absorbers, e.g. one- or multi-stage process as will be described in the following. The choice to use the highest temperature is justified also by the peeling of the CIS films from the substrates observed if 250°C is used.

When the CIS deposition is finished after about one to two hours (step 10), the shutters of the thermal evaporation sources are closed and cooled down, whereas the sulphur crucible is kept at the process temperature in order to supply the chalcogenide atmosphere during the cooling down process of the substrates to about 80°C-100°C (step 11). This last step is needed to avoid re-evaporation of sulphur from the deposited films because of its high vapour pressure. Moreover, this step is particularly relevant as it has been shown in the past (by in-situ energy dispersive X-ray diffraction) that for absorber grown in Cu-excess, during the cooling down process, the secondary phase Cu_2S transform into CuS (at around 300°C) [100]; thus more sulphur is needed to allow the formation of this phase and to avoid the creation of surface defects if sulphur from the CIS absorber is “used” to convert the secondary phase. In the optimization of the growth process carried out in this work, it has been also observed experimentally that the ratio between band gap luminescence (around 1.5 eV) and deep defect band increases if sulphur is supplied during the cooling down process (see Figure 3.6). A more detailed description of the PL spectra will be given in the chapter 4.

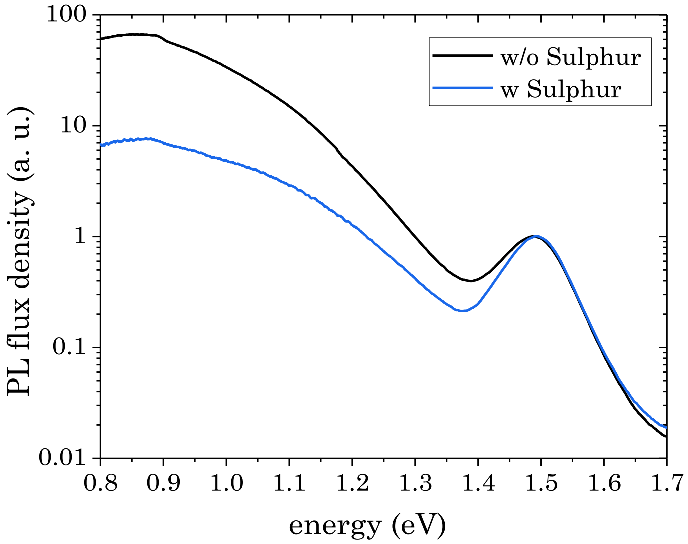

Figure 3.6: PL spectra normalized to the band gap luminescence of two samples grown in Cu-excess (Cu/In ratio about 1.7) with and without sulphur evaporation during the cooling process: in the first case, the sulphur source is turned off when the substrates reach a temperature of about 100 °C, while in process “w/o sulphur” it is turned off right after the ending of the CIS deposition, i.e. closing of the Cu and In shutters.

3.4 One- vs multi-stage evaporation process

The growth processes used to evaporate the $CuInS_2$ absorbers investigated in this work are primarily of two kinds: one-stage and two-stage process. Although with both it is possible to reach the same final bulk composition (thus the Cu/In ratio), the structural and optoelectronic properties are significantly altered by the specific growth conditions, as will be shown in the following. Both processes are schematically illustrated in Figure 3.7.

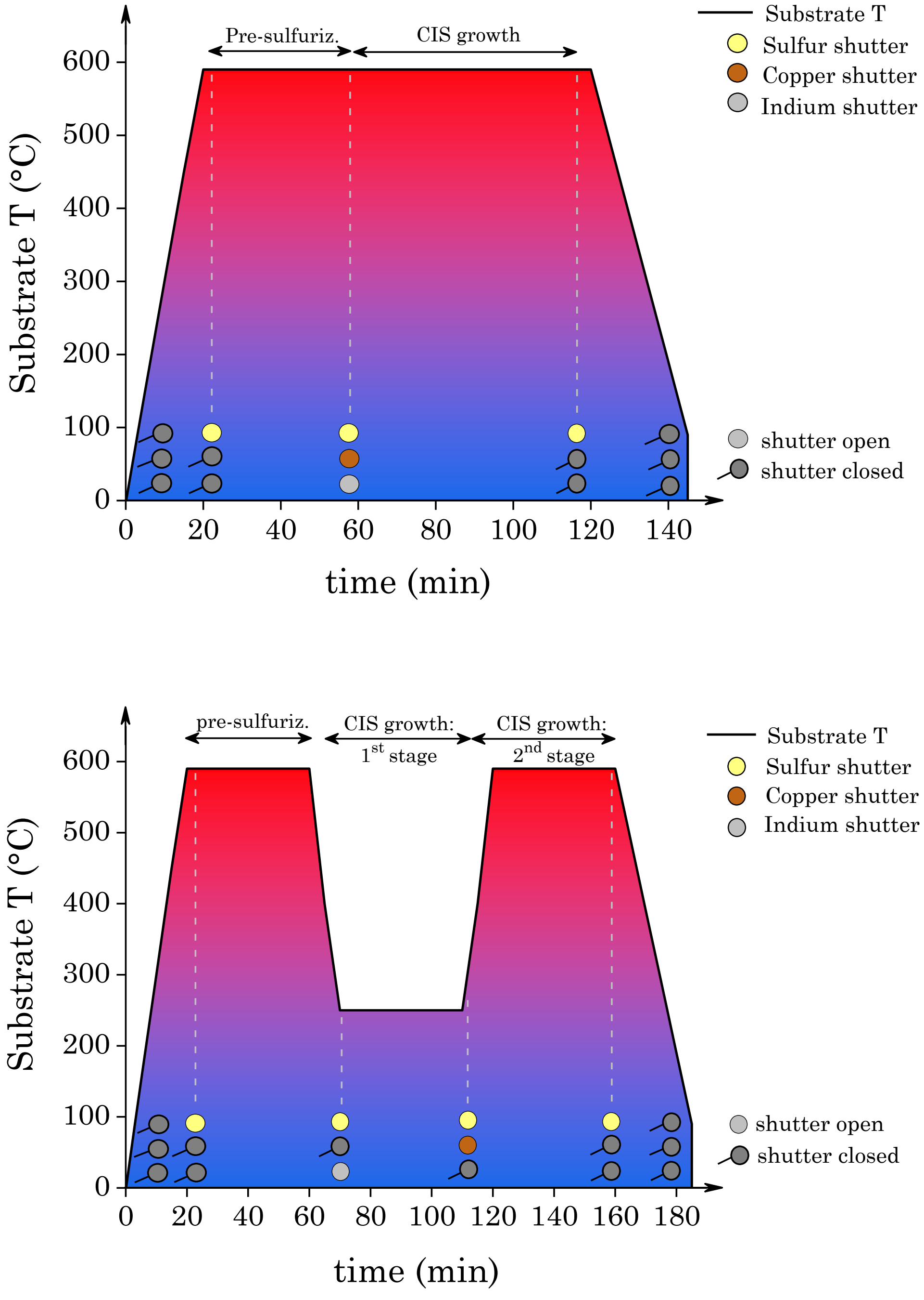

Figure 3.7 schematic illustration of the two processes used to deposit $CuInS_2$ absorber layers. (Top) One-stage process and (bottom) two-stage process. The temperature profile and the status of the elemental fluxes over time are depicted.

As mentioned before, regardless of the deposition process, the pre-sulfurization process is performed for about 40 min at 590°C to form a thin layer of MoS_2.

The thickness of the absorbers grown is about 2-2.5 µm, measured by analysing the cross section of the thin films acquired by SEM.

The single stage (1-stage) process has been used to deposit films grown both in Cu-deficiency and under Cu-excess. In this method, all elements are evaporated at the same time with constant fluxes together with a constant temperature for the substrates (590°C in Figure 3.7). As indium and copper are evaporated for the same time, the final Cu/In ratio of the absorbers depends mainly on the two metal fluxes. In particular, to get different compositions from process to process, the copper flux has been kept constant, whereas the indium one has been tuned by adjusting the temperature of the corresponding thermal evaporation source.

The two-stage (2-stage) process has been used only to evaporate thin films under Cu-excess, readapting a procedure already employed in the past [48, 101]. In the present work, after the pre-sulfurization process to form the MoS_2 layer, the temperature is lowered (250 °C in Figure 3.7) to start the deposition of indium and sulphur to form In_2S_3 precursor layer. Afterwards, the indium shutter is closed and the second stage starts by opening the copper shutter and by increasing the substrate temperature (590°C in Figure 3.7). During the second part of the process, the supplied copper forms together with the precursor (already evaporated) the $CuInS_2$ phase. In addition, the Cu/In ratio increases to a value well above 1, leading to a transition from a Cu-poor regime to a Cu-rich regime. This last condition helps the recrystallization of the chalcopyrite phase and increases the grain size [48]. Therefore, by adjusting the length of the second stage, thus the Cu evaporation, different Cu/In ratios for the composition of the as-grown films can be achieved: as the Cu/In reaches a value above 1, a longer second stage leads to a thicker layer of the Cu_xS secondary phase, as the $CuInS_2$ layer cannot be grown off-stoichiometric [33].

In addition, the transition from Cu-poor to Cu-rich regime can be easily tracked by an increment in the power needed to keep constant the temperature in the second stage. In fact, due to the metallic nature of the secondary phase, the emissivity of the Cu_xS is higher than $CuInS_2$, thus there is a stronger heat dissipation. This is clearly reported in Figure 3.8, where the data of the second stage of a 2-stage process are shown.

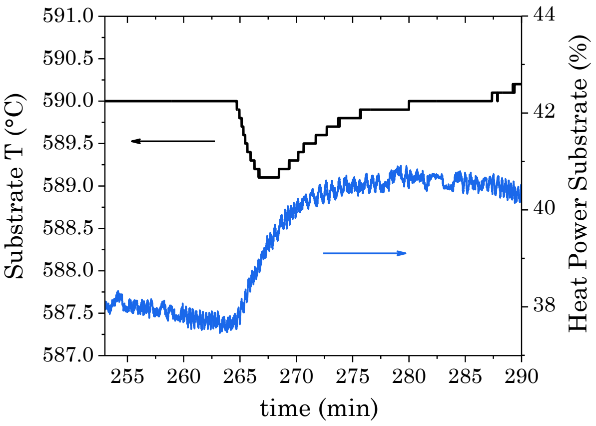

Figure 3.8: Substrate temperature profile (black) together with the power (blue) applied to the lamps of the substrate heater. Data taken during the second stage of a 2-stage process.

3.5 Cu-rich vs Cu-poor absorbers

As mentioned already in the previous sections, this thesis will be focused on Cu-poor and Cu-rich $CuInS_2$ thin films. The distinction is based on the composition of the as-grown films, which includes the chalcopyrite phase and eventually any secondary phase (like Cu_xS), if there are [33]. For Cu/In ratio above 1, an increment of this ratio translates into a thicker layer of the Cu_xS phase: in fact, according to the phase diagram [33], the CIS layer cannot have an off-stoichiometric composition. Once the secondary phase is removed (the procedure will be explained shortly), the CIS layer has a composition very close to the stoichiometric value, as confirmed by EDX analysis. Nevertheless, in this thesis, for simplicity, CIS layers grown in these conditions will be named as Cu-rich. Additionally, the Cu/In ratios reported throughout this thesis are values measured by EDX and they refer to the whole composition of the as-grown films (unless otherwise specified), thus the chalcopyrite phase together with any secondary phase, if present.

For Cu-rich films, the Cu_xS phase has to be etched away to get working devices. In this work, this secondary phase is removed by a potassium cyanide (KCN) etching performed with a 10% aqueous solution for five minutes: this etching acts extremely selective on the Cu_xS phase [34]. Recently, it has been proposed that in the close related $CuInSe_2$, the KCN etching causes a selenium related defect at the surface, contributing in this way to the surface recombination, thus lowering the Voc [102].

The effectiveness of the KCN etching can be checked by analysing the same sample (grown under Cu excess), before and after etching by means of X-Ray Diffraction analysis.

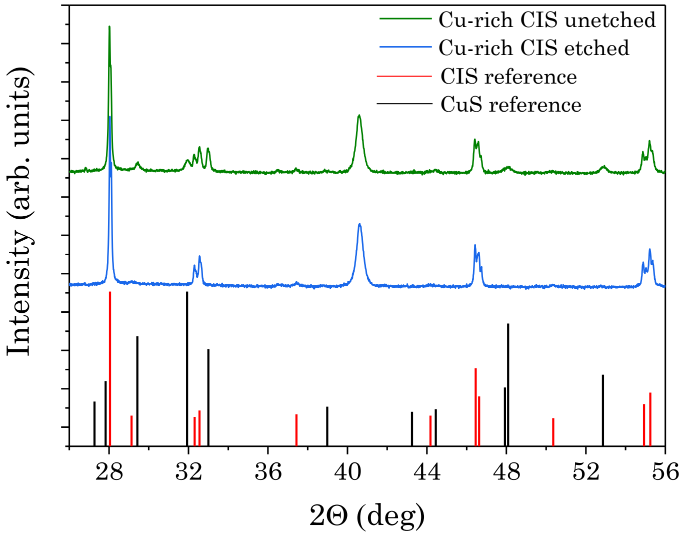

Figure 3.9: XRD patterns measured before and after KCN etching of a CIS absorber grown under Cu-excess with Cu/In ratio 1.8. Reported also the reference CIS (ICDD PDF 00-047-1372) and CuS (ICDD PDF 00- 006-0464).

Figure 3.9 shows the XRD patterns of a Cu-rich $CuInS_2$ sample before and after etching. It clearly shows that all peaks belonging to the phase CuS disappear after KCN etching, thus the secondary phase is effectively removed. Moreover, as reported in literature [100], the pattern measured before the selective etching illustrates that the secondary phase mainly consists of the covellite CuS phase, that is the most stable secondary phase at room temperature [33]. A more detailed discussion about the texturing and orientation of the chalcopyrite phase will be given in the next section.

Absorbers grown under Cu deficiency or Cu excess exhibit significantly different structural and optoelectronic properties, as will be shown in the following. Moreover, as will be discussed, the substrate temperatures plays a substantial role as well in affecting the quality of the absorbers depending on the compositions of the films.

Thus, in the next sections of this chapter, the effect of the composition and of the substrate temperature (T_{sub}) on the structural properties of the CIS absorbers will be analysed by means of X-ray diffraction, Scanning electrical Microscopy (SEM) and Scanning Transmission Electron Microscopy (STEM).

Afterwards, chapter 4 will be focused on effects that those changes (composition and T_{sub}) have on the optical and electrical properties: the first one will be analysed by means of photoluminescence, the second one by investigation of the devices based on the corresponding absorbers.

In both cases (structural and optoelectronic properties) the consequence of using the 1-stage or the 2-stage process to grow Cu-rich CIS absorbers will be discussed.

3.6 Effect of stoichiometry on (micro) structural properties

Although the last record efficiency device (η = 15.5 %) has been made with a Cu-poor absorber [26], most of the high efficiencies achieved with Cu(In,Ga)S_2 solar cells over the last decades used thin films deposited under Cu excess. This is in contrast with the trend in the closely related Cu(In,Ga)Se_2 where all the record efficiencies have been achieved with Cu-poor absorbers.

Thus, in the first place, it is essential to investigate the effect of the composition on the structural properties of the films, in order to find out whether it affects the crystal quality of the absorbers.

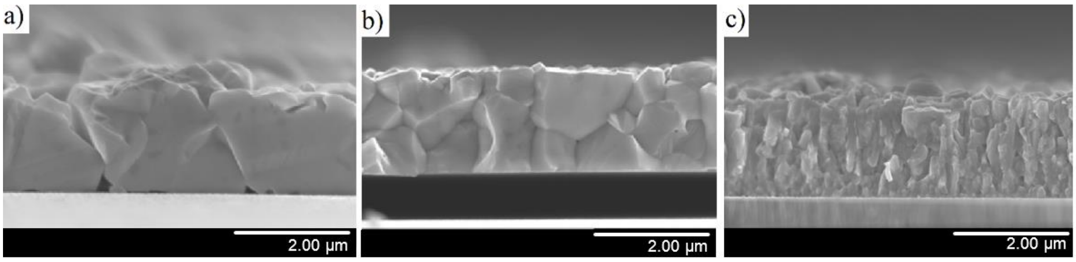

Figure 3.10: SEM cross sections showing the morphology of the $CuInS_2$ layers grown at 550°C by (a) Cu-rich one stage, (b) Cu-rich two-stage, and (c) Cu-poor one-stage process.

Figure 3.10 shows the SEM cross sections of $CuInS_2$ absorber layers deposited under Cu-excess following the one-stage and two-stage process (with T_{sub} of 550°C and 250°C+550°C, respectively) and under Cu deficiency (one-stage process with T_{sub} of 550°C). They have been measured after etching of the Cu_xS secondary phase, which, as described previously, is present in as-grown Cu-rich films. It is clear for both the Cu-rich films that the grain size is in the micrometer range, whereas the Cu-poor sample has much smaller grain size. Therefore, the larger grains that constitute the thin films are a first sign of the higher crystal quality of the samples deposited under Cu-excess. This feature has been reported as well in the counterpart chalcopyrite $CuInSe_2$ [103]. Beside the grain size, the morphology of the Cu-rich films presents differences between sample grown in one-stage and the one grown following the two-stage process. The first one presents deep trenches between the grains, voids and poor adhesion on the back side of the film together with a rough surface. The morphology of the two-stage Cu-rich film, in contrast, is characterized by a denser layer with a smoother surface. Although the morphology can slightly be changed by adjusting the deposition rates during the growth or by varying the overall Cu/In ratio (thus with lower or higher segregation of Cu_xS), these characteristic features between the two types of processes have been found systematically during the whole thesis work. Thus, it can be excluded as well that the poor adhesion of the absorber layer to the molybdenum is a consequence of the sample preparation for SEM, which includes breakage of the substrate. They can be attributed to the different kind of segregation of the secondary phase Cu_xS. In fact, in a two-stage process, this phase segregates only during the last part of the growth of the second stage, whereas in a one-stage growth the Cu_xS is formed throughout the duration of the whole deposition, likely segregating not only at the film surface, but also along the grain boundaries and at the back interface (between substrate and absorber). Therefore, once the secondary phase is etched away from the absorbers by the KCN solution, it leaves deeps trenches and voids behind. This is clearly shown in Figure 3.11 where the SEM cross sections of the same Cu-rich sample are reported, before and after etching, respectively.

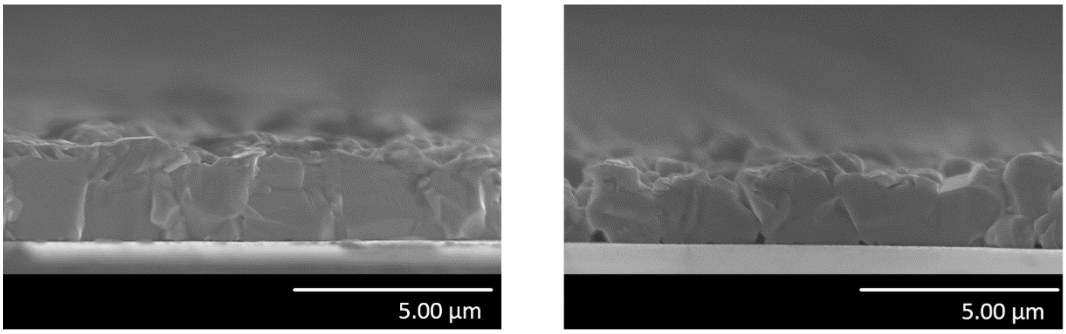

Figure 3.11: SEM cross section showing the morphology of a 1-stage Cu-rich $CuInS_2$ absorber (Cu/In 1.8) before (left) and after (right) KCN etching to remove the Cu_xS secondary phase.

The same Cu-poor and Cu-rich thin films deposited following the one-stage process (with SEM cross section displayed in Fig. 3.10a and 3.10c) have been analysed in terms of microstructure by TEM.

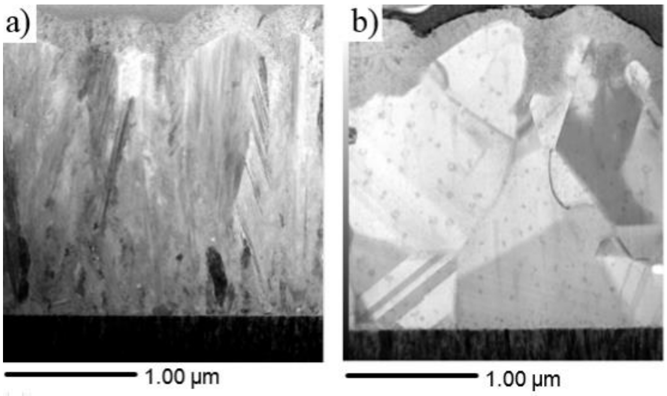

Figure 3.12: STEM cross section images showing the microstructure of the $CuInS_2$ absorber layers grown in one-stage configuration with T_{sub} 550°C (a) under Cu-deficiency and (b) under Cu-excess.

It has been found that the overall stoichiometry of the absorbers influences significantly the microstructure, as well, as it is reported in Figure 3.12, which displays cross section scanning TEM images of $Mo/CuInS_2/CdS$ stacked layers. The absorber grown with a copper deficient composition, indeed, shows a dense network of defects, such as dislocations and stacking faults as well small-sized grains; by contrast, the microstructure of the Cu-rich sample is characterized by a drastic reduction in defect density. A common feature for both thin films is the presence of smaller grains at the interface between the molybdenum back contact and the absorber.

The crystal structure and the phases involved in the absorbers growth have been analysed by XRD.

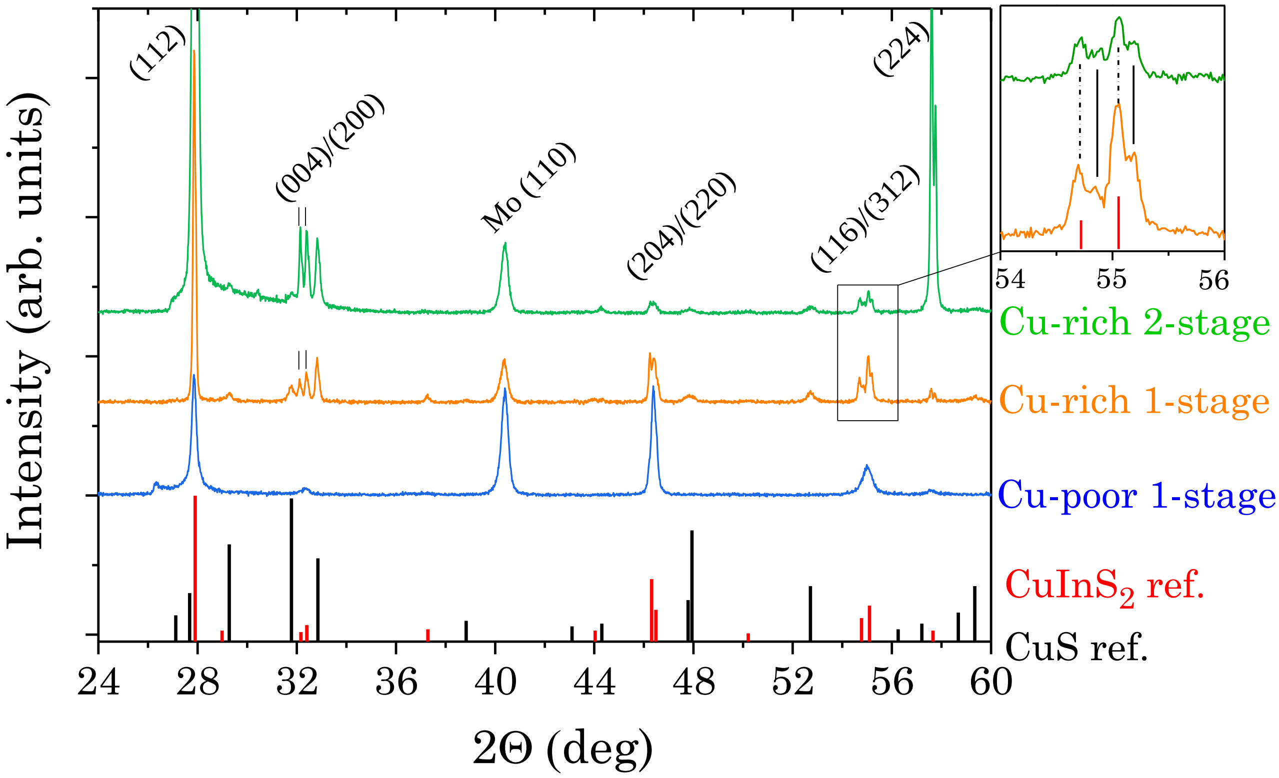

Figure 3.13: XRD diffractograms of $CuInS_2$ absorber layers deposited at 550°C on Mo-coated SLG, together with the labels of the main peaks of the chalcopyrite phase and Molybdenum. Reported also the references CIS (ICDD PDF 00-047-1372) and CuS (ICDD PDF 00- 006-0464). The inset shows a magnification of the (116)/(312) lines for the Cu-rich films: the dashed lines indicate the tetragonal splitting, whereas the presence of additional peaks highlighted by the continuous lines are the results of the radiation line $Cu_{K\alpha1/K\alpha2}$. The tetragonal splitting is also marked for the (004)/(200) lines to discriminate the CIS lines from the CuS ones.

Figure 3.13 illustrates the X-ray diffraction patterns of the absorbers shown in Fig. 3.10, but before removing the CuS secondary phase with KCN etching for the Cu-rich samples. The labels of some of the peaks related the chalcopyrite phase are reported as well, together with the peak associated to the molybdenum.

The diffractograms reveal that the texture of $CuInS_2$ is sensitive to growth conditions: according to powder diffraction data (ICDD PDF 00-047-1372) and by analysing the integrated intensity ratio $I_{(112)}/(I_{(204)}+I_{(220)})$, it can be concluded that the Cu-rich samples grown in 1-stage process show a slightly preferred (112) orientation. The (112) becomes clearly the preferred and dominant orientation for the Cu-rich film deposited by the 2-stage process. The films deposited under Cu-deficiency do not show a preference for the (112) orientation.

The higher crystal quality for the absorbers grown under Cu-excess is confirmed by two features of the XRD patterns. The first one is the splitting that can be observed at high angles (e.g. the (116)/(312) lines, see the inset in figure 3.13) due to the $Cu_{K\alpha1}$ and $Cu_{K\alpha2}$ radiation lines, which for the same crystal plane cause the appearance of two peak close to each other. This observation is possible experimentally for small linewidth of the peaks, which consequently proves the good crystal quality of the corresponding films. The second feature is, instead, the splitting observed for the (004)/(200) and (116)/(312) diffraction lines (slightly visible also the one related to the (204)/(220) lines): this splitting is due to the tetragonal distortion. In fact, for a tetragonal structure, the unit cell is described by the lattice constant *a* along the x and y axis, whereas by the lattice constant *c* along the z direction. Nevertheless, due to the slightly different bond length between In-S and Cu-S, respectively, the ratio c/a is different from 2, which is the value expected by just doubling the unit cell of the cubic face. In this last case, the planes (004) and (200) (same for (204)-(220) or (116)-(312)) would be equivalent, therefore they would give rise to the same XRD peak. The mismatch between *c* and *2a* leads to the so called tetragonal distortion and in the XRD pattern to the tetragonal splitting. This splitting can be observed experimentally only if Cu and In are well ordered in their sublattice, thus it is a characteristic sign of high crystal quality thin films.

Concerning the Cu-poor sample, in figure 3.13 an additional peak can be observed at lower angle compared to the main (112) peak (2θ around 26.3°). This feature has been already observed in other reports and it is characteristic of Cu-poor prepared material [104-106]; nevertheless, the assignment is not straightforward and still remains unclear. Although in some study it is correlated to the (211) diffraction line of ß-In_2S_3 phase [106], this attribution cannot be confirmed by the presence of the corresponding additional peaks of this phase. Due to the massive presence of structural defects observed by STEM (Fig. 3.12a) for thin film grown under Cu-deficiency, this peak might be a signature of stacking faults, and not to the presence of additional phases in the absorber. In fact, such planar defects of the (112) planes cause the disturbance of the chalcopyrite symmetry. Similar observations of additional peak together with broadening of the main (112) peak have been reported for Cu poor Cu(In,Ga)Se_2 thin film absorbers deposited without the intermediate Cu-rich stage: these structural defects can be annihilated by a subsequent annealing or by using the conventional three-stage process (thus with a transition from Cu-poor to Cu-rich during the second stage) [107-109]. Analogous effects of stacking faults on the X-Ray diffraction profiles have been observed for other materials, like SiC [110].

It is worth mentioning that the Cu-poor samples investigated in this work have been grown in a compositional range of $0.9 < Cu/In < 1.0$. Beside the optoelectronic properties, which become progressively worse as soon as the Cu/In ratio is lowered below 1 (as will be explained in the chapter 4), the reason of this choice lies in the phase stability of the Cu_2S-In_2S_3 system. It has been reported, in fact, through a systematic structural investigation of the ternary system Cu_2S-In_2S_3-Ga_2S_3 that the sulphide CIGS system has lower adaptability of the chalcopyrite structure than the selenide CIGSe system in the Cu deficiency region [28]. For gallium free compounds, the film films deposited under Cu deficiency with $Cu/In < 0.9$ clearly exhibit in the XRD patterns the chalcopyrite $CuInS_2$ phase related peaks together with those belonging to the cubic thiospinel structure $CuIn_5S_8$. The proposed explanation is the instability, in sulphide compounds, of the tetrahedral-based structure for In-content compounds with copper vacancies (i.e. Cu-poor films) that thus leads In being octahedrally coordinated [28, 111].

This has been further confirmed in this work by XRD patterns measured on samples grown in strong Cu-deficiency, i.e. Cu/In 0.81, as shown in figure 3.14. In fact, beside the peaks related to the chalcopyrite phase and the one (at around 40.5°) due to the molybdenum substrate, those belonging to the thiospinel $CuIn_5S_8$ are clearly visible. For the sake of completeness, figure 3.14 shows the reference peaks of the $CuIn_3S_5$ phase as well. Although the last ones are at positions close to the lines of thiospinel phase reference, with a careful observation (e.g. right figure 3.14 shows a narrower 2θ region of the same XRD pattern shown in the left, for a better view), it can be concluded that the additional phase present in the Cu-poor absorbers is actually the $CuIn_5S_8$ one.

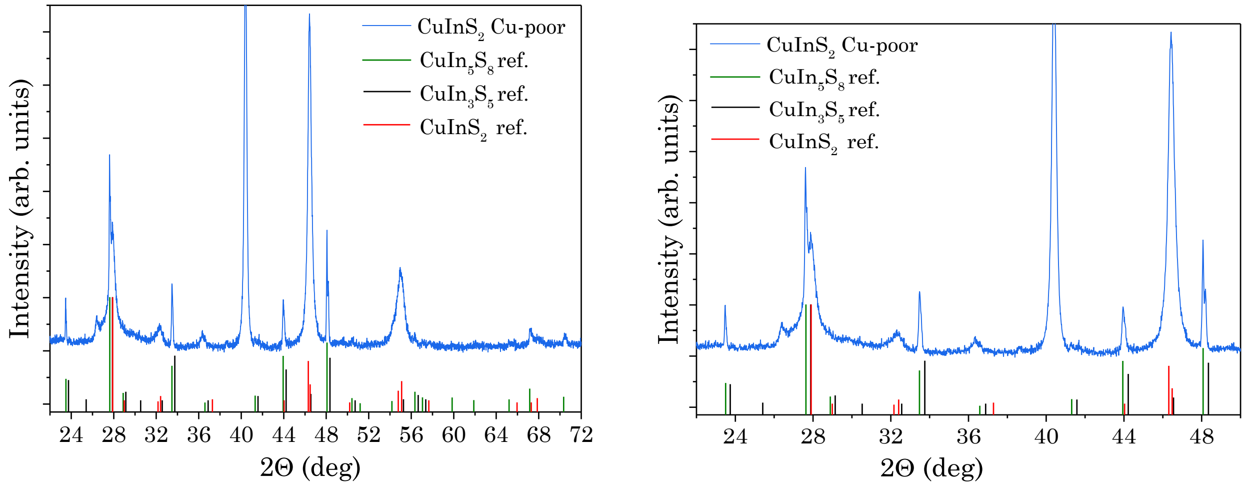

Figure 3.14: (left) XRD pattern of a sample grown in Cu-deficiency (Cu/In = 0.81) together with the references patterns of $CuInS_2$ (ICDD PDF 00-047-1372), $CuIn_3S_5$ (ICDD PDF 00-063-0729) and $CuIn_5S_8$ (ICDD PDF 04-006-4964). (right) same XRD pattern displayed with a narrower 2θ region for a better view.

3.7 Effect of temperature on (micro) structural properties

The set of samples investigated in the previous section have pointed out how the stoichiometry, as well as the process itself (one- or multi-stage), can influence or drastically change the morphology and the structural properties of the corresponding absorbers, both from a macro and micro point of view. This section will rather be focused on the effect of the substrates temperature during the process growth, in order to investigate whether it has any effect on the absorbers. For this purpose, and for a better comparison, the set of samples investigated have been deposited following the same kind of processes and with a similar stoichiometry of those presented in the previous section. Therefore the absorbers discussed in the following are mainly three: a CIS deposited under Cu deficiency with a T_{sub} of 600°C and a Cu-rich CIS deposited at T_{sub} of 590°C, both grown in a 1-stage process; additionally, a Cu-rich deposited in a 2-stage process with a T_{sub} of 250°C and 590°C, in the first and in the second stage, respectively.

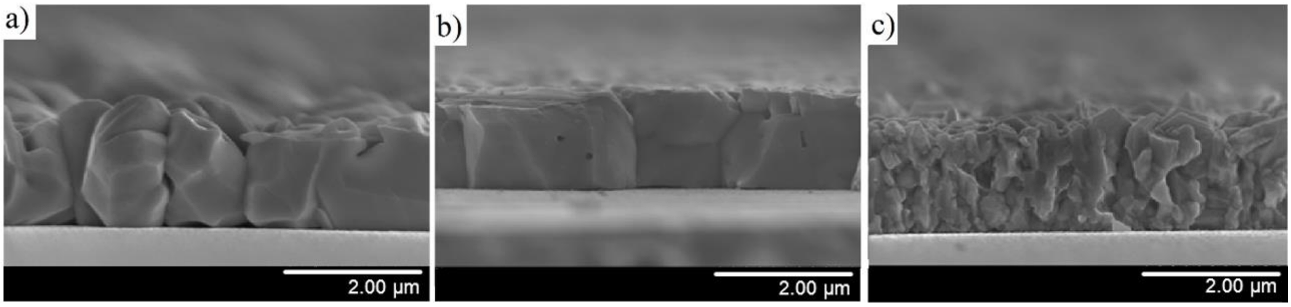

Figure 3.15: SEM cross sections showing the morphology of the $CuInS_2$ layers grown by (a) Cu-rich one stage with T_{sub} 590°C, (b) Cu-rich two-stage with T_{sub} at 250°C + 590°C and (c) Cu-poor one-stage process with T_{sub} 600 °C.

Figure 3.15 shows the SEM cross sections of $CuInS_2$ absorber layers deposited at higher temperatures, as described above. By comparison with those presented in figure 3.10, it can be concluded that the increment of the growth temperature by +40/50 °C does not induce drastic changes in the morphology of the absorbers and grain size. In fact, as already discussed, Cu-rich samples show large grains, in contrast to the absorber grown under Cu deficiency. Moreover, deep trenches between grains and voids at the back surfaces are characteristic features of the Cu-rich CIS deposited in 1-stage process, whereas the one grown in 2-stage process has a more dense and compact morphology; this is in line with the observations discussed for the corresponding absorbers deposited at lower temperature (see figure 3.10). The only difference which can be noticed in figure 3.15b is the presence of grains that extend from the back surface Mo/absorber towards the front surface, while in figure 3.10b, for the Cu-rich 2-stage sample deposited at lower temperature, shows the cross section of the absorber composed by at least two big grains, with a size always in the micrometer range. Nevertheless, grains extending along the whole absorber thickness is not a characteristic feature of this specific process (2-stage 250°C + 590°C) as it has not been observed systematically for other absorbers deposited in a similar run.

Similarly, the microstructure of these absorbers (figure 3.16) deposited at higher temperature is rather independent from the temperature growth, although, as observed already in figure 3.12, it is considerably sensitive to the composition, with an improvement if Cu-rich regime is used.

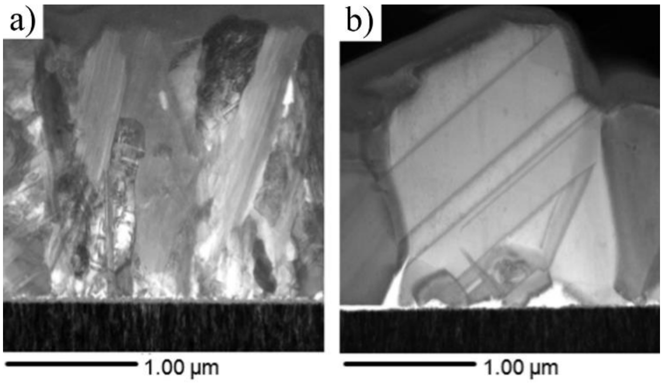

Figure 3.16: STEM cross section images showing the microstructure of the $CuInS_2$ absorber layers grown in one-stage configuration (a) under Cu-deficiency with T_{sub} 600°C and (b) under Cu-excess with T_{sub} 590°C.

Within the range investigated (550°C to 590°C), also the texture and the preferred orientation of the samples investigated are not affected by the growth temperature, as shown for example in figure 3.17, where the XRD patterns of the Cu-rich absorber deposited in a 1-stage process are reported. In fact, for both samples, the integrated intensity ratio $I_{(112)}/(I_{(204)}+I_{(220)})$ is not affected by the growth temperature.

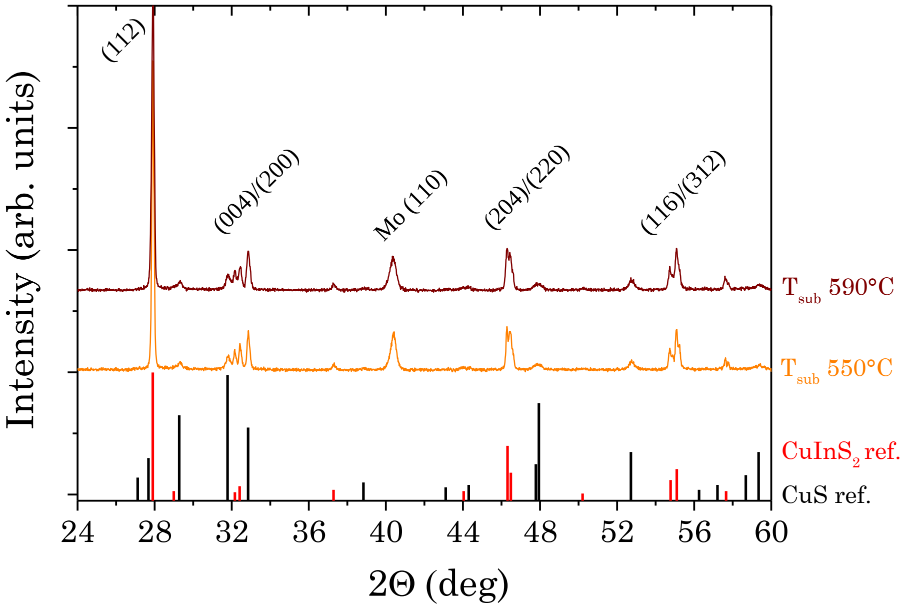

Figure 3.17: XRD diffractograms of 1-stage Cu-rich $CuInS_2$ absorber layers deposited at 550°C and 590 °C on Mo-coated SLG, together with the labels of the main peaks of the chalcopyrite phase and Molybdenum. Reported also the references CIS (ICDD PDF 00-047-1372) and CuS (ICDD PDF 00- 006-0464).

Additionally, the samples grown in 1-stage process at high temperature (Cu poor with T_{sub} 600°C and Cu-rich with T_{sub} 590°C) have been analysed by atom probe tomography (APT), which allows to detect the chemical composition at atomic scale. The APT measurements have been carried out and evaluated by Torsten Schwarz of MPIE and a more detailed analysis will be published in [112] . Particular attention has been paid to fluctuation in chemical composition at planar defects, such as grain boundaries, twin boundaries and stacking faults. Figure 3.18 shows the chemical composition at a stacking fault measured in a Cu-rich and Cu-poor sample, respectively.

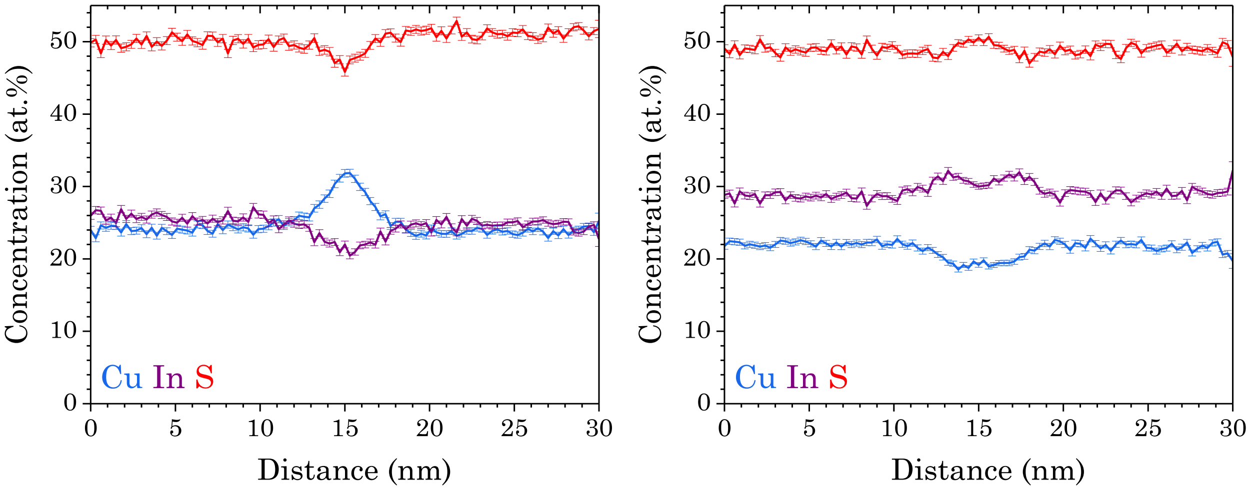

Figure 3.18: APT data of concentration profiles across stacking faults in (left) Cu-rich absorber and (right) Cu-poor absorber.

The data clearly demonstrate an opposite trend in terms of chemical composition across the planar defect between the two kinds of samples: the CIS absorber grown under Cu-excess indicates a copper enrichment together with an indium and sulphur depletion, whereas the CIS grown under Cu deficiency shows a copper depletion with indium accumulation and slight sulphur enrichment. The enrichment and depletion profiles observed in the Cu-poor sample resemble a W-like shape rather than a kind of Gaussian profile as detected in the Cu-rich sample. The origin of this W-shape is not clear: a possible explanation might be a very high In enrichment during the growth which becomes energetically unfavourable at some point of the deposition process, such as during the cooling step. Therefore Cu atoms diffuse from grain interiors towards the planar defect and kick out In atoms, giving rise to the W-like shape profiles [112].

The same trend in terms of chemical composition fluctuations has been found for other kinds of planar defects, as reported in Table 3.1, where a statistics of the chemical fluctuation is given.

Except for twin boundaries, all the other planar defects follow the same trend shown in figure 3.18; only for sulphur, the chemical fluctuation is not always clear.

Thus across grain boundaries and stacking faults, a Cu enrichment and In depletion are characteristic features of Cu-rich absorbers, while Cu-poor absorbers are characterized by the opposite trend. Whether a certain chemical compositional fluctuation is beneficial or detrimental for the optoelectronic properties (such as charge carriers transport across grain boundaries) in these sulphide based chalcopyrite layers, cannot be concluded at the moment.

Table 3.1: chemical fluctuation across planar defects of (left) Cu-rich and (right) Cu-poor $CuInS_2$ absorbers. For each element, “+” indicates an enrichment, “-” a depletion, “o” no fluctuation whereas the round brackets “( )” no clear/slight fluctuation. For each planar defect, the numbers of defects investigated is also indicated in the first column “Nr”.

Cu-rich sample				
Nr.	Planar defect	Cu	In	S
1x	GB	+	-	-
2x	RHAGB	+	-	o
3x	∑9 TB	+	-	-
4x	Stacking fault	+	-	-
8x	∑3 TB	o	o	o

Cu-poor sample				
Nr.	Planar defect	Cu	In	S
4x	GB	-	+	+/-
1x	RHAGB	-	-	o
3x	Stacking fault	-	+	(-)
1x	Stacking fault	-	+	+
2x	∑3 TB	o	o	o

Nevertheless, a comparison with the closely related $Cu(In,Ga)Se_2$ can be done; in fact, for high efficiency selenide based chalcopyrite, it has been found as well that along some line and planar defects there is a change in composition, that in turn leads to a charge density accumulation (positive or negative), thus to a band bending (hole or electron barrier, respectively) [113]. Recently it has been proven that the properties of grain boundaries can be improved through alkali-fluoride post-deposition treatments [114]. Moreover, analysis carried out combining EBIC and APT have shown that detrimental GBs are mainly enriched in Cu and O, whereas beneficial GBs are characterized by Cu depletion [115]. Similar studies need to be done on pure sulphide $Cu(In,Ga)S_2$ absorbers to elucidate, if there, a correlation between local composition of planar defect and their electrical activity, thus if they limit the performance of the corresponding devices.

3.8 Summary absorber growth

The growth method and the processes used to fabricate $CuInS_2$ absorbers have been presented. In particular, CIS layers grown under Cu-excess and Cu-deficiency have been studied: for both a one-stage process has been used; additionally, Cu-rich samples have been deposited also by a two-stage process.

Cu-rich absorbers show better macro- and micro-structural properties than those deposited under Cu-deficiency: this is supported by the observation of large grains and by a lower density of planar defects. The higher crystal quality is further confirmed by XRD analysis, which displays a (112) preferred orientation together with tetragonal splitting.

The multi stage process, used for Cu-rich layers, greatly enhances the crystallographic orientation and leads to a morphology characterized still by large grains, but furthermore by a compact and dense layer, which may affect the performances of the devices based on these absorbers.

The stoichiometry affects as well the composition along the planar defects, which are doubtless characterized by a Cu enrichment and In depletion for Cu-rich $CuInS_2$ absorbers, while the opposite trend is found in Cu-poor ones.

Despite the substantial influence of the composition on the aforementioned properties, these are rather independent of the growth temperatures within the range investigated (essentially from 550 °C to 590-600 °C). This is somehow an unexpected observation, which can be explained assuming the variation of 40-50 °C at these temperatures is not enough to lead drastic alterations in the micro- and macro-structure of the films that could be observed experimentally. On the other hand, in chapter 4 the same samples will be analysed in terms of their optoelectronic quality, which does change when the deposition temperature is varied by the same amount.

Chapter 4

Quasi Fermi level splitting of $CuInS_2$ absorber layers

In chapter 3, the effects of the composition and of the process temperatures on the (micro) structural properties of the CIS layers have been discussed. This chapter will be focused on the optoelectronic properties of the absorbers as a function of the same parameters (i.e. as a function of the Cu/In ratio and T_{sub}) together with the electrical performances of the corresponding devices.

The main figure of merit will be the quasi Fermi level splitting (QFLS) which, as described in section 2.5, is an indicator of the recombination activity of a semiconductor and it represents the highest open circuit voltage an absorber is capable of.

The QFLS has been measured by absolute calibrated photoluminescence performed at room temperature and by analysing the PL yield in terms of Planck's generalized law, as explained in section 2.5.4.

As it has been shown in the past that $CuInSe_2$ and $Cu(In,Ga)Se_2$ absorbers degrade in presence of air [116, 117] and light [118], similar studies have been carried out on $CuInS_2$ absorber layers and are discussed in the following. Then, a comparison of the QFLS on absorbers prepared by using a wide range of parameters will be given. In particular, the effect of the deposition temperature as well as the composition (Cu-poor and Cu-rich CIS layers) on the recombination properties of the absorbers will be discussed in detail. The samples investigated in the first part of this chapter are the same ones analysed in terms of crystal quality (studied and discussed in the previous chapter 3). Moreover, samples deposited at very high temperature (650°C) on HT glasses will be discussed.

Additionally, the effect of the growth conditions on the photovoltaic devices, mainly in terms of open circuit voltage will be shown.

As for the crystal quality in the previous chapter, the effect of the process used to grow CIS under Cu-excess, i.e. one- or two-stage process will be discussed as well.

Finally, this chapter ends with an overview on the QFLS of the $CuInS_2$ samples grown in the framework of this thesis, with a comparison with QFLS of the closely related $Cu(In,Ga)Se_2$ films, discussing possible causes of the lower efficiencies of the pure-sulphides-based solar cells .

4.1 Stability of QFLS

It has been found for CuInSe$_2$ and Cu(In,Ga)Se$_2$ bare absorbers (thus without passivation layer such as CdS) that, after KCN etching (or after taking them out from the growth chamber), the QFLS degrades with time if they are exposed to air [116, 117]. This has been related mainly to oxidation of indium, with Cu-poor selenide layers showing generally a faster decay than the Cu-rich ones. The surfaces can be improved and refreshed with an additional short KCN etching.

As CuInS$_2$ and Cu(In,Ga)S$_2$ are systems closely related to the selenide-based counterpart, they might face a similar degradation when absorbers are exposed to oxygen-containing atmosphere. Thus, as a first step, the degradation of thin films CuInS$_2$ has been investigated, analysing absorbers deposited both in Cu deficiency and Cu excess as well as those grown both in one- and two-stage process. The measurements have been carried out as follows: firstly, the PL setup has been calibrated in order to measure absolute number of photons/cm^2/s/eV, thus to extract the QFLS. In order to minimize as much as possible the time frame between KCN etching and first measurement, all the acquisition parameters need to be adjusted before, like excitation intensity, exposure time, position of the sample, number of scans etc. As the samples investigated show different photon flux density (depending on their optoelectronic quality), the incident excitation photon flux has been regulated to get a reasonable signal to noise ratio, while avoiding the use of high power laser which could heat up the thin film. Therefore, after KCN etching (5% solution for 30s or 10% for 5 min for Cu-poor and Cu-rich absorbers, respectively), the samples are directly transferred into photoluminescence setup and the measurements begin. The time between KCN etching and the first acquisition has been roughly 120 ±20 s, taking into consideration the transfer process from the chemistry to the optical laboratory.

The longest degradation studies performed in this work have been carried out on one- and two-stage Cu-rich samples for about 24 h (measuring the same point during the experiment). Figure 4.1 reports their QFLS splitting plotted over time at an equivalent illumination of 6 and 11 suns, respectively. It is evident there is not any strong degradation which affects the QFLS for such long time, that remains stable beside fluctuations or initial decay within less than 5 meV. In absence of surface sensitive composition measurements (like XPS), the formation of oxides compounds at the surface cannot be ruled out. Figure 4.1 shows also the spectra of the two-stage Cu-rich sample investigated, acquired at 5 min and 21 hours after KCN etching, indicating once more no changes of the PL flux over such long time. Similar degradation studies, but over shorter time scales, have been conducted on a Cu-poor CIS deposited on Mo-coated SLG and on Cu-rich and Cu-poor samples deposited at high temperature (650 °C) on Mo-coated HT glass. The QFLS trends plotted over time are depicted in figure 4.2.

Although the two Cu-poor samples show slight decays of less than 10 meV which tend to flatten after 20-30 minutes, for all samples the QFLS do not vary more than 5-10 meV over the time scales investigated. The QFLS change is minor in Cu-rich films, considering also the trends plotted in figure 4.1. These results differ significantly from the observations found for the selenium-based compounds [116, 117], where drops of QFLS up to about 100 meV have been measured on time scales of about 50-100 min. The degradation of the absorber layer surfaces exposed to oxygen-containing atmosphere has been studied in the past for CuInSe$_2$ (both single crystal and thin films) [119, 120]: it has been found that the oxygen exposition leads to a formation of an oxide mainly constituted by an In_2O_3 outer layer with an additional Cu_2Se interface layer (between the oxide and the chalcopyrite).

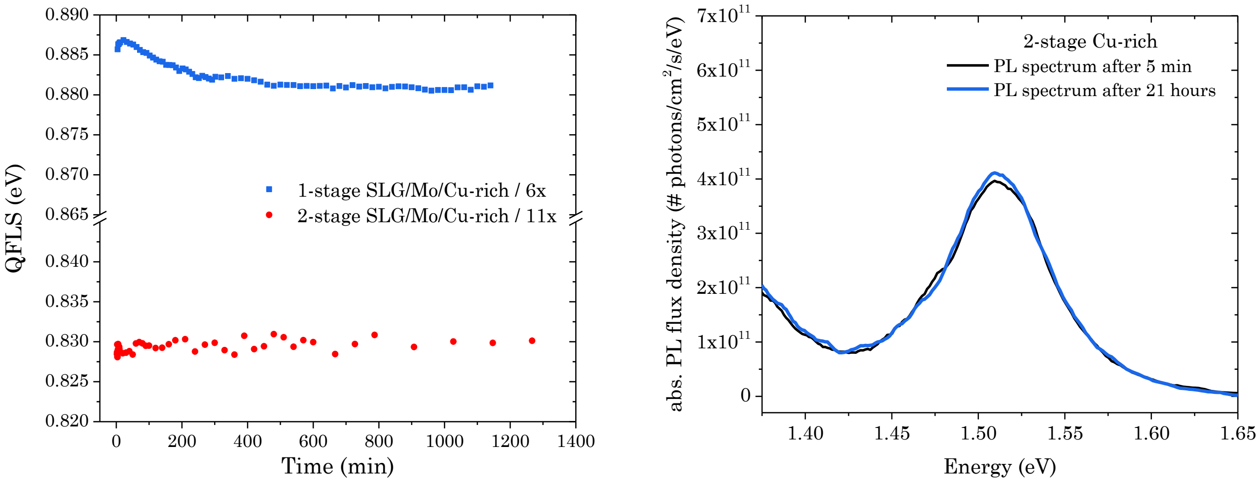

Figure 4.1: (left) QFLS plotted over time for a one- and two-stage Cu-rich CIS samples grown on a Mo-coated SLG measured at an equivalent illumination of 6 and 11 suns, respectively. Note the break on QFLS-axis. The first measurement has been acquired 2 min after KCN etching. (right) comparison of photoluminescence spectra of the two-stage Cu-rich sample, acquired at 5 min and 21 hours after KCN etching, to highlight the unchanged PL flux over time.

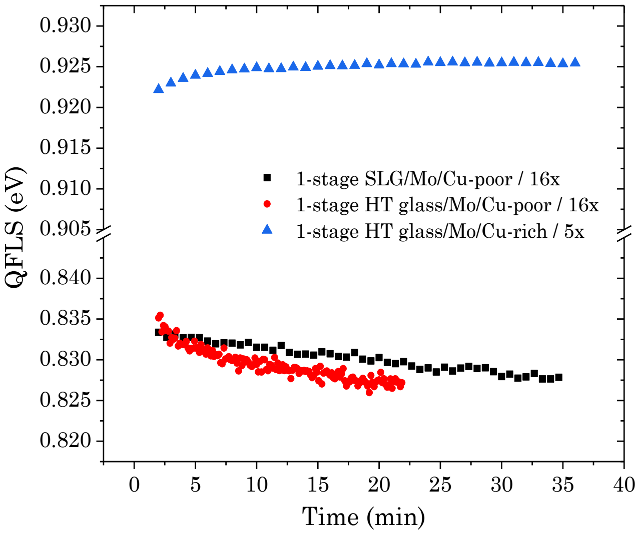

Figure 4.2: degradation study of a Cu-poor CIS deposited on Mo-coated SLG and of Cu-rich and Cu-poor samples deposited at high temperature (650 °C) on Mo-coated HT glass. Note the break on QFLS-axis. Higher illumination (16 suns) is needed for the Cu-poor samples compared to the Cu-rich one (5 suns) because of their lower flux at the band gap. The first measurement (for all degradations studies) has been acquired at 2 min after KCN etching.

Although there are no similar compositional studies on the oxides and their evolution on $CuInS_2$ thin films or single crystals, it is reasonable (due to the very similar nature of the two chalcopyrite compounds) to assume a similar process and composition at the surface of the sulphide based chalcopyrite. Thus, likewise to what has been proposed by Colombara and co-workers for $CuInSe_2$ [121], a possible chemical reaction which takes place at the surface of the absorber in presence of oxygen is as follows:

$$2\,CuInS_{2(s)} + \frac{3}{2}O_{2(g)} \leftrightarrow In_2O_{3(s)} + Cu_2S_{(s)} + \frac{3}{n}S_{n(s,l,g)} \qquad \text{eq. 4.1}$$

with *s, l* and *g* respectively solid, liquid and gas phase.

Given the substantial stability of the QFLS of pure sulphides compounds compared to the selenides ones, the Gibbs free energy of bulk In_2O_3 formation from $CuInS_2$ has been computed, in order to find out the reason behind this dissimilar behaviour against oxygen. Figure 4.3 reports the trend of the Gibbs free energy as a function of the absolute temperature T (assuming the oxide forms through the reaction described in equation 4.1), together with the corresponding trend for the oxidation of $CuInSe_2$, for comparison, as reported in [121].

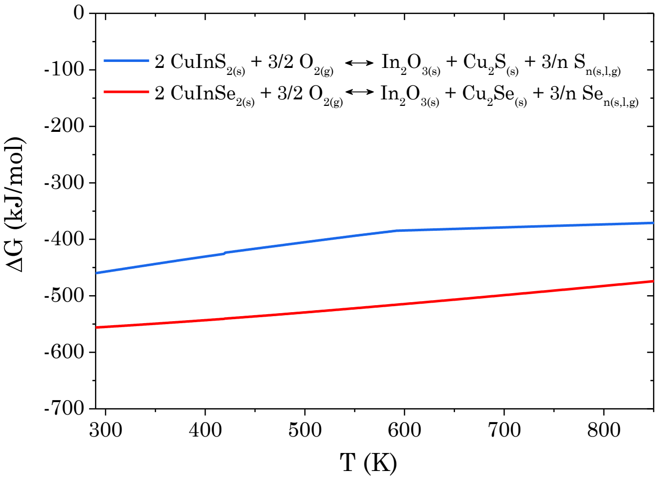

Figure 4.3: Gibbs free energies for the conversion of the $CuInS_2$ ($CuInSe_2$) into In_2O_3 and Cu_2S (Cu_2Se). Calculations made by D. Colombara. Thermochemical treatment elaborated using tabulated values of [122] together with an enthalpy of the ternary compounds formation from [123]. The bent trend observed for the oxidation of $CuInS_2$ is caused by the phase transition of In_2S_3.

For both ternary compounds, the oxidation process described in equation 4.1 is very thermodynamically favourable in air (as ΔG is negative for both cases). Additionally, figure 4.3 clearly shows a lower driving force for the formation of oxide layer from $CuInS_2$ compared to $CuInSe_2$ due to a higher ΔG for the oxidation reaction on the surface of the sulphide compound. The degradation experiments shown in Figure 4.1-4.2 have been performed at room temperature: at this temperature, 300 K, the difference of driving force is about 100 kJ/mol. It is worth saying the favourable thermodynamic driving force is necessary but not sufficient for a reaction to happen. In fact, the chemical kinetics might play a significant role on the experimental trends founds for the QFLS degradation for both sulphide and selenides compounds. Nevertheless, an increment of 100 kJ/mol (about 1 eV/molecule) of the Gibbs free energy at room temperature could represent a possible explanation to the lower QFLS degradation observed for $CuInS_2$ (few meV) compared to the ones measured for $CuInSe_2$ (up to 100-150 meV).

The lower change in QFLS found for Cu-rich CIS compared to Cu-poor ones (although minor, see figure 4.1-4.2) is in line with the trend observed for selenides, where a faster decay has been reported for Cu-poor CISe compared to Cu-rich CISe. The higher tendency of Cu-poor absorbers to oxidize can be explained considering the reaction expressed in equation 4.1. In fact, assuming that for thin films with Cu/In < 1 there is a higher relative amount of In at the surface, this leads to a faster formation of the In_2O_3 layer, increasing consequently the recombination.

Independently of the trends shown in Figure 4.1-4.2, all samples degrade over days (even if they are stored in desiccators). Typical values of QFLS drops are in the range of 20-30 meV for Cu-rich samples, measured roughly 2-3 weeks after KCN. However, as for selenium-based chalcopyrite [116], aged absorbers can be refreshed and the initial QFLS can be fully recovered by an additional weak KCN etching (5% solution for 30s, regardless of the initial nature of the absorber, i.e. Cu-poor or Cu-rich). This is shown in Figure 4.4, which reports the PL spectra and corresponding QFLS of a Cu-rich 1-stage absorber deposited on a molybdenum coated HT glass after initial etching, aged (after 3 weeks) and after recovery, respectively.

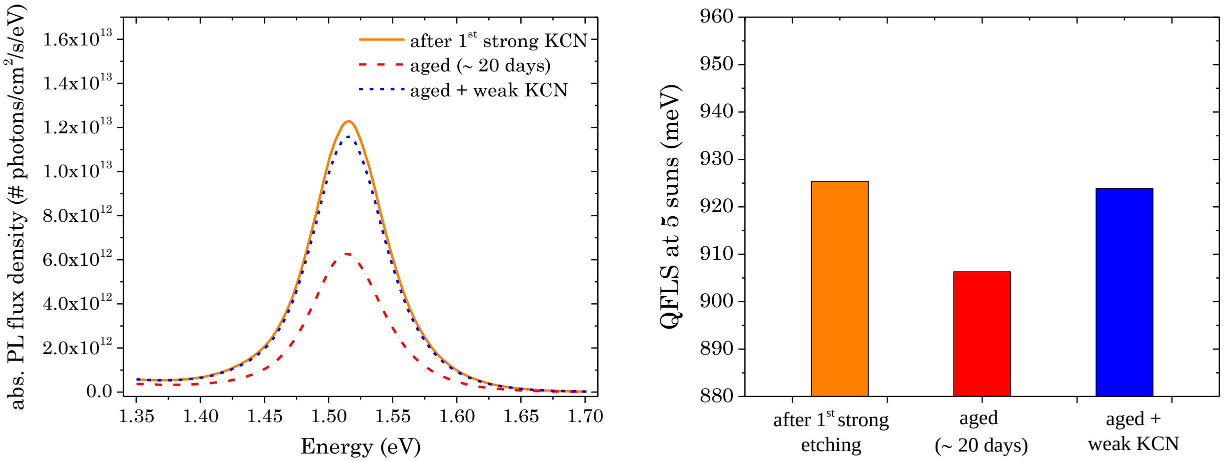

Figure 4.4: (left) PL spectra acquired at an equivalent illumination of 5 suns of a Cu-rich 1-stage absorber deposited on Mo-coated HT glass at 650°C. The spectra refer to the sample after the 1st KCN etching (to remove the secondary phase CuS), then same sample aged (after roughly 20 days) and after a weak KCN etching to refresh the surface. (right) corresponding QFLS at 5 suns, showing a full recovery of the aged absorber after an additional KCN etching.

Hence, it can be concluded the recovery of the absorber quality after additional weak etching is due to the removal of the oxides by the KCN solution. The reason behind might be the selective etching of In_2O_3 as suggested in [116]. Alternatively, for $CuInSe_2$ the oxidation process involves also the formation of a Cu_2Se interface layer between the chalcopyrite and the oxide layer, as shown in [120] by means of SIMS and XPS analysis. Although there are no similar studies for the sulphide system, the oxidation could involve an analogous formation of Cu_2S interface layer: therefore the KCN etching would selectively remove this phase and consequently the oxide layer which lies on the top of it.

Summarizing, CuInS$_2$ absorbers show a significant lower degradation of the QFLS compared to the closely related Cu(In,Ga)Se$_2$. This enhancement in QFLS stability is attributed to the lower driving force of the oxidation processes which take place at the surfaces when they are exposed to oxygen. As for selenides, the surfaces of the sulphide absorbers can be fully recovered in terms of QFLS by applying a KCN-based etching.

4.2 Effect of the buffer layer deposition on QFLS

For selenium-based chalcopyrite, as also described in the previous section, cadmium sulphide (CdS) buffer layer, commonly used in CIGSe solar stack, acts also as passivation layer [116, 117]. In fact, bare absorbers tend to oxidize quickly with huge drop of QFLS (up to 100-120 meV), but the degradation process is hindered if a thin CdS layer (~ 50 nm) is deposited. It has been shown that CISe samples passivated with CdS have the same QFLS of the bare absorbers just after KCN etching (i.e. first measurement of the degradation study). The passivation is essential to investigate the electronic structure of these semiconductors (for example for excitation intensity or temperature-dependent PL); otherwise, if such measurements are performed while the oxidation takes place, it would not be possible to get reliable and reproducible results.

As shown in the previous section, $CuInS_2$ thin films do not show a remarkable degradation like their selenium-based counterpart. Thus, for PL characterization of this semiconductor, such as QFLS evaluation or low T PL analysis, a passivation layer is not required, as these measurements take place over only few hours. Nevertheless, similar studies have been conducted in this work, looking at the effect of both CdS and Zn(O,S) on the optoelectronic quality of $CuInS_2$ thin films. For this purpose, Cu-rich 1-stage absorbers, belonging to the same deposition run, have been used to check the QFLS on bare absorber, bare absorber + CdS and bare absorber + Zn(O,S).

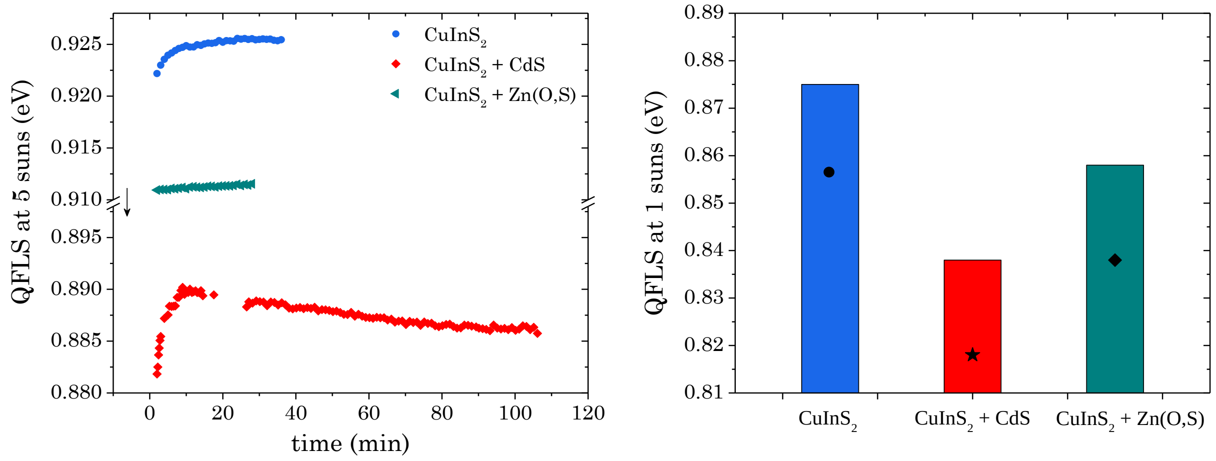

Figure 4.5: (left) QFLS trend measured at an equivalent illumination of 5 suns on bare absorber after KCN etching and after buffer layer deposition (Zn(O,S) or CdS). Note the break on the QFLS-axis for a better data view, highlighted with an arrow. (right) QFLS at an equivalent illumination of 1 sun for the three samples investigated. Additional values (indicated by a circle and a star) are added for the bare CIS and CIS coated with CdS: they have been measured 20 days after the KCN etching and buffer layer deposition, respectively. The QFLS at 1 sun for CIS coated with Zn(O,S) has been measured also after 80 days the deposition, indicated in the plot by a diamond symbol.

Figure 4.5 reports the trend of the QFLS (measured at 5 suns) over time for the three different samples investigated. The one related to bare absorber (KCN etched just before the optical analysis) has been shown in Figure 4.2. Additionally, figure 4.5(right) shows a comparison of the QFLS at 1 sun. The first observation is a drop of the QFLS if the CIS absorber is coated with a buffer layer (independently of which specific buffer is deposited). Secondly, this reduction is enhanced for the absorber coated with CdS (i.e. lowest QFLS for CuInS$_2$ + CdS sample). For the samples coated with buffer, in Figure 4.5 additional data are provided. Particularly, for CuInS$_2$ + CdS sample, the QFLS has been measured after 20 days, showing an additional drop, down to 820 meV at 1 sun, whereas the CuInS$_2$ + Zn(O,S) sample was showing an additional reduction down to 838 meV after 80 days from the buffer deposition. The absorber coated with CdS has been measured also after additional 80 days (not shown in Fig. 4.5), without showing any further lowering of the QFLS. The degradation of the QFLS of bare absorber measured several days after KCN etching has been discussed in the previous section (see figure 4.4).

This trend of the QFLS for bare absorber with and without buffer is drastically different from what is usually observed in Cu(In,Ga)Se$_2$. In fact, for this last chalcopyrite material, as said previously, CdS is used to prevent any degradation of the absorber, confirmed by the QFLS that remains constant over time with a value similar to a freshly KCN etched absorber [116]. Concerning the trends observed in Figure 4.5, a possible explanation might be an increment of the interface recombination at the absorber/buffer interface as soon as a buffer (Zn(O,S) or CdS, in this case) is deposited on the top the absorber, leading to the conclusion that CdS buffer is worse than Zn(O,S), as it leads to higher QFLS reduction. Alternatively, a lower doping of the absorbers after buffer layer deposition might also explain the drop in QFLS. In fact, this is given by the difference of the conduction band quasi Fermi level (E_{fC}) and the valence band quasi Fermi level (E_{fV}). As the absorber is a p-type material, E_{fV} does not shift significantly upon illumination, in low injection conditions, and the QFLS is mainly due to E_{fC}. Nevertheless, after buffer deposition, which is n-type, inter-diffusion at the interface may cause a lower doping in the absorber, thus shifting the hole Fermi level closer to midgap. Consequently, upon illumination E_{fV} will be closer to midgap as well, leading a reduction of the QFLS. To get an idea about the change of the doping needed for such drop in QFLS, the Zn(O,S) case is taken as example. From the effective hole mass $m_h^* = 1.3m_0$ [67], the effective density of states of the valence band for CuInS$_2$ can be estimated, which is roughly $3.7 \times 10^{19}\ cm^{-3}$. Equation 2.5.5 can be rearranged in the following way:

$$\frac{N_V}{p_0} = \exp\left(\frac{E_{F,0}-E_V}{k_B T}\right) \qquad \text{eq. 4.2}$$

Knowing the doping value p_0 would allow to get an estimation of the position of the Fermi level $E_{F,0}$ within the band gap. On the other hand, the doping change required to get a certain QFLS drop is the quantity to be determined. Therefore assuming the QFLS drop is just given by the shift ΔE_F of the hole quasi Fermi level, i.e. of the Fermi level in thermal equilibrium E_F, the following expression can be derived:

$$\frac{N_V}{p_1} = \exp\left(\frac{E_{F,1}-E_V}{k_B T}\right)\ and\ \frac{N_V}{p_2} = \exp\left(\frac{E_{F,2}-E_V}{k_B T}\right) \xrightarrow{E_{F,2}-E_{F,1}=\Delta E_F} \frac{p_1}{p_2} = \exp\left(\frac{\Delta E_F}{k_B T}\right) \qquad \text{eq. 4.3}$$

assuming $E_{F,1}$ and $E_{F,2}$ being the Fermi level before and after buffer layer deposition relatively to the valence band edge, respectively. Taking into consideration the Zn(O,S) case, the observed drop of about 15 meV in QFLS would require a change of the doping by a factor of 1.8, which is not unrealistic.

Moreover, the inter-diffusion may take place over a certain amount of time (days or weeks), explaining the reason why the samples coated with buffer show an additional QFLS drop if they are measured again after few weeks (star and square symbol in figure 4.5). Alternatively, the further drop of the QFLS observed on coated CIS layers after few weeks might come from the degradation of the absorber itself: in fact, the bare absorber presents a similar lowering (in the range of 20 meV) after about 20 days, as indicated by a circle in figure 4.5. This would confirm that the buffer layer not only lead to a drop of the QFLS as soon as it is deposited, but in addition it does not hinder the degradation of the chalcopyrite layer which lies below.

Therefore, in contrast to the effects observed for selenium-based compounds [116, 117], the deposition of buffer layers do not passivate the surfaces of $CuInS_2$. Both Zn(O,S) and CdS lead to a substantial drop of the QFLS, which is worse for the CdS case. Moreover, the QFLS of coated samples still face a degradation over time, showing a lower value when measured after several days. These observations make the buffer layers unsuitable to passivate $CuInS_2$ surfaces. As will be shown in the following, the higher QFLS drop in CIS coated with CdS compared to the one coated with Zn(O,S) will translate in worse performance of solar cells devices based on these samples. The same experimental evidence (i.e. QFLS decrease if a buffer layer is deposited) has been observed for Cu-rich samples grown following the 2-stage process, as reported in [124].

4.3 Effect of deposition temperature on the optoelectronic properties

As has been stated in chapter 1, the recent improvement for Cu(In,Ga)S$_2$ based solar cells has been reached by using higher process temperature during the absorber growth. In this section the effect of the deposition temperature on the optoelectronic properties of the absorbers will be investigated and discussed, together with their effect on the corresponding final solar cells. Some of the results presented in the following are published in [125] and in [126].

As shown in the previous section, the deposition of a buffer layer on CuInS$_2$ absorbers leads to a reduction of the QFLS. Additionally, the degradation of the bare absorbers exposed to air is negligible in time scale of few minutes, i.e. the time scale of a QFLS measurement. For these reasons, if not mentioned otherwise, all the QFLS values reported from now on will refer to bare absorbers, measured after KCN etching (to remove secondary phase or oxides).

The same samples analysed in terms of microstructure in chapter 3 will be evaluated in terms of optoelectronic properties: Cu-poor and Cu-rich absorbers deposited on Mo-coated SLG, analysing as well the effect of the one- and two-stage process on those grown under Cu-excess. In section 4.4 a brief discussion on the effect of a further increment of the process temperature as high as 650 °C will be given: for these depositions, Mo-coated HT glass have been employed as substrates.

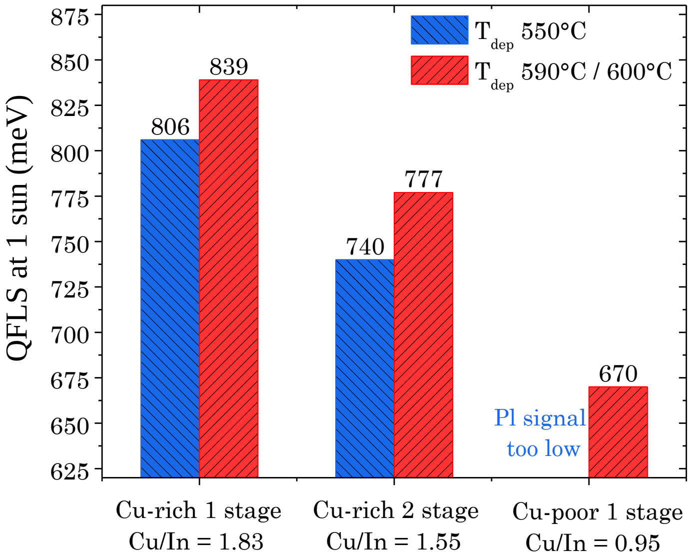

Figure 4.6: QFLS measured at an equivalent illumination of 1 sun for the samples deposited on Mo-coated SLG as described in the plot. For absorbers grown in 2-stage process, the temperature indicated refers to the second stage, while the temperature of the first one has been kept constant at 250°C. For high T deposition, 590 °C has been used for Cu-rich films, whereas 600°C for 1-stage Cu-poor films.

Figure 4.6 shows an overview of the QFLS values measured at an equivalent illumination of 1 sun for the absorbers deposited on Mo-coated SLG. In all cases, an increment of deposition temperature leads to an improvement of the QFLS. One-stage and two-stage Cu-rich samples show higher QFLS, +33 and +37 meV respectively, when the substrate temperature during the growth is increased from 550 °C to 590°C. The Cu-poor sample deposited at lower T_{dep} manifests a PL signal of the band gap luminescence too low (almost absent) to analyse in terms of QFLS, which is an indication of a very low QFLS; for the absorber deposited at 600 °C, a QFLS of 670 meV is found.

The values reported in figure 4.6 reveal that the composition of the films affects the quality of the absorbers as well. This is clear by comparing the one-stage samples grown under Cu deficiency and Cu excess: the average QFLS of the latter is higher by 170 meV. Cu-rich samples deposited following the one- or two-stage process manifest different QFLS. Whether this is caused by the different processes (thus to different structural properties, as shown in chapter 3) or by the dissimilar composition of the as-grown films (Cu/In ratio of 1.83 and 1.55, respectively), will be clarified in the following.

The higher QFLS measured for Cu-rich $CuInS_2$ absorbers is in contrast to the observations on selenide chalcopyrites. In fact, despite a range of favourable properties [127], Cu-rich selenide absorbers show lower QFLS than their Cu-poor counterparts [117]: a possible explanation has been recently proposed, which attributes the lower QFLS to the presence of a deep defect in Cu-rich CISe [90] (that enhances the non-radiative recombination).

The effect of the deposition temperature on the recombination properties can be visualized as well in the trend of the photoluminescence spectra measured at room and at low temperature (80 K) on Cu-rich 1-stage CIS absorbers (after KCN etching) displayed in Figure 4.7.

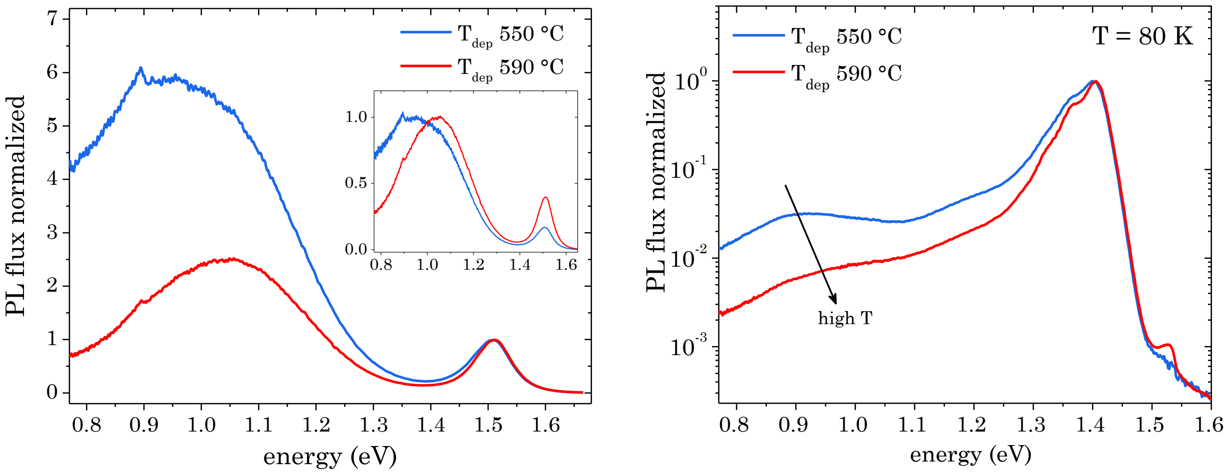

Figure 4.7: photoluminescence spectra measured at (left) room temperature and (right) at 80 K of Cu-rich 1-stage CIS absorbers deposited at 550 °C and 590 °C normalized to the band edge emission. The arrow in the right-hand side plot highlights the presence a band at around 0.9 eV which lowers with a higher deposition temperatures. Note that results are displayed (left) in a linear scale and (right) in a log scale. The inset on the left shows the same room temperature PL spectra normalized to the deep band instead of the band gap luminescence. The feature at around 0.9 eV visible for the room temperature PL spectra is due to water absorption (infrared band at around 1375 nm) which leads to a not perfect and not smooth spectral correction.

The room temperature PL spectra are characterized by a band around 1.51 eV, which is related to band-band transitions (given the band gap of this material) and a broad deeper band. The spectra are normalized to the band-band transition. When the process temperature is increased by +40 °C, a lower intensity of the broad deeper band relative to the band-band transition is observed. This is an indication of a lower concentration of deep defects, hence of a better optoelectronic quality of the absorber deposited at 590 °C. The corresponding two-stage Cu-rich samples grown at different T_{dep} show a similar trend in terms of the broad deep-band intensity (see Appendix, figure A4.1). Concerning the Cu-poor absorbers, the one grown at 550 °C does not manifest a band-gap luminescence, and the PL spectrum is dominated essentially by the low-energy deep band; on the contrary, the Cu-poor sample deposited at high temperature (600 °C) has luminescence also at about 1.5 eV (see Appendix, figure A4.2). Figure 4.8 presents a comparison of the room-temperature PL spectra of the CIS films deposited at high T_{dep}. The features observable in the broad PL band at energies below 1.3 eV for Cu-rich 2-stage and Cu-poor 1-stage are not given by the presence of multiple bands but they are rather due to interferences, as demonstrated in figure A4.3 (in appendix) by means of angle resolved photoluminescence. In fact, as shown in cross section SEM images in chapter 3, those films (in contrast to 1-stage Cu-rich) exhibit very smooth surfaces, which significantly enhance the specular reflection of the photons generated within the film, which in turn leads to undesired interference pattern in the PL spectral shape [128]. This is particularly relevant in low temperature PL, and if not correctly analysed, may lead to misinterpretations. Recently, polystyrene particles have been employed to form a scattering layer and remove inference effects [129]. An example will be shown in chapter 5.

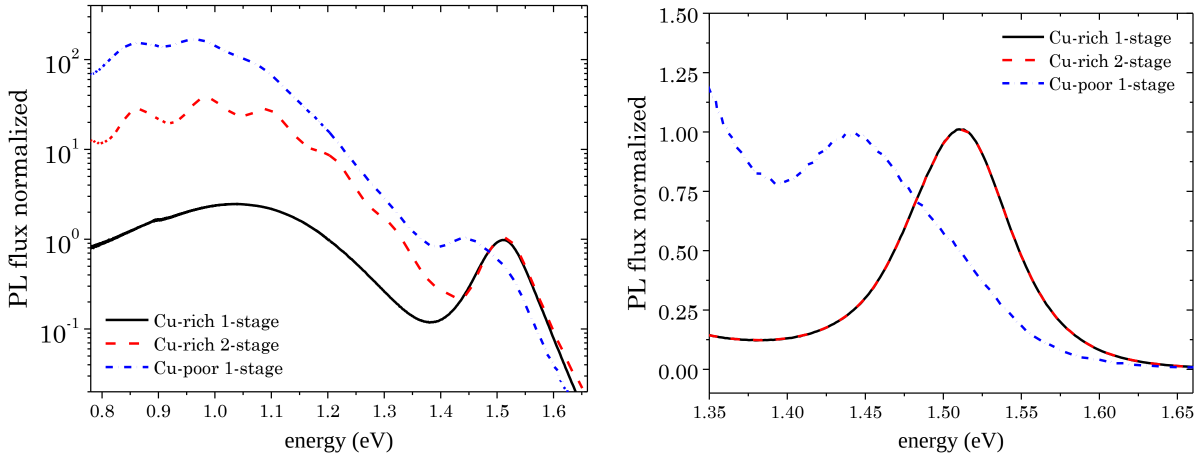

Figure 4.8: (left) Room temperature PL spectra of CIS samples deposited at high temperature (590 °C and 600 °C for Cu-rich and Cu-poor, respectively) normalized to the band gap luminescence. Note that the flux-axis is in log-scale. (right) Enlargement of the band gap luminescence for the same samples: note that flux-axis is in linear scale.

Figure 4.8 clearly shows that the relative ratio between the deep band and the band gap luminescence increases if the Cu-rich sample is deposited by the two-stage process; this relative ratio increases further when the composition of the absorbers turns into the Cu-poor regime. It is worth noting that when the relative contribution of the deep PL flux gets higher, the corresponding QFLS lowers (see figure 4.6, which illustrates the Cu-poor absorbers has the lowest QFLS). This is a first hint that the two trends, i.e. QFLS and relative contribution of the deep

PL flux, might be related to each other, as will be discussed shortly. The red-shift of the luminescence peak at the bad gap observed for the Cu-poor sample will be analysed in the following.

Besides the lowering observed in PL spectra when the process temperature rises, the deep-defect luminescence also gets narrower, as clearly visible in the inset of figure 4.7. This is a first indication that there might actually be two transitions and the one at lower energies around 0.8–0.9 eV decreases more with higher growth temperatures.

The PL spectra acquired at 80 K (figure 4.7(right)) for the same samples shows again the same trend: a lower contribution of deep-defect luminescence with higher growth temperature. Moreover, it confirms that a deep-defect luminescence around 0.9 eV is present with an intensity that decreases with higher deposition temperatures, as highlighted by the arrow in the figure. Both films show luminescence peaks around 1.4 eV: these transitions have been observed in the past and have been attributed to shallow defects [74, 82]. They will be analysed in detail in chapter 5. The low temperature PL spectrum of the film grown at 590 °C shows band-gap luminescence around 1.52 eV, related to the excitonic emission. The observation of the excitonic emission confirms once more the higher optoelectronic quality of the film grown at higher temperature.

Summarizing, the results obtained by means of photoluminescence analysis show that the higher growth temperature leads to (i) a reduction of the intensity of the PL band related to the deep defect and to (ii) an increment in the quasi-Fermi-level splitting. It is reasonable to assume that the defects involved in the deep luminescence increase the non-radiative recombination, thus reduce the QFLS. For this purpose, in order to establish the correlation between the QFLS values and the intensity of the broad deep band, the room temperature PL spectra of several Cu-rich one-stage samples are fitted with three different Gaussian bands, as shown in Fig. 4.9. Cu-rich one-stage samples have been chosen because their PL spectra shape are not distorted by interference fringes. The band around 1.5 eV is indisputably present and is due to the band-gap luminescence. Concerning the deep band: although at first sight it could be described by a single band, it is actually a convolution of two distinct bands: the one around 1.05 eV and the one around 0.83 eV. The PL band around 0.83 eV is justified because (i) the room-temperature broad deep PL band is asymmetric as seen in figure 4.9, (ii) the room-temperature deep-defect PL becomes narrower with increasing growth temperature, as seen in figure 4.7(left), (iii) the low-temperature PL in Fig. 4.7(right) shows that the band shape of the deep luminescence indicates the presence of a distinct band in this spectral region.

Taking into consideration only the room temperature PL spectra, one might argue that the asymmetric broadening (to the low energies) of the deep band is given by electron-phonon interaction of the band with PL peak at 1.05 eV. In fact, deep defects have a strong electron-phonon coupling due to their nature of being more localized, which leads to high Huang-Rhys factor (a factor that describes the number of phonons involves in the optical transitions [70], see section 2.5.2), which in turn causes a deviation from a standard Gaussian line shape. An example of these asymmetric broadening can be found in [90] and in [130]. Nevertheless, a further proof of the existence of an additional band at around 0.83 eV is given in Figure 4.10, where the room temperature PL spectrum of a Cu-rich one-stage sample is given. This absorber belongs to a series of samples deposited in the optimization phase of the $CuInS_2$ growth.

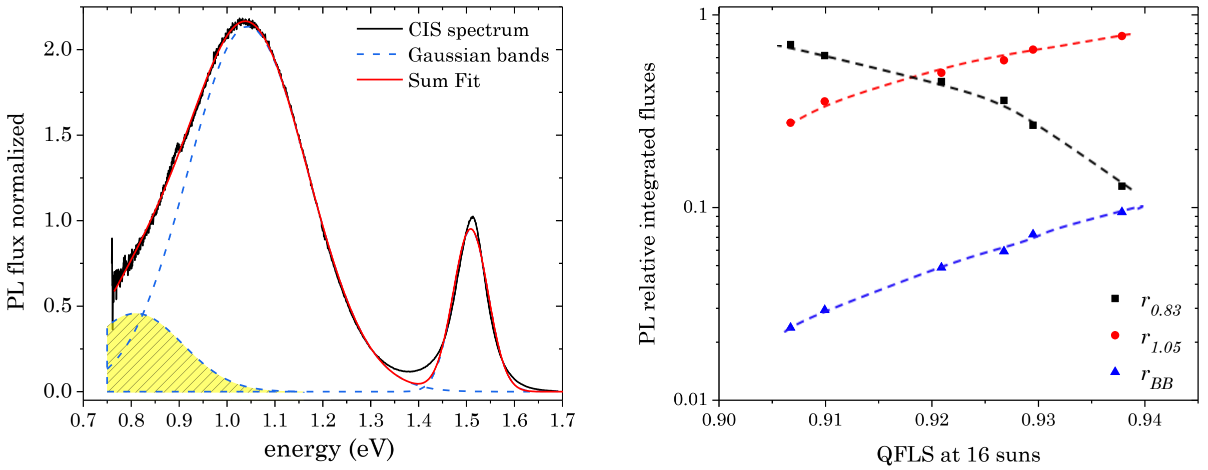

Figure 4.9: (left) example of fitting performed on a Cu-rich one-stage CIS room-temperature PL spectrum together with three single Gaussian bands. The deeper band centered at around 0.83 eV is highlighted in yellow. An additional example of fitting with higher contribution of the 0.83 band is shown in appendix in figure A4.4. (right) PL relative ratio of the integrated fluxes for each Gaussian band used to fit different PL spectra. The legend refers to the PL peak of the defects bands ($r_{0.83}$ and $r_{1.05}$) and to band-to-band transition (r_{BB}). The dashed lines are intended to be guide lines.

For a better view (and because of the high enough intensity of the deep band) the spectrum has been measured over a wider range than that displayed traditionally, employing the extended InGaAs-CCD detection camera, which allows to measure down to 0.6 eV. It is clear from the reported PL spectrum that the deep band at around 0.83 eV dominates the spectrum and allows the determination of its PL maximum, which has been used in the fitting procedure shown in figure 4.9. Additionally, such high deep band denotes a significant non-radiative recombination thus, for a better view, the bad gap luminescence at around 1.5 eV have been plotted also rescaled by a factor of 300. Therefore a third band centered at around 0.83 eV is needed and it is not an arbitrary choice, albeit less evident in PL spectra such as the one reported in figure 4.9.

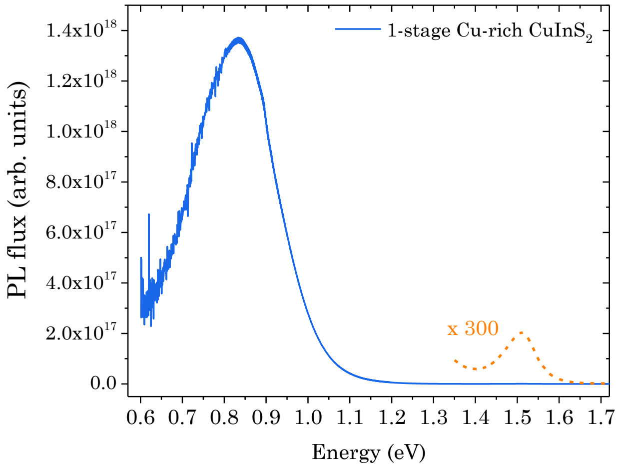

Figure 4.10: PL spectrum of a Cu-rich one-stage CIS absorber with low optoelectronic quality. This spectrum has been reported to confirm the presence of a band at around 0.83 eV, which, in this case, dominates the PL spectrum. The band gap luminescence (in orange) has been plotted multiplied by a factor of 300 for a better view.

Hence, with the fitting procedure described above, for each of these bands, the relative ratio of the integrated single-band PL flux over the entire PL-spectra flux has been calculated, i.e.

$$r_i = I_i / \sum I_i \tag{eq. 4.4}$$

with r_i the relative ratio, I_i the integrated PL flux of the band i and $\sum I_i$ the integrated PL spectrum flux. The three different ratios are labelled, respectively, r_{BB}, $r_{1.05}$, $r_{0.83}$. Figure 4.9(right) reports the trend of these ratios with the QFLS of the samples. QFLS are measured at higher fluxes than 1 sun, to ease the measurements. The trend of r_{BB} with QFLS is expected as in an ideal absorber, where only radiation recombination takes place, the PL spectrum should display only the band-to-band transition. Therefore, when r_{BB} increases, the quality of the absorber is improved and this is reflected into higher QFLS. An unexpected trend is the one of $r_{1.05}$: the QFLS increases with an increasing share of this deep-defect luminescence. The reason becomes clear, when investigating the ratio $r_{0.83}$: it shows an opposite trend compared to $r_{1.05}$, and its drop leads to a higher QFLS value. This indicates that the QFLS is limited by the defects involved in the transition around 0.83 eV. With a lower contribution of deep defects around 0.83 eV, all other radiative transitions are increased, including the one at 1.05 eV. Thus, the fewer deep defects involved in the transition around 1.05 eV do not limit QFLS in the given set of absorbers. In fact, from the spectra normalized to the amplitude of the broad deep band shown in the insert in Fig. 4.7, the main difference using a higher growth temperature occurs for energies lower than 1 eV. Once the density of deep defects is reduced sufficiently, it is expected that the QFLS might then be limited by the defects of the 1.05 eV transition.

In order to check if the higher QFLS translates into an increment in the open circuit voltage of the photovoltaic solar cells, devices are made with CIS absorbers prepared by the same deposition runs as the absorbers analysed and discussed so far.

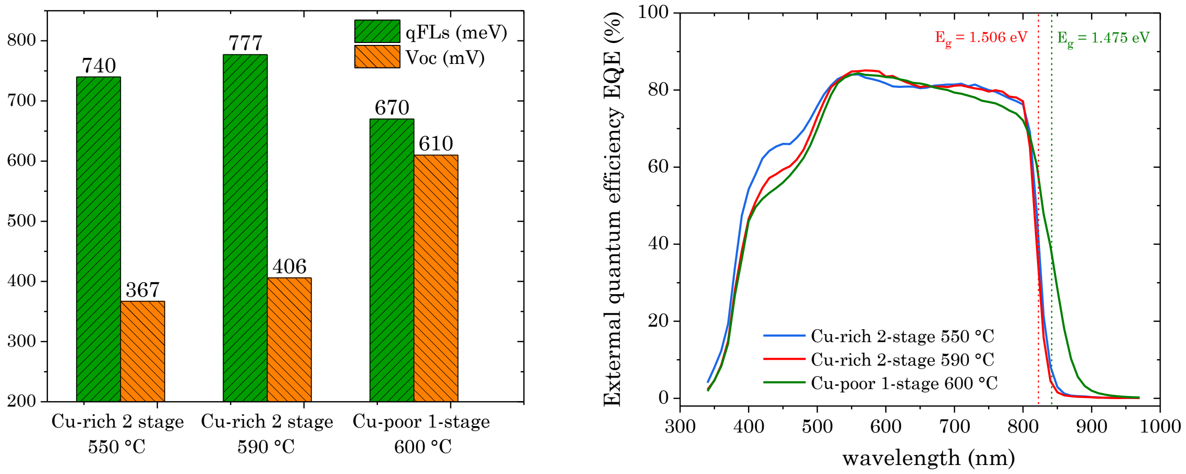

Figure 4.11: (left) comparison of the V_{OC} and QFLS of Cu-rich 2-stage and Cu-poor 1-stage absorbers; solar cells based on Cu-rich 1-stage films are not included because of their significant shunting behaviour, whereas devices based on Cu-poor one-stage absorbers deposited at low temperature (550 °C) do not show any diode behaviour. (right) external quantum efficiency measured for Cu-rich 2-stage and Cu-poor one-stage devices together with band gaps extrapolated from the maximum of the first derivative of the EQE.

To ensure the differences in the devices are given only by the changes in the absorbers used, all solar cells have been treated by the same baseline process, thus a chemical bath deposition for CdS deposition, sputtered intrinsic ZnO and ZnO:Al window layers and e-beam deposited Ni/Al contact grids. Figure 4.11 reports the open circuit voltages averaged over eight devices for each kind of absorber layer together with the corresponding QFLS. External quantum efficiencies are presented as well.

Open circuit voltages of the solar cells based on absorbers grown under Cu-excess in one-stage process are not included in figure 4.11 as their current-density-voltage characteristics show a significant shunting behaviour. This is mainly attributed to the unfavourable morphology of these thin films, characterized by a rough surface, trenches between grains and voids at the back interface molybdenum/CIS, as shown in details in chapter 3. This is a common issue for devices made from Cu-rich 1-stage absorbers, as often reported in literature [44, 48, 101] and represents the main reason why 2-stage processes have been developed to grow CIS layers. To get a closer view about the solar cell layers stack, an EDX compositional mapping has been measured on a cross section CIS absorber coated with CdS, reported in figure 4.12. It is evident that during the chemical bath deposition, CdS grows and extends deep into the absorber layer along the grain boundaries (in some cases it has been found also at the back interface, likely filling the voids) down to the interface between molybdenum and absorber. The increment of the process temperature (from 550 °C to 590 °C) does not modify the morphology of this films, thus the penetration of the buffer layer. For comparison, it is also shown the Cd distribution for a Cu-poor absorber (deposited at low T_{dep}), where the buffer covers only the top surface. Given the morphology of the Cu-rich two-stage samples presented in chapter 3, it reasonable to assume the Cd distribution mapping is similar to the Cu-poor one. The deposition of the buffer along the grains is expected to generate the low shunting resistance of the Cu-rich cells based on one-stage absorbers (in some cases through a direct contact of the ZnO/CdS to the Mo back contact), and have to be avoided to achieve working devices. Nevertheless, it is worth saying that in the framework of this thesis, the optimization of Cu-rich one-stage process growth has led to working devices up to 7.6 % of electrical conversion efficiencies, although always exhibiting low shunt resistance (as reported in figure A4.5).

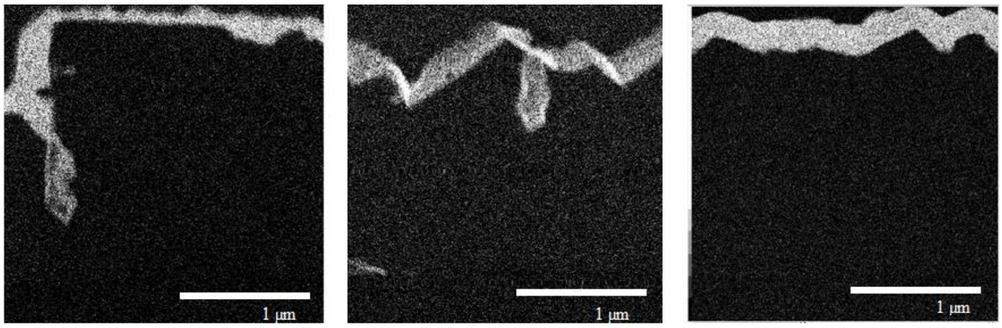

Figure 4.12: Cd distribution measured by EDX in a STEM for cross sections of CIS absorbers grown in 1-stage process under Cu-excess at (left) 550 °C) and (middle) 590 °C and (right) under Cu-deficiency at 550°C. Analysis performed by Torsten Schwarz of MPIE.

For the devices based on two-stage Cu-rich absorbers deposited at low and high temperature, the increment with higher growth temperature in QFLS of 37 meV is reflected into the improvement in the V_{OC} of 39 mV. However, the Cu-rich cells, although exhibiting higher QFLS, show a considerably lower V_{OC} than the Cu-poor cells. The Cu poor solar cells show an average V_{OC} value of 610 mV. The J -V characteristic under AM 1.5 illumination for the best Cu-poor cell is reported in figure 4.13. It is based on a Cu-poor absorber grown by the one-stage process at 600 °C and has an efficiency η of 8.3%, with a short-circuit current J_{SC} = 20.5 mA/cm², V_{OC} = 613 mV, and fill factor FF = 66 %. This efficiency compares not unfavourably with the best efficiencies reported for pure $CuInS_2$ [24, 49, 131]. It is also worth mentioning that in our lab the baseline process (thus thickness and resistivity of the different layers that form the solar cell structure) has been optimized for Cu-poor pure-selenides solar cells, thus with similar sulphides absorbers higher efficiencies could potentially be achieved.

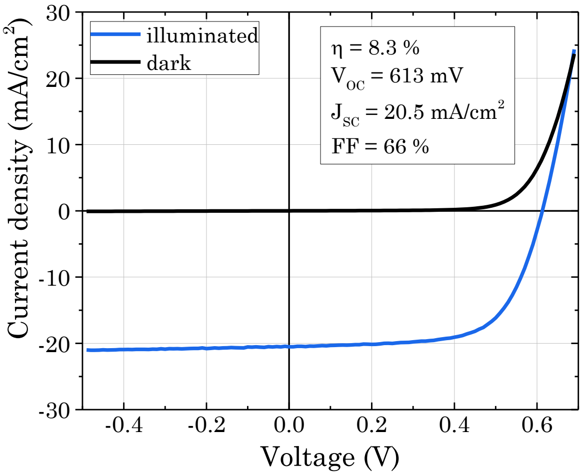

Figure 4.13: J –V characteristic under dark and under AM1.5 illumination for the best solar cell based on Cu-poor absorber deposited at high temperature (600 °C), with a device area of around 0.5 cm².

As it has been discussed previously, the QFLS is limited by the presence of deep defects. Nevertheless, the devices based on Cu-rich two-stage films show a huge gap between the QFLS and the V_{OC} (gap in the range of 370, independently of process temperature), which cannot be attributed to the absorber itself, but originates from a loss that occurs at the interfaces of the solar cell and is likely due to the buffer layer and/or the buffer-absorber interface. It is well known that Cu-rich chalcopyrite-based solar cells are dominated by interface recombination, in contrast to solar cells based on Cu-poor absorbers, as reported in [132] by means of temperature-dependent current-voltage measurements. In fact, using this analysis, is it possible to determine the dominant recombination path of solar cells, hence if the main issue of the device is bulk or surface recombination. It has been widely studied and proved that Cu-rich Cu(Ga,In,)S_2 [25, 55, 133] suffer from interface recombination, and this has been confirmed as well in this work by IVT measurement performed on the device based on Cu-rich two-stage sample, reported in appendix in figure A4.6, which clearly shows that the activation energy extrapolated at 0 K (around 0.85 eV) is well below the band gap energy (around 1.5 eV). A similar study has been carried out on the Cu-poor sample whose J-V characteristic is displayed in figure 4.13. The measurements could not give meaningful results because of a significant degradation of the device in terms of electrical parameters observed over time.

The interface of the Cu-rich absorbers can be improved by changing the buffer layer deposition process or by using a different kind of buffer. In the first case, Braunger et al. in [131] have shown the preparation conditions of the chemical bath deposition of CdS, particularly the thiourea concentration used in the solution, can significantly affect the final device performance. They found higher thiourea concentration in the CdS CBD is beneficial for device efficiency, reducing the interface recombination as confirmed by higher activation energies extrapolated at 0 K. Following this reasoning, in this work solar cells have been fabricated using the same kind of absorber with a QFLS of 740 meV (i.e. 2-stage and low T_{dep}), but with thiourea concentration three times higher than what is usually used in the baseline process for the CdS deposition. Additionally, solar cells with Zn(O,S) as buffer layer have been fabricated: in the standard recipe for the chemical bath deposition, the thiourea concentration is about eight times the standard concentration used for CdS deposition. More details about the chemical bath deposition of the two buffers can be found in [50]. In both cases, an increment of the open circuit voltage has been measured compared to the baseline process, with an average value of 480 mV and 600 mV, respectively, as reported in figure 4.14.

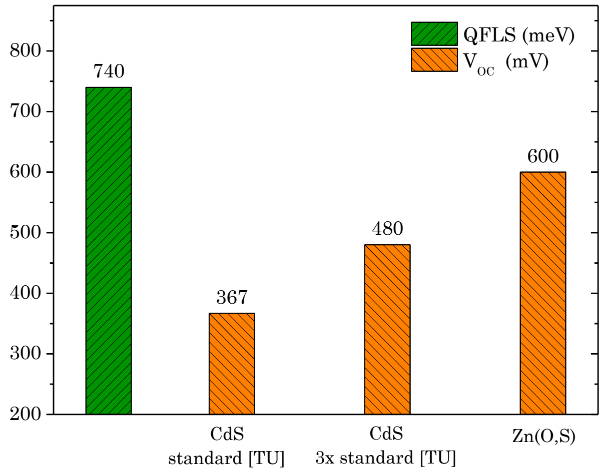

Figure 4.14: QFLS splitting of the Cu-rich two-stage sample deposited at 250 °C + 550 °C, together with the average V_{OC} of the devices made from same absorber but with 3 different buffer layers: CdS standard [TU] refers to the standard CdS deposition used in the baseline process, with a TU concentration of 50 mM, whereas 3x standard [TU] refers to the same kind of CdS deposition, using a TU concentration three times higher, thus 150 mM. The last column refers to devices where the CdS has been replaced by Zn(O,S) buffer layer. J-V characteristics and EQE of the corresponding devices are reported in figure A4.7 in Appendix.

The improvement in the open circuit voltage in devices fabricated with same absorber (thus same QFLS) proves once more that QFLS is a good indicator of the optoelectronic quality of an absorber, whereas the V_{OC} may be affected by several limitations, like indeed interface recombination. Devices based on Cu-poor absorbers deposited at high T_{dep} have been finished with Zn(O,S) as buffer layer as well, without significant difference in terms of open circuit voltage (always around 600 mV). This might suggest that one of the limitations of Cu-rich sulphides solar cells is interface recombination, which in turn is partially related to sulphur-related defects at the interface absorber/buffer. Similar evidences have been observed for Cu-rich CISe solar cells, and the interface, thus the final performance of the devices, can be improved by a post deposition treatment (PDT) in chalcogenide atmosphere [102]. The mechanism suggested is the formation of selenium-related defects during the KCN etching (performed to remove the secondary phase) and their passivation during the PDT. Recently, we have observed improvement in the open circuit voltages if the absorbers are treated with sulphur-containing solutions before the buffer layer deposition, with devices reaching efficiencies up to 9 % and V_{OC} close to 700 mV. The increase in the V_{OC} has been correlated to improvements in the interface recombination, as confirmed by temperature dependent open circuit voltages measurements [124].

Before discussing the effect of the stoichiometry on the QFLS, one more difference can be observed between Cu-poor and Cu-rich sulphides absorbers, and it is related to the band gap. In fact, figure 4.8, together with an overview of the PL spectra over the whole spectral range, reports, for the same spectra, a closer sight on the band gap luminescence. Although the band gap luminescence shape of the Cu-poor sample might be slightly deformed by the interference pattern, it is evidently shifted to lower energies, compared to the Cu-rich films (both one- and two-stage). The same trend is observed from the band gaps extrapolated from the maximum of the first derivative of the external quantum efficiency, as shown in figure 4.11: a band gap of 1.475 eV is extrapolated for the Cu-poor absorber, whereas 1.506 eV for the Cu-rich 2-stage one. Similar values of band gap (around 1.50-1.51 eV) have been determined for working devices made from Cu-rich one-stage films. During the same deposition runs of the above mentioned absorbers, substrates without molybdenum back contact have been used, in order to analyse the transmittance and reflectance of the absorbers, thus to get the band gap of the corresponding films from the Tauc plot. The corresponding plots of the Cu-poor one-stage and Cu-rich two-stage sample are reported in figure A4.8 in Appendix. The absence of molybdenum layer leads to a different emissivity of the substrates, thus lower deposition temperature during the process growth. Additionally, the diffusion of elements (particularly the alkali ones) is modified due to lack of an additional layer (Mo) between the glass and the absorber. For these reasons, the comparison of the same kind of sample deposited either on glass or on Mo-coated glass is not straightforward. Nevertheless, the band gaps measured from the Tauc plots of samples deposited on glass show the same trend found in photoluminescence and external quantum efficiency measurements: that is, Cu-poor $CuInS_2$ thin films have lower band gaps of Cu-rich ones, with a difference of around 30-40 meV. Analogous results have been found for $CuInSe_2$ system, with Cu-poor absorbers still showing lower band gaps then those grown under Cu-excess [134, 135]. This trend is the consequence of two mechanisms which almost compensate each other. The first one is the tendency of lowering the band gap if the anion displacement u decreases (u is a parameter which describes the deformation of the anion tetrahedron, due to the different bonding lengths with copper and indium, as already described in chapter 2 and 3). Experimentally, it has been found u decreases from samples grown in Cu-rich regime to those grown under Cu-poor regime [134]. On the other hand, according to theoretical calculations, the bad gap enlarges if the concentration of Cu vacancies increases, which it is reasonable to assume is higher for samples deposited under Cu deficiency [136]. Therefore, for Cu-poor samples, the variation in the density of Cu vacancies would induce an enlargement in the band gap, which is actually counterbalanced by the reduction induced by the change of the lattice distortion. The combination of these two mechanisms is the reason behind the band gap stability with respect to deviation from stoichiometry and equilibrium structure. Although the two contributions almost cancel each other out, it has been theoretically calculated that the contribution given by the lattice distortion slightly dominates [134], which in turn leads to a lower band gap for samples grown under Cu deficiency. Although there have been theoretical calculation also on $CuInS_2$ [136], this is the first time that its band gap is experimentally studied as a function of the composition, analysing samples grown within the same deposition technique.

Taking into account the band gap difference between Cu-poor and Cu-rich sulphides absorbers (around 30-40 meV), one would expect lower absolute QFLS for films deposited under Cu deficiency compared to those grown under Cu-excess (even assuming no changes in the optoelectronic quality of the absorbers). Nevertheless, the variation in QFLS for Cu-poor absorbers compared to Cu-rich ones is well above 100 meV (figure 4.6) and the variation of the band gap is not sufficient to justify the higher loss in QFLS. The band gap change as a function of the composition is relevant also for the correct attribution of point defects energy levels, as will be discussed in chapter 5.

4.4 Effect of the composition on the QFLS (HT glass)

In the previous section the influence of the deposition temperature on the recombination properties, thus on the QFLS, has been discussed. Higher process temperature leads to better recombination properties, confirmed by an increment of the corresponding QFLS. It has been shown as well that analysing samples grown by similar deposition process (one-stage), Cu-rich samples have higher QFLS than Cu-poor ones, with a Cu/In ratio of about 1.8 and 0.95 respectively. Still, a detailed investigation of the effect of the composition on the QFLS is missing. To shed light on this, $CuInS_2$ thin films have been grown with different composition. Some of the results presented in the following are published in [126].

The elemental composition has been changed by keeping the copper flux constant and by adjusting the indium flux to get the desired composition. Additionally, all of them have been grown in a one-stage process using a constant deposition temperature of 650 °C throughout the whole process. The choice of using 650 °C is based on the deposition temperatures used to reach the current record champion device, although the deposition technique is different [26]. For such high process temperature, the standard soda lime glass cannot be employed, due to its annealing point around 550 °C. For this reason, Mo-coated HT glasses have been used as substrates for the growth of these samples. Before measuring absolute calibrated photoluminescence, the samples have been etched in KCN-containing solutions to remove secondary phases or oxides, then directly transferred to the PL setup. The time between etching and the first PL measurement is approximately 2 min. The QFLS measurement for each sample takes only a few minutes, thus the slight degradation, if there is any as discussed in section 4.1, is negligible or within the error of the QFLS determination.

Figure 4.15 report the measured QFLS values at an equivalent illumination of 1 sun as a function of the Cu/In ratio of the absorbers. The narrow Cu-poor range investigated is mainly due to the low band-to-band luminescence of samples with Cu/In < 0.95. In fact, the room temperature PL spectra of such samples resemble the one reported in figure A4.2 for the Cu-poor CIS deposited at low temperature, i.e. PL spectra essentially dominated by the deep PL band. As said previously, these absorbers cannot be analysed in terms of QFLS.

The effect of the composition on the QFLS is clear: once more the better quality of the Cu-rich samples is confirmed in terms of recombination properties, as they always show higher QFLS than Cu-poor ones, even for Cu/In slightly above 1. As soon as the Cu/In ratio approaches 1 or slightly lower, there is a drastic drop in QFLS well below 800 meV. In the Cu-rich regime, it is also possible to see an increment for thin films deposited under higher Cu-excess, with a gain in QFLS that is stronger for moderated Cu/In ratios, whereas it seems to saturate for highly Cu-rich absorbers (Cu/In >1.40). It is worth noting that the highest qFLs corresponds to a Cu/In of about 1.8, which might explain the use of this ratio between the two metals in several reports on CIS for solar cells [24, 137]. Moreover, the difference in QFLs for absorbers with a Cu/In ratio of 1.8 and 1.2 is about 35 meV, a value similar to the difference in open circuit voltages found for solar cells fabricated using those ratios in the precursors, as reported in [137].

Besides the effect of the composition, the comparison with samples grown on Mo-coated SLG at lower temperatures allows to analyse as well the changes in QFLS induced by the very high deposition temperature used for this series of samples.

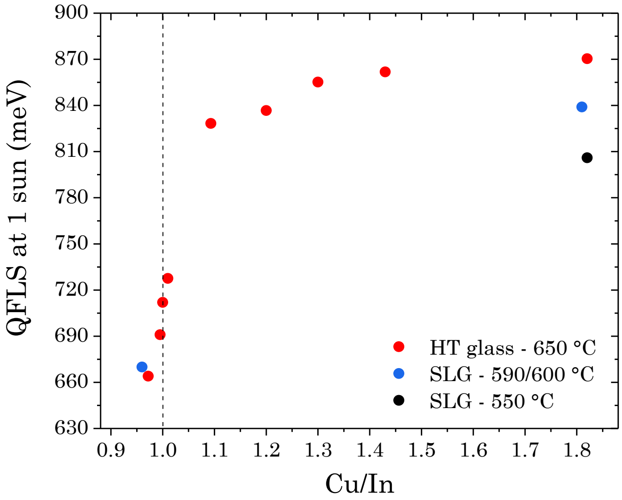

Figure 4.15: quasi Fermi level splitting measured at an equivalent illumination of 1 sun plotted over the Cu/In ratio. The composition has been measured by EDX on the as-grown samples before any kind of etching. For comparison, the QFLS of samples deposited at lower temperature are reported as well, as indicated in the legend, specifying also the type of glass used. All data refer to films deposited by using 1-stage process. Even if not explicitly reported, the glasses were all coated with the Mo back contact layer. The dotted line separates the Cu-poor and Cu-rich region, respectively. Figure adapted from [126].

Figure 4.15 clearly shows its influence on the recombination properties of the resulting absorbers differs from Cu-rich regime to Cu-poor regime. Particularly, looking at the CIS films with a Cu/In ratio of about 1.8, higher deposition temperature leads to an improvement of the QFLS, independently of the specific glass used, with the highest QFLS of 871 meV for the absorber grown on Mo-coated HT glass at T_{dep} of 650 °C. A different trend is observed for the Cu-poor samples grown with a metal ratio of about 0.95, where an increment of about 50 °C in temperature process does not bring any evident enhancement in terms of QFLS, with a value of around 670 meV, similar to what has been found previously on the Cu-poor CIS deposited at 600 °C.

The dissimilar behaviour observed between the Cu-poor and the Cu-rich regime might be the consequence of the different glass used as substrate. In fact, as shown in Appendix 3.1, the compositional analysis performed by XRF revealed a lower sodium and potassium concentration in the HT glass compared to SLG, by a factor of 2.7 and 16, respectively. As the Mo back contact layer has always a thickness around 500 nm, it is reasonable to assume that the amount of these alkali elements diffused into the absorber during the process growth is strongly reduced in the case of the HT glass. It is well known that alkali elements dramatically change the structural and optoelectronic properties of chalcopyrite thin films, particularly those grown under Cu-deficiency [138-140]. Several studies have been conducted to investigate their effect on the thin films properties, by introducing the alkali elements as precursors, during the growth or during post deposition treatments [114, 138, 140-142].

Specifically to $CuInS_2$, it has been shown in the past that sodium does not vary the efficiencies of the final devices based on this kind of absorber, if grown in Cu-rich regime (Cu/In of 1.8) [77]: in this cited study, the amount of sodium incorporated into the absorbers has been varied by using different glass substrate types (such as alkali-free, standard SLG, with sodium barrier..).

In fact, although the PL spectra measured at low temperature of the corresponding absorbers were differing significantly, open circuit voltages, fill factors and short circuit currents were barely affected. On the contrary, performances of devices based on Cu-poor pure-sulphides absorbers were shown to be strongly affected by the sodium incorporation, as reported in [140], where the alkali element was introduced as precursor (NaF). An increment of the open circuit voltage has been observed for thicker layer precursors, thus with higher Na incorporated during the absorber growth.

The lower sodium concentration into the Cu-poor absorber grown at 650 °C on HT glass compared to the one deposited on SLG at 600 °C has been further confirmed by SIMS analysis. The Na/Cu profile for both samples is shown in figure 4.16. Except the concentration ratio at the surface of the samples, through the whole thickness the Na/Cu profile is always lower for the CIS film deposited at higher temperature on the HT glass. The reason of the increment at the surface is unclear: it might be related to an artefact of the measurement, to a surface contamination of the samples during the weak KCN etching or it could be characteristic of the samples during the growth. The Na/Cu profile has been plotted because SIMS measurements can only provide a detected flux of a certain element (in counts/s), which is proportional to the concentration of the element itself. Thus the Na signal has been normalized to the Cu one, assuming the concentration of the last one very similar in both samples, as the Cu/In ration is the same. In figure A4.9 the SIMS profiles of Cu, Na and Mo for both samples are reported individually for comparison.

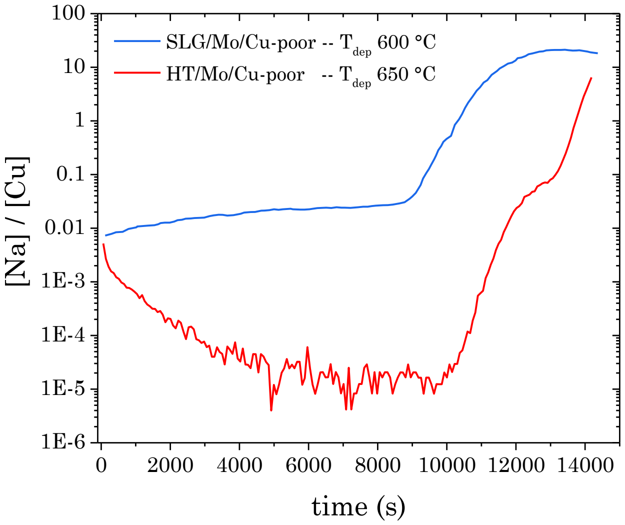

Figure 4.16: ratio of the sodium to copper SIMS profiles (each of them in count/s) plotted over time for the two Cu-poor CIS layers deposited at different temperature on Mo coated HT glass and SLG. 0 s is the front surface. In appendix, the SIMS profiles of Cu, Na and Mo are reported individually.

An additional proof of the lower Na concentration due to the glass used comes from APT measurements performed on the same samples investigated by SIMS. Usually, in such measurements, the interest is rather focused on the alkali segregation, i.e. their concentration difference, along structural defects, like dislocations and grain boundaries. These concentrations are usually given as normalized excess values compared to the bulk (or grain interior) [143], where any Na concentration is treated as background. While it was possible to do this for the CIS grown on SLG, during the measurements on the HT glass film the sodium peak could not be measured at all even for the grain interior. Therefore, for this specific sample, the sodium concentration was similar or lower than the detection limit of the APT setup, which is around 2 ppm for the specific setup and parameters used for the measurements.

4.5 Overview and comparison of the QFLS in sulphides and selenides systems

In section 4.3 Cu-rich samples deposited both by one- and two-stage processes have been analysed, with the latter showing lower QFLS. This might be caused by a lower Cu/In ratio (1.55 and 1.83 for two-stage and one-stage CIS, respectively) or by the different process employed to deposit the absorber layers. A first hint that this second option could play the major role comes from the study discussed in the previous section 4.4, where a detailed investigation of the effect of the composition on the QFLS has been conducted. For a range of composition described by the Cu/In between 1.3 and 1.8, the QFLS is barely affected (see figure 4.15). On the other hand, the introduction of an additional stage in the two-stage process leads to a higher number of parameters that can be varied independently from each other, such as the substrate temperature kept during the first and the second stage. To shed light on whether an optimized two-stage growth can lead to absorbers with comparable electronic quality to one-stage CIS layers, several attempts have been carried out, by varying both composition and process temperatures. The results are summarized in figure 4.17, which gives an overview of the QFLS of the most representative samples grown in the framework of this work.

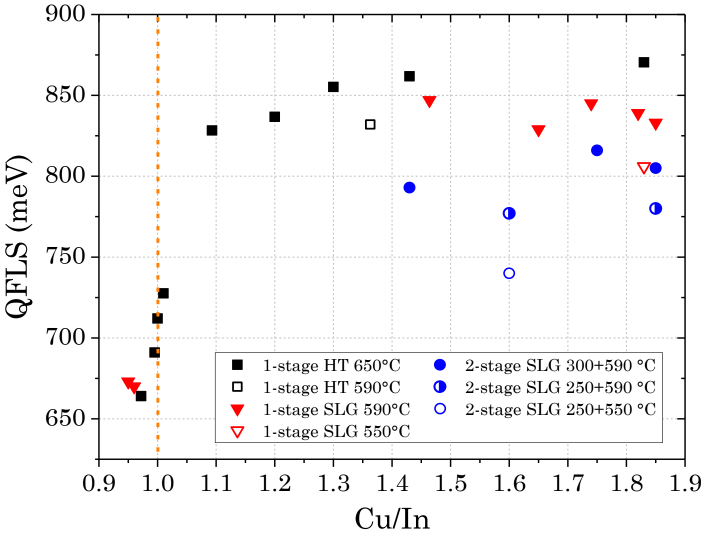

Figure 4.17: Quasi Fermi level splitting measured at an equivalent illumination of 1 sun plotted over the Cu/In ratio for several $CuInS_2$ absorber layers grown in the framework of this work. The composition has been measured on the as-grown samples before any kind of etching. Even if not explicitly reported, the glasses were all coated with the Mo back contact layer. The vertical dashed line (orange) separates the Cu-poor and Cu-rich region, respectively.

Beside the effect of the composition (Cu-poor vs Cu-rich), already discussed previously, the QFLS data for samples grown in Cu-rich regime on SLG confirm the trend observed in section 4.4. In the same way, by employing the same deposition process (e.g. one-stage on SLG at 590°C), a variation of the as-grown composition does not alter significantly the QFLS, at least for Cu-In ratios above 1.4. Additionally, the effect of employing the one- or the two-stage process to grow Cu-rich samples becomes obvious (considering the same final composition, for example

Cu/In about 1.8). Using the same final temperature as used for 1-stage process (in the present case 590 °C), the QFLS of the 2-stage samples can be improved by means of higher temperature during the first stage (from 250°C to 300°C in the plot). Still, the QFLS for these samples is lower than the corresponding value found for the 1-stage absorbers grown with the same Cu/In and deposition temperature of 590 °C. It is reasonable to assume that the QFLS could be improved by a further increment of the temperature of the first stage. Several attempts have been made in this work, for example using 350 °C as temperature of the first stage, but the electronic quality of the film decreases (there is a drop of the QFLS to values well below 800 meV) and in some cases the peeling of the absorber from molybdenum has been observed. Thus, samples grown following the 2-stage process seem to have intrinsically lower QFLS than those deposited in 1-stage process. Although they can both have the same final composition, the steps involved in the chalcopyrite film growth are different: in fact, during the second stage, the deposited film before turning into Cu-rich, goes through a Cu-poor regime, whereas 1-stage samples are always in Cu-rich regime. This might have consequences on formation energies of point defects, thus altering their final density in the absorber, as shown in Figure 4.8, which compares PL spectra measured at room temperature. It is evident, in fact, that the relative contribution of deep defect radiative transitions is higher in Cu-rich 2-stage absorbers than in Cu-rich 1-stage ones.

Having established that Cu-poor CIS layers have lower QFLS than Cu-rich ones and that within the Cu-rich regime, two-stage CIS absorbers have lower QFLS than one-stage ones, still the highest QFLS achieved in the framework of this thesis is about 875 meV (in the plot shown in the “1-stage HT 650 °C” series). With such QFLS, the deficit relative to the band gap (around 1.5 eV) still remains remarkable. To get a better view about these intrinsic limitations, figure 4.18 shows an overview of the quasi Fermi level splitting and open circuit voltage for several selenides and sulphides chalcopyrite absorbers and devices plotted over the corresponding band gap. A Cu(In,Ga)S$_2$ (CIGS) deposited in the framework of this work (band gap around 1.6 eV) is also included, together with another CIGS (band gap 1.7 eV) provided by Sudhanshu Shukla. Both CIGS samples have been deposited by 1-stage process and do not have any intentional band gap (gallium) gradient towards the back surface.

The main observation is the lower QFLS deficit (compared to the Shockley-Queisser limit) in low band-gap selenides than in sulphides absorbers, which explains the better performances of devices based on selenides. By way of example, the best QFLS achieved in this work lays just above the 0.4 eV-deficit guide line, whereas the Cu-poor CISe (open triangle at the extreme left with band gap 0.97 eV) has a deficit around 0.25 eV. By widening the band gap with Ga alloying, thus lowering back contact recombination through band gap gradient, the deficit in CIGSe is further reduced to values well below 0.2 eV. On the other hand, even the highest ever reported V_{OC} for sulphides (973 mV [144], with band gap gradient) presents a deficit of more than 0.3 eV, although the QFLS-deficit of the corresponding absorber, which is unknown, might be slightly lower. The QFLS-deficit of the Cu(In,Ga)S$_2$ samples (Cu-rich and Cu-poor with the band gap around 1.6 eV and 1.7 eV, respectively) is roughly unchanged compared to their corresponding pure CuInS$_2$ absorbers.

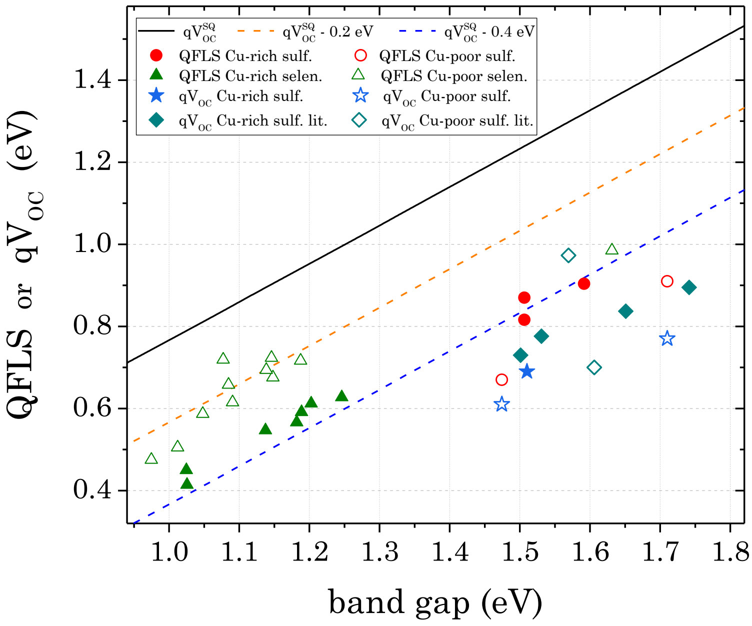

Figure 4.18: Quasi Fermi level splitting (QFLS) or open circuit voltage (V_{OC}) of several chalcopyrite absorbers and devices. For all the samples, data reported with an open symbol refer to Cu poor samples (absorbers or devices based on them) while full symbols refer to Cu-rich samples. The black line represents the Shockley-Queisser limit (determined assuming a back reflector) as a function of the band gap, which is also reported with a deficit of 0.2 eV (orange dashed line) and 0.4 eV (blue dashed line) as guides. The V_{OC} lit. data for sulphides samples are taken from [101], [144] and [140]. The selenides data represent samples grown and/or measured in-house (data provided by Finn Babbe, Florian Ehre and Max H. Wolter, reported partially in [135], [90] and in [145]): the best of these QFLS data, 0.719 eV, leads for the corresponding solar cell device an efficiency above 20.0 %.

The open symbols in figure 4.18 refer to Cu-poor samples, whereas the full symbols to Cu-rich ones. The different trend between the two kinds of chalcopyrite is clear, as already discussed previously: for selenides, Cu-poor absorbers have higher QFLS than Cu-rich ones, whereas for sulphides there is an opposite behaviour. The trend observed for selenides has been discussed in [90] where, by comparing experimental evidences to the previously reported theoretical calculations, the second charge state of Cu_{In} acceptor defect has been proposed as main cause for the higher loss in Cu-rich CIGSe. High band gap selenides (in the plot, for simplicity, only one example is reported, with a band gap of about 1.63 eV) show high deficit as well, comparable to the sulphides, which is likely caused by the deep donor Ga_{Cu}. This deep donor acts as a major recombination center both in Cu-rich and Cu-poor CGSe and CIGSe with high gallium content [89, 90]. A deep donor will be tentatively proposed in chapter 5 for CuInS$_2$ too, as possible origin of the deep broad band observed in room temperature PL spectra with maximum at around 1 eV.

A similarity between selenides and sulphides is found, instead, in the lowering of band gaps as the materials are grown in Cu-poor regime. As stated in section 4.3 (see figure 4.8 or 4.11), for pure CuInS$_2$, the band gap decreases by 30-40 meV when the composition of the absorbers has a Cu/In of about 0.95. It is worth noting that the GGI used to grow the CIGS with a band gap of about 1.6 eV is similar to the front GGI reported in [144] where the highest ever reported V_{OC} for sulphides (973 mV) is shown. Although they have the same GGI, they show a dissimilar band gap: around 1.6 eV for the Cu-rich CIGS grown in the framework of this thesis, while the record device is based on a Cu-poor absorber with band gap close to 1.57 eV. This difference (in the range of 30 meV) is likely due to the composition of the as-grown absorbers (Cu-rich and Cu-poor, respectively).

Few words about the highest Voc achieved in Cu(In,Ga)S$_2$. Similar high open circuit voltages have been reached by the same group in [27] and [26], leading to the current champion device with a power conversion efficiency of 15.5 %. These Voc values well above 900 mV definitively show a remarkable improvement in the electronic quality compared to the other sulphides data reported in figure 4.18, both those related to the results of this thesis and those found in literature. This gap might be caused by a combination of different factors. Firstly, the QFLS data measured in this work refer to either pure CIS or CIGS without intentional band gap gradient. As clearly visible for the Cu-poor CIGSe series depicted in the plot, the Ga alloying (with band gap gradient) has a significant beneficial effect on the QFLS of the corresponding absorbers, bringing a reduction of the QFLS deficit from about 0.27 eV to about 0.2 eV. Secondly, the substrate used plays a role, as shown in section 4.4, where the lack of sodium diffusion from the HT glass into the absorber during the deposition has been identified as one of the possible causes that hinders an improvement in Cu-poor sample when very high substrate temperatures are used. At the moment, there is no information available about the specific glass (and its composition) used to replace the standard SLG to deposit the CIGS layers that give the current record efficiencies.

Finally, the process employed in this work is totally different than the one used to fabricate the champion absorbers, where a very fast rapid thermal annealing (RTA) in H_2S atmosphere is used, with ramp-up speeds and annealing temperatures as high as 140 °C/min and 675 °C, respectively. These growth conditions, together with the annealing gas H_2S which likely leads to a different chalcogenide reactivity compared to the elemental sulphur used in this work, might drastically change the formation energies of point defects, altering their concentration and therefore the final electronic structure.

4.6 Summary quasi Fermi level splitting of CIS absorber layers

In this chapter the effect of both deposition temperature and composition on the optoelectronic quality of CIS absorbers has been shown, mainly investigated in terms of quasi Fermi level splitting. The QFLS measurements have been performed directly on bare absorbers to avoid any influence of buffer layer deposition. In fact, the air exposure barely affects the QFLS in time scales of minutes or hours. This dissimilar behaviour compared to experimental evidence found for selenium-based chalcopyrite is partially explained by the lower driving force of the oxidation process which takes place at the surface. The effect of the buffer layer deposition is different as well, as it does not act as passivation layer like for selenides, but it actually lowers the QFLS: this observation could be explained by a possible increment of the interface recombination or by a lower doping in the bulk of the absorber after buffer layer deposition. In addition, the QFLS of absorbers coated with buffer layers degrade with time.

The increase in process temperature is beneficial for the optoelectronic quality of absorbers deposited on Mo-coated SLG, as confirmed by QFLS values, independent of the composition. Cu-rich $CuInS_2$ films show higher QFLS than Cu-poor ones, which is in contrast to the observations on selenide chalcopyrites, even taking into account the lower band gaps for Cu-poor $CuInS_2$ or different Cu/In ratios in Cu-rich regime. The electronic structure is improved with higher deposition temperature by reducing the density of deep defects, particularly the one that is responsible for the PL band at around 0.8 eV. This deep defect is the main responsible for the limitation of the QFLS for the CIS layers investigated in this work. It is reasonable to assume that higher QFLS will be achieved by decreasing the deep defect responsible of the 1.05 eV band only once the deeper defect is reduced sufficiently.

The use of very high temperature for the absorber growth (650 °C) induces a further improvement in QFLS for samples deposited under Cu-excess, whereas those grown in Cu-poor regime do not show any enhancement. This last observation can be explained by the lower sodium diffusion into the samples if HT glass is used, due to its different chemical composition compared to the standard SLG.

The higher QFLS in Cu-rich samples do not necessarily translate into higher open circuit voltages: the devices based on 1-stage Cu-rich absorbers are usually dominated by low shunting resistance, due essentially to their morphology, while devices based on 2-stage Cu-rich absorbers show a huge deficit between QFLS and V_{OC}. This deficit is mainly due to interface recombination and can be partially reduced by modifying the buffer layer deposition, which leads to an increment in the open circuit voltage.

Two-stage Cu-rich absorbers, which are preferred for device fabrication, show systematically lower QFLS than one-stage Cu-rich layers: this has been related to the specific process employed, that in the first case includes a transition from Cu-poor to Cu-rich composition and that likely modifies the concentration of point defects in the final films.

The overview of the QFLS between the selenides and sulphides systems highlights the intrinsic lower electronic quality of the latter one, which translates into lower efficiencies of pure-sulphide based solar cells. Therefore, better performances for $Cu(In,Ga)S_2$-based solar cells can be achieved by improving the interface recombination and, above all, by a significant enhancement of the bulk material quality, which the QLFS is an indicator of.

Chapter 5

Defects in $CuInS_2$ absorber layers

In chapter 4, the effect of the process temperatures and composition of the thin films have been discussed, particularly in terms of a specific optoelectronic parameter, which is the quasi Fermi level splitting.

This chapter will rather be focused on the analysis and characterization (mostly by low temperature photoluminescence spectroscopy) of electronic defect states in $CuInS_2$ thin films. The first part will discuss the band edge emission as a function of the Cu/In ratio for the same series of absorbers deposited on HT glass analysed in chapter 4. Then, the effect of sodium precursor (in the CIS growth) on the electronic structure will be analysed, revealing the existence of an additional shallow acceptor defect. In the last part a brief discussion and analysis of the deeper bands (centered at around 1 eV and 1.25 eV) will be given, together with preliminary insights about their origin. Finally a revised model of electronic defects will be proposed, with a comparison to previous models emerged in the past from both experiments and theoretical calculations (as illustrated in section 2.6). Throughout the chapter and in the final model, some parallelisms with the closely related $CuInSe_2$ or $CuGaSe_2$ systems and their point defects will be presented.

All measurements reported in this chapter are performed on KCN-etched absorbers (if not otherwise specified) to remove oxides or any secondary phases formed during the growth: a weak etching has been used for samples showing a Cu/In < 1, while a strong etching has been used for Cu-rich ones, thus with Cu/In > 1. All reported Cu/In ratios refer to the compositions of the as-grown samples, determined by EDX spectroscopy.

Some of the results presented in the following are published in [146] or will be published in [147].

5.1 Near band edge photoluminescence of CIS

In this section one-stage $CuInS_2$ thin films deposited on Mo-coated HT glass at deposition temperature of 650 °C are investigated. The series of samples analysed in the following is the same considered for QFLS evaluation, which has been studied in chapter 4 (see figure 4.15). Thus, in the first place, the effect of the as-grown composition of $CuInS_2$ thin films on the shallow defect structure is discussed. Figure 5.1 shows an overview of the PL spectra for absorber layers with varying Cu/In measured with the same excitation intensity. It is important to underline that those Cu/In values refer to the as-grown compositions of the samples, including both the chalcopyrite and the Cu_2S secondary phase [33], which forms for Cu-rich compositions. On the other hand, the PL measurements have been performed after KCN etching, which selectively removes the secondary phase [34], as shown also in chapter 3. Thus any radiative transitions observed by means of low temperature PL spectroscopy are characteristic of the chalcopyrite phase (excitonic or defect-related lines), hence they are not due to the presence of additional phases in the samples investigated.

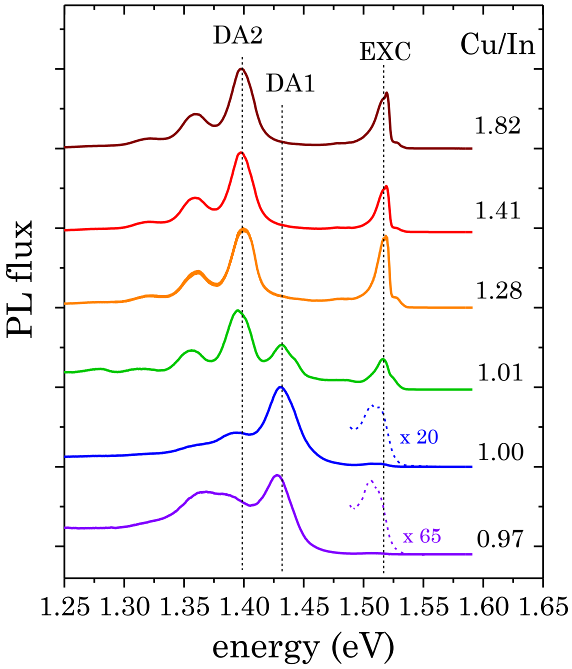

Figure 5.1: Photoluminescence spectra of $CuInS_2$ thin films with different compositions (indicated with Cu/In) measured at 10 K. The main transitions are highlighted with vertical dashed lines and labelled with EXC (excitonic) and DA1 and DA2 (donor-acceptor) transitions, respectively. The excitonic luminescence for the two samples with the lowest Cu/In ratio is magnified for a better visibility.

Figure 5.1 shows the following trend: at high Cu-excess (Cu/In > 1.2) there is a strong band edge emissions around 1.52 eV together with a peak at 1.39 eV followed by other peaks at lower energies with lower intensities; for low Cu-excess, the transition at 1.43 eV appears and becomes the dominant one and the band edge emission is much lower in intensity compared to the donor-acceptor transitions at 1.39 eV and 1.43 eV (in the plot, in fact, it has been magnified for a better visibility). In the next two sub-sections, firstly the band edge emissions will be discussed (i.e.

the excitonic transitions) together with the band gap dependence on the composition, then the donor-acceptor transition, explaining the labelling given for DA1 and DA2, respectively.

5.1.1 Band edge emissions

The band edge emission will be discussed using the data of the sample with Cu/In ratio of 1.8 as it shows the highest intensity and the best-resolved emissions, thus it allows both a more precise determination of the energetic position of the emissions lines and a wider range of excitation intensities. Figure 5.2 reports these emissions measured at different excitation intensities.

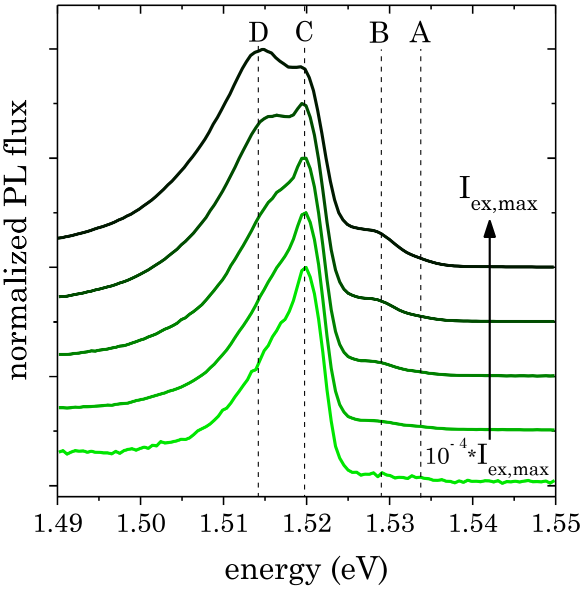

Figure 5.2: intensity dependence (over about four orders of magnitude) of the band edge photoluminescence spectra measured at 10 K on the sample with a Cu/In of 1.8. The spectra have been normalized and shifted in intensity for a better visualization. The vertical dashed lines mark the energies of the different emissions (A, B, C and D).

The first clear feature is that they do not show any peak shift with different excitations over four orders of magnitude, thus, as explained in section 2.5.1, they cannot be interpreted as donor-acceptor transitions [56], as the Coulomb contribution would lead a blue shift for higher excitation intensity. At this low temperature they are either excitonic lines or free-to-bound transitions of shallow defects [56]. Four different transitions are identified, at 1.534 eV (A), 1.528 eV (B), 1.520 eV (C) and 1.514 eV (D), which are also highlighted with vertical dashed lines in the aforementioned plot. Except for the line C, the identification of the other energy positions it is not straightforward as the peaks are not well resolved. For this purpose, the same sample has been measured with the same experimental conditions and PL setup but with two different fibers, used to collect the photoluminescence signal, which is then spectrally resolved by the monochromator (as schematically illustrated in section 2.5.3). Particularly, figure 5.3 illustrates the comparison of the photoluminescence spectra measured on the same sample with Cu/In of 1.8 and same excitation intensity, but with a fiber of 200 µm and 25 µm, respectively (these values refer to the core diameter of the corresponding fibers). The use of a smaller fiber, although decreasing the signal to noise ratio, improves the resolution. The spectra are shown as raw data, thus represented as normalized PL intensity (in counts) in dependence of the wavelength (in nm). This choice is justified by two aspects: firstly, the spectral correction would be the same for both, without altering the lines positions (the lower diameter only attenuates the PL signal); secondly and above all, the PL signal acquired with the thinner fiber would appear more noisy just due to higher noise in the measurement of the reference lamp spectrum used to spectrally correct the spectrum, thus leading to a higher error in the identification of the line positions.

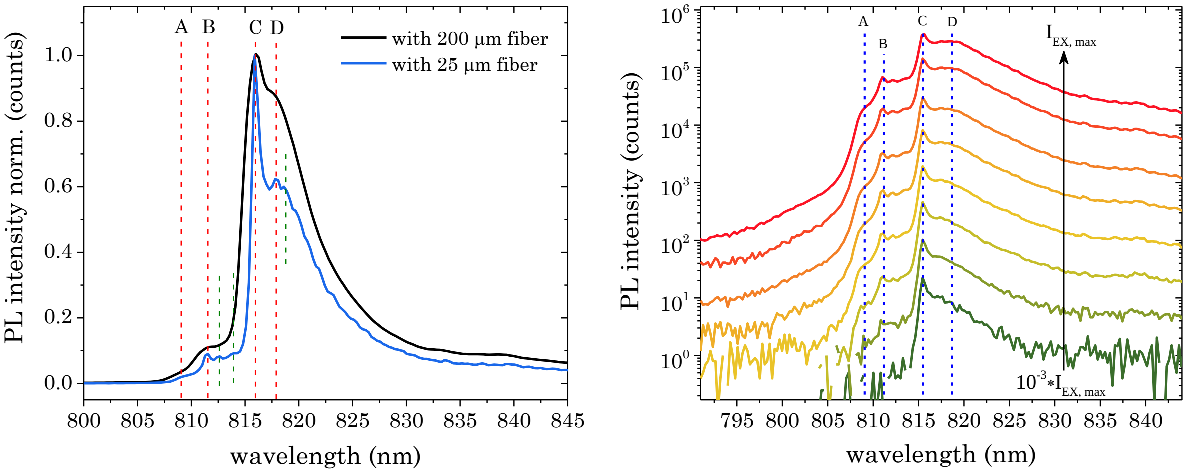

Figure 5.3: (left) comparison of the PL intensity raw data of the same sample with a Cu/In ratio of 1.8 acquired using the same excitation intensity but different fibers to collect the signal (with a core diameter of 200 and 25 μm, respectively); note that the y-axis is in linear scale and the PL intensities have been normalized to the 815 nm line. (right) excitation intensity dependence (over about three orders of magnitude) of the band edge photoluminescence spectra ot the sample with a Cu/In of 1.8 measured at 10 K with the 25 μm fiber, which allows a more precise energy lines identification. The energy positions are marked with dashed blue lines. Note that the y-axis is in log scale.

The spectrum measured with a lower core diameter fiber shows obviously a better resolution. The different relative intensity ratio between the lines in the two spectra reported in the comparison (figure 5.3) might be due to a slight different spot analyzed on the same sample. The energy position of the line C is clear, and it is 815.6 nm, as determined from the PL peak maximum. The energy position of the line A has been determined from the spectra acquired at intermediate excitation intensities: in fact, as seen from figure 5.3(right), for high excitation intensities the line A appears as a shoulder of line B, whereas for intermediate ones it is slightly better resolved and has a position around 808.5 nm: the intensity ratio change between the two lines is given by the different *k* factor, as will be discussed shortly. The spectra measured with the lowest excitation intensities cannot be used to determine the energy position of the transition A as its intensity is comparable with the background noise. With the higher resolution, the determination of the energy positions for line B and D becomes more complex: for both, as is seen from figure 5.3(left), there are some additional small peaks at higher wavelengths (marked with dashed green lines). Whether these peaks are effectively additional excitonic lines or just given by the lower signal to noise ratio (unavoidable characteristic feature of the spectrum acquired with the 25 μm fiber), cannot be discerned with the present data. Additionally, the analysis of the excitation intensity dependence in terms of power laws has been performed on the PL spectra acquired with the 200 μm fiber, which allows more collection of the PL signal, thus a wider range of investigation. Figure 5.3(left) shows that in the spectrum acquired with the 200 μm fiber, the multiple peaks for line B and D convolute both in broader bands. Therefore, for the following analysis, only two bands will be considered, centered at around 811.2 nm and 817.5 nm, respectively, as indicated by the red dashed lines in the plot. Table 5.1 reports the energy positions of the four lines identified so far, expressed both in wavelength and in energy (the last values already mentioned previously and marked in figure 5.2).

Table 5.1: energy position of the band edge emissions determined from the PL spectra measured at 10 K with a core diameter fiber of 25 μm as reported in figure 5.3.

Line	Position (nm)	Position (eV)
A	808.5	1.534
B	811.2	1.528
C	815.6	1.520
D	818.5	1.514

Figure 5.4(a) reports the PL integrated flux (I_{PL}) of these transitions as a function of the excitation intensity (I_{ex}) in a double logarithmic plot. Excitons should follow a power law as $I_{PL} \sim (I_{ex})^k$ with a super-linear behavior [69], i.e. with $k > 1$. The corresponding exponents for each transition, determined over about four orders of magnitude in excitation intensity, are reported as well in the plot.

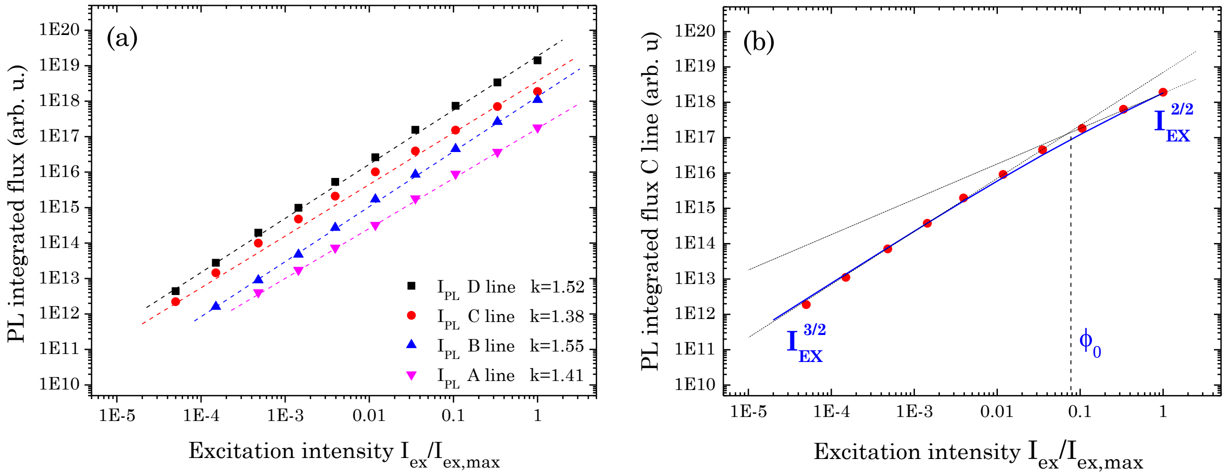

Figure 5.4. (a) Excitation intensity dependence of the integrated PL flux of the four band edge emissions taken from the sample with a Cu/In ratio of 1.8, with the corresponding *k* values obtained by fitting the trends with a single power law; (b) trend of the 1.520 eV emission (line C) together with 2 power laws with a k value of 3/2 and 2/2, respectively. Φ_0 indicates the excitation threshold. $I_{ex,max}$ is about 10^4 mW/cm^2, which correspond to a flux of about 6.7×10^{19} /(cm^2 × s).

All exponents are close to 3/2. The higher *k* exponent for the B line compared to the A line is the reason why the last one gets slightly more resolved at low excitation in figure 5.3: in other words, for lower excitation the B line integrated flux decreases faster than the A one. The emission D (1.514 eV), B (1.528 eV) and A (1.534 eV) are well described by a single power law. The C line (1.520 eV) however, does not show a straight line in the log-log plot, although it can be fitted by a single power law with exponent 1.38. Figure 5.4(b), in fact, shows that its trend might be well fitted as a combination of two power laws, with exponents of 3/2 and 2/2, respectively. Equation 2.5.18 has been used to fit the transitions between different exponents, with a crossover excitation Φ_0 found to be close to 8×10^{-2} $I_{ex,max}$.

For low excitation, the trend observed for the C line has a single power law behaviour with exponent k_{low} = 3/2, while at high excitation the power law exponent converges to k_{high} = 1. Referring to table 2.1 in section 2.5.1, the behaviour measured for the line C is best explained by a free-to-bound transition; the change of the power law exponent (from to 3/2 to 1) is due to the saturation (for excitations close to the crossover point) of either a shallow defect or a deep level in a competing recombination path [68]. An exciton, in fact, according to the model discussed in [68] and reported in table 2.1, can switch from exponent 4/2 (at low excitation) to 3/2 (at mid excitation) to 1 (at high excitation) when a competing defect related transition saturates. This would, however, affect all excitonic transitions (both free and bound ones), which is not what is observed in figure 5.4. A donor-acceptor pair transition would be an alternative option as it also shows the same switch (from 3/2 to 1), when one of the shallow defects involved in the emission or a competing deep defect (i.e. from (a) to (c) or from (a) to (b) case, as shown in table 2.1) saturates. It can, however, clearly be excluded that transition C is a DA transition, because it shows no blue shift with increasing excitation (see figure 5.2 or 5.3). Consequently, the line C is attributed to a free-to-bound transition. This FB emission is attributed to a shallow donor, as discussed in the following.

The A line (1.534 eV) has been attributed in the past to the recombination of free exciton [62]. The attribution of this line to a free exciton in ref. [62] is due to it being the line with the highest photon energy (as the bound excitons, given their higher total binding energies, emit necessarily at lower energies). Moreover in ref [62], the temperature dependent analysis of the band edge emissions reveal a faster quenching of the lines at lower energies, which in turn can be explained considering that the additional binding energy for binding an exciton to a center (donor or acceptor, neutral or ionized) is smaller than the free exciton dissociation energy. A further confirmation of this attribution is reported in ref. [61], where the authors could measure, for high quality single crystal, the peak related to the free exciton (at 1.5355 eV) together with the first (n = 2) and second excited state (n = 3) of the free exciton, with all the three relative intensities following the n^{-3} rule, typical of the excited state of the free exciton. For CuInS$_2$, as discussed in section 2.5, a binding energy of about 20 meV has been reported for free exciton, determined both by the analysis of the quenching of the emission intensity [62] and by comparison of the first and second excited states of the free exciton [61]. Adding this ionization energy to the emission energy of the A-line, a band gap of 1.554 eV at 10 K can be determined. This value matches well those reported in literature [61, 62, 148]. The power law exponent of the free excitonic emission approaches 3/2 (see figure 5.4a). The investigation for this emission line has been conducted for a narrower excitation range (compared to the other lines) because of its low luminescence flux at very low excitation intensities. The analysis of this line, in fact, is the most affected one by the background noise of the PL setup. In annex, figure A5.1 displays the log-log plot of the free exciton emission (line A) obtained taking into consideration this background, which mostly influence the data analysed at low excitation (lowering them along the PL flux-axis). In this way, a *k* value of 1.46 is obtained from the fitting with a single power law. The trend of the other lines is not affected by the background noise. Within the range of excitation intensities investigated, no crossover point is observed for the free excitonic line. Referring to table 2.1 in section 2.5.1, this might be explained by saturation of the deep level (in a competing recombination channel), i.e. from (c) to (d) case, that does not translate in a change of the power law exponent.

Concerning the other two lines, B and D, they have been attributed in the past to bound excitons [62]. Although their analysis extends over a wider excitation intensity range, they do not show a crossover excitation as well, and they can be well fitted by single power law with an exponent close to 3/2, which is the same value found for the free exciton line. As explained in section 2.5.1, the *k* values related to bound excitonic emissions are typically higher compared to the *k* value of the free exciton line, as they include an additional term due to density of the defect to which the exciton is bound. Given the absence of crossover excitations and similar *k* values between line A, B and D, the experimental trends observed for the excitonic lines can be explained assuming that the defect(s) to which these excitons are bound is(are) saturated. In these conditions, the *k* values of bound excitons transitions equal the *k* value of the free exciton emission.

By using Hayne's rule (equations 2.5.14 and 2.5.15), it is possible to correlate the bound exciton emission energies to the activation energy of the corresponding donor or acceptor [63, 65, 66, 149, 150] (considering the band gap of 1.554 eV above determined).

Table 5.2 summarizes all calculations. The uncertainty of the band gap value and of the spectral positions of the two lines gives rise to the errors for the activation energies. Caution has to be taken in comparing the activation energies listed in table 5.2 with those reported in literature [62, 148] (estimated from bound excitonic emissions as well). In fact, the number of excitons observed strongly depends on the crystal quality of the samples investigated and on the experimental setup used to measure and resolve the lines. Typically, single crystals have lower PL emission linewidths than polycrystalline samples. In [62] and [148], three bound excitons have been observed, at 1.513 eV, 1.516 eV and 1.518 eV, which likely merge in the PL spectrum of sample analysed in this work to the 1.514 eV emission. Similarly, while in the present work only one excitonic emission has been identified close to 1.528 eV, in [62] two excitonic lines have been measured, at 1.525 eV and 1.530 eV, respectively, whereas in [148] three lines have been observed at 1.525 eV, 1.529 eV and 1.531 eV. These aspects make the comparison of the defect binding energies estimated (by using Hayne's rule) between different works (included the present one) not straightforward and generate the discrepancies in the obtained values. Still, a few considerations can be done. The emissions at 1.514 eV and 1.528 eV can be related to neutral donor at about 74 meV and to neutral donor at about 22 meV, respectively. These activation energies, within the error, are in line with the values found in [62] (i.e. 80 meV and 35 meV) associated to the 1.513 eV and 1.525 eV emissions, respectively. Nevertheless, it cannot be excluded that the emission line B belongs to a neutral acceptor with an energy of about 100 meV (as will be discussed in the following section 5.1.2) and the emission line D to an ionized donor with an energy of 38 meV. In addition, as reported in section 2.6 (about the defects review in

CuInS$_2$) an acceptor close to 300 meV from the valence band has been often found by admittance spectroscopy and DLTS. Therefore the attribution of the line D to this deep defect cannot be ruled out.

Table 5.2. Possible values of donor and acceptor activation energies (in meV) calculated using equations 2.5.14 and 2.5.15 for the emission lines B and D. The errors reported have been estimated assuming an uncertainty of ± 2 meV for both the band gap value and the spectral positions of the two lines.

Emission line	Emission energy (eV)	Exciton binding energy (meV)	Neutral donor	Ionized donor	Neutral acceptor	Ionized acceptor
B	1.528	26	22 ± 14	25 ± 4	100 ± 65	18 ± 3
D	1.514	40	74 ± 14	38 ± 4	335 ± 65	26 ± 3

Finally, analysing the PL flux as a function of the excitation intensity, the C line at 1.520 eV has been already ascribed to a free-to-bound (FB) transition of a shallow defect: an energy defect of 34 meV is derived as difference between the band gap energy and peak energy line. This defect has been attributed to a donor in the literature [62]. This shallow defect is most likely a donor because the electron effective mass in CuInS$_2$ is smaller than the hole one [67], leading to smaller activation energy for donor assuming the hydrogen model for shallow defects [150]. Within this model, the donor activation energy is estimated to be about 22 meV, while the acceptor one is about 175 meV. The activation energy of the donor will be further discussed in the following section 5.1.2.

Thus from the near band edge emissions, two lines have ben related to bound excitons (B and D), one to free excitonic emission (A), which leads to an estimation of the band gap of 1.554 eV at 10K, and the last one (C) to a FB emission, that belongs to a donor defect with an energy about 34 meV.

It is worth mentioning that for all samples grown with different compositions, shown in figure 5.1, similar transitions have been observed, although less well resolved; the C line appears always as the most visible transition. The samples with the lowest Cu/In ratios (1.00 and 0.97) show excitonic lines at lower energies: even though at first sight they can be interpreted as new bound exciton and/or new free-to-bound transitions, they are actually the same lines analysed so far, but with a shift to lower energies. This observation can be explained by a lower band gap of the corresponding samples. Figure 5.5 compares the band gap luminescence of the samples with Cu/In 1.82 and 1.00 measured at different temperatures. The latter always shows a shift to lower energy of 8 meV, thus indicating a corresponding band gap of about 1.546 eV at 10K. It has been already discussed in the previous chapter (section 4.3) that CuInS$_2$ thin films grown in Cu-poor conditions exhibit a lower band gap than those deposited under Cu-excess (similar to CuInSe$_2$ [134]). Thus it is reasonable to assume that absorbers deposited with a metal ratio close to stoichiometry display already a lowering of the band gap (in this case roughly 8 meV).

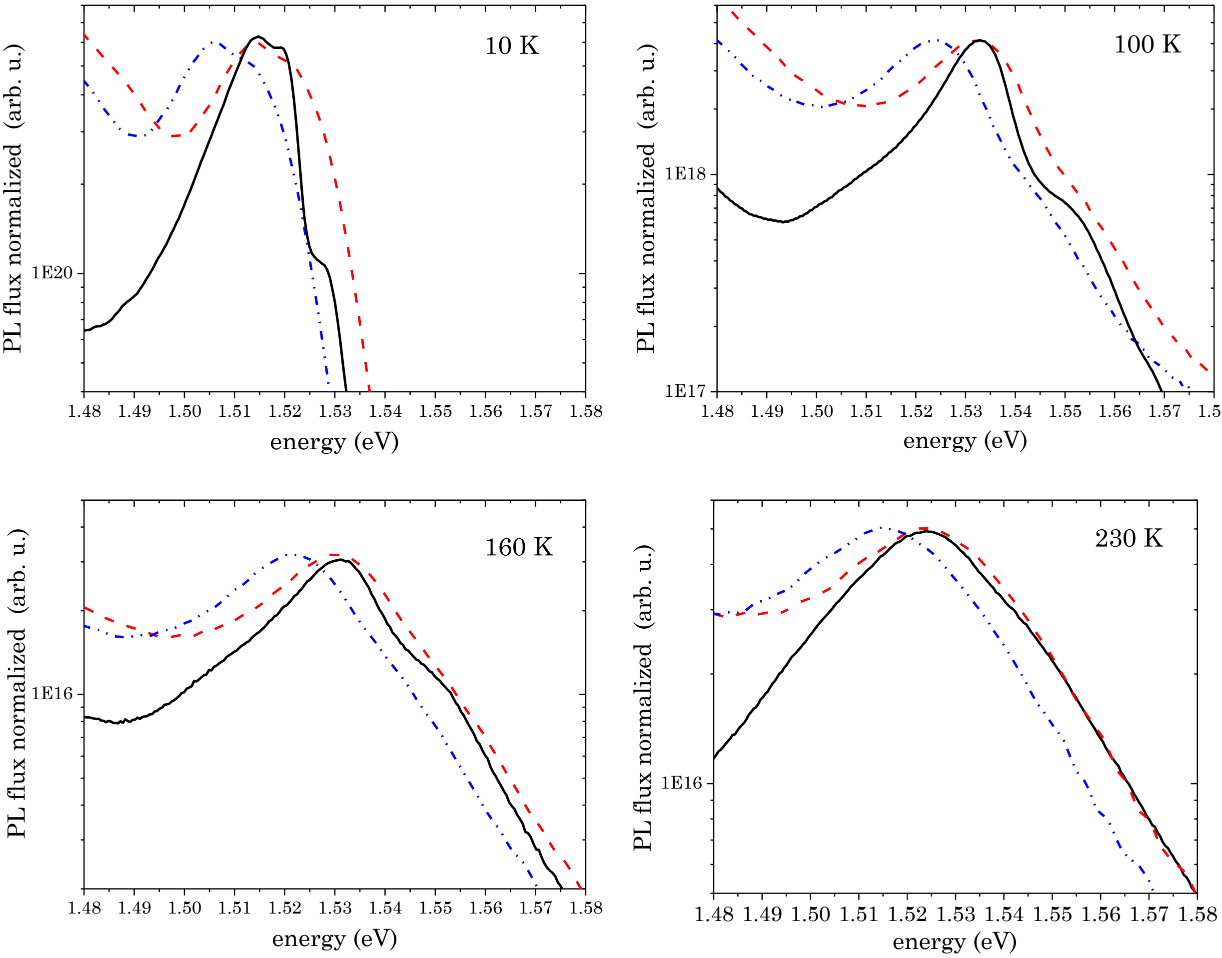

Figure 5.5: photoluminescence spectra measured at different temperatures (10-230 K) of $CuInS_2$ with Cu/In 1.83 (solid line) and Cu/In 1.00 (dashed dotted line). The spectra of the sample with Cu/In ratio of 1.00 have been plotted also with a shift of 8meV to higher energies (red dashed line). The overlapping, more visible for the high energy wing of the band edge luminescence at higher temperature, confirms the difference in energy gap of about 8 meV between the two samples considered in this comparison.

The band gap values determined for the two samples (with Cu/In 1.8 and 1, respectively) will be crucial for an accurate determination of the activation energies of the defects involved in DA1 and DA2 transitions, discussed in the next section. Additionally, these two transitions will be analysed also as a function of the temperature to convert them into free-to-bound transitions. Therefore, it is essential as well to determine the band gaps at those higher temperatures. In the present case, the interest is focused on the band gap values in the range of 80 - 90 K (the reason of this choice will be explained in the following section, where the DA transitions are discussed). Binsma *et al.* have already shown in ref. [62] that the band edge emission lines shift by the same amount in energy with temperature and their mutual positions (energy separations) remain unchanged; this is the indication that the shift is given by the temperature shift of the band gap.

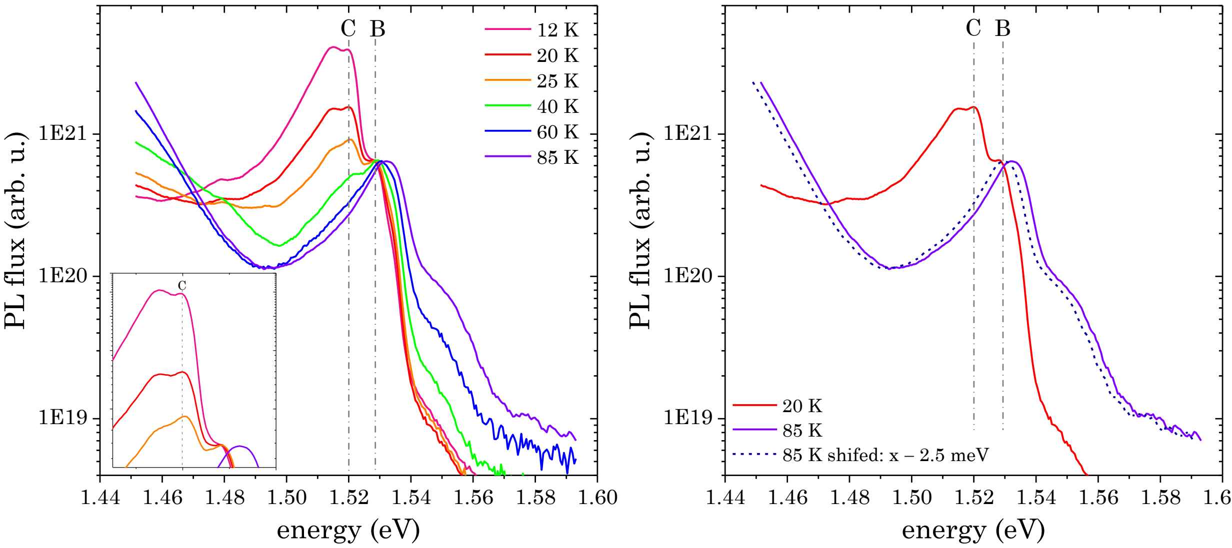

Figure 5.6: (left) temperature dependence of the band edge emission of the CIS sample with Cu/In 1.8. Highlighted the B and C lines as guides for the shift (the dashed dotted lines have been drawn at the spectral positions corresponding to the PL spectrum acquired at 12 K). The shift starts at around 25 K as it is pointed out by the inset that, for better view, reports only four spectra (12, 20, 25 and 85 K, respectively). (Right) comparison of the band edge emission acquired at 20 K and 85 K, together with the spectrum at 85 K plotted with a shift of 2.5 meV at lower energies.

A similar study has been carried out in this work on the sample with a Cu/In ratio of 1.8 (because, as mentioned previously, it shows the strongest and the best resolved peaks structure). Contrary to the work of Binsma *et al.*, the free exciton line is not well resolved, thus, as reference for the shift, the B and C line are considered, as their peaks are more visible. From figure 5.6, particularly form the inset, it can be seen (looking at the emission line C) the shift starts for temperatures above 20 K (the spectrum at 25 K already shows a slight shift to higher energies). As the quenching of the emission line C is faster than that of the B one, the last one is considered to compare the spectra at 20 K and 85 K, as reported in figure 5.6(right), hence the spectra are normalized to the intensity of this line. In the comparison, the spectrum at 20 K is considered because it does not show any shift compared to the one measured at 12 K, but additionally the B line is slightly more resolved, thus it is preferred for the shift evaluation. From the comparison, a shift of around 2.5 meV at higher energies (at 85 K) is found, in good agreement to what is reported in ref. [62]. Therefore it can be concluded that for CIS polycrystalline thin film investigated the band gap at 10 K is 1.554 eV, whereas in a range of 80-90 K it is about 1.556 eV. Assuming a similar shift for the sample grown with a Cu/In of 1, its band gap at 80-90 K can be assumed equal to 1.548 eV (i.e. 8 meV lower than the other one).

Summarizing this section, from the band edge analysis, four emissions are identified and correlated to a free exciton line, two bound-exciton lines and to a FB transition: a shallow donor at about 30 meV from the conduction band is responsible of this last emission.

5.1.2 Shallow defects: phonon coupling

In the previous section the band edge emission has been discussed; this section will be rather focused on the donor-acceptor transitions, DA1 and DA2, as already shown in figure 5.1. Figure 5.7 shows particularly the low temperature PL spectra in the spectral range 1.2-1.5 eV: the DA1 transition dominates the PL spectrum of the CIS sample with Cu/In ratio 1.0, while the DA2 emission line dominates the PL spectrum of the CIS sample with an as-grown composition of 1.8.

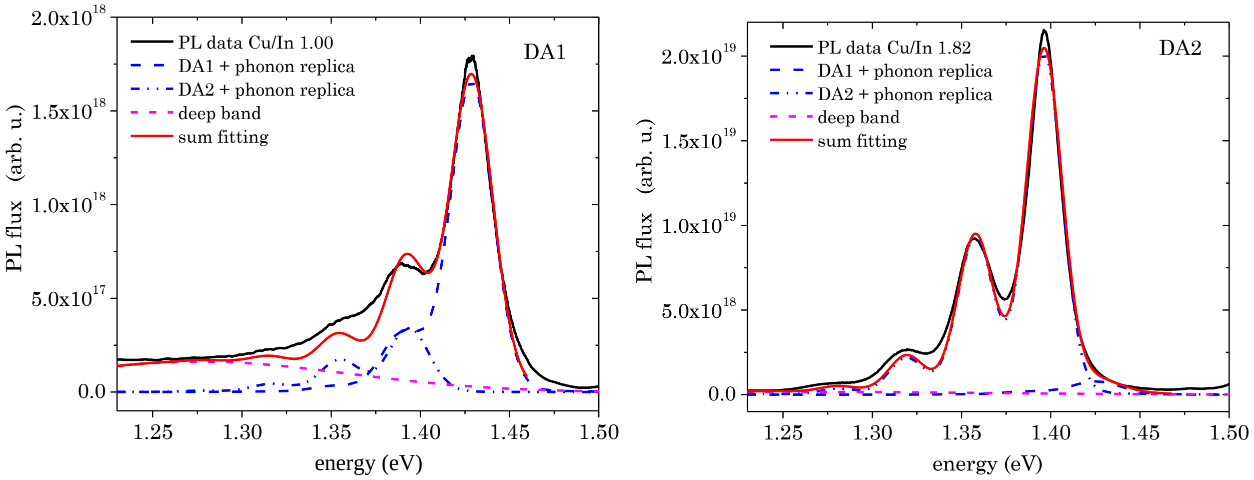

Figure 5.7: Measured photoluminescence spectra at 10 K (black) of $CuInS_2$ thin film with Cu/In (left) 1.00 and (right) 1.83. Both spectra are fitted reasonably well with a Huang-Rhys spectrum of the DA1 and the DA2 plus a contribution of an additional deep emission (purple dotted line). The various peaks are fitted with a Gaussian profile.

It is clear that in both cases the main peak is followed by other transitions at lower energies with lower intensities. These emissions are attributed to phonon replicas. Three arguments support this attribution:

I. the spectral spacing between two consecutive lines is about 39±1 meV (~315 cm^{-1}), the energy of one of the phonons characteristic of $CuInS_2$ [151], attributed in the past to (LO) mode (LO denotes the longitudinal optical mode) [151, 152].

II. the low energy peak positions follow the same trend as the main peaks, as a function of the excitation intensity and temperature (as shown in annex in figure A5.2);

III. they can be well fitted by a Huang-Rhys model, which describes the spectrum as a Poisson distribution of phonon replicas according to equation 2.5.21 as explained in section 2.5.2 [70].

The Huang-Rhys factor determined from the fit of the DA1 and DA2 transitions is about $S = 0.22\pm0.03$ and $S = 0.48\pm0.03$, respectively. The higher S factor found for the DA2 transition is expected: in fact, the Huang-Rhys factor describes the strength of the electron-phonon coupling for a particular defect and it is typically higher for deeper defect, as it should show a stronger electron – phonon coupling, because it is more localised [56].

As seen from figure 5.7, a third deeper band centered at about 1.25 eV is needed to fit well the low energy side of the PL spectra (this is more critical, and more visible, for the fitting of the PL spectrum of the sample with lower Cu content). A very similar emission has been reported in literature: in those previous studies the intensity of this emission was comparable to the one of the shallow transitions (that in this work are named DA1 and DA2) [77, 82]. This high intensity of the deep emission hid the phonon replicas with n > 1, and the first of the phonon replica (n = 1), if present, has been always attributed as an additional donor-acceptor transition (involving a deeper donor, as discussed in section 2.6).

For simplicity, the PL flux measured at lower energies (E < 1.35 eV), beside the phonon replicas, has been fitted with just one broad band with a peak close to 1.25 eV, which becomes clearly visible at higher temperature (T > 100 K): this deep band will be discussed in detail in section 5.4. On the other hand, the presence of additional shallow DA transitions cannot be ruled out, as they might be hidden by the main transitions (and their related phonon replicas) but still contribute to the PL flux at these low energies. In fact, in section 5.2, a third DA shallow transition will be discussed, which becomes clearly visible and dominates the near edge luminescence if a modified growth process (i.e. with NaF precursor) is used to deposit CIS absorbers. Nevertheless, the samples considered in this section to discuss DA1 and DA2 emissions are prepared without this additional precursor and the PL spectra are clearly dominated by the two DA transitions. Therefore, a possible contribution of the third DA transition can be neglected for the PL analysis of DA1 and DA2 lines.

Summarizing, all four peaks clearly visible in the energy range near DA1 and DA2 are attributed in each case to a single DA transition with its phonon replicas. Therefore, in the following, only the main transitions (DA1 and DA2) will be analysed and discussed, in terms of excitation intensity and temperature dependent photoluminescence.

5.1.3 Shallow defects: excitation and temperature dependence of DA1 and DA2

Figure 5.8 shows the excitation intensity dependence of the energy positions for the peak DA1 and DA2: both peaks shift to higher energies with excitation.

The blue shift of the peak position E_{PL} as a function of the excitation intensity is a mark of the donor-to-acceptor nature of these transitions [56]: in fact, as stated in section 2.5, increasing the excitation leads to a reduction of the average distance between the defects involved, thus a change in Coulomb energy, which in turn leads to a blue shift of E_{PL}. This blue shift as a function of excitation intensity can be described by the empirical equation 2.5.13. For the above mentioned peaks, a β factor of 3.8 meV and 3.0 meV per decade have been determined for DA1 and DA2, respectively, which is typical for donor-acceptor transitions in weakly compensated semiconductors [153].

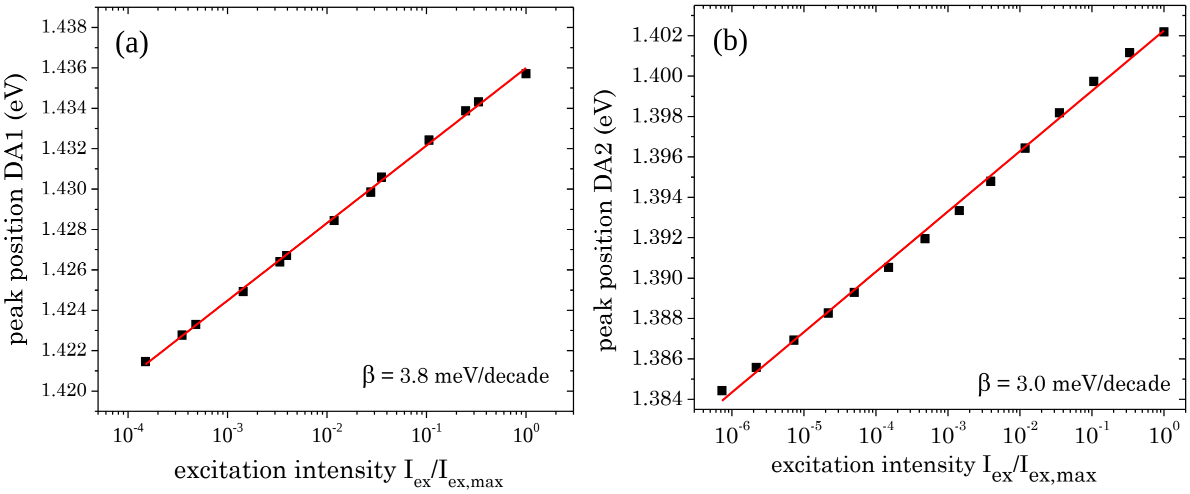

Figure 5.8: excitation intensity dependent energy position of the two DA transitions in $CuInS_2$ taken from the spectra of the samples with Cu/In ratio of (a) 1.00 and (b) 1.82. $I_{ex,max}$ is about 10^4 mW/cm^2.

Figure 5.9 reports, instead, the PL fluxes (I_{PL}) of these transitions as a function of the excitation intensity (I_{ex}) in a double logarithmic scale. The fitting performed using a single power law leads to a k value of 0.93 and 0.92 for DA1 and DA2, respectively. Nevertheless, as discussed in detail in section 2.5.1 and as mentioned before in the band edge section, the *k* value at low temperatures can take on only fixed values of multiples of *1/2*, and values different from *n/2* are just due to transitions regions between two limiting cases. Indeed, in both DA1 and DA2 case, the experimental trend can be fitted as a combination of multiple power laws, as shown in the figure 5.9. Equation 2.5.18 has been used as fitting function. While the data of DA1 is compatible with an exponent close to 1, the log-log plot of DA2 is clearly curved, changing the exponent from *1* to *1/2*. This happens when one of the defects involved in the DA transition, or in one of the competing recombination channel paths, saturates. Referring to table 2.1 (in section 2.5.1) with the overview of the power law exponents, the transition from 1 to 1/2 for a donor-acceptor transition occurs when either the shallow acceptor becomes saturated (i.e. (b) to (d) case) or the shallow donor saturates (i.e. (b) to (e) case) or, with shallow acceptor already saturated, when the deep level saturates as well (i.e. (c) to (d) case). It is worth noting that the crossover excitation Φ_2 for the DA2 transition occurs in the same range (~ 8×10^{-2}) of Φ_0, found previously for the FB transition (C line, Figure 5.4). This can be explained assuming that in both situations, i.e. FB (C line) and DA2 transition, the same defect becomes saturated. This defect might be involved in the transition itself or in a competing recombination channel. The saturation of this defect leads to the curved log-log plot observed for both FB1 and DA2 trend.

To determine the defects energies involved in the DA1 and DA2 transitions, temperature dependent measurements have been performed. Usually, with increasing temperature the shallower of the two defects involved in a DA transition is thermally emptied, leaving a free-to-bound (FB) emission.

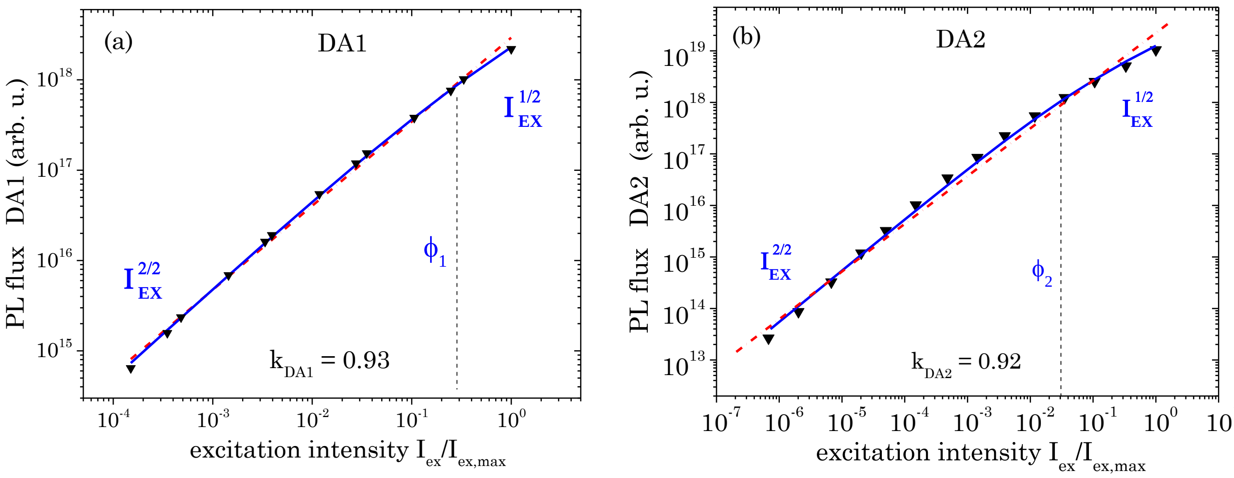

Figure 5.9: excitation intensity dependent intensity of the two DA transitions in $CuInS_2$ taken from the spectra of the samples with Cu/In ratio of (a) 1.00 and (b) 1.82. The dash-dotted lines represent the single power law fit, while the blue line the fit with multiple power laws. The corresponding k-values are reported as well. Φ1 and Φ2 indicate the excitation thresholds.

Figure A5.3 reports the case for the DA2 transition, which has been measured in a temperature range of 15 K – 90 K. Thus, the activation energies of the defects involved in each transition could be obtained by the analysis of the quenching of the corresponding transitions[153]. Nevertheless, this implies the integration of the emitted flux of the transition also at higher temperature (> 100 K) where the FB transition has a comparable intensity (or even much lower, as the temperature rises) of the deep band centered at around 1.25 eV. The influence of this deep band (in terms of intensity) is almost negligible at 10 K, as shown in figure 5.7, but it becomes relevant for higher temperature (see e.g. figure 5.10(a)); this, in turn, would lead an erroneous integration of the peaks under investigation, thus to not reliable activation energy values. For this reason, in this work, the binding energy of the defects involved in FB1 and FB2 are obtained directly from their peak position, following the equation 2.5.11. Therefore, in case of FB transitions, the peak position is excitation-independent due to the absence of the Coulomb contribution between the charged defects: this feature can be used to prove that the DA transition has become a FB emission.

Figure 5.10 reports the excitation intensity dependence PL flux of the two main transitions, at 80 K and 90 K, respectively. As can be seen, both do not shift with excitation intensity (over three orders of magnitude), which means the transition has become a free-to-bound emission at these temperatures and the shallower defect is thermally emptied: FB1 at 1.444 eV and FB2 at 1.411 eV. The lower temperature (80 K) for FB1 is needed because of the deeper band centered at around 1.25 eV: in fact, the intensity of this last band does not allow to fully resolve the peak of FB1 for higher temperatures. This issue, as said previously, makes the analysis of the quenching of the DA intensity very challenging. In section 5.1.1, the band gap values for both samples at these temperatures have been determined (1.548 eV and 1.556 eV, respectively). Therefore, from the energy difference between band gap and FB emission it is possible to obtain the defect energy involved in the two transitions: i.e. 104 ± 5 meV for the defect responsible of the FB1 emission and 145 ± 5 meV for the one responsible for the FB2 emission.

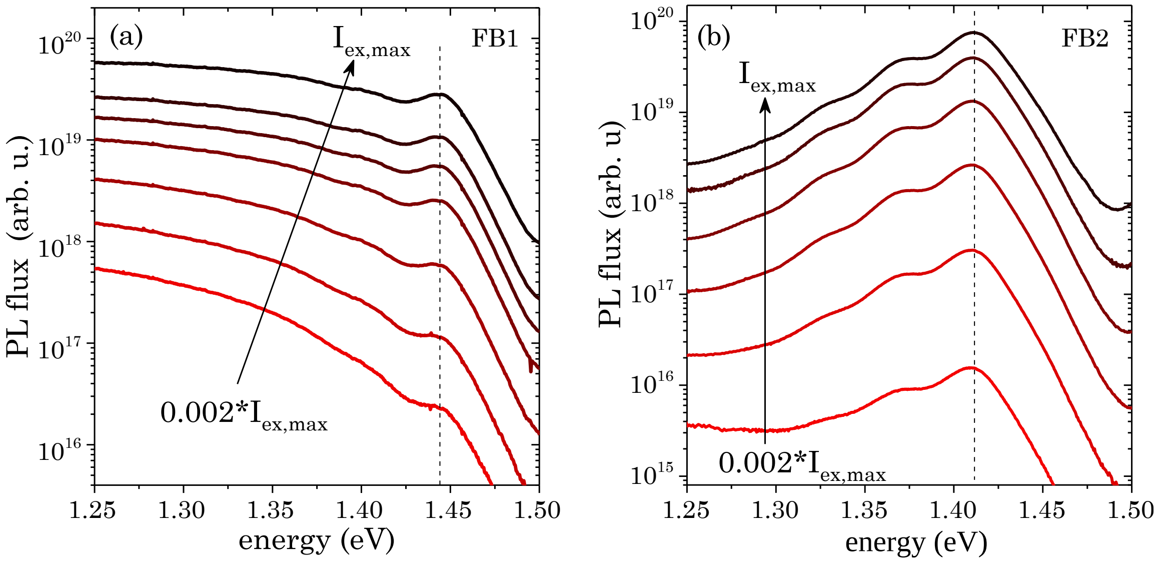

Figure 5.10: excitation intensity dependent spectra over three orders of magnitude of the two FB transitions in $CuInS_2$ taken from the spectra measured at 80 / 90 K of samples with Cu/In ratio of (a) 1.00 for FB1 and (b) 1.82 for FB2. The FB transitions are highlighted with dashed lines.

Having determined the activation energy of the defect responsible of the FB1 emission, which is close to 100 meV, it is now possible to take a step back to the attribution of the exciton B line (at about 1.528 eV). Firstly, it is worth noting that to fit properly the spectrum (figure 5.7) in which DA2 peak dominates, the DA1 peak is needed as well to fit the high energy wing (E > 1.40 eV): therefore, even if its intensity is much lower than DA2 one, the DA1 transition, thus the defects involved, is present also in very Cu-rich sample (in the present case Cu/In 1.8). This is a clear indication that the attribution of the bound excitonic B line (section 5.1.1) is not straightforward and, as already mentioned, it can actually be interpreted as bound exciton to neutral acceptor with energy about 100 meV. Binsma et al. in [62] ruled out this designation because they observed this excitonic emission (line B) in all compositions of the single crystals investigated, whereas the acceptor only in a particular range of composition: thus they related the B excitonic line to an exciton-neutral donor complex.

The presence of a defect with activation energy close to 145 meV in absorbers grown in Cu-rich conditions has been confirmed by admittance measurements performed both on $Mo/CuInS_2/Al$ and on $Mo/CuInS_2/Zn(O,S)/(i)ZnO/ZnO{:}Al/Ni/Al$ stacks, as reported in figure 5.11. In both cases, in the temperature range 100-180 K, a capacitance step has been found with activation energies of about 140-145 meV, that well matches the one found by PL investigation.

As mentioned in the previous chapters (Ch. 3 and Ch. 4), CIS absorbers grown under Cu-rich conditions have been deposited also following the two-stage process, because their final morphology is better suited for device fabrication. The defect with an activation energy of about 145 meV has been found by low temperature photoluminescence also in this kind of absorbers (as shown in figure A5.4), which therefore makes this defect a characteristic feature of Cu-rich CIS samples.

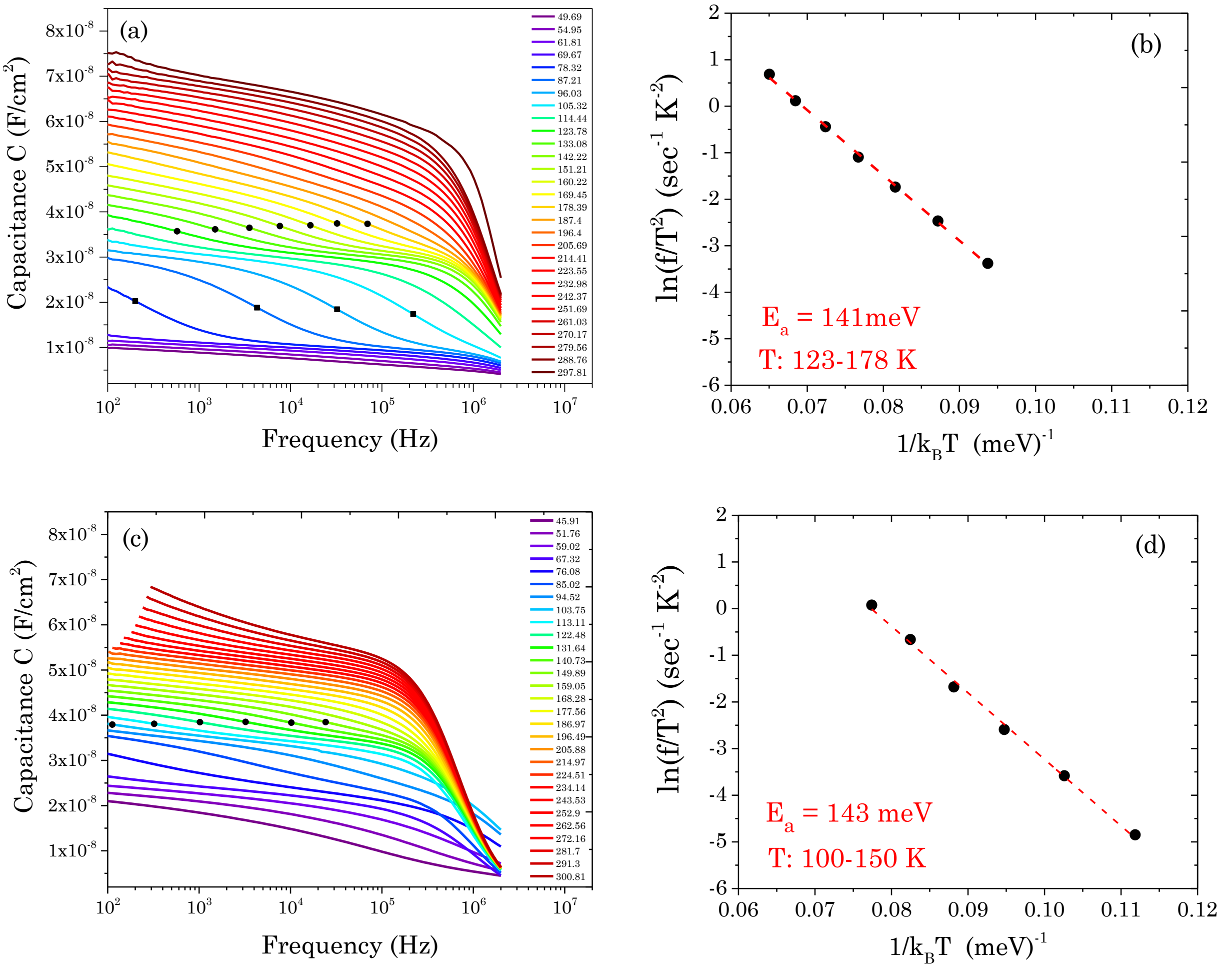

Figure 5.11: capacitance C plotted semi-logarithmically over the frequency for temperatures ranging from about 50 to 300 K for the (a) Mo/CuInS$_2$/Al and (c) Mo/CuInS$_2$/Zn(O,S)/(i)ZnO-AZO/Ni/Al stack; the inflection points of the main step are marked with black circles. In (b) and (d) the corresponding Arrhenius plot of the inflection points with the linear fit (dashed red line) to extract the activation energies, which are reported together with the temperature range. The CIS investigated in both cases has an as-grown Cu/In of 1.8. In (a), a second step is found, indicated with black squares: it will be discussed in the next section 5.2. Measurements performed by Mohit Sood.

With these two activation energies determined, together with the peak positions of DA1 and DA2 shown in figure 5.8, the activation energy of the shallower defect involved in both transitions can be determined. As discussed in equation 2.5.12, the peak position of a DA transition shifts due to the Coulomb energy contribution. For the peak positions measured at the lowest excitation intensity, this contribution is expected to be almost negligible. For the DA1 transition, the peak positions measured at the lowest excitation intensity is at 1.421 eV: the deeper defect involved has an energy of 104 meV, then the shallower defect activation energy can be estimated at about 21 meV. From the DA2 transition, the estimated activation energy of the shallower defect is about 25 meV. From the FB transition observed at low temperatures (line C of the band edge emission), a defect energy of 34 meV has been extracted. It is thus reasonable to assume that all three transitions (DA1, DA2 and FB) involve the same shallow defect at 30±10 meV. A possible explanation for the discrepancy in the energy values obtained by the analysis of the C line and by the analysis of the peak positions at the lowest excitation is a remaining Coulomb contribution in the last case: in fact, if there, it leads to an underestimation (few meV) of the donor activation energy.

Summarizing this whole section 5.1, from the near edge emissions analysis, a band gap at 10 K of 1.554 eV for Cu-rich absorbers has been measured, which well matches those found for single crystals. In line with the results presented in chapter 4, the band gap lowers when the composition of the films approaches the stoichiometry. The DA1 and DA2 transitions are explained as radiative recombination between a common shallow donor with activation energy of about 30 meV and two shallow acceptors at about 105 meV and 145 meV from the valence band. There is no evidence of a second deeper shallow donor (as often reported in literature), as the peaks that follow the DA emissions at lower energies are identified as phonon replicas of the main ones. In the next sections, the presence of an additional DA transition will be discussed and a revised recombination model for shallow defects will be given.

5.2 Detection of a third acceptor in CuInS$_2$ through sodium doping

In the previous sections, CIS absorbers layers have been analysed in terms of their electronic structures, characterizing the point defects responsible of the near edge emissions as a function of the as-grown film compositions (Cu/In ratio tuned from 0.97 to 1.82). So far the CIS absorbers investigated have been deposited by coevaporation (one- or two-stage process) on Mo-coated glass, without any additional doping through post deposition treatment or interlayer (precursor) between the back metal contact and the absorber. Additionally, the samples analysed in section 5.1 to study the shallow defects have been grown on HT glass as substrates (coated with Mo), which has a much lower sodium content than standard soda lime glass (see appendix 3.1). In this section, instead, absorbers deposited on Mo-coated HT glass covered with a thin layer of NaF precursor (deposited prior the CIS deposition) will be discussed. The CIS deposition itself has been carried out by using the one-stage growth process. The NaF precursor has been deposited by electron-beam evaporation and its thickness has been measured by a profilometer, finding a value of about 10 ± 4 nm. Then, within the same CIS deposition run, both Mo-coated HT glass and those coated with an additional NaF layer have been used as substrates: in this way, any observable changes in the chalcopyrite layers, if there are any, are due to the different substrates used, avoiding slight compositional variation which may likely occur from run to run. It is worth mentioning that Colombara et al. have shown alkali doping can take place also unintentionally in chalcogenide gas phase environment [154], modifying the optoelectronic quality of the films. Although their experiments were focused on sodium doping in Cu(In,Ga)Se$_2$, similar effects for the pure sulphide chalcopyrite films are expected; therefore an “accidental” sodium doping of the film deposited on the substrate without NaF precursor cannot be excluded. Nevertheless, the results discussed in the following prove that the addition of the NaF precursor prior the CIS deposition does induce substantial change in the electronic properties of the films deposited on the top of the precursor.

By adding the NaF precursor layer it is possible to introduce sodium during the CIS formation, thus to understand its effect on the electronic properties of the corresponding layers. There have been studies in the past about sodium incorporation in Cu-poor or in Cu-rich CuInS$_2$ [77, 138], but without a detailed analysis of the point defects alteration due to the (only) alkali incorporation. For instance, in [77] the analysis was mostly focused on the variation of the performances of the final devices, while in [138] sodium was introduced through Na$_2$O$_2$ precursor, which does not allow to discern modifications induced by the alkali and by the oxygen incorporation, respectively.

In the following two samples will be investigated: both have been grown within the same deposition run with a metal ratio close to stoichiometry (Cu/In 0.98, as measured by EDX) deposited by one-stage process with a substrate temperature of about 650 °C. Both have Mo-coated HT glass as substrate; additionally, on one of them a NaF precursor layer has been deposited. For simplicity, these two sample will be named in the following as “CIS w/o NaF” and “CIS w/ NaF”, respectively. These samples have been investigated also in terms of QFLS: the difference found between the two (below 10 meV) is within the error of the QFLS evaluation. Moreover, this small change in QFLS may be also attributed to a small variation in the composition of the chalcopyrite films (still within the error of the EDX analysis); indeed, as described in figure 4.15 which reports the QFLS plotted over the compositions, significant variations in QFLS values are observed for small changes in Cu/In ratio in the proximity of the stoichiometric ratio. Despite an almost negligible effect on the QFLS, the introduction of sodium during the growth significantly modify the defect structure of the corresponding sample, as shown in the following mostly by means of low temperature photoluminescence spectroscopy.

5.2.1 A third acceptor in $CuInS_2$ absorber layers

Before discussing the donor-acceptor transitions characterizing the two samples, “CIS w/o NaF” and “CIS w/ NaF”, their band gaps are analysed and determined at low temperatures. The knowledge of the band gap values is essential for an accurate evaluation of the activation energies of the defects involved in the emissions discussed in the following.

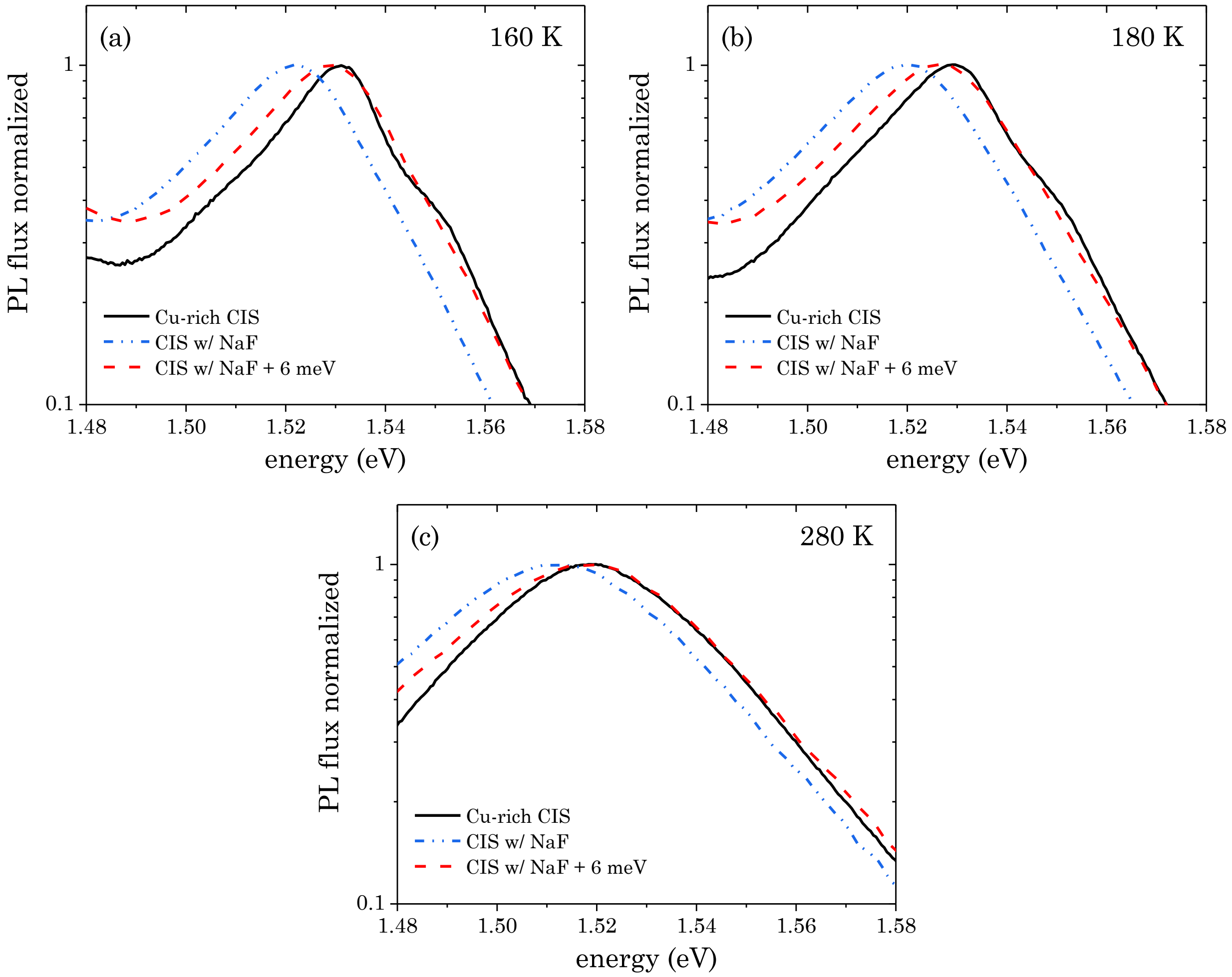

Figure 5.12: photoluminescence spectra measured at 160 K, 180 K and 280 K of Cu-rich $CuInS_2$ with Cu/In 1.83 (black solid line) and of “CIS w/ NaF” with Cu/In 0.98 (dashed dotted blue line). The spectra belonging to “CIS w/ NaF” sample have been plotted also with a shift of 6meV to higher energies (red dashed line). The overlapping of the band edge luminescence confirms the difference of about 6 meV in energy gap between the two samples.

The influence of the thin film composition on the band gap has been discussed in the previous section and in chapter 4. The band edge emission of the “CIS w/ NaF” sample is not well resolved in terms of bound or free excitons; therefore the band gap at 10 K of this absorber cannot be determined by just adding the binding energy of the free exciton [62] to the free excitonic emission line. For this reason, the band gap has been determined by comparing at different temperatures the band-to-band luminescence of the “CIS w/ NaF” sample and a sample with known band gap. For this purpose, the Cu-rich absorber (with Cu/In ratio of 1.8) analysed in detailed in the previous section has been chosen, which has a band gap at 10 K of 1.554 eV. As the “CIS w/ NaF” sample has a composition slightly lower than the stoichiometry, a difference of few meV in the band gap values is expected. In fact, as figure 5.12 shows, the band gap of “CIS w/ NaF” is lower than the Cu-rich CIS sample by 6 meV, which is in line with the difference found in the previous section between the same Cu-rich sample and a stoichiometric (“stoich.” in the following) CIS film. Therefore, assuming the same variation at low temperature, the band gap at 10 K of “CIS w/ NaF” sample is about 1.548 eV. The same band gap lowering (about 6 meV) has been estimated also for “CIS w/o NaF” sample.

Having determined the band gaps of “CIS w/o NaF” and “CIS w/ NaF” samples, the analysis of the band edge emissions, particularly DA transitions, is given in the following. Similarly to the results presented in section 5.1, the characterization has been conducted by means of intensity and temperature dependent photoluminescence spectroscopy.

Figure 5.13 shows the PL spectra of the two samples, acquired at 10 K, together with that measured on the Cu-rich sample with Cu/In 1.83. To properly compare the peak positions of the PL emissions, the “Cu-rich CIS” PL spectrum has been shifted to lower energy (6 meV) to take into account the different band gap.

The PL emissions of the “Cu-rich CIS” sample have been analysed in the previous section, thus its spectrum is not discussed here. The PL spectra of the “CIS w/o NaF” and “CIS w/ NaF” samples show three evident features: both present excitonic emission at around 1.51 eV; in addition, the “CIS w/o NaF” sample spectrum is dominated by the DA1 emission, which has been attributed in the previous section as transition between a shallow donor with an energy of 30 meV and a shallow acceptor with an energy of about 105 meV. This feature is expected, as this sample has been grown in similar conditions as those used for the samples which show the DA1 transitions in figure 5.1, i.e. one-stage process carried out at temperature of 650 °C and metal ratio close to 1. However, the “CIS w/ NaF” sample, although deposited within the same run, exhibits a remarkable change in its photoluminescence spectrum: beside the excitonic line, it still shows the DA1 transition but with lower intensity together with an additional peak centered around 1.372 eV, which has been labelled DA3. The comparison with the PL spectrum of the “Cu-rich CIS” sample (which has been red shifted to consider the band gap change) clearly demonstrates that the DA3 emission cannot be ascribed to the DA2 transition.

In figure 5.13 the DA3 peak is followed at lower energies by other peaks with lower intensities. These are likely phonon replicas of the main transition. Hence, in the following, firstly the nature of these peaks will be analysed to find out if they are related to the electron-phonon coupling or to additional DA emissions, then the main transition will be characterized, to finally get insights about the defects involved on it.

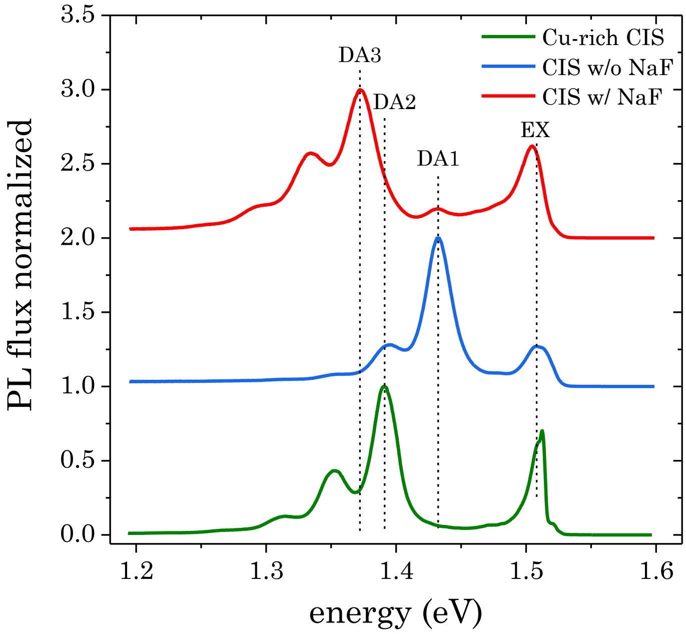

Figure 5.13: Photoluminescence spectra measured at 10 K with the same excitation intensity of $CuInS_2$ thin films: from the bottom, “Cu-rich CIS” with Cu/In 1.82, “CIS w/o NaF” with Cu/In 0.98 and “CIS w/ NaF” with Cu/In 0.98. The first of these spectra (“Cu-rich CIS”) has been shifted to lower energy (6 meV) in order to take into consideration the band gap change. The Cu-rich sample is the same one analysed in detailed in the previous section. The main transitions are highlighted with vertical dashed lines and labelled with EX (excitonic) and DA1, DA2 and DA3 (donor-acceptor) transitions, respectively. The spectra have been normalized to the main transition and shifted vertically for a better visibility.

5.2.2 Phonon coupling of the DA3 transition

Similarly to what has been shown for the DA1 and DA2 analysis in section 5.1, also the DA3 transition shows peaks at lower energies with a spectral distance between each other close to 39 meV, which is the energy of one the phonons (LO) characteristic of $CuInS_2$[151, 152]. This is the first indication that those peaks can be attributed to phonon replica of the main transition. Additionally, those peaks follow the main one both in terms of peak positions and relative intensity if the excitation intensity or the temperature is changed, as shown in appendix in figure A5.5.

The phonon coupling nature of these peaks is finally proved by the good matching of their relative intensities with the Huang-Rhys model, which describes the spectrum as a Poisson distribution of phonon replica according to equation 2.5.21[70], as reported in figure 5.14. Particularly, a Huang-Rhys factor of $S = 0.61 \pm 0.05$ is found for this DA3 transition and its phonon replicas. To fit the DA1 transition, an S value of 0.22 has been fixed (because its phonon replicas are not resolved), keeping intensity and peak position as free parameters. This Huang-Rhys factor for the DA1 transition was found in section 5.1. Similarly to DA1 and DA2 emissions (figure 5.7), an additional deep band centered at around 1.25 eV is needed to fit the PL flux at low energy side of the spectrum.

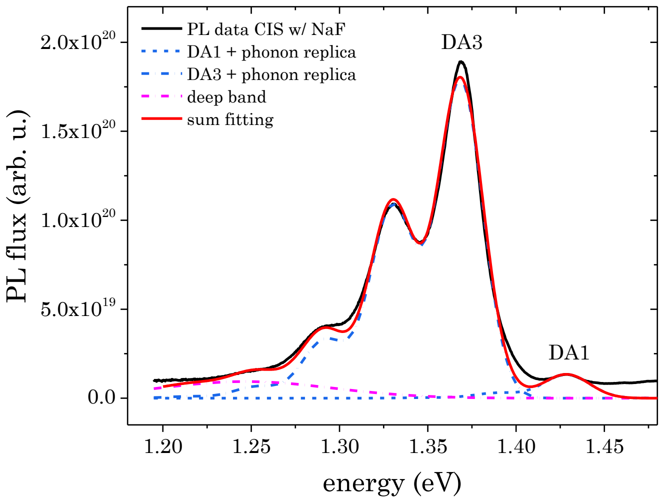

Figure 5.14: Measured photoluminescence spectra at 10 K (black) of $CuInS_2$ thin film w/ NaF precursor with Cu/In about 0.98. The spectrum is fitted with a Huang-Rhys spectrum of the DA1 and the DA3 plus a contribution of an additional deep emission (purple dotted line).

Therefore, having established that the peaks on the low energy side of DA3 are phonon replicas instead of additional DA transitions, in the following the main emission DA3 will be further analysed to shed light on the defects involved into the recombination process.

5.2.3 Excitation intensity and temperature dependence of DA3 transition

The following results have been obtained by fitting several spectra measured at different excitation intensity using two Huang-Rhys spectra for DA1 and DA3 and a Gaussian band centered at around 1.25 eV, in a similar way shown in figure 5.14. S values for DA1 and DA3 have been kept constant at 0.22 and 0.61 respectively. Figure 5.15(a) reports the integrated PL flux of DA3 plotted double-logarithmically over the normalized excitation intensity. Fitting the experimental trend linearly, the linear slope gives the single power law exponent, which is 0.82 (green dashed-dotted line in figure 5.15). However, as already shown in the previous section for DA1 and DA2, if the measurements are carried out for a wide range of excitation intensity (higher than three orders of magnitude), bent trends can be observed for this kind of plot, which cannot be fitted with a single power law. This occurs when one of the defects involved in the transition under investigation or in one of the competing recombination channel paths gets saturated [68] (as explained in section 2.5.1). The experimental trend can thus be fitted with a combination of power laws, each of them with a k exponent multiple of ½, according to equation 2.5.18. In the present case, indeed, the experimental trend found for the DA3 transition can be well fitted with a combination of two power laws (red line in figure 5.15a), with a k exponent of 1 and 0.5, needed to fit the low and the high excitation regime, respectively. The transition between the two regimes is marked with a patterned box. These k values are characteristic of free-to-bound and donor-acceptor transitions.

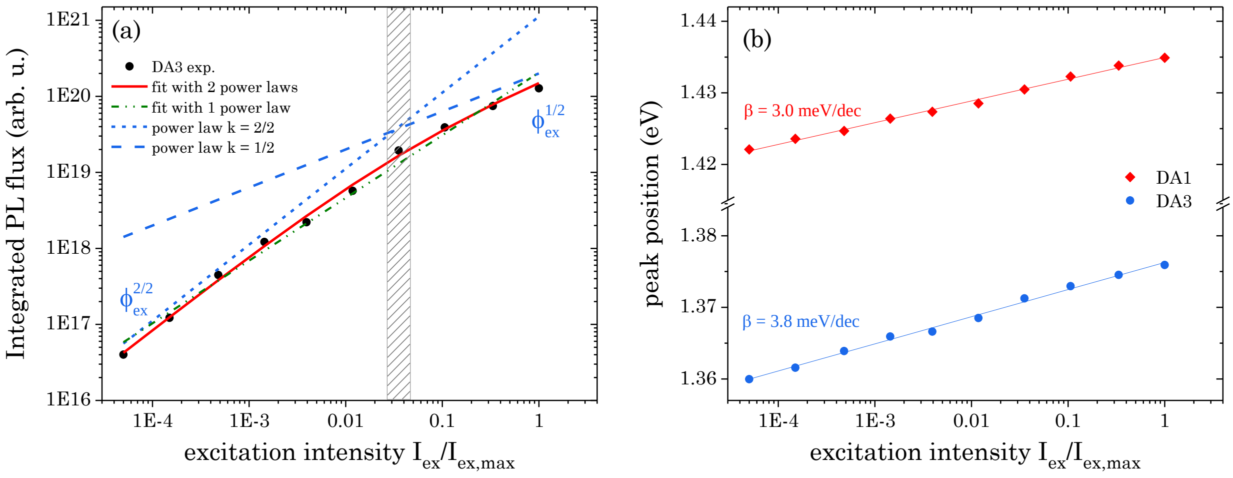

Figure 5.15: (a) integrated PL flux of DA3 transition plotted double-logarithmically over the normalized excitation intensity (black circles) together with the fitting with both single and multiple power laws. For guide lines, the single power laws with exponents $k = 2/2$ and $k = 1/2$ are reported. The transition between the two regimes is highlighted with a patterned box. (b) Peak positions obtained by fitting DA1 and DA3 transitions plotted semi-logarithmically over the normalized excitation intensity together with the corresponding linear fit and the blue shift obtained from the slopes. Note the break along the energy-axis. $I_{ex,max}$ is about 10^4 mW/cm^2.

To discriminate the assignment, the peak position of the DA3 peak is plotted semi-logarithmically over the normalized excitation intensity in figure 5.15(b), which shows also the trend for the DA1 peak. A blue shift is observed for both peaks when the excitation intensity is increased: 3.0 meV/decade and 3.8 meV/decade for DA1 and DA3, respectively. The blue shift is a characteristic sign of a donor-acceptor transition, so the free-to-bound hypothesis can be ruled out.

To gather more information about the DA3 transition and its defects involved, temperature dependent measurement with constant excitation illumination have been performed. The presence of the deep band (centered at around 1.25 eV), with a relative intensity that becomes higher and higher as the temperature rises, does not allow an accurate estimation of the defects involved through the analysis of the quenching of the transition [153]. Therefore, similarly to the procedure used in section 5.1 to obtain the energies of the defects involved in DA1 and DA2, the DA3 transition is rather investigated from the peak position of its corresponding free-to-bound transition, which will be called FB3. It has been found (see appendix, figure A5.3) that the shallower defect involved in the DA3 transition is emptied for temperature above 50-60 K. To corroborate the nature of the FB3, excitation intensity dependence measurements have been carried out at 90 K. The measurements are shown in figure 5.16. The peak of the FB3 transition does not shift with the excitation, which proves the transition has become a free-to-transition at this temperature due to the thermal quenching of the shallower defect. Particularly, a PL peak of 1.381 ± 0.001 eV is measured. Moreover, figure 5.16(b) shows the integrated PL flux of the FB3 transition plotted double-logarithmically over the excitation intensity (over a range of almost two orders of magnitude).

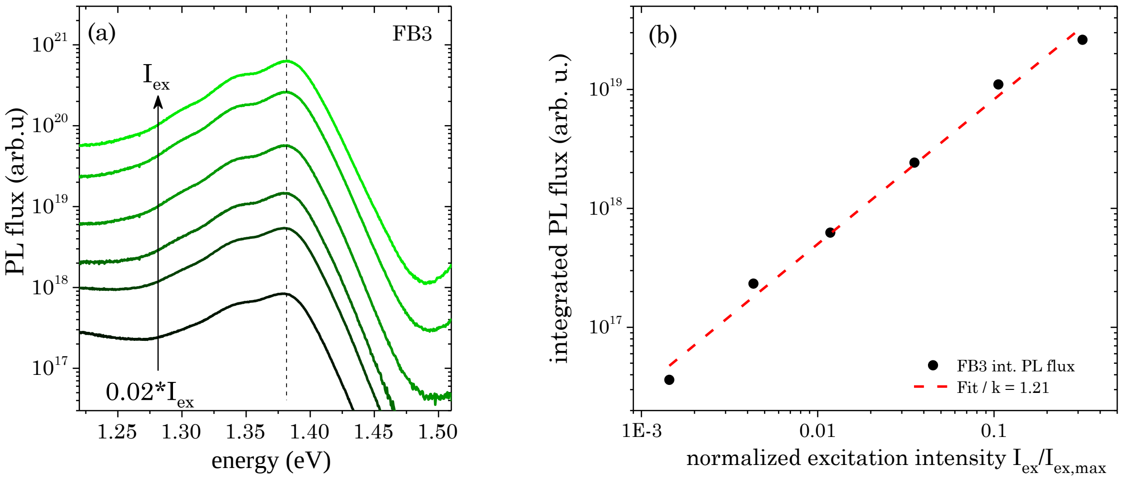

Figure 5.16: (a) photoluminescence spectra of the "CIS w/ NaF" sample acquired at 90 K at different excitation illumination over a rage of about two orders of magnitude. The FB3 transition is marked with a vertical dashed line. (b) Integrated PL flux of the FB3 transition plotted double-logarithmically over the normalized excitation intensity together with the fit, assuming a single power law. The k exponent extracted from the fitting is also reported. $I_{ex,max}$ is about 10^4 mW/cm^2.

Due to the narrower range investigated compared to figure 5.15(a), it is not possible to discriminate two different power laws in the experimental range, thus the measured trend has been fitted with a single one. From the linear fit, an exponent k of about 1.21 if found. It is reasonable to assume that the range of excitation investigated covers the transition region between a power law with exponent 3/2 (at low excitation) and one with exponent 2/2 (at higher excitation). Alternatively, the range investigated (which is limited at low excitation by the low luminescence) is not wide enough to clearly see a crossover excitation, i.e. a curved dependence in the log-log plot.

It has been found previously that the band gap of the "CIS w/ NaF" sample at 10 K is 1.548 eV. Supposing the same trend for the band gap as a function of temperature found for the Cu-rich sample investigated in section 5.1, it can be assumed that the band gap at 90 K increases by 2 meV at 90 K, thus 1.550 eV. Therefore, taking into consideration the PL peak measured for FB3, the activation energy of the defect responsible for the FB3 emission can be deducted, which is 169 ± 5 meV.

To gather information on the shallower defect involved in the DA3 transition (which is thermally emptied at 90 K), it is possible to compare the defect energy just obtained (169 meV) with the band gap of the material at 10 K and the peak position of the DA3 transition at the lowest excitation measured. In this last case, indeed, as mentioned in section 2.5.1 (and in the previous section on DA1 and DA2 emissions), the Coulomb energy in equation 2.5.12 has the lowest contribution: in this way, it has only a minor influence on the defect energy determination. Considering the emission energy of the DA3 transition measured at the lowest excitation (see figure 5.15), the shallower defect activation energy is estimated to be about 20 meV. It is worth to mention that a very similar energy has been estimated with the same procedure (by comparing band gap, PL peak of the DA emission and defect energy responsible of the FB emission) for both DA1 and DA2 transition: 21 meV and 25 meV, respectively, as discussed in section 5.1. Additionally, as for DA1 and DA2 emissions, also DA3 turns to a free-to-bound transition in a temperature range of 40-70 K (see appendix, figure A5.3). These observations strongly indicate that all these DA transitions have a common shallow donor with an energy of about 30 meV (as obtained through the band edge emission analysis in section 5.1.1) and these emissions are the results of the transition between this donor and three different acceptors, placed at 105 meV, 145 meV and 170 meV above the valence band edge.

5.2.4 Comparison with admittance spectroscopy

The "CIS w/ NaF" sample analysed so far by photoluminescence spectroscopy has been investigated also by means of admittance spectroscopy, in order to check the presence of a defect around 170 meV. However, the capacitance spectra are dominated by inflection points attributed to deep defects which cannot be fully resolved. On the other hand, a capacitance step with an activation energy of about 165 meV has been found for a Cu-rich sample (Cu/In 1.82) deposited at 650 °C on Mo-coated HT glass, investigated in the previous section to analyse the DA2 transition (section 5.1). The corresponding capacitance spectra are reported in figure 5.17 (the same spectra are reported in figure 5.11) together with the Arrhenius plot of the inflection points marked with black squares. This capacitance step (with activation energy of about 165 meV) is observable for the sample grown with Cu/In of 1.82 likely because the recombination activity of deep defects in Cu-rich samples has a lower contribution than that in Cu poor (or stoichiometric) samples (as seen in chapter 4 and shown in the following). In this way, the capacitance steps attributed to shallow defects can be measured.

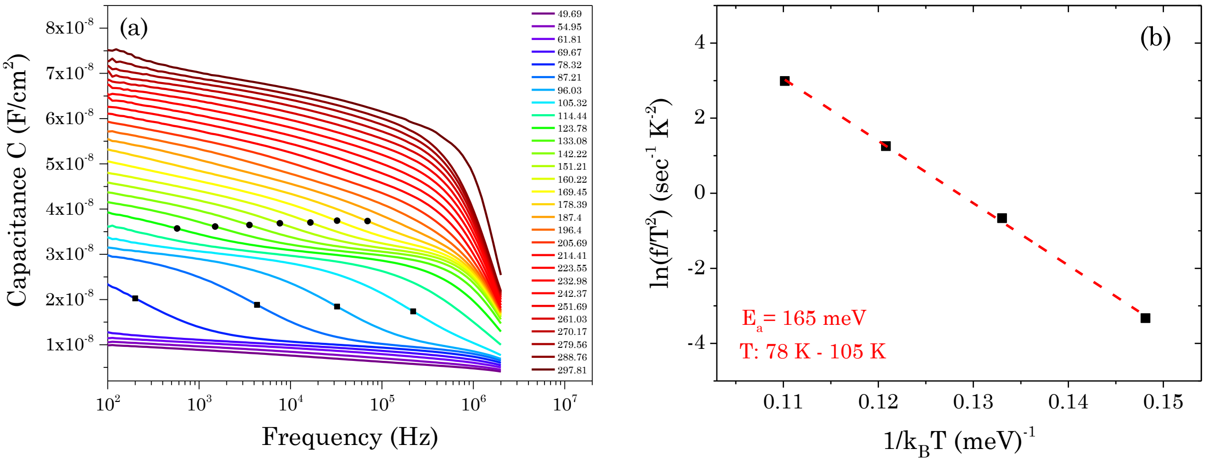

Figure 5.17: (a) capacitance C plotted semi-logarithmically over the frequency for temperature range from about 50 to 300 K for Mo/CuInS$_2$/Al stack (with HT glass as substrate, without NaF precursor); the inflection points of the main steps are marked with black circles and squares. The first ones have been discussed in section 5.1 and lead to an activation energy step of about 145 meV. The black square inflection points are instead analysed in (b) which shows the corresponding Arrhenius plot of the inflection points with the fit (dashed red line) to extract the activation energy, which is reported together with the temperature range. Measurements performed by Mohit Sood.

These results may suggest this defect, with an activation energy of about 165-170 meV, is present also in absorbers grown under Cu-excess, but its related transitions cannot be detected by photoluminescence spectroscopy because of the presence of the DA2 transition and its phonon replica which hide the DA3 emission line.

Summarizing this section 5.2, an additional donor-acceptor (DA3) transition is identified in samples grown with a NaF precursor. This emission is attributed to the radiative recombination between a shallow donor at 30 meV from the conduction band and a shallow acceptor at about 170 meV from the valence band.

5.3 A revised model for shallow defects in $CuInS_2$

Before discussing the deep defects and their related bands in $CuInS_2$, this section gives a summary on the findings presented so far in this chapter, i.e. on the shallow defects.

The shallow defects electronic structure in $CuInS_2$ has been studied in the past, mostly by means of photoluminescence spectroscopy, as discussed in section 2.6. The two main transitions observed at low temperature, at 1.39 eV and 1.43 eV, have been attributed to donor-acceptor transitions between a common shallow donor and two acceptors. Additionally, both transitions were always followed at lower energy by one more emission line, interpreted as donor-acceptor transitions involving the same acceptors and a deeper donor. The measurements presented in this chapter show, instead, there is no need of a second donor to explain these transitions at lower energies. In fact, through the analysis of high quality absorbers, it is clear the emissions at lower energies are just the first of the phonon replicas of the main transitions. The difficulty in the past arose by the fact that the difference in the defect activation energy of the shallow acceptors is very close to the LO phonon energy (about 39 meV) of this material. Therefore, in samples where at least two of the three DA transitions coexist, with an intensity of a DA emission comparable to the first phonon replica of the emission at higher energy, an accurate analysis may become challenging, due to the overlapping of different transitions and their related phonon replicas. Nevertheless, with the detailed investigation illustrated in this chapter, a new defect model of shallow defects for $CuInS_2$ can be proposed, which is given in figure 5.18.

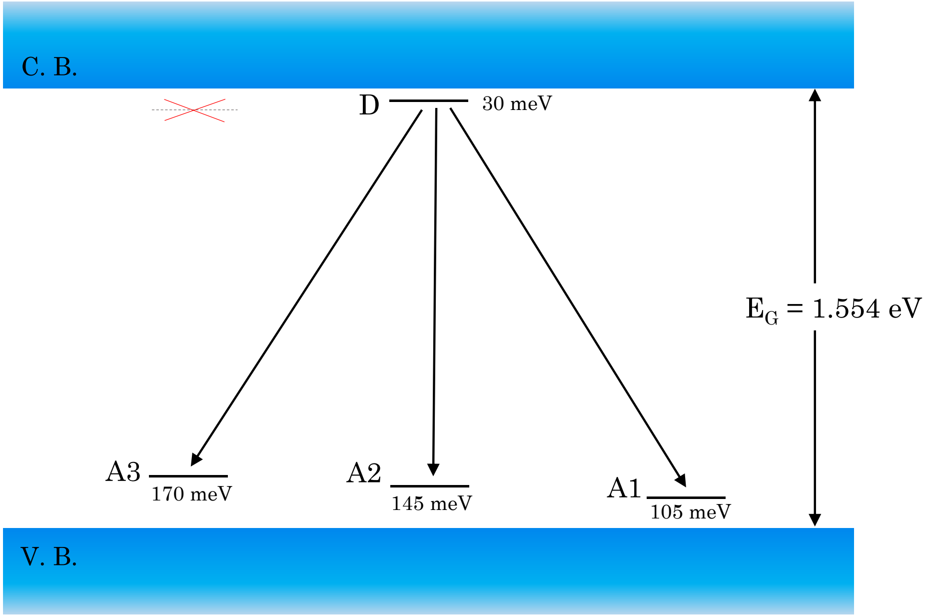

Figure 5.18: electronic structure of $CuInS_2$ representing the shallow defects detected in this work by means of photoluminescence and admittance spectroscopy. The band gap refers to the value found for Cu-rich absorber (Cu/In 1.82) at 10 K. The defect energies reported have to be assumed with an error of about ± 5 meV. The second deeper donor, proposed in literature as responsible of additional DA transitions, is also drawn and struck through to highlight all DA transitions observed (and their related phonon replicas) can be explained with a common donor and three acceptors.

This model includes a shallow donor with an energy about 30 meV and three shallow acceptors with an activation energy of about 105 meV, 145 meV and 170 meV, respectively.

In figure 5.18 the second deep donor (at about 75 meV from the conduction band as proposed in literature, e. g. in [74]) is also drawn and struck through, in order to highlight all DA transitions found in the frame of this work can be explained with a recombination model that includes only a shallow donor, beside the three acceptors. The other transitions attributed in literature to additional DA emissions can be well described as phonon replicas of the main DA ones. But one has to keep in mind this does not exclude the existence of a second shallow donor with the aforementioned activation energy: however, there are no observations of emissions or clear indications from alternative measurements (besides PL) which could confirm its presence.

5.4 Deep defects in $CuInS_2$: 1.05 eV and 1.25 eV bands

In the previous sections, 5.1 and 5.2, the near edge photoluminescence has been analysed, and it is mainly characterized by three donor-acceptor transitions, which can be explained as recombination between a shallow common donor and three shallow acceptors, as summarized in section 5.3. It has been highlighted as well that in all spectra, for DA1, DA2 and DA3 emissions, a deeper band centered at around 1.25 eV is needed to fit the low energy range of the PL flux. This section will discuss this band (which from now on will be called DDA1, i.e. deep donor-acceptor) and a deeper one, centered at around 1.05 eV (that will be named as DDA2), which has been already shown in room temperature PL spectra in chapter 4. Both these two bands have been observed in the past, as reported in section 2.6 on the defects review in $CuInS_2$, although their detailed investigation is still missing, thus their origin still unknown. The difficulty arises from their higher broadening compared to the near edge emissions and from the partial overlapping of the two deep bands, which make their analysis quite challenging. At the time of writing, their origin is still under investigation, thus in this section some preliminary insights are given.

Figure 5.19 shows low temperature PL spectra plotted over a wide range, 0.8 eV – 1.6 eV, of two CIS samples grown by 1-stage process at 650 °C on Mo-coated HT glass, but with a different composition: one with a Cu/In ratio of 1.83 (named “Cu-rich CIS”) and a second one with a Cu/In ratio of 0.98 (named “Stoich. CIS”).

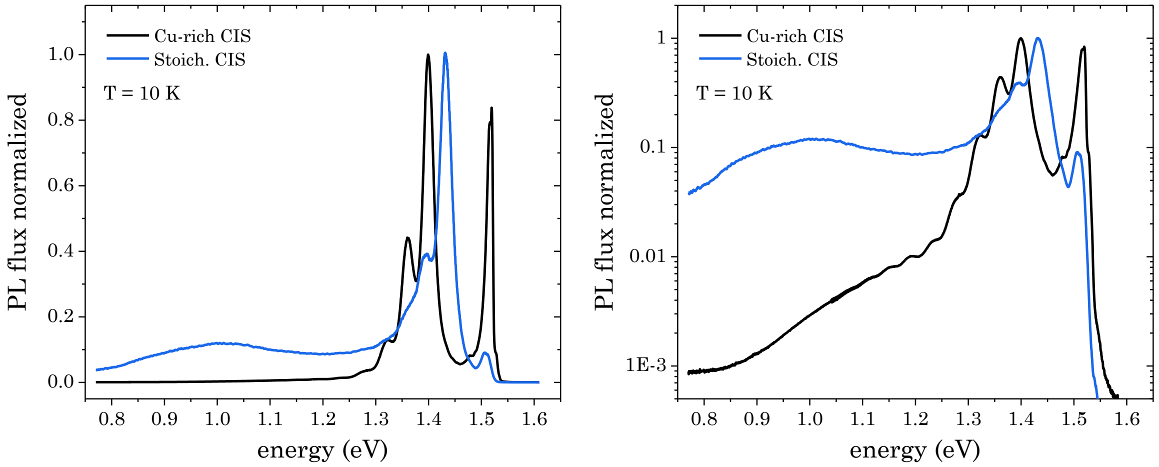

Figure 5.19: PL spectra acquired at 10 K of Cu-rich CIS and stoichiometric CIS (with Cu/In of 1.83 and 0.98, respectively). In both cases, the PL flux has been normalized to the highest emission line, i.e. a shallow donor-acceptor transition. The PL flux is reported in (left) linear and (right) logarithmic scale.

These two samples have been used in section 5.1 to characterize the DA1 and the DA2 transitions, which dominate the near edge photoluminescence which will not be further discussed here. By comparing the two spectra, the first clear evidence is that both show a deep PL signal at energies below 1.3 eV which cannot be ascribed to background of the PL setup. Secondly, the relative ratio between this deep PL flux and the near edge photoluminescence increases when the films are grown with a stoichiometric composition.

The relative intensity of the deep PL signal depends as well on the growth process and conditions. By way of example, in [24] Cu-rich absorbers deposited by rapid thermal process manifest at low temperature a deep broad band close to 1.2 eV with an intensity comparable to the excitonic emission. On the other hand, epitaxial and polycrystalline thin CuInS$_2$ deposited by means of MBE manifest a drastic change in the PL flux share, which is dominated by the deep PL signal (bands close to 1.0 eV and 1.2 eV) in the former case, whereas the near edge emissions dominate the latter case [82].

The DDA2 band is clearly visible in stoich. CIS spectrum; the DDA1 band, close to 1.2 eV, is instead hidden by the shallow donor-acceptor emissions and their phonon replicas. As the defects involved in the two DDA transitions are expected to be deeper than those responsible for the shallow DA emissions, these last ones should quench faster with temperature. Indeed, this is the trend observed for temperature dependent photoluminescence performed on the Cu-rich CIS, as shown in figure 5.20.

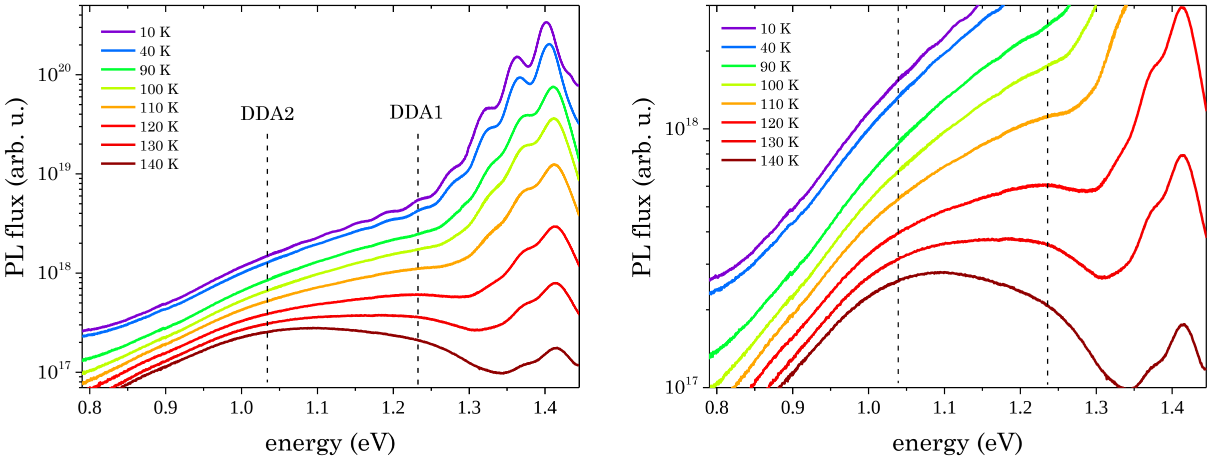

Figure 5.20: temperature dependent photoluminescence performed on the Cu-rich CIS with a constant illumination and varying the temperature from 10 K to 140 K. The two DDA transitions are highlighted with vertical dashed lines. The plot on the right shows a closer view of these two DDA for a better visibility.

As the temperature raises, the shallow donor-acceptor transition manifests a stronger quenching, which translates in a drastic reduction of its PL flux of more than three orders of magnitude when temperature is increases from 10 K to 140 K. This strong reduction makes the DDA1 band (along with the DDA2 one) visible for temperature above 100 K (see figure 5.20(right)).

A deeper investigation through excitation intensity dependent photoluminescence spectroscopy has been conducted on a slight Cu-poor sample (Cu/In = 0.96) deposited on Mo-coated SLG at 590 °C by 1-stage coevaporation process. This sample has been chosen as it shows both DDA bands clearly visible at low temperature and thus it allows to characterize them over a wide range of excitation intensity. The low energy part of the PL spectra ($E < 1.3\ eV$) has been tentatively fitted with two broad Gaussian bands (FWHM in the order of 200 meV) for the two DDA. The near edge luminescence can be described by the three shallow DA transitions discussed in the previous sections: the fitting functions for the DA1, DA2 and DA3 have been adjusted to describe phonon replicas with a Huang-Rhys factor of 0.22, 0.48 and 0.62 as found previously in those sections. Figure 5.21a reports an example of fitting following this procedure, while figure 5.21b shows the integrated PL flux of DDA1 and DDA2 plotted double-logarithmically over the excitation intensity.

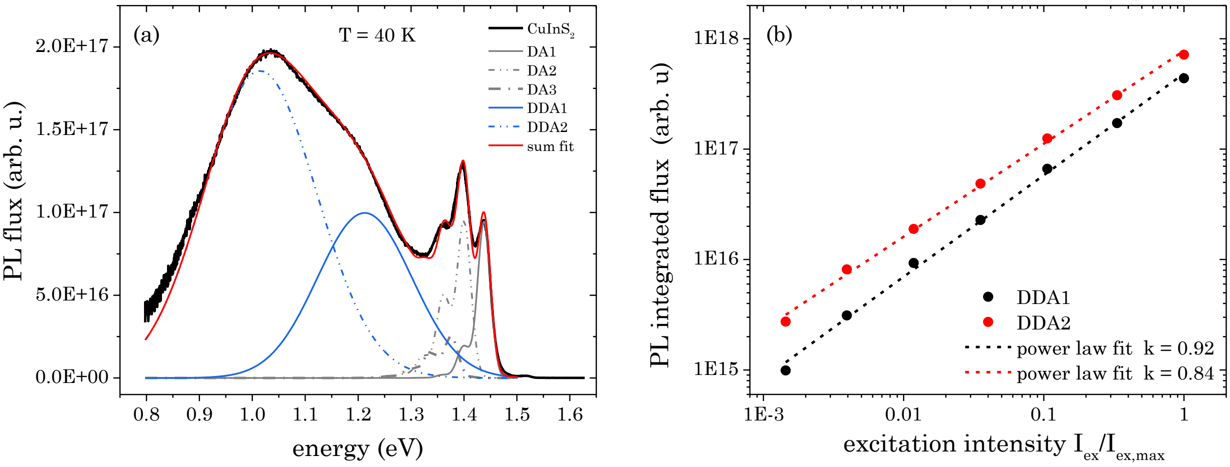

Figure 5.21: (a) PL spectrum measured at 40 K of a Cu-poor CIS sample (Cu/In = 0.96, deposited on Mo-coated SLG at 590 °C) together with the fitting functions: two broad Gaussian bands for DDA1 and DDA2 and three shallow DA transitions with their phonon replicas. (b) PL integrated fluxes of the two DDA1 and DDA2 bands plotted double-logarithmically over the excitation intensity, together with the fit and the corresponding k values.

The experimental trends can be well fitted by a single power law, with a k value of 0.92 and 0.84 for DDA1 and DDA respectively. The range of excitation intensity investigated is narrower compared to the one measured for the shallow DA emissions studied in section 5.1, explaining the absence of a visible bent trend with excitation. The explored range lies likely in a transition regime between a power law with exponent 1 and 1/2. These k values are characteristic of donor-acceptor or free-to-bound transitions. The last case can be ruled out as both bands show a blue shift with the excitation intensity, typical of DA emissions, as shown in figure 5.22a. A shift of 10.5 meV/decade and 15 meV/decade has been found for DDA1 and DDA2 bands, respectively. A comparison of two spectra acquired a low and high excitation is given in figure 5.22b: beside the high blue shift, a change of the relative intensity between the two deep broad bands is observed, which is reflected in a higher k value for the DDA1 band, as discussed previously. The shift per decade measured for the shallow transitions (section 5.1 and 5.2) are three to five times lower than those found for DDA1 and DDA2. High blue shifts in the order of 10-15 meV/decade have been reported in the past for $CuInS_2$ for broad bands close to 1 eV [155] and close to 1.2 eV [155, 156].

High blue shifts in the order of 10 meV/decade are observed in compensated semiconductors [153], which are characterized by a high density of both acceptors and donors. The local accumulation of charges leads to local variations of the potential, which in turn cause distortion of the band structure, hence of the band edges.

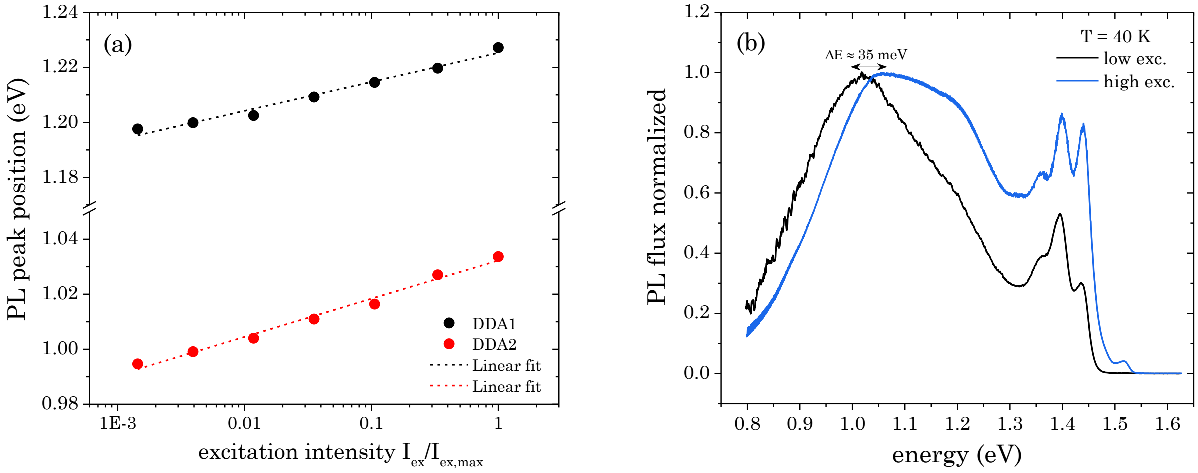

Figure 5.22: (a) PL peak positions of the two bands DDA1 and DDA2 plotted semi-logarithmically over the excitation intensity, together with the linear fit to extract the blue shift/decade. Note the break on the y-axis. (b) CIS spectra acquired at 40 K with low and high excitation (about 40 mW/cm^2 and 10^4 mW/cm^2, respectively): the blue shift of the DDA1 band is about 35 meV.

A characteristic fingerprint of potential fluctuation is the asymmetric broadening of the radiative emissions. As the band edge emissions in figure 5.22b (and all samples investigated in this thesis) are characterized by narrow and rather symmetric shallow DA transitions, potential fluctuations can be ruled out as possible cause of the high blue shifts.

An alternative explanation can derive from the defects involved in these two deep transitions. In a DA transition, the peak shift with excitation illumination is due to a change of the Coulomb contribution, as reported in equation 2.5.12. Assuming the shallower of the defects involved produces a shallow hydrogen like energy level (whereas the other is much deeper), then the maximum Coulomb contribution to the PL shift is proportional to the effective mass: electron one if the shallower defect is a donor, hole one if it is an acceptor [157, 158]. In CuInS$_2$, like for other chalcopyrite semiconducting materials, the hole effective mass is much higher than electron effective mass: $m_h^* = 1.3m_0$ and $m_e^* = 0.16m_0$, as estimated in [67]. Therefore, a shallow acceptor, forming a hydrogen-like energy level, leads to a much higher Coulomb contribution due to the larger hole effective mass and thus smaller Bohr radius, which in turn is reflected into a high blue shift/decade when the excitation intensity is varied. On the other hand, a shallow donor leads to a higher Bohr radius, so to a low Coulomb contribution that is reflected into a low blue shift/decade.

The shallow donor-acceptor emissions previously analysed (DA1, DA2 and DA3) have been explained as transitions from a very shallow donor to shallow acceptors, and blue shifts of few meV/decade have been measured.

The two DDA emissions, by contrast, both show high blue shift/decade; therefore the shallower of the two defects involved in these transitions must be the one with the larger effective mass (which leads to smaller Bohr radius), i.e. the acceptor. Whether the two DDA bands originate from two deep donors and a shallow acceptor, one deep donor and two shallow acceptors or they are two independent donor-acceptor transitions, it cannot be determined at the time of writing this thesis. A parallelism with deep defect bands detected in $CuGaSe_2$ will be given in the following.

Alternatively, the high blue shift observed when the excitation illumination is increased may be due to the presence of a broad density of states which, at the same time, gives rise to the high broadening measured for the two DDA bands (in the order of hundreds of meV). In fact, by increasing the excitation intensity, the average energy of the occupied states increases, thus the minority quasi Fermi level is shifted upwards within the defect distribution. This shift of the quasi Fermi level leads to a blue shift of the maximum of the radiative transition. On the other hand, for similar reasons, if each of this bands was due to a broad density of states, their maxima should shift red when the temperature raises (as the minority quasi Fermi level is shifted downwards), which is not actually observed, as shown in figure 5.20 or even more clearly in annex in figure A5.6. Therefore, the two bands are ascribed to donor-acceptor transition, but the high broadening is unlikely caused by the presence of a broad density of states.

The characteristic features observed for the two deep bands DDA1 and DDA2 may be explained as well considering a significant contribution of the electron-phonon coupling in the two DA transitions. As discussed in section 2.5.2, the wave function of a deep defect is extremely localized and when it changes its charge state (during a PL experiment), its surrounding rearranges. Thus, the radiative recombination involves the emission of several phonons, depending on the strength of electron-phonon coupling. For deep defects, the transition may appear as a broad asymmetric band, which sometimes may also look similar to a Gaussian band (for high Huang-Rhys factors). Assuming that the electron-phonon coupling is the reason behind the high broadening observed for DDA1 and DDA2, then their maxima are red shifted compared to the zero-phonon lines. The knowledge of the ZPL is crucial for the determination of the activation energies of the defects involved in such transitions. Similar double-peaked bands have been observed in $CuGaSe_2$, which has a band gap of about 1.7 eV at low temperature and shows two deep bands close to 1.1 eV and 1.24 eV [90]. By adding indium during the deposition process (GGI = 0.78), the shallower of these two bands disappears, making the investigation on the deeper one more feasible due to absence of the overlapping of two bands. For $CuGaSe_2$ the band close to 1.1 eV (about 0.6 eV far from the band edge) has been related to a deep donor Ga_{Cu} placed at 1.3-1.33 eV above the valence band, with almost a difference of 200 meV between the ZPL and the PL band maximum.

At the time of writing and with the available data, the occurrence of only one single deep band in $CuInS_2$ has not been observed at low temperatures, making the analysis in terms of phonon coupling of both DDA transitions at the same time too arbitrary, thus their ZPL cannot be determined.

It is worth mentioning that one more difficulty in analysing these deep bands may arise if a third deeper band is considered, centered at around 0.85 eV. This band has been discussed in chapter 4 (section 4.3) and attributed to a major recombination center which limits the QFLS. Even though the higher deposition temperatures drastically reduce its intensity (see figure 4.7), this band is still present in room temperature PL spectra and leads to an asymmetric broadening of the 1.05 eV (or DDA2) band (see figure 4.9).

In this section, two broad Gaussian bands (representing the DDA1 and DDA2 bands) have been used to fit the deep PL signal of low temperature PL spectra. Still, the presence of a deeper band can't be ruled out with certainty. In fact, as figure 5.23 displays, the deep PL signal of the same spectrum reported in figure 5.21 can be well fitted with three Gaussian bands: those introduced previously, DDA1 and DDA2, with PL maxima close to 1 eV and 1.2 eV and a third deeper band close to 0.87 eV (named "low-energy band").

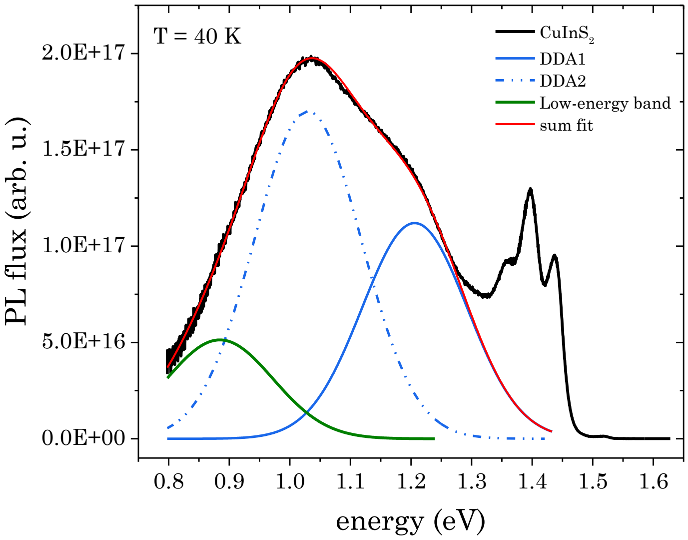

Figure 5.23: PL spectrum measured at 40 K of a Cu-poor CIS sample (Cu/In = 0.96, deposited on Mo-coated SLG at 590 °C) together with the fitting functions: three broad Gaussian bands for DDA1 and DDA2 and for the deeper band close to 0.87 eV. The same PL spectrum is displayed in figure 5.21, where the deep PL signal is fitted with only two Gaussian bands. For the fitting of the band edge emissions, see figure 5.21.

The presence of the "low energy band" would not affect the validity of the results discussed so far for the DDA1 and DDA2 bands; e.g., they would still show high blue shift with increasing excitation. The "low energy band" rather influences slightly the peak positions of the two DDA bands (at a given excitation intensity, both are blue-shifted by 10-15 meV) and their intensity, both in terms of amplitude and FWHM. Particularly, the FWHM are lowered by about 50 meV for both DDA bands when the third Gaussian band is added in the fitting procedure.

This additional "low energy band", if present, would make the study of the deep PL signal extremely challenging; moreover, as its peak is not resolved, it would make the fitting analysis more arbitrary than using just the two DDA bands.

Summarizing, at low temperature both Cu-rich and Cu-poor CIS absorber show two bands close to 1.05 eV and 1.25 eV: the last one quenches at temperature above 200-230 K, while the deeper one is still present at room temperature. Both bands can be ascribed to donor-acceptor transitions, although the knowledge about the defects involved is still missing. The high broadening of the two bands is likely given by the high contribution of phonon coupling, characteristic of transitions which include deep defects. In section 5.5, a possible defect responsible of the DDA2 band will be proposed.

5.5 Comparison with previous models

In section 2.6 a review on point defects in $CuInS_2$ has been given, discussing both the model derived experimentally and those derived through theoretical calculations. This section compares these results with the findings obtained in this thesis.

5.5.1 Comparison with experimental results

To initiate the discussion, the defect models of figure 2.6.1 are reillustrated in figure 5.24, together with the activation energies of the shallow defects found experimentally in this work.

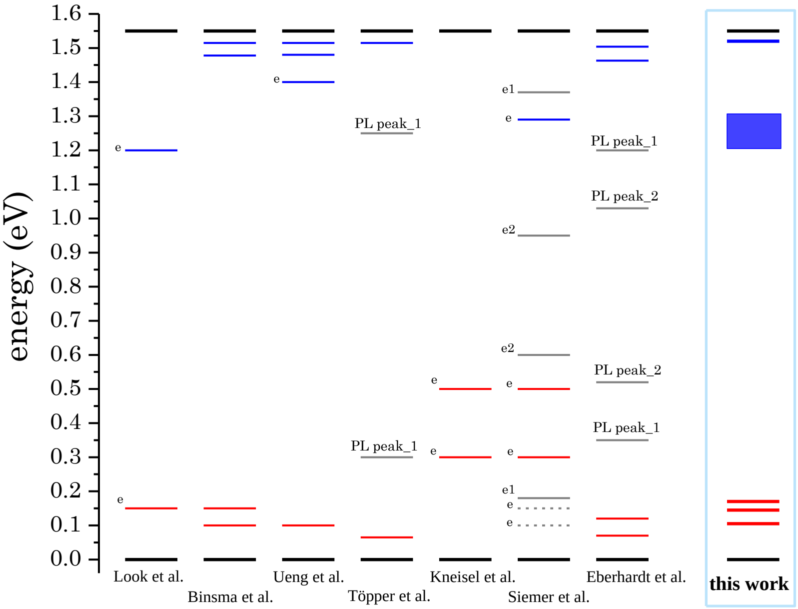

Figure 5.24: recombination defects models derived in the past by photoluminescence and electrical (marked with “*e*”) measurements together with the recombination model for shallow defects measured in this thesis. The deep donor proposed is highlighted with a blue box due to the uncertainty of its activation energy. For a more detailed description of the labelling, refer to figure 2.6.1.

The shallow acceptors measured in this work are placed at 105 meV, 145 meV and 170 meV above the valence band edge. The shallowest of these defects, at 105 meV, is likely the one already found previously by Binsma [74] and Ueng [75]. The discrepancy with the shallowest defects found by Töpper [76] and Eberhardt [82] may be ascribed to errors in the activation energy determination, e.g. strong influence of deep bands on activation energies of shallow defects determined by analysing their quenching with temperature.

The shallow acceptor at 145 meV perfectly matches the value found by Look [67] by evaluating the temperature dependence of the hole concentration with Hall measurements and the one found by Binsma [74] through photoluminescence spectroscopy. It is also likely that the second shallower acceptor found by Eberhardt [82] has the same origin.

By admittance spectroscopy Siemer et al. [80] revealed the presence of two defects, close to 100 meV and 140 meV which were tentatively depicted as interface defects. Due to the strong similarity with the activation energies found in this thesis and with those already reported in the past, there is a high chance they are actually defects.

In the same work [80], the authors found also a defect with an activation energies close to 170-180 meV for CIS coevaporated absorbers grown under slightly Cu-poor conditions (Cu/In ratio is not given), although its origin is unknown and not discussed. Similar conditions have been used to deposit "CIS w/ NaF" sample, discussed in section 5.2, which shows a band edge luminescence dominated by the DA3 emission. This transition has been related to the radiative recombination between a shallow donor and an acceptor at 170 meV above the valence band edge. Thus, it is reasonable to assume this is the same defect, detected by PL in this work and by admittance spectroscopy in [80].

Finally, the recombination model for shallow defects proposed in this thesis includes a donor at about 30 meV from the conduction band edge. Shallow donors with similar activation energy have been proposed in the past, as shown in figure 5.24.

As already discussed throughout this chapter, a second deeper donor has been proposed in the past, with activation energies close to 70-80 meV. The measurements conducted in the framework of this thesis do not support its presence as all near edge emissions observed can be well explained by the recombination between one donor and three shallow acceptors.

All samples investigated in this thesis (Cu-rich, stoichiometric and slightly Cu-poor) show two deep broad bands close to 1-1.05 eV and 1.2-1.25 eV. From the preliminary investigations discussed in section 5.4, they are likely related to recombination where at least one deep donor is included, which, given its strong localization, leads to a high electron-phonon coupling, thus to very broad bands. Whether these two bands originate from radiative recombination between two deep donors and one common shallow acceptor, one common deep donor and two shallow acceptors or two independent donor-acceptors cannot be clarified at the time of writing. For Cu-rich sample, the deeper of these two bands has a PL maximum at about 1.05 eV at room temperature, where it is reasonable to assume the transition has become a free-to-bound transition. For a rough estimation of the activation energy of the deep donor and due to the strong similarity with $CuGaSe_2$ [90], a Frank-Condon shift of about 150-200 meV can be considered, which would then place the defect at 1.2-1.25 eV above the valence band edge (i.e. 300-350 meV from the conduction band). This defect is shown in figure 5.24 as a blue box, given the uncertainty of its position within the band gap. Two donor defects have been reported in the past with an energy close to the one proposed in this work. In both cases, these defect have been detected by electrical measurements. Particularly, in [67], a deep donor placed at 350 meV from the conduction band has been found by analysing the temperature dependence of electron density in n-type single crystals of $CuInS_2$; in [81] a deep donor at 260 meV has been measured by deep level transient spectroscopy carried out on $CuInS_2$ solar cells. It is possible to assume, within the errors of the measurements, both defects refer to the same one with an activation energy close to 300 meV, which is perfectly in line with the energy range proposed in the current work for the defect that causes the 1.05 deep band.

The origin of the band close to 1.2-1.25 eV is unknown and any attempt for its explanation would be purely speculative with the present data. It can be proposed, e.g., it is given by the recombination of a shallow acceptor with a deep donor: the last one could be the defect found by Ueng at. al [75] at about 150 meV from the conduction band, even though no other works in literature report such defect. Due to its activation energy, it is reasonable to assume it gets completely emptied at room temperature, leaving the low energy side of the PL spectra dominated by the broad band at 1 eV. This activation energy of about 150 meV, considering a lower Frank-Condon shift than the defect placed at about 300 meV, would also explain the energy difference between the DDA1 and DDA2 maxima. Nevertheless, a deeper investigation would be required, although the DDA1 band always appears (and partially overlaps) together with the deeper DDA2 band and it quenches completely at room temperature, making its studying extremely challenging.

No evidences have been found in this thesis which would corroborate the existence of a deep acceptor at about 300 meV from the valence band, as reported in [79] and [80].

Finally, few words about the deep acceptor at about 500 meV from the valence band. It has been reported for Cu-rich CIS absorbers (this does not exclude its presence in Cu-poor absorbers) by admittance spectroscopy. Additionally, it has been shown that the concentration of this deep defect correlates with the open circuit voltage lowering. Due to its energy position within the band gap, a high electron-phonon coupling is expected: considering a Frank-Condon shift in the order of 150-250 meV, the peak of its luminescence would lie in a spectral range of 0.8-0.9 eV. A band with a luminescence in this range has been discussed in chapter 4 (see e.g. figure 4.10) and the deep defect involved is a major recombination center. It has been discussed as well that the integrated PL flux of this band correlates with the quasi Fermi level splitting loss. Hence, there is a strong similarity between the trend observed by electrical measurements between the concentration of this deep defect and the Voc loss and the trend discussed in chapter 4 between the relative share of this deep band close to 0.83 eV and the quasi Fermi level splitting loss. For these reasons it can be speculated the deep acceptor at 500 meV from the valence band is involved in the recombination processes which gives rise to the deep band close to 0.83 eV.

The findings discussed in section 5.1 and 5.2 doubtless support the presence of one shallow donor and three shallow acceptors. On the other hand, the attribution and the correlations made in this section between the deep bands observed in the framework of this work and the defects measured in the past need to be corroborated by additional analysis which are not subject of this thesis.

5.5.2 Comparison with theoretical calculations

Having compared the results obtained in this thesis for point defects with those experimentally found in the past, a comparison with the theoretical models calculated for CIS is given in the following. Figure 5.25 compares the charge transition levels of point defects calculated for $CuInS_2$ in [91] and [92] with the defects found in this thesis. A deep donor at about 300 meV from the conduction band is also drawn with a blue box, which indicates the uncertainty of its activation energy.

In chapter 2 a detailed discussion on how the calculation parameters may significant alter both the final band gap calculated as wells as the charge transition levels in the forbidden gap is given.

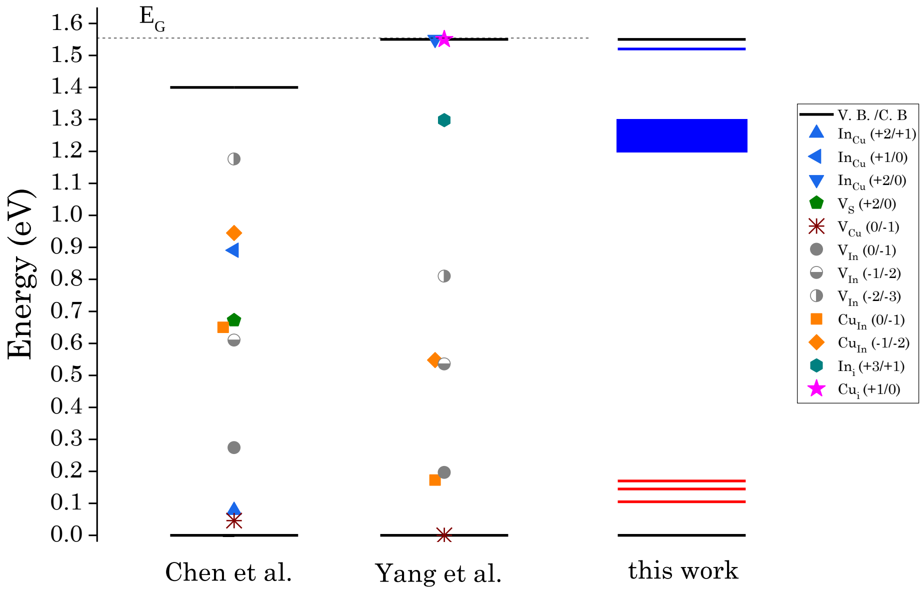

Figure 5.25: overview of the charge transition levels of point defects calculated for $CuInS_2$ in [91] and [92] plotted together with the defects experimentally observed in this thesis. A deep donor is proposed as responsible for the DDA2 emission and it is reported as blue box to highlight its activation energy uncertainty: it is not intended to be considered as a broad density of states. On the right, the labelling indicates both the kind of point defect and the charge change of each transition level. The band gap refers to the low temperature value, 1.55 eV.

Therefore, one needs to carefully compare the experimental findings of this thesis with the calculated energy levels, as these last ones are derived from (i) only two published reports which are (ii) not conducted in the optimum conditions, such as number of atoms in the supercells, as done for the selenium-based chalcopyrites.

Nevertheless, some correlations between the experiments and the calculations may be done. Firstly, both reports agree that the shallowest acceptor is copper vacancy V_{Cu}. If the activation energy lies in an energy range of 50-100 meV, which is usually the error attributed to these calculations, the defect is drawn directly on the band edge, as can be seen in figure 5.25. Hence, the shallow defect found in this thesis with an activation energy of 105 meV is likely a V_{Cu}. Chen's report does not present any other shallow acceptor, beside the first charge state of V_{In} at about 300 meV from the valence band. This is in strong contradiction to the experiments of this thesis and to those reported in the past (see, e.g., the defects overview in figure 5.24). On the other hand, Yang's report shows two more shallow acceptors, both with an activation energy of about 200 meV, i.e. the first charge state of Cu_{In} and V_{In}. They are likely the shallow acceptors close to 145 meV and 170 meV from the valence band found in this work. The calculations also show they are close to each other in terms of energy within the band gap: this is also reflected by the lower difference in the activation energy between A_2 and A_3 compared to A_1. Due to the uncertainty of the calculations, it cannot be discerned if A_2 (A_3) is related to Cu_{In} or V_{In} (V_{In} or Cu_{In}). In fact, the DA1 emission has been observed for CIS sample with a composition close to stoichiometry or slightly Cu-poor, which is in line with the attribution to V_{Cu}. On the other hand, the DA2 emission has been observed as domination line for Cu-rich samples, which in principle could be related to either Cu_{In} or V_{In}. According to Yang's report, the calculated formation energy of V_{In} is always higher than Cu_{In}, which makes this last defect as most probable candidate for the DA2 emission. Consequently, V_{In} would be responsible for the DA3 emission. It has been discussed in section 5.2 and 5.3 that due to the small energy difference between A2 and A3, the A3 defect may be present as well in Cu-rich samples (as confirmed by admittance spectroscopy, see figure 5.17), but its luminescence is likely always hidden by the DA2 emission and the related phonon replicas. This might be explained considering that V_{In} has higher formation enthalpies than Cu_{In}, thus a lower concentration of this defect is expected, which translates into a lower intensity for the DA3 emission. In samples with a composition close to stoichiometry (Cu/In 0.98) grown with NaF precursor, the DA3 emission dominates the band edge luminescence. It can be speculated that for this composition, the V_{In} formation enthalpy is still not as high as it would be if the sample was grown with a strong Cu-deficiency, thus it still allows the formation of a considerable amount of V_{In} defects.

The shallow donor close to 30 meV from the valence band is likely given by Cu_i as suggested in Yang's report, which calculated a low energy formation for this defect over a wide range of chemical potentials of the elements, i.e. sample growth conditions. According to Yang's report, In_{Cu} has as well a charge transition level close the conduction band, which would make it a potential candidate for the shallow donor at 30 meV. Nevertheless, the theoretical calculations for this defect in Yang's report are in strongly contradiction to those performed in Chen's report, which shows In_{Cu} has both charge transition levels in the forbidden gap and none of them is a shallow donor. As said previously, at the time of writing, three are only these two publications which attempt to calculate the electronic structure of $CuInS_2$ by using hybrid functionals: this makes any try of attribution challenging and too arbitrary. This is valid as well for other point defects considered in the calculations in one report but neglected in the other one, such as V_S. Additionally, in both reports, complex defects such as (V_S -V_{Cu}) are not studied, although they might have charge transition levels in the forbidden gap, as reported in $CuInSe_2$ and $CuGaSe_2$ [84]. For similar reasons, the attribution of the deep donor at about 300 meV from the conduction band to In_i would be forced given the absence of other options, as it could be related to other defects which are just not taken into account in the theoretical calculations.

5.6 Summary of defects in CuInS$_2$ absorber layers

As already discussed in section 2.6, there has been no general agreement on the activation energies of the shallow defects in CuInS$_2$, making any progress in understanding the recombination processes in this material challenging.

In this chapter the electronic structure of CuInS$_2$ has been deeply analysed mostly by low temperature photoluminescence spectroscopy. Absorbers deposited under Cu-excess at high temperature (650 °C) show high electronic quality as confirmed by the observation of the excitonic emission and by the low relative intensity of the deep PL signal compared to the band edge emissions. This last feature allows a detailed study of the shallow donor-acceptor transitions characterizing the PL spectra at low temperature. Three main DA emissions are found, named DA1, DA2 and DA3 and they can be attributed to the radiative recombination between a common donor at about 30 meV from the conduction band and three shallow acceptors at about 105 meV, 145 meV and 170 meV from the valence band. Two of these three acceptors are also found by admittance spectroscopy, The DA1 emission is observed mostly for samples with composition close to the stoichiometry, whereas the DA2 emission dominates the spectra measured on Cu-rich absorbers. The DA3 emission is likely present also in Cu-rich as suggested by admittance spectroscopy, but it cannot be resolved in PL as it is hidden by the DA2 emission. It is, instead, well resolved and dominates the band edge luminescence in CIS samples grown under slight Cu-deficiency, but still close to the stoichiometric value, which are deposited on substrates coated with NaF.

The high quality of the absorbers investigated is reflected also in the observation of phonon replicas of the main shallow DA transitions, which questions the existence of a second deeper donor (at about 70-80 meV): this defect, in fact, has been suggested in the past to explain the emission that in this work is attributed to the first replica, whereas the other replicas were always hidden by the deeper band close to 1.2 eV.

The low energy side of the PL spectra is characterized by the two deep broad band close to 1 eV and 1.2 eV. Based on the temperature and excitation dependent PL, it is believed they are related to two DDA transitions with a significant contribution of phonon coupling. A deep donor at about 300 meV from the conduction band is proposed as responsible for the band close to 1 eV.

By comparing the experimental findings of this chapter with recombination models proposed in the past, a revised and more accurate shallow defects model has been given. Additionally, the comparison with the only two reports on theoretical calculations on CuInS$_2$ performed with hybrid functionals gives some preliminary feedbacks about the nature of the defects found in this thesis. The three shallow acceptors are likely related to V_{Cu} and to the first charge states of Cu$_{In}$ and V_{In}, whereas a possible candidate for the shallow donor is Cu_i.

The revised recombination model elaborated in this chapter shows a remarkable similarity to the results obtained for CuInSe$_2$ and CuGaSe$_2$. In fact, it is well known both these two selenium-based compounds have recombination models for shallow defects which include a shallow donor and two shallow acceptors, with a predominance that depends on the composition of the absorbers [159, 160]. Additionally, in CuInSe$_2$ a third shallow acceptor has been observed when sample are deposited under specific growth conditions, such as high Se overpressure [161], while in $CuGaSe_2$ the presence of a third shallow DA transition is still unclear [90]. Another relevant similarity is found between $CuInS_2$ and $CuGaSe_2$: they both show at low temperature a double peak deep band at energies about 0.5-0.6 eV below the band gap and in both cases the PL spectra acquired at room temperatures are dominated by the deeper of these bands [90]. The deeper of these bands in $CuGaSe_2$ (close to 1.1 eV) has been explained by considering a deep donor at about 350-400 meV from the conduction band, which is in line with what has been proposed for the DDA2 band in $CuInS_2$.

Still, more accurate theoretical calculations and more experiments are required to get new insights into the complex electronic structure of this semiconductor and to correlate the experimental evidences, particularly for deep defects, to specific recombination centers.

Chapter 6

Conclusions and outlook

$Cu(In,Ga)S_2$ is an interesting semiconducting material given its tunable band gap between 1.5 and 2.4 eV, depending on the gallium concentration in the alloy: this makes it a good candidate as absorber in both single- and multi-junction solar cells. Despite a lot of efforts undertaken in the past to improve the performance of solar cells based on CIGS, they still suffer from low efficiency, especially when compared to their counterpart CIGSe, which show efficiency as high as 23.3 % [10].

The interest for the sulphide compound arose again in 2016: by means of a deposition process carried out at very high temperatures and with a Cu-poor absorber, the record of power conversion efficiency of 15.5 % could be achieved [26], whereas all previous records have been attained with Cu-rich absorbers. This breakthrough leads one to wonder by which mechanism the deposition temperature and the absorber composition affect the performance of the final photovoltaic devices. The aim of this thesis was to shed light on these aspects, particularly investigating the electronic properties of bare $CuInS_2$ absorber layers.

In the first part, the (micro-) structural properties of the absorber layers are investigated, as a function of the composition and growth temperature. In line with findings reported in literature, Cu-rich absorbers exhibit better structural properties compared to Cu-poor layers, reflected in larger grains and lower density of planar defects, together with a (112) preferred orientation. The structural properties of the absorbers seem to be rather independent on the deposition temperature, within the range investigated (550 °C → 590 °C).

The optoelectronic properties are mainly investigated by photoluminescence (PL) spectroscopy, which allows the determination of the quasi Fermi level splitting (QFLS). The QFLS is a mark of the recombination activity within the absorber and represents an upper limit of the open circuit voltage. The QFLS strongly depends both on the composition and on the process temperature.

The analysis performed on a first set of samples deposited on Mo-coated soda lime glass (SLG) reveals that an increment of the deposition temperature leads to an increase of the QFLS, independently of the specific growth process or composition. The higher QFLS is also reflected in an improvement of the Voc in the finished devices. The increment of the QFLS is found to correlate with the lowering of the concentration of a defect which manifests itself with a PL band close to 0.85 eV. Thus, this defect is a major recombination center and limits the QFLS of the CIS samples.

A second set of samples deposited on Mo-coated HT glass at 650 °C is used to investigate the effect of a further increment of deposition temperature (comparable to that used to fabricate the champion device). The composition of these samples is also varied systematically to look at its effect on the electronic properties of the absorber layers. Cu-rich samples deposited at this high temperature do show an increase of the QFLS (up to 875 meV), whereas the QFLS of the Cu-poor absorbers remains unchanged (compared to the sample deposited on SLG and at lower temperature): this different behaviour is attributed to the lack of sodium in the substrate used (HT glass), which could significantly affect the quality of the absorbers grown under Cu deficiency. Overall, Cu-poor absorbers always show lower QFLS than Cu-rich ones, in contrast to the trend observed in selenides. A comparison of the QFLS and Voc between the two systems (sulphides and selenides) clearly points out that the lower efficiencies exhibited by CIGS-based solar cells are mainly caused by a lower intrinsic optoelectronic quality of the corresponding absorbers, as they show a much higher QFLS loss (or Voc loss) than CIGSe absorber (or –based devices).

The set of CIS samples deposited at 650 °C is investigated also by means of low temperature photoluminescence to gain more insights about the electronic structure of this semiconductor. Two main donor-acceptor transitions dominate the band edge luminescence, DA1 and DA2; they are explained as radiative recombination between a common donor placed at about 30 meV from the conduction band and two shallow acceptors, A1 at 105 meV and A2 at 145 meV from the valence band. A1 is more abundant in samples with a composition close to the stoichiometry, while A2 dominates in Cu-rich samples. A third acceptor at about 170 meV from the valence band is detected when stoichiometric samples are grown on Mo-coated HT glass with an additional Na source (in the present work with NaF as precursor). The diffusion of sodium into the absorber leads to a reduction of the DA1 transition, making the DA3 emission observable, which otherwise would be hidden.

The presence of a shallow donor and three shallow acceptors strongly resembles the shallow defects electronic structure found in $CuInSe_2$, remarking the similarity between the two compounds. By comparing the experimental findings of this thesis to the theoretical calculation performed in the past on the $CuInS_2$ compound, A1 is tentatively attribute to V_{Cu}, while A2 and A3 to first charge states of Cu_{In} and V_{In}.

The high quality of the absorbers investigated allows the detection (for the first time for this semiconductor) of phonon replicas of the three shallow DA emissions. A second deeper donor has been proposed in the past as responsible of an emission red shifted compared to the main DA1 or DA2 transition. The present work demonstrates that these emissions are just the first phonon replica of the main transitions, hence there is no need of a second shallow donor to explain the features observed in low temperature PL spectra. All these observations lead us to propose a revised model for shallow defects in $CuInS_2$.

Finally, preliminary analysis conducted on the deeper bands which always appear at low temperature, the one close to 1-1.05 eV and the one close to 1.2-1.25 eV, suggest they may be attributed to donor-acceptor transition where at least one deep donor is present. Additionally, the high broadening observed for both these bands are likely due to the strong phonon coupling characteristic of deep defects. A deep donor placed at about 300 meV from the conduction band is proposed as responsible of the 1 eV band, which is also observed in room temperature PL spectra.

Thus, the results discussed in this thesis represent a progress beyond the state of the art in several aspects of the comprehension of the complex electronic structure of $CuInS_2$; they can be considered as a starting point for future research to optimize and characterize further this material, in order to improve its optoelectronic quality, consequently the efficiency of solar cells.

The presented work raised further questions that need to be addressed in the future for a more complete understanding of the electronic structure of this material and its consequences for the efficiency of solar cells. Some of them are outlined in the following.

Two-stage processes have been used to grow Cu-rich samples, as they show better morphology to fabricate solar cell. However, 2-stage Cu-rich absorber always show lower QFLS values than 1-stage Cu-rich ones. The reason is still unclear; a further optimization of the 2-stage process might be needed, by employing also HT glass to perform deposition at very high temperatures. A gain in QFLS, if reached, could be translated into higher Voc of the finished devices based on two stage absorbers. Alternatively, 1-stage process could be optimized, focusing on morphology improvement to avoid deep trenches and voids within the thin films, thus to make them suited for working devices with negligible shunting behaviour.

Solar cells based on Cu-rich absorbers show also strong interface recombination, as confirmed by temperature dependent open circuit voltage analysis. Mohit Sood at LPV has shown that the interface can be improved by treating bare absorbers with sulphur containing solutions; although improved, interface recombination still remain [124]. Similar interface issues have been found in solar cells based on $CuInSe_2$: in this case, a post deposition treatment based on evaporation of In and Se could fix the problem of interface recombination as main recombination channel [162]. Therefore, in a similar way, it would be worth trying to develop an analogous treatment for sulphide absorbers based on In and S evaporation. These improvements, if achieved, would lead to a drastic reduction of the loss found in this work between QFLS and Voc for Cu-rich absorbers and devices.

Even improving the interface recombination of the final devices, the QFLS of the CIS absorbers would still be limited to values below 900 meV, therefore new strategies need to be undertaken to boost the electronic quality of the thin films and to reach efficiencies as high as the current record device. Particularly Cu-poor absorbers show QFLS around 700 meV. A key role might be played by sodium, thus high temperature depositions of films grown under Cu-deficiency could be carried out by using NaF as precursor or as post deposition treatment. Additionally, Ga alloying and band gap grading (by employing 3-stage process) might help to improve charge carrier collection and reduce back surface recombination.

CIS films show higher stability in terms of QFLS when exposed to air, in contrast to the findings in selenides. From the author's point of view, it would be worth investigating deeply this trend, including different kind of absorbers, such $CuGaSe_2$, $CuGaS_2$ and tellurium based chalcopyrites, such as $CuInTe_2$. This analysis could shed light on whether the stability of the QFLS correlates to higher Gibbs free energy of the oxidation process.

More studies need to be conducted for a better understanding about the deep defects in CIS, which lead to recombination transitions close to 0.85 eV, 1.05 eV and 1.25 eV. By comparing experimental results to improved theoretical calculations, more insights about their chemical nature (e.g. In_{Cu}, Cu_{In}, V_S..) could be gained and new strategies of absorber deposition or post deposition treatments can be developed to improve the electronic quality of this semiconducting material.

Summarizing, there are still a lot of topics which need to be investigated for a deeper understanding of the potential of this semiconducting material; addressing one topic or answering one question could lead to more questions. However, this thesis has shed light on some fundamental properties of this material and the knowledge acquired throughout this work may represent an essential key for future research in this field.

Appendix Chapter 3

Annex 3.1: comparison of soda lime glass and high-temperature glass

To investigated the effect of the process temperature on the properties of the CIS layers, two different glass substrates have been employed in this thesis work: the standard soda lime glass (SLG) and a high softening temperature(a) glass (HT glass). The second one is needed as temperatures as high as 650 °C have been used during the growth processes. With these deposition temperatures, the SLG would bend during the growth because of its annealing point(a), which is about 550 °C. The linear coefficient of thermal expansion (CTE) has been taken into account as well in the selection of a proper glass for high temperature depositions. The thermal mismatch between glass and CIS layer can cause an increment in the defect density in the chalcopyrite layer, as proposed in [39] for $Cu(In,Ga)Se_2$. SLG has a CTE of $8-9\times10^{-6}$ /°C which matches well the CISe one, i.e. about 8.6×10^{-6} /°C as measured in [163]. A similar value has been determined for $CuInS_2$ [164]. By decoupling the influence of the substrate chemical composition from the CTE, Hultqvist et al. found in [39] that a lower CTE (than standard SLG) correlated with lower open circuit voltage.

Based on these requirements (i.e. high softening point and a CTE close to the standard SLG), the N-LASF9 Schott glass has been chosen: it has an annealing point of 700 °C and a linear CTE of about 8.4×10^{-6} /°C. In order to get an estimation about its composition, an XRF analysis has been performed on both a standard SLG and on this Schott glass. The results are displayed in table A3.1.

The HTG has an amount of La close to 5.5 %. This comes from the corresponding oxide, i.e. La_2O_3. Given the high molecular weight of this oxide (325.8 u), it is the main constituent of the HTG, i.e. about 25 % of the glass weight. This is the reason why its technical name includes "LA". As it is possible to see from the listed values, the HTG contains a lower amount of both Na and K compared to SLG (by a factor of 2.7 and 16.2, respectively). This substantial difference in the alkali concentration may significant affect the properties of the absorber layers as a lower diffusion, thus a lower concentration in the final films is expected.

(a): the softening and annealing temperatures of a glass are related to its viscosity. The viscosity of glass decreases with temperature. Particularly, the annealing point is defined as the temperature corresponding to viscosity of $10^{13.4}$ Poise, whereas at the softening temperature the viscosity assumes a value of $10^{7.6}$ Poise [165].

Table A3.1: chemical composition given in atomic % of soda lime glass (SLG) and high temperature glass (HTG) determined by XRF analysis. In the first part of the table the common elements are listed, then the one found either in SLG or in HTG.

Element	SLG atomic %	HTG atomic %
Na	9.4279	3.5087
Si	23.3687	12.1673
Ca	2.1714	0.0525
K	0.3893	0.0239
Fe	0.0046	0.0262
Zr	0.0033	1.9855
P	0.0021	0.0166
O	61.7915	62.1424
Sr	0.0008	0.0028
As	0.0248	
Rb	0.0006	
Mg	2.2431	
Al	0.5039	
S	0.0681	
Ti		5.0592
Zn		1.7695
Nb		2.6727
Ba		5.0072
La		5.5472
Hf		0.0183

Appendix Chapter 4

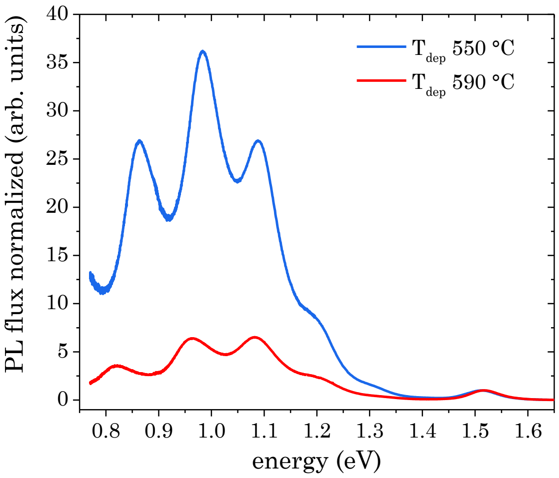

Figure A4.1: room temperature photoluminescence spectra of Cu-rich two-stage $CuInS_2$ absorbers (Cu/In 1.6). Spectra normalized to the band gap luminescence (around 1.51 eV). The temperature indicated in the legend refers to second stage of the deposition. In both cases, the first stage has been kept constant at 250 °C.

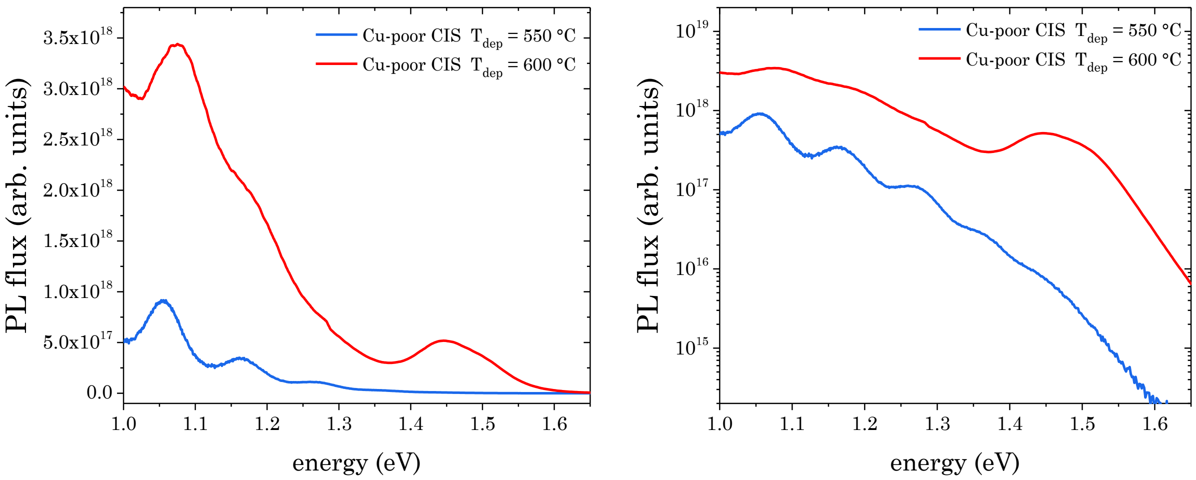

Figure A4.2: room temperature photoluminescence spectra of Cu-poor CIS absorbers (Cu/In about 0.95) deposited following the one-stage process with a substrate temperature of 550 °C and 600 °C, respectively. The spectra are displayed in (left) linear and (right) log scale. The spectra have been acquired exciting the two samples with the same flux. An increment of deposition process by +50 °C leads to a significant improvement of the band gap luminesce, which is almost absent in the sample deposited at lower temperature precluding any analysis in terms of QFLS.

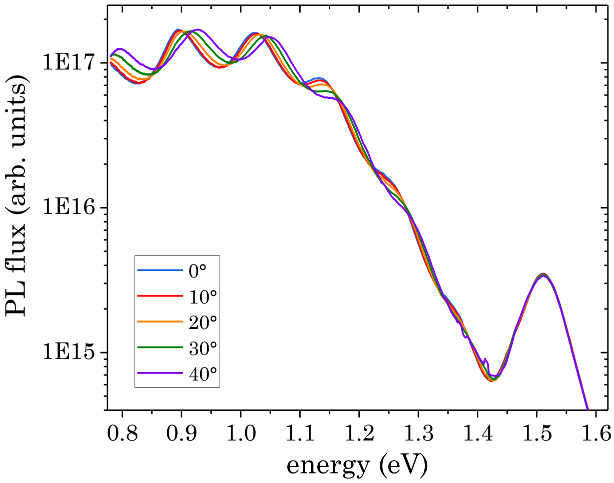

Figure A4.3: angle resolved photoluminescence of a Cu-rich 2-stage CIS absorber grown at 250°C+550°C. The PL spectra have been measured in step of 10° from angles between 0° (normal incidence) to 40° and plotted rescaled by a factor of $\cos^2\theta$. The interferences fringes (for energies below 1.4 eV) shift with increasing angle, proving they are due to different defect-related bands. Additionally, for different angles, the high energy wing of the band gap luminescence does not change, thus the QFLS measurement and evaluation is not affected by the interference pattern, as also proved in [128].

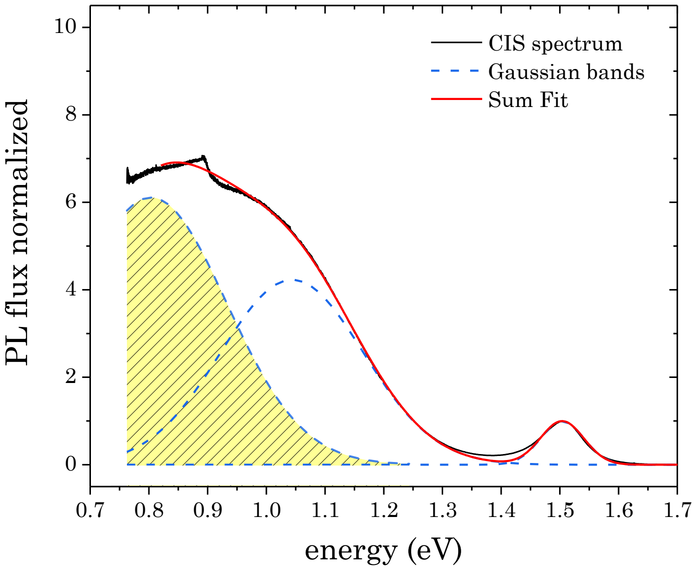

Figure A4.4: example of fitting performed on a Cu-rich one-stage CIS room-temperature PL spectrum together with three single Gaussian bands. The deeper band centered at around 0.83 eV is highlighted in yellow. This PL spectrum has been measured on a Cu-rich deposited at 550 °C, which shows a QFLS of about 910 meV at an equivalent illumination of 16 suns. The relative ratios calculated for each Gaussian band are displayed in figure 4.9.

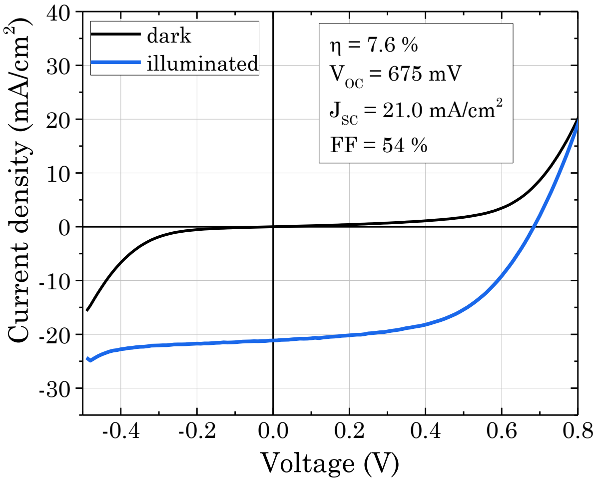

Figure A4.5: J –V characteristic under dark and under AM1.5 illumination for the best solar cell based on a Cu-rich one-stage absorber (Cu/In about 1.6) deposited at high temperature (590 °C), with a device area of around 0.2 cm^2.

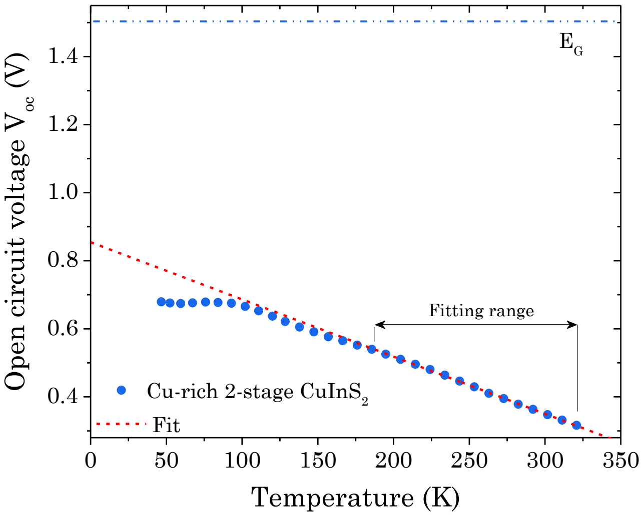

Figure A4.6: open circuit voltage as a function of temperature for a Cu-rich two-stage $CuInS_2$ sample. The solar cell layers stack include CdS as buffer layer, (i)-ZnO + AZO as window layer and Ni/Al as front contact. The fitting performed within a range of 200-325 K clearly shows that the extrapolated activation energy at 0 K (around 0.85 V) is well below the band gap energy (around 1.5 eV). Hence the device performance is strongly influenced by a significant interface recombination.

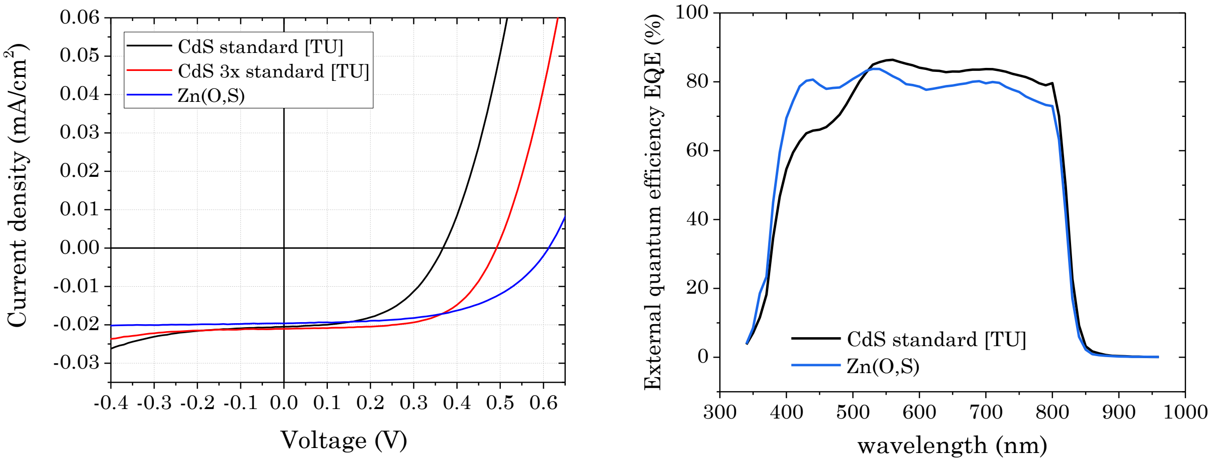

Figure A4.7: (left) J-V characteristics of devices made from Cu-rich 2-stage absorbers deposited at 250 °C + 550 °C with different kind of buffer: the V_{OC} clearly improves if higher TU concentration is used during the CBD or if the CdS is replaced by Zn(O,S) buffer layer. (right) external quantum efficiencies of 2 devices employing respectively a CdS buffer layer deposited with standard TU concentration and Zn(O,S). Although there is a significant gain at low wavelength due to the wider band gap of the Zn(O,S) (thus less absorption), the whole J_{SC} is not affected (see J-V plot on the left) due to lower average EQE. The shape of the EQE with Zn(O,S) may indicated it is mainly reduced by a higher reflectivity of the corresponding device.

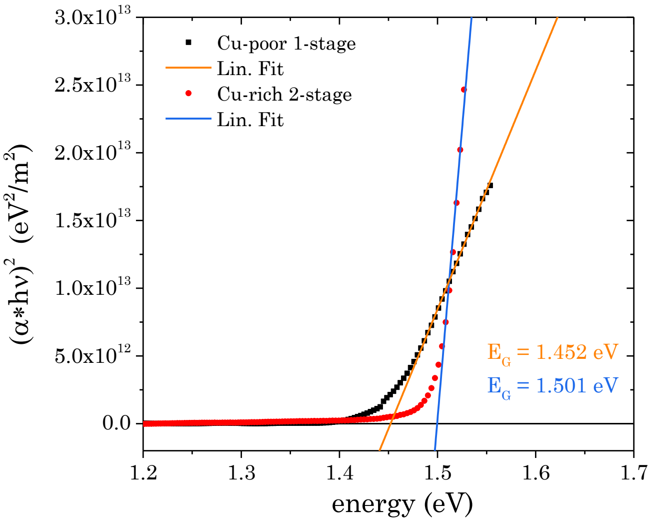

Figure A4.8: Tauc plot of Cu-poor 1-stage and Cu-rich 2-stage $CuInS_2$ thin films deposited on SLG. The band gaps determined from the interception of the linear fit and the energy-axis are given. The Cu-poor clearly shows lower band gap of the Cu-rich one.

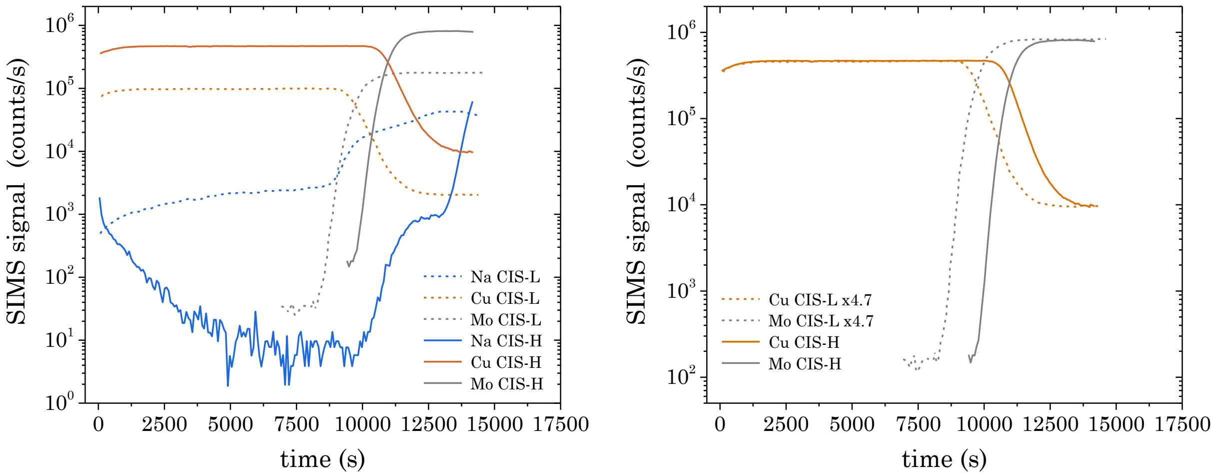

Figure A4.9: (left) SIMS profiles of Na, Cu and Mo for the two Cu-poor CIS samples with a Cu/In = 0.95 deposited on Mo-coated SLG at 600°C (labelled as CIS-L) and on Mo-coated HT glass at 650 °C (labelled as CIS-H). As both samples have the same Cu/In and they have been deposited on a similar Mo layer (500 nm), the SIMS (bulk) signals regarding these two samples should be the same. This is not the case as the two samples have been analysed with different acquisition parameters (such as different filters), which alter the collected counts. In fact, multiplying both signals related to CIS-L by a factor of 4.7 (as shown on the right), there is a perfect match of the SIMS signal for Cu and Mo between the two samples. Thus, it is reasonable to assume that the Cu profile is very similar for both samples and it is possible to get rid of the influence of the acquisition parameters if the Na signal is normalized to the Cu one, as figure 4.16 reports. The different trend with time between the two samples (at about 10 000s) for both Cu and Mo is likely due to a different thickness of the layers analysed.

Appendix Chapter 5

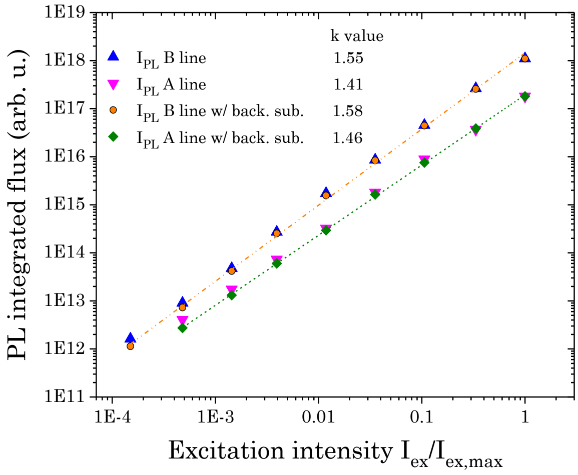

Figure A5.1: Excitation intensity dependence of the integrated PL flux of the A and C lines emissions taken from the sample with a Cu/In ratio of 1.8, with the corresponding k values obtained by fitting the trends with a single power law. Both lines have been analysed with and without subtracting a constant background in the PL spectra to take into account the background noise of the PL setup. This background affects the trends mostly at low excitations, with a greater influence on the A line due to its lower PL intensity compared to the B line, as seen by the variation of the *k* value as well. $I_{ex,max}$ is about 10^4 mW/cm^2, which correspond to a flux of about 6.7×10^{19} /(cm^2 × s).

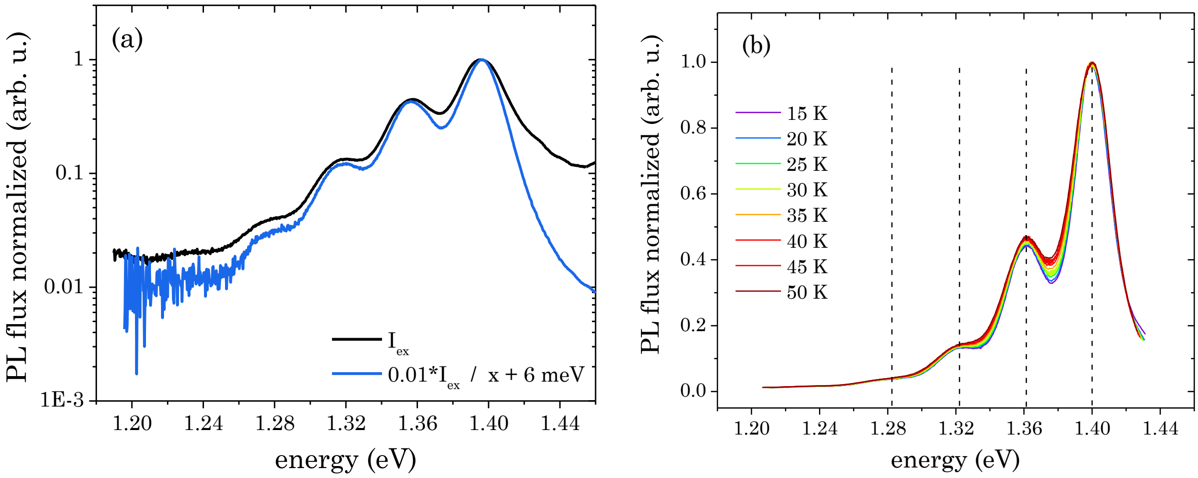

Figure A5.2: (a) comparison of photoluminescence spectra of Cu-rich CIS acquired at 10 K with two different excitation intensity (the variation is about two order of magnitude). The spectra have been normalized also in energy, i.e., the spectrum measured at lower excitation has been shifted to higher energy by 6 meV. The overlapping of the peaks is a clear indication of the phonon replica nature of the peaks at lower energies and lower intensities: in fact it is unlikely that several defect which generate the above mentioned peaks have all the same blue shift with increasing excitation, thus same Coulomb energy change as a function of the excitation. (b)

Comparison of photoluminescence spectra of Cu-rich CIS acquired with the same excitation intensity in a temperature range 15 K - 50 K: the spectra have been normalized both in intensity and in energy position taking the main transition at 1.40 as reference. The vertical dash line are drawn with a spectral distance of 39 meV (i.e. phonon energy).

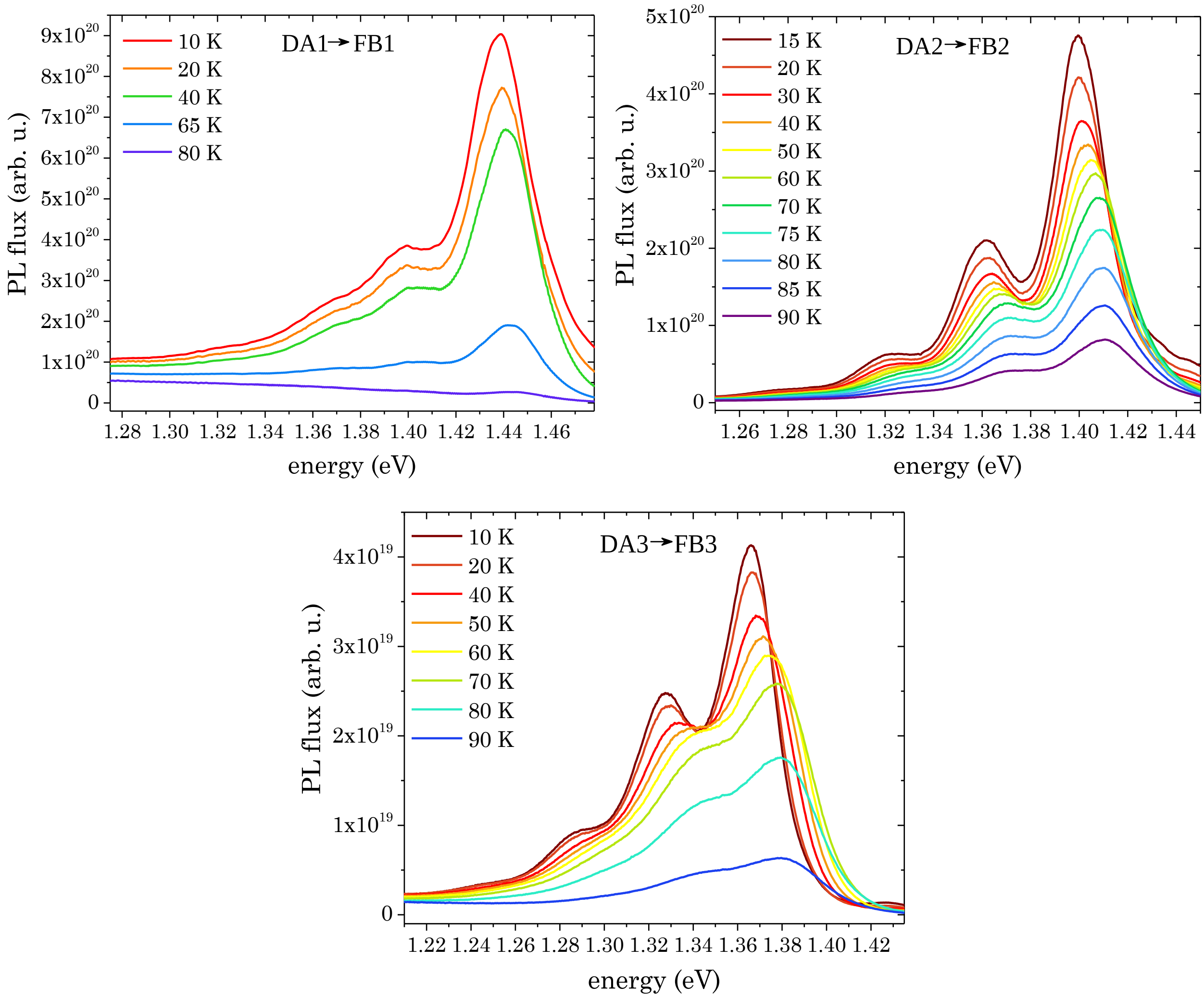

Figure A5.3: temperature dependent photoluminescence spectra between 10/15 K and 90 K measured with constant excitation intensity on: (top-left) 1-stage stoichiometric CIS absorber (Cu/In 1.00, T_{dep} 650 °C); (top-right) 1-stage Cu-rich CIS absorber (Cu/In 1.8, T_{dep} 650 °C); (bottom) 1-stage "CIS w/ NaF" absorber (Cu/In 0.98, T_{dep} 650 °C). The main emissions and related phonon replicas blue shifted with temperature. The main shift for all cases occurs between 40 K and 70 K, where the shallower defect is emptied, thus leaving a free-to bound transition, as confirmed by excitation intensity dependent measurement reported in figure 5.10 and 5.16. The very similar temperature range where the shallower defect is emptied suggests all DA emissions have a common shallower defect, which is a donor as explained in the main text in chapter 5.

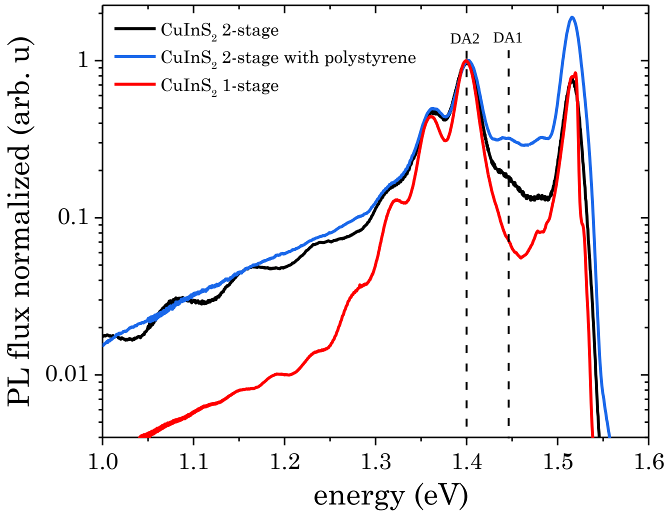

Figure A5.4: low temperature photoluminescence spectra acquired at 10 K of Cu-rich $CuInS_2$ absorbers grown in 2-stage process, with and without scattering layer (polystyrene layer). The scattering layer is needed for this kind of absorber due to its morphology (very smooth surface) which enhances interference effect, creating additional bands which can be misinterpreted as defect related band or phonon replica. For comparison, the 1-stage Cu-rich absorber with Cu/In 1.8 (analysed in section 5.1.2) is plotted as well. The DA2, thus, is characteristic also of Cu-rich 2-stage absorbers. Although not fully resolved, the band at 1.44 eV is likely an indication of the presence of DA1 transition. Figure adapted from [129].

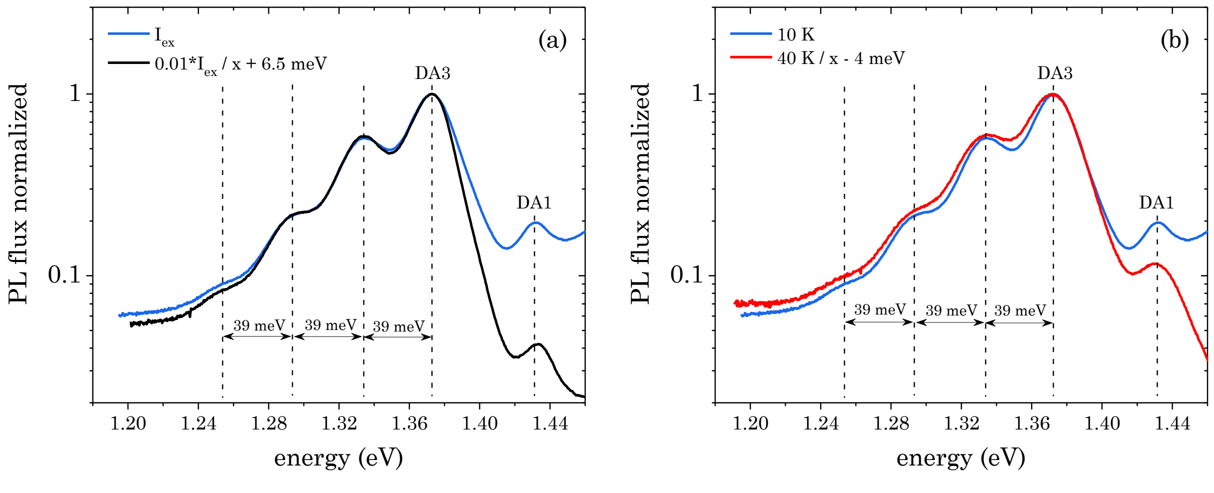

Figure A5.5: semi-logarithmic plot of the normalized photoluminescence flux over the energy of (a) two spectra acquired with different excitation intensity (the excitation has been changed by almost two orders of magnitude) and (b) two spectra measured at 10 K and 40 K respectively. In both cases, (a) and (b), the spectra have been “aligned” also in energy, i.e. the spectrum measured at lower excitation and the one measured at 40 K have been shifted by +6.5 meV and – 4 meV to overlap the DA3 peak. The dashed vertical lines are drawn with a spectral distance of 39 meV (LO phonon energy). In addition, the DA1 transition is also marked with a dotted line.

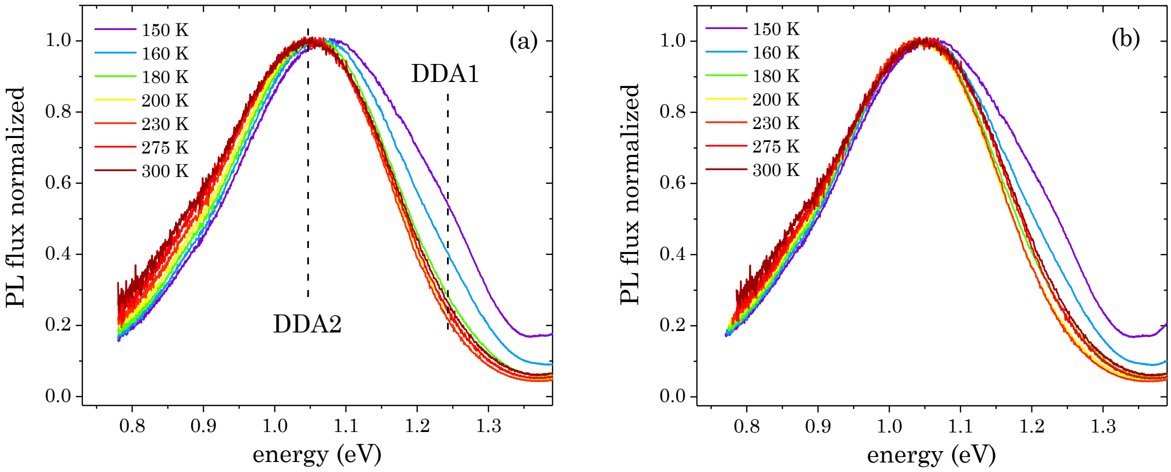

Figure A5.6: (a) photoluminescence spectra of Cu-rich 1-stage CIS absorber deposited on Mo-coated HT glass at 650°C acquired in the temperature range of 150 K to 300 K. The spectra have been normalized to the maxima of the DDA2 band. (b) same as (a), but the spectra have been "normalized" also along the energy-axis, taking into account the band gap lowering with temperature: all spectra, except the 300 K one, have been shift red by the same amount of the band gap shift compared to the band gap luminescence peak 300 K, taken as reference. E.g., the spectrum measured at 150 K has a band gap peak at 16 meV higher than 300 K, thus it has been red shifted by 16 meV. The band gap luminescence bands are not shown for a better view of the deep bands.

First of all, the DDA1 band completely quenches for temperatures above 200-230 K. Although at first sight the DDA2 could show a slight red shift, for investigations over a wide temperature range (150 K), the band gap shrinking needs to be included. If this is taken into account, see figure A5.6b, then the DDA2 does not show any observable shift when the temperature is raised, which in turn makes the hypotheses of broad density of states as possible origin very unlikely.

List of publications

First-author

1. Lomuscio A., M. Melchiorre, and S. Siebentritt. *Influence of stoichiometry and temperature on quasi Fermi level splitting of sulfide CIS absorber layers*. in *2018 IEEE 7th World Conference on Photovoltaic Energy Conversion (WCPEC) (A Joint Conference of 45th IEEE PVSC, 28th PVSEC & 34th EU PVSEC)*. 2018. IEEE.
2. Lomuscio, A., T. Rödel, T. Schwarz, B. Gault, M. Melchiorre, D. Raabe, and S. Siebentritt, *Quasi-Fermi-Level Splitting of Cu-Poor and Cu-Rich* $CuInS_2$ *Absorber Layers.* Physical Review Applied, 11(5): p. 054052, 2019.
3. Lomuscio A., M. Sood, M. Melchiorre, and S. Siebentritt, *Phonon coupling and shallow defects in* $CuInS_2$. Physical Review B, 101(8), p: 085119, 2020.
4. Lomuscio, A., M. Sood, and S. Siebentritt, *Detection of a third shallow acceptor in* $CuInS_2$ *through NaF incorporation,* in preparation, 2020

Co-author

5. Arnou, P, A. Lomuscio, T.P. Weiss, D, Siopa, G. Giraldo, E. Saucedo, M.A. Scarpulla, P. J. Dale, *Continuous-wave laser annealing of metallic layers for* $CuInSe_2$ *solar cell applications: effect of preheating treatment on grain growth*, RSC Advances, 10(1), 2020.
6. Sood, M, H. Elenzeery, D. Adeleye, A. Lomuscio, F. Werner, F. Ehre, M. Melchiorre, and S. Siebentritt, *Absorber composition: a critical parameter for the effectiveness of heat treatments in chalcopyrite solar cells*, Progress in Photovoltaics: Research Applications, 1-14, 2020.
7. Sood, M, A. Lomuscio, F. Werner, P. J. Dale, M. Melchiorre, and S. Siebentritt, *Passivating surface defects in Cu-rich copper indium disulphide solar cells using sulphur treatment*, submitted, 2020
8. Schwarz, T, A. Lomuscio, S. Siebentritt, B. Gault, and D. Raabe, *On the chemistry of extended defects in* $CuInS_2$ *films*, in press, 2020
9. Siopa, D., K. Hajraoui, S. Tombolato, A. Lomuscio, F. Babbe, M. H. Wolter, P. Anacleto, K. Abderrafi, Sascha Sadewasser, and P. J. Dale, *Thin film solar cells via electrochemical selective area deposition for concentrator photovoltaics application*, submitted, 2020

10. Wolter, M. H, D. Siopa, A. Lomuscio, T. P. Weiss, P. Thiele, P. J. Dale, R. Carron, E. Avancini, B. Bissig, S. Buecheler, P. Jackson, W. Witte and S. Siebentritt, *Applying a surface treatment to semiconducting thin films to eliminate interference effects*, submitted, 2020.
11. Levine I., K. Shimizu, A. Lomuscio, M. Kulbak, C. Rehermann, Arava Zohar, S. Siebentritt, H. Ishii, T. Dittrich, N. H. Nickel, A. Kahn, G. Hodes and D. Cahen, *Direct detection and quantification of in-gap states in Halide Perovskite by highly sensitive variable energy ultraviolet photoelectron spectroscopy*, in preparation, 2020.

Conference presentations

1. Lomuscio, A., T. Rödel, M. Melchiorre and S. Siebentritt, *Quasi-Fermi-Level Splitting of Cu-Poor and Cu-Rich $CuInS_2$ Absorber Layers*, 27th PVSEC, Otsu, 2017. Oral presentation.

2. Lomuscio A., M. Melchiorre, and S. Siebentritt. *Influence of stoichiometry and temperature on quasi Fermi level splitting of sulfide CIS absorber layers*. 7th World Conference on Photovoltaic Energy Conversion (WCPEC) (A Joint Conference of 45th IEEE PVSC, 28th PVSEC & 34th EU PVSEC), Waikoloa, 2018. Poster presentation.

3. Lomuscio A., M. Sood, M. Melchiorre, and S. Siebentritt, *Phonon coupling and shallow defects in $CuInS_2$*, Materials research society (MRS) Spring Meeting & Exhibit, Phoenix, 2019. Oral presentation.

Acknowledgements

Although the PhD candidate is the main responsible for his own project, many people are always involved in a PhD project. This has been surely my case: they helped me as a guide, giving feedbacks or sharing ideas, they helped me to get data presented in this work and they encouraged and motivated me throughout this period.

At the top of the list there is Susanne Siebentritt: a supervisor, a mentor and a friend. She leads a wonderful team, the LPV, and she gave me the opportunity to be part of it. I really thank her for this chance. I'm so grateful to have been working on a challenging project, for the fruitful discussions and for giving me the opportunity of sharing my results at international conferences around the world.

I also thank Thomas Schmidt and Simona Binetti for being part of the thesis supervision committee as well as Roland Scheer and Alex Redinger for the willingness to join the dissertation committee.

A big thanks goes to Patricia Ramoa and Thomas Schuler: most of the times they are "behind the scenes" but their work is essential for the team. Thanks to Patricia for her endless paper working (including placing orders or travel authorizations), while I thank Thomas for his technical support (above all leak tests and pump maintenances) as well as for scheduling kitchen meetings.

Most of the results presented in this work have been obtained by means of PL spectroscopy. Thus, a very special thanks goes to the "PL team members" of the LPV, with them I discussed about the measurements and their interpretations as well as tips to avoid artefacts during experiments. Above all, I would like to thank Conrad Spindler, Finn Babbe and Max H. Wolter for explaining and teaching me all the important practical details about measurements in the "dark room" and for transferring to me their knowledge, above all about defect interpretation.

I would like to thank as well the members of the "sulphide team": Mohit Sood, Damilola Adeleye and Sudhanshu Shukla. I especially thank Mohit, who performed a lot of electrical characterizations and buffer layer optimizations; thanks to him, we could confirm some of the defects (found by PL) also by admittance spectroscopy.

A big thanks to Michele Melchiorre is needed for his work on the baseline process and KCN etching; but above all, for his patience on doing a countless number of EDX and cross sections analysis. His efforts and willingness in doing so many measurements made possible the optimizations of deposition processes carried out in two new PVD systems.

I would like to thank Tobias Bertram and Tobias Rödel, former members of the LPV, who contributed to put one of the two new PVD into service. A thanks goes to Daniel Siopa as well, for the Raman measurements.

Special thanks go to all former and current members of the LPV, LEM and SPM group: the friendly atmosphere in our groups makes the time at work very enjoyable.

Moreover, I would like to thank Torsten Schwarz and Baptiste Gault from MPIE for the TEM and APT measurements and for the rewarding discussions within the collaboration in the CorrKest project. Additionally, I thank Natalie Valle from LIST for the SIMS measurements.

Last but not least, a very special thanks goes to my family and to Maria Elisa, for always supporting and motivating me during the PhD, in both good and tough times.

I'm certainly forgetting to thank some people who contributed somehow to achieve this goal. If you are not mentioned here, forgive me, and I can just say: *Grazie*!

Bibliography

1. *https://unsdg.un.org/resources/shared-responsibility-global-solidarity-responding-socio-economic-impacts-covid-19,* 2020, United Nations; Available from:
2. Leyen, U.v.d., *Adoption of the European Green Deal Communication,* 2019, Brussels; Available from: https://ec.europa.eu/commission/presscorner/detail/en/speech_19_6749
3. *https://unfccc.int/process-and-meetings/the-paris-agreement/the-paris-agreement,* 2015, United Nations.
4. Fraunhofer Institute for Solar Energy Systems, ISE, *Photovoltaics report,* 2019, Freiburg; p. 15-25, Available from: https://www.ise.fraunhofer.de/en/renewable-energy-data.html
5. Creutzig, F., et al., *The underestimated potential of solar energy to mitigate climate change.* Nature Energy, 2017. 2(9): p. 17140.
6. Green, M.A., et al., *Solar cell efficiency tables (Version 55).* Progress in Photovoltaics: Research Applications, 2019. 28(NREL/JA-5900-75827).
7. UNEP, Hertwich, E., et al., *Green Energy Choices: The benefits, risks, and trade-offs of low-carbon technologies for electricity production. Report of the International Resource Panel,* 2016, (eds.), p. 33, Available from: https://www.resourcepanel.org/reports/green-energy-choices-benefits-risks-and-trade-offs-low-carbon-technologies-electricity
8. Carron, R., et al., *Advanced Alkali Treatments for High-Efficiency* $Cu(In,Ga)Se_2$ *Solar Cells on Flexible Substrates.* Advanced Energy Materials, 2019. 9(24): p. 1900408.
9. Shockley, W. and H.J. Queisser, *Detailed balance limit of efficiency of p-n junction solar cells.* Journal of applied physics, 1961. 32(3): p. 510-519.
10. Nakamura, M., et al., *Cd-free* $Cu(In,Ga)(Se,S)_2$ *thin-film solar cell with record efficiency of 23.35%.* IEEE Journal of Photovoltaics, 2019. 9(6): p. 1863-1867.
11. Quiroz, C.O.R., et al., *Balancing electrical and optical losses for efficient 4-terminal Si–perovskite solar cells with solution processed percolation electrodes.* Journal of Materials Chemistry A, 2018. 6(8): p. 3583-3592.
12. Shen, H., et al., *Mechanically-stacked perovskite/CIGS tandem solar cells with efficiency of 23.9% and reduced oxygen sensitivity.* Energy Environmental Science, 2018. 11(2): p. 394-406.
13. Kim, D., et al., *Efficient, stable silicon tandem cells enabled by anion-engineered wide-bandgap perovskites.* Science, 2020. 368(6487): p. 155-160.
14. Kim, D.H., et al., *Bimolecular Additives Improve Wide-Band-Gap Perovskites for Efficient Tandem Solar Cells with CIGS.* Joule, 2019. 3(7): p. 1734-1745.
15. Laboratory, N.R.E., *Best Research-Cell Efficiency Chart,* 2020, Available from: https://www.nrel.gov/pv/cell-efficiency.html
16. Nagabhushana, G., R. Shivaramaiah, and A. Navrotsky, *Direct calorimetric verification of thermodynamic instability of lead halide hybrid perovskites.* Proceedings of the National Academy of Sciences, 2016. 113(28): p. 7717-7721.
17. Tell, B., J. Shay, and H. Kasper, *Electrical Properties, Optical Properties, and Band Structure of* $CuGaS_2$ *and* $CuInS_2$*.* Physical review B, 1971. 4(8): p. 2463.
18. Siebentritt, S., *What limits the efficiency of chalcopyrite solar cells?* Solar Energy Materials Solar Cells, 2011. 95(6): p. 1471-1476.
19. Karg, F., *High efficiency CIGS solar modules.* Energy Procedia, 2012. 15: p. 275-282.

20. Kato, T., *$Cu(In,Ga)(Se,S)_2$ solar cell research in Solar Frontier: Progress and current status*. Japanese Journal of Applied Physics, 2017. 56(4S): p. 04CA02.

21. Binsma, J., L. Giling, and J. Bloem, *Phase relations in the system Cu_2S-In_2S_3*. Journal of Crystal Growth, 1980. 50(2): p. 429-436.

22. Mitchell, K.W., G.A. Pollock, and A.V. Mason, *7.3% efficient $CuInS_2$ solar cell*, in *Conference Record of the Twentieth IEEE Photovoltaic Specialists Conference*. 1988: Las Vegas. p. 1542-1544.

23. Scheer, R., et al., *$CuInS_2$ based thin film solar cell with 10.2% efficiency*. Applied Physics Letters, 1993. 63(24): p. 3294-3296.

24. Siemer, K., et al., *Efficient $CuInS_2$ solar cells from a rapid thermal process (RTP)*. Solar Energy Materials Solar Cells, 2001. 67(1-4): p. 159-166.

25. Merdes, S., et al., *$CdS/Cu(In,Ga)S_2$ based solar cells with efficiencies reaching 12.9% prepared by a rapid thermal process*. Progress in Photovoltaics: Research Applications, 2013. 21(1): p. 88-93.

26. Hiroi, H., et al., *New world-record efficiency for pure-sulfide $Cu(In,Ga)S_2$ thin-Film solar cell with Cd-free buffer layer via KCN-free process*. IEEE Journal of Photovoltaics, 2016. 6(3): p. 760-763.

27. Hiroi, H., et al., *960-mV open-circuit voltage chalcopyrite solar cell*. IEEE Journal of Photovoltaics, 2016. 6(1): p. 309-312.

28. Thomere, A., et al., *Chemical crystallographic investigation on Cu_2S-In_2S_3-Ga_2S_3 ternary system*. Thin Solid Films, 2018. 665: p. 46-50.

29. Abrahams, S. and J. Bernstein, *Piezoelectric nonlinear optic $CuGaS_2$ and $CuInS_2$ crystal structure: sublattice distortion in $A^IB^{III}C_2^{VI}$ and $A^{II}B^{IV}C_2^V$ type chalcopyrites*. The Journal of Chemical Physics, 1973. 59(10): p. 5415-5422.

30. Alonso, M., et al., *Optical functions and electronic structure of $CuInSe_2$, $CuGaSe_2$, $CuInS_2$, and $CuGaS_2$*. Physical Review B, 2001. 63(7): p. 075203.

31. Scheer, R. and H.-W. Schock, *Chalcogenide photovoltaics: physics, technologies, and thin film devices*. 2011: John Wiley & Sons.

32. Bodnar, I. and A. Lukomskii, *The concentration dependence of the band gap for $CuGa_xIn_{1-x}S_2$ and $AgGa_xIn_{1-x}S_2$ solid solutions*. physica status solidi, 1986. 98(2): p. K165-K169.

33. Fiechter, S., et al., *On the homogeneity region, growth modes and optoelectronic properties of chalcopyrite-type $CuInS_2$*. physica status solidi, 2008. 245(9): p. 1761-1771.

34. Weber, M., et al., *Microroughness and composition of cyanide-treated $CuInS_2$*. Journal of The Electrochemical Society, 2002. 149(1): p. G77-G84.

35. Scheer, R. and H. Lewerenz, *Photoemission study of evaporated $CuInS_2$ thin films. II. Electronic surface structure*. Journal of Vacuum Science Technology A, 1994. 12(1): p. 56-60.

36. Würfel, P. and U. Würfel, *Physics of solar cells: from basic principles to advanced concepts*. 2016: John Wiley & Sons.

37. Sze, S.M. and K.K. Ng, *Physics of semiconductor devices*. 2006: John wiley & sons.

38. Caballero, R., et al., *High efficiency low temperature grown $Cu(In,Ga)Se_2$ thin film solar cells on flexible substrates using NaF precursor layers*. Progress in Photovoltaics: Research Applications, 2011. 19(5): p. 547-551.

39. Hultqvist, A., et al., *Performance of $Cu(In,Ga)Se_2$ solar cells using nominally alkali free glass substrates with varying coefficient of thermal expansion*. Journal of Applied Physics, 2013. 114(9): p. 094501.

40. Abou-Ras, D., et al., *Formation and characterisation of $MoSe_2$ for $Cu(In,Ga)Se_2$ based solar cells*. Thin Solid Films, 2005. 480: p. 433-438.

41. Kohara, N., et al., *Electrical properties of the $Cu(In,Ga)Se_2/MoSe_2/Mo$ structure*. Solar Energy Materials Solar Cells, 2001. 67(1-4): p. 209-215.

42. Brus, V., et al., *Electrical properties of thin-film semiconductor heterojunctions n-TiO_2/p-$CuInS_2$*. Semiconductors, 2014. 48(8): p. 1046-1050.
43. Kazmerski, L. and G. Sanborn, *$CuInS_2$ thin-film homojunction solar cells*. Journal of Applied Physics, 1977. 48(7): p. 3178-3180.
44. Unold, T., I. Sieber, and K. Ellmer, *Efficient $CuInS_2$ solar cells by reactive magnetron sputtering*, in *Applied Physics Letters*. 2006, AIP. p. 213502.
45. Hwang, H., et al., *Growth and properties of $CuInS_2$ epitaxial layers obtained by chemical vapour transport*. Solar Energy Materials, 1980. 4(1): p. 67-79.
46. Krunks, M., et al., *Growth and recrystallization of $CuInS_2$ films in spray pyrolytic process*. Applied Surface Science, 1999. 142(1-4): p. 356-361.
47. Hodes, G., et al., *Electroplated $CuInS_2$ and $CuInSe_2$ layers: Preparation and physical and photovoltaic characterization*. Thin Solid Films, 1985. 128(1-2): p. 93-106.
48. Walter, T., et al., *Sequential processes for the deposition of polycrystalline $Cu(In,Ga)(S,Se)_2$ thin films: Growth mechanism and devices*. Solar Energy Materials Solar Cells, 1996. 41: p. 355-372.
49. Braunger, D., et al., *An 11.4% efficient polycrystalline thin film solar cell based on $CuInS_2$ with a Cd-free buffer layer*. Solar Energy Materials Solar Cells, 1996. 40(2): p. 97-102.
50. Sood, M., et al., *The effect of chemical potential and composition on the effectiveness of heat treatments in chalcopyrite solar cells*. under review, 2020.
51. Weinhardt, L., et al., *Band alignment at the CdS/$Cu(In,Ga)S_2$ interface in thin-film solar cells*. Applied Physics Letters, 2005. 86(6): p. 062109.
52. Hashimoto, Y., K. Takeuchi, and K. Ito, *Band alignment at CdS/$CuInS_2$ heterojunction*. Applied physics letters, 1995. 67(7): p. 980-982.
53. Rau, U., P. Grabitz, and J. Werner, *Resistive limitations to spatially inhomogeneous electronic losses in solar cells*. Applied Physics Letters, 2004. 85(24): p. 6010-6012.
54. Hála, M., et al., *Highly conductive ZnO films with high near infrared transparency*. Progress in Photovoltaics: Research Applications, 2015. 23(11): p. 1630-1641.
55. Hengel, I., et al., *Current transport in $CuInS_2$:Ga/CdS/ZnO – solar cells*. Thin Solid Films, 2000. 361: p. 458-462.
56. Pankove, J.I., *Optical processes in semiconductors*. 1975, New York: Dover Publications Inc.
57. Unold, T. and L. Gütay, *Photoluminescence Analysis of Thin-Film Solar Cells*. Advanced Characterization Techniques for Thin Film Solar Cells, 2011: p. 275-297.
58. Pelant, I. and J. Valenta, *Luminescence spectroscopy of semiconductors*. 2012: Oxford University Press.
59. Cardona, M. and Y.Y. Peter, *Fundamentals of semiconductors*. 2005: Springer.
60. Wurfel, P., *The chemical potential of radiation*. Journal of Physics C: Solid State Physics, 1982. 15(18): p. 3967.
61. Yakushev, M., et al., *Excited states of the A free exciton in $CuInS_2$*. Applied Physics Letters, 2008. 92(11): p. 111908.
62. Binsma, J., L. Giling, and J. Bloem, *Luminescence of $CuInS_2$: II. Exciton and near edge emission*. Journal of Luminescence, 1982. 27(1): p. 55-72.
63. Hopfield, J.J. in *7th International Conference on the Physics of Semiconductors*. 1964. Paris.
64. Haynes, J.R., *Experimental proof of the existence of a new electronic complex in silicon*. J. Physical Review Letters, 1960. 4(7): p. 361.
65. Atzmüller, H., F. Fröschl, and U. Schröder, *Theory of excitons bound to neutral impurities in polar semiconductors*. Physical Review B, 1979. 19(6): p. 3118.

66. Sharma, R.R. and S. Rodriguez, *Theory of excitons bound to ionized impurities in semiconductors*. Physical Review, 1967. 153(3): p. 823.
67. Look, D.C. and J.C. Manthuruthil, *Electron and hole conductivity in $CuInS_2$*. Journal of Physics Chemistry of Solids, 1976. 37(2): p. 173-180.
68. Spindler, C., et al., *Excitation-intensity dependence of shallow and deep-level photoluminescence transitions in semiconductors*. Journal of Applied Physics, 2019. 126(17): p. 175703.
69. Schmidt, T., K. Lischka, and W. Zulehner, *Excitation-power dependence of the near-band-edge photoluminescence of semiconductors*. Physical Review B, 1992. 45(16): p. 8989.
70. Alkauskas, A., M.D. McCluskey, and C.G. Van de Walle, *Tutorial: Defects in semiconductors - Combining experiment and theory*. Journal of Applied Physics, 2016. 119(18): p. 181101.
71. Reshchikov, M., et al., *Two yellow luminescence bands in undoped GaN*. J Scientific reports, 2018. 8(1): p. 1-11.
72. Mooney, J. and P. Kambhampati, *Get the basics right: Jacobian conversion of wavelength and energy scales for quantitative analysis of emission spectra*. The Journal of Physical Chemistry Letters, 2013. 4: p. 3316–3318.
73. Regesch, D., *Photoluminescence and solar cell studies of chalcopyrites. Comparison of Cu-rich vs. Cu-poor and polycrystalline vs. epitaxial material,* 2014, University of Luxembourg,Esch-sur-Alzette,Luxembourg, PhD Thesis,
74. Binsma, J., L. Giling, and J. Bloem, *Luminescence of $CuInS_2$: I. The broad band emission and its dependence on the defect chemistry*. Journal of Luminescence, 1982. 27(1): p. 35-53.
75. Ueng, H. and H. Hwang, *The defect structure of $CuInS_2$. Part I: Intrinsic defects*. Journal of Physics and Chemistry of Solids, 1989. 50(12): p. 1297-1305.
76. Töpper, K., et al., *Effects of post-deposition treatment on the PL spectra and the hydrogen content of $CuInS_2$ absorber layers*. Solar energy materials solar cells, 1997. 49(1-4): p. 383-390.
77. Luck, I., et al., *Influence of Na on the properties of Cu-rich prepared $CuInS_2$ thin films and the performance of corresponding $CuInS_2$/CdS/ZnO solar cells*. Solar energy materials solar cells, 2001. 67(1-4): p. 151-158.
78. Yuan, Z.K., et al., *Na-diffusion enhanced p-type conductivity in Cu(In,Ga)Se_2: A new mechanism for efficient doping in semiconductors*. Advanced Energy Materials, 2016. 6(24): p. 1601191.
79. Kneisel, J., et al., *Admittance spectroscopy of efficient $CuInS_2$ thin film solar cells*. Journal of Applied Physics, 2000. 88(9): p. 5474-5481.
80. Siemer, K., et al., *Defect Distribution of $CuInS_2$ solar sells from different preparation processes as determined by admittance spectroscopy*. Japanese Journal of Applied Physics, 2000. 39(S1): p. 270.
81. Siemer, K., et al., *DLTS measurements on $CuInS_2$ solar cells*. Thin Solid Films, 2001. 387(1-2): p. 222-224.
82. Eberhardt, J., et al., *Epitaxial and polycrystalline $CuInS_2$ thin films: a comparison of opto-electronic properties*. Thin Solid Films, 2007. 515(15): p. 6147-6150.
83. Heyd, J., G.E. Scuseria, and M. Ernzerhof, *Hybrid functionals based on a screened Coulomb potential*. The Journal of chemical physics, 2003. 118(18): p. 8207-8215.
84. Pohl, J. and K. Albe, *Intrinsic point defects in $CuInSe_2$ and $CuGaSe_2$ as seen via screened-exchange hybrid density functional theory*. Physical Review B, 2013. 87(24): p. 245203.
85. Saniz, R., et al., *Structural and electronic properties of defects at grain boundaries in $CuInSe_2$*. Physical Chemistry Chemical Physics, 2017. 19(22): p. 14770-14780.

86. Huang, B., et al., *Origin of Reduced Efficiency in Cu(In,Ga)Se$_2$ solar sells with high Ga concentration: alloy solubility versus intrinsic defects.* IEEE Journal of Photovoltaics, 2013. 4(1): p. 477-482.

87. Yee, Y.S., et al., *Deep recombination centers in Cu$_2$ZnSnSe$_4$ revealed by screened-exchange hybrid density functional theory.* Physical Review B, 2015. 92(19): p. 195201.

88. Malitckaya, M., et al., *First-Principles Modeling of Point Defects and Complexes in Thin-Film Solar-Cell Absorber CuInSe$_2$.* Advanced Electronic Materials, 2017. 3(6): p. 1600353.

89. Spindler, C., *Optical detection of deep defects in Cu(In,Ga)Se$_2$,* 2018, University of Luxembourg,Esch-sur-Alzette,Luxembourg, PhD Thesis, http://hdl.handle.net/10993/37016.

90. Spindler, C., et al., *Electronic defects in Cu(In,Ga)Se$_2$: Towards a comprehensive model.* Physical Review Materials, 2019. 3(9): p. 090302.

91. Chen, H., et al., *First-principles study of point defects in solar cell semiconductor CuInS$_2$.* Journal of Applied Physics, 2012. 112(8): p. 084513.

92. Yang, P., et al., *Tuning to the band gap by complex defects engineering: insights from hybrid functional calculations in CuInS$_2$.* Journal of Physics D: Applied Physics, 2017. 51(2): p. 025105.

93. Pohl, J. and K. Albe, *Thermodynamics and kinetics of the copper vacancy in CuInSe$_2$, CuGaSe$_2$, CuInS$_2$, and CuGaS$_2$ from screened-exchange hybrid density functional theory.* Journal of Applied Physics, 2010. 108(2): p. 023509.

94. Han, M., et al., *Defect physics in intermediate-band materials: Insights from an optimized hybrid functional.* Physical Review B, 2017. 96(16): p. 165204.

95. Maissel, L.I., R. Glang, and P.P. Budenstein, *Handbook of thin film technology.* Journal of The Electrochemical Society, 1971. 118(4): p. 114C.

96. Ruckh, M., et al., *Thermal decomposition of ternary chalcopyrite thin films.* Japanese Journal of Applied Physics, 1993. 32(S3): p. 65.

97. Neumann, H. and G. Kühn, *Thermal decomposition of CuInSe$_2$.* Journal of the Less Common Metals, 1989. 155(1): p. L13-L17.

98. Wiedemeier, H. and R. Santandrea, *Mass spectrometric studies of the decomposition and the heat of formation of CuInS$_2$(s).* Zeitschrift für anorganische und allgemeine Chemie, 1983. 497(2): p. 105-118.

99. Meyer, B., *Elemental sulfur.* Chemical Reviews, 1976. 76(3): p. 367-388.

100. Scheer, R., et al., *CuInS$_2$ based thin film photovoltaics.* Solar Energy, 2004. 77(6): p. 777-784.

101. Kaigawa, R., et al., *Improved performance of thin film solar cells based on Cu(In,Ga)S$_2$.* Thin Solid Films, 2002. 415(1-2): p. 266-271.

102. Elanzeery, H., et al., *Challenge in Cu-rich CuInSe$_2$ thin film solar cells: Defect caused by etching.* Physical Review Materials, 2019. 3(5): p. 055403.

103. Deprédurand, V., et al., *Current loss due to recombination in Cu-rich CuInSe$_2$ solar cells.* Journal of Applied Physics, 2014. 115(4): p. 044503.

104. Oja, I., et al., *Crystal quality studies of CuInS$_2$ films prepared by spray pyrolysis.* Thin Solid Films, 2005. 480: p. 82-86.

105. Luck, I.V., et al., *Growth Monitoring of Cu-Poor Prepared CuInS$_2$ Thin Films.* MRS Online Proceedings Library Archive, 2001. 668.

106. Scheer, R., K. Diesner, and H.-J. Lewerenz, *Experiments on the microstructure of evaporated CuInS$_2$ thin films.* Thin solid films, 1995. 268(1-2): p. 130-136.

107. Stange, H., et al., *Stacking fault reduction during annealing in Cu-poor $CuInSe_2$ thin film solar cell absorbers analyzed by in situ XRD and grain growth modeling.* Journal of Applied Physics, 2019. 125(3): p. 035303.
108. Mainz, R., et al., *Annihilation of structural defects in chalcogenide absorber films for high-efficiency solar cells.* Energy Environmental Science, 2016. 9(5): p. 1818-1827.
109. Rodriguez-Alvarez, H., et al., *Recrystallization of $Cu(In,Ga)Se_2$ thin films studied by X-ray diffraction.* Acta Materialia, 2013. 61(12): p. 4347-4353.
110. Pujar, V.V. and J.D. Cawley, *Effect of stacking faults on the X-ray diffraction profiles of β-SiC powders.* Journal of the American Ceramic Society, 1995. 78(3): p. 774-782.
111. Paorici, C., L. Zanotti, and L. Gastaldi, *Preparation and structure of the $CuIn_5S_8$ single-crystalline phase.* Materials Research Bulletin, 1979. 14(4): p. 469-472.
112. Schwarz, T., et al., *On the chemistry of extended defects in $CuInS_2$ films.* in preparation, 2020.
113. Abou-Ras, D., et al., *Compositional and electrical properties of line and planar defects in $Cu(In,Ga)Se_2$ thin films for solar cells–a review.* Physica status solidi – Rapid Research Letters, 2016. 10(5): p. 363-375.
114. Nicoara, N., et al., *Direct evidence for grain boundary passivation in $Cu(In,Ga)Se_2$ solar cells through alkali-fluoride post-deposition treatments.* Nature communications, 2019. 10(1): p. 1-8.
115. Keutgen, J., O. Cojocaru-Mirédin, and M. Raghuwanshi, *Using Correlative EBIC-EBSD-APT to Identify Limitations in $Cu(In,Ga)Se_2$ Photovoltaic Cells*, in *MRS*. 2019: Phoenix.
116. Regesch, D., et al., *Degradation and passivation of $CuInSe_2$.* Applied Physics Letters, 2012. 101(11): p. 112108.
117. Babbe, F., L. Choubrac, and S. Siebentritt, *Quasi Fermi level splitting of Cu-rich and Cu-poor $Cu(In,Ga)Se_2$ absorber layers.* Applied Physics Letters, 2016. 109(8): p. 082105.
118. Hölscher, T., et al., *Light induced degradation of $Cu(In,Ga)Se_2$ thin film surfaces.* Applied Physics Letters, 2017. 111(1): p. 011604.
119. Nelson, A.J., et al., *Characterization of the native oxide of $CuInSe_2$ using synchrotron radiation photoemission.* Applied Physics Letters, 1990. 57(14): p. 1428-1430.
120. Kazmerski, L., et al., *Initial oxidation of $CuInSe_2$.* Journal of Vacuum Science Technology, 1981. 19(3): p. 467-471.
121. Colombara, D., et al., *Chemical instability of chalcogenide surfaces: technological impact well beyond the surface.* Submitted, 2019.
122. Knacke, O., O. Kubaschewski, and K. Hesselmann, *Thermochemical properties of inorganic substances*. Vol. 1. 1991: Springer.
123. Cahen, D. and R. Noufi, *Free energies and enthalpies of possible gas phase and surface reactions for preparation of $CuInSe_2$.* Journal of Physics Chemistry of Solids, 1992. 53(8): p. 991-1005.
124. Sood, M., et al., *Passivating surface defects in Cu-rich copper indium disulfide solar cells using sulfur treatment.* submitted, 2020.
125. Lomuscio, A., et al., *Quasi-Fermi-Level Splitting of Cu-Poor and Cu-Rich $CuInS_2$ Absorber Layers.* Physical Review Applied, 2019. 11(5): p. 054052.
126. Lomuscio, A., M. Melchiorre, and S. Siebentritt. *Influence of stoichiometry and temperature on quasi Fermi level splitting of sulfide CIS absorber layers*. in *2018 IEEE 7th World Conference on Photovoltaic Energy Conversion (WCPEC)(A Joint Conference of 45th IEEE PVSC, 28th PVSEC & 34th EU PVSEC)*. 2018. IEEE.
127. Siebentritt, S., et al., *Why do we make $Cu(In,Ga)Se_2$ solar cells non-stoichiometric?* Solar Energy Materials Solar Cells, 2013. 119: p. 18-25.
128. Wolter, M.H., et al., *Correcting for interference effects in the photoluminescence of $Cu(In,Ga)Se_2$ thin films.* physica status solidi c, 2017. 14(6): p. 1600189.

129. Wolter, M., et al., *Applying a surface treatment to semiconducting thin films to eliminate interference effects* submitted, 2020.
130. Reshchikov, M., et al., *Two yellow luminescence bands in undoped GaN.* Scientific reports, 2018. 8(1): p. 1-11.
131. Braunger, D., et al. *Improved open circuit voltage in CuInS$_2$ based solar cells.* in *Conference Record of the Twenty Fifth IEEE Photovoltaic Specialists Conference*. 1996. Washington, DC, USA IEEE.
132. Turcu, M., O. Pakma, and U. Rau, *Interdependence of absorber composition and recombination mechanism in Cu(In,Ga)(Se,S)$_2$ heterojunction solar cells.* Applied Physics Letters, 2002. 80(14): p. 2598-2600.
133. Merdes, S., et al., *Recombination mechanisms in highly efficient thin film Zn(S,O)/Cu(In,Ga)S$_2$ based solar cells.* Applied Physics Letters, 2009. 95(21): p. 213502.
134. Gütay, L., et al., *Feedback mechanism for the stability of the band gap of CuInSe$_2$.* Physical Review B, 2012. 86(4): p. 045216.
135. Babbe, F., *Optical analysis of efficiency limitations of Cu(In,Ga)Se$_2$ grown under copper excess,* 2019, University of Luxembourg,Esch-sur-Alzette,Luxembourg, PhD Thesis,
136. Vidal, J., et al., *Strong interplay between structure and electronic properties in CuIn(S,Se)$_2$: a first-principles study.* Physical review letters, 2010. 104(5): p. 056401.
137. Klenk, R., et al., *Solar cells based on CuInS$_2$ - an overview.* Thin Solid Films, 2005. 480: p. 509-514.
138. Watanabe, T. and T. Yamamoto, *Control of defects in CuInS$_2$ thin films by incorporation of Na and O.* Japanese Journal of Applied Physics, 2000. 39(12B): p. L1280.
139. Kaigawa, R., T. Wada, and R. Klenk, *The microstructure of Cu(In,Ga)S$_2$ solar cell absorber films prepared using three-stage and two-stage evaporation.* Thin Solid Films, 2008. 516(20): p. 7046-7050.
140. Marsen, B., et al., *Effect of copper-deficiency on multi-stage co-evaporated Cu(In,Ga)S$_2$ absorber layers and solar cells.* Thin Solid Films, 2011. 519(21): p. 7224-7227.
141. Babbe, F., et al., *Potassium fluoride postdeposition treatment with etching step on both Cu-rich and Cu-poor CuInSe$_2$ thin film solar cells.* Physical Review Materials, 2018. 2(10): p. 105405.
142. Carron, R., et al., *Advanced Alkali Treatments for High-Efficiency Cu(In,Ga)Se$_2$ Solar Cells on Flexible Substrates.* Advanced Energy Materials, 2019: p. 1900408.
143. Hellman, O.C. and D.N. Seidman, *Measurement of the Gibbsian interfacial excess of solute at an interface of arbitrary geometry using three-dimensional atom probe microscopy.* J Materials Science Engineering: A, 2002. 327(1): p. 24-28.
144. Hiroi, H., et al., *Progress toward 1000-mV open-circuit voltage on chalcopyrite solar cells.* IEEE Journal of Photovoltaics, 2016. 6(6): p. 1630-1634.
145. Wolter, M., *Optical investigation of voltage losses in high-efficiency Cu(In,Ga)Se$_2$ thin-film solar cells,* 2019, University of Luxembourg,Esch-sur-Alzette,Luxembourg, PhD Thesis,
146. Lomuscio, A., et al., *Phonon coupling and shallow defects in CuInS$_2$.* Physical Review B, 2020. 101(8): p. 085119.
147. Lomuscio, A., M. Sood, and S. Siebentritt, *Detection of a third shallow acceptor in CuInS$_2$ through NaF incorporation* in preparation, 2020.
148. Yakushev, M., et al., *Energy of excitons in CuInS$_2$ single crystals.* Applied physics letters, 2006. 88(1): p. 011922.
149. Haynes, J.R., *Experimental observation of the excitonic molecule.* Physical Review Letters, 1966. 17(16): p. 860.

150. Yu, P.Y. and M. Cardona, *Fundamentals of semiconductors: physics and materials properties*. 2010: Springer.
151. Koschel, W. and M. Bettini, *Zone-centered phonons in AIBIIIS2 chalcopyrites*. Physica status solidi, 1975. 72(2): p. 729-737.
152. Wakita, K., et al., *Resonant Raman scattering and luminescence in* $CuInS_2$ *crystals*. Journal of applied physics, 1998. 83(1): p. 443-447.
153. Siebentritt, S. and U. Rau, *Wide-gap chalcopyrites*. Vol. 1. 2006: Springer.
154. Colombara, D., et al., *Deliberate and accidental gas-phase alkali doping of chalcogenide semiconductors:* $Cu(In,Ga)Se_2$. Scientific reports, 2017. 7(1): p. 1-18.
155. Eberhardt, J., et al., *Defect-related photoluminescence of epitaxial* $CuInS_2$. Thin Solid Films, 2005. 480: p. 415-418.
156. Yamamoto, T., T. Watanabe, and Y. Hamashoji, *Effects of codoping using Na and O on Cu–S divacancy in p-type* $CuInS_2$. Physica B: Condensed Matter, 2001. 308: p. 1007-1010.
157. Zacks, E. and A. Halperin, *Dependence of the peak energy of the pair-photoluminescence band on excitation intensity*. Physical Review B, 1972. 6(8): p. 3072.
158. Spindler, C., D. Regesch, and S. Siebentritt, *Revisiting radiative deep-level transitions in* $CuGaSe_2$ *by photoluminescence*. Applied Physics Letters, 2016. 109(3): p. 032105.
159. Siebentritt, S., et al., *Do we really need another PL study of* $CuInSe_2$*?* physica status solidi, 2004. 1(9): p. 2304-2310.
160. Bauknecht, A., et al., *Radiative recombination via intrinsic defects in* $Cu_xGa_ySe_2$. Journal of Applied Physics, 2001. 89(8): p. 4391-4400.
161. Babbe, F., et al., *The hunt for the third acceptor in* $CuInSe_2$ *and* $Cu(In,Ga)Se_2$ *absorber layers*. Journal of Physics: Condensed Matter, 2019. 31(42): p. 425702.
162. Bertram, T., V. Depredurand, and S. Siebentritt. *In-Se surface treatment of Cu-rich grown* $CuInSe_2$. in *2014 IEEE 40th Photovoltaic Specialist Conference (PVSC)*. 2014. IEEE.
163. Paszkowicz, W., et al., *Thermal expansion of* $CuInSe_2$ *in the 11–1073 K range: an X-ray diffraction study*. Applied Physics A, 2014. 116(2): p. 767-780.
164. Makovetskaya, L., et al., *Thermal conductivity, thermoelectric power, and thermal expansion of* $CuInS_{2x}/Se_{2(1-x)}$. Physica Status Solidi A: Applied Research, 1982. 74(1): p. K59-K62.
165. Bansal, N.P. and R.H. Doremus, *Handbook of glass properties*. 2013: Elsevier.